The high grade Mo-Re Merlin deposit, Cloncurry District, Australia

Thesis submitted by:

João Babo BSc. (Hons)

August 2014

for the degree of Doctor of Philosophy

in the School of Earth and Environmental Sciences

James Cook University, Australia

Abstract

The Mount Dore and Merlin deposit, discovered in 2008 by Chinova Resources (previously Ivanhoe Australia), is the world's highest grade Mo-Re deposit. The deposit is located in the Cloncurry District of the Mount Isa Inlier, Australia; a region renowned for its IOCG type mineralization. In the same year the Lanham's Shaft prospect, another Mo-rich occurrence was found 50 km to the north of the Merlin deposit. These discoveries have created a new exploration paradigm, and this thesis represents the first in-depth study of this new mineralization type. This work integrates detail core logging, petrography, geochronology, and trace element and isotope geochemistry.

The Mount Dore and Merlin deposit is hosted by the Proterozoic Kuridala Formation metasedimentary package, which is composed of interbedded phyllites and carbonaceous slates above calc-silicate rocks, and silicified siltstones at the footwall. The Mount Dore granite is thrust above the metasedimentary rocks and overlies the bulk of the mineralization. The mineralization consists of a Cu-polymetallic stage (chalcopyrite ± sphalerite ±± galena) (Mount Dore) mainly hosted by the carbonaceous slates in angular clast-supported carbonate breccias, and Mo-Re mineralization (Merlin) that locally cuts the Cu-polymetallic mineralization, mainly along or near rheologic boundaries between the carbonaceous slates and the calc-silicate rocks. The bulk of the Mo-Re appears as infill of matrix-supported breccias with rounded clasts.

The hydrothermal alteration is highly complex, consisting of three main stages, from oldest to youngest: Na-(Ca), Cu-polymetallic, and Mo-Re. These stages were dated using U-Pb in titanite and Re-Os in molybdenite at the Mount Dore and Merlin deposit and at the Lanham's Shaft prospect.

The Na-(Ca) alteration (1557 ± 18 Ma) is similar to a regional Na-(Ca) alteration event with formation of albite + amphibole ± quartz ± titanite ± apatite ± carbonates. The alteration fluids are interpreted to be bittern brine(s) and the widespread regional Na-(Ca) alteration is thought of having been responsible for the release of potassium, iron, barium, and possibly copper and carbonate from the regional metasedimentary rocks.

The Cu-polymetallic mineralization is accompanied by K-feldspar + tourmaline + carbonates ± quartz. This alteration stage is also interpreted to have formed by a bittern brine fluid that reacted with the metasedimentary host rocks. This reaction resulted in a strong decrease in the fO_2 of the fluid, due to the minor graphite contained in the carbonaceous

slates that host the Cu-polymetallic mineralization. The fO_2 drop is proposed as the main chemical mechanism responsible for the sulfide precipitation, and the sulfur was sourced from both the bittern brine and the metasedimentary host rocks. Zinc, and at least part of the Pb and Ag, was possibly sourced from the carbonaceous slates.

The third hydrothermal stage can be subdivided into three events, with the first and main event being responsible for the bulk of the Mo-Re mineralization and the last two events being remobilizations of the first event.

The main Mo-Re event occurred at ~1535 Ma and formed the strongly mineralized breccias that were accompanied by K-feldspar ± chlorite alteration. Fluid derived from a Williams-Naraku type felsic intrusive is proposed as the source of the mineralization with ore mineral precipitation triggered by a strong to moderate fO_2 drop during fluid reaction with the metasedimentary host rocks. Again, the sulfur is thought to be derived from both the mineralizing fluid and the host rocks.

The second, relatively minor, Mo-Re event occurred at ~1521 Ma and formed veins and disseminations that extend from the Mo-Re breccias into the calc-silicate rocks for several metres. This event is inferred to have developed from the previously formed Mo-Re mineralization by remobilization, due to the emplacement of the Mount Dore granite (~1517 Ma), with formation of K-feldspar + chlorite ± apatite ± rutile ±± monazite. A fO_2 drop was again the ore precipitation mechanism, but the fO_2 decrease was not as strong in this mineralization, due to the relatively oxidized nature of the calc-silicate host rocks compared to the proximity (partly hosting) of the bulk of the Mo-Re mineralization to the carbonaceous slates. The sulfur was sourced from the previously formed molybdenite and therefore both mineralization styles have similar $\delta^{34}S$ signatures.

A very minor Mo-Re event occurred at ~1500 Ma and consists of millimetric Mo-Re veins in carbonate ± chlorite veins. This event was likely formed in response to the thrust of the Mount Dore granite over the metasedimentary host rocks, which is possibly responsible for the formation of the molybdenite stylolitic veins, which are a common feature in the deposit.

The Lanham's Shaft prospect displays a similar hydrothermal alteration evolution, except that significant remobilization of the Mo-rich mineralization did not occur at this location. However, the absolute timing of the Na-(Ca) alteration (~1575 Ma) and Mo-rich mineralization (~1560 Ma) is earlier than at the Mount Dore and Merlin deposit. These older ages indicate the existence of hydrothermal activity with mineralizing capability during a time period that has previously been regarded as unprospective for ore deposit formation. The

mineralization at the prospect is less abundant in grade and tonnage than the deposit, consisting of mineralized veins. The bulk of the Cu-rich and Mo-rich veins are a few metres from the carbonaceous slates, hosted in calc-silicate rocks. The distance of the mineralization to the graphitic rocks resulted in a weaker fO_2 drop in both stages. The mineralizing fluids are interpreted as also felsic igneous sourced and mixing of sulfur between the fluids and the metasedimentary rocks also occurred.

The Merlin and Mount Dore and Lanham's Shaft mineralization have clear spatial and temporal affinities with IOCG mineralization in the Cloncurry District. Broad genetic relationships between these mineralization styles are also likely, so a denomination for this this new mineralization style is proposed as *Mo-rich IOCG type deposits*. The key criteria and ingredients for such deposits are: 1. Mo-rich felsic igneous source(s) and; 2. Suitable tectonic trap(s) contained within, or at close proximity to, reduced host rocks (e.g. carbonaceous or graphitic metasedimentary rocks).

Statement of Access

I, the undersigned, the author of this thesis, understand that the following restriction placed by Ivanhoe Mines Ltd on this thesis will not extend beyond four years from submission.

Ivanhoe Mines Ltd wishes to place restriction on access to this thesis as follows:

"Access not to be permitted by a period of two years with a subsequent two years period were authorization has be granted by a qualified officer of Ivanhoe Mines Ltd"

After this period has elapsed I understand that James Cook University will make it available for use within the University Library and, by microfilms or other photographic means, allow access to users in other approved libraries. All users consulting this thesis will have to sign the following statement:

> *"In consulting this thesis I agree not to copy or closely paraphrase it in whole or part without the written consent of the author; and to make proper public written acknowledgement for any assistance which I have obtained from it."*

_____ _____

Signature Date

Statement of Sources Declaration

I declare that this thesis is my own work and has not been submitted in any form for another degree or diploma at any university or other institution of tertiary education. Information derived from the published or unpublished work of other has been acknowledged in the text and a list of references is given.

_____ _____

Signature Date

Acknowledgments

I wish to thank Ivanhoe Australia Ltd. for their financial and logistical support. I appreciate greatly the opportunity of studying the unique Merlin deposit. The entire Ivanhoe Australia Ltd. staff was very helpful but I wish to extend a particular thanks to Tosi Firman, Graeme Corlett and Duncan Spring.

The supervision by Carl Spandler, Nick Oliver, Mike Rubenach, and Mat Brown was beyond the scientific and technical assistance. Their supervision was in all professional aspects outstanding, but I would like to thank them also for the emotional support given.

I also would like to mention the support and useful discussions provided by the JCU lectures and all the logistical help provided by the JCU staff, with a special mention to Adella Edwards, Andrew Norton, Beth Moore, Christa Placzek, Judy Botting, Kevin Blake, Melissa Crawford, Rebecca Steele, Tom Blenkinsop, and Yi Hu.

I wish to extend thanks to Nicolas Greber of the University of Bern, Switzerland and Robert Creaser of the University of Alberta, Canada for their analytical expertise and all the help provided.

I wish to recognise my appreciation for **all** my colleagues and friends, with a special thanks to Cassian Pirard for all the smoke breaks and his help in keeping me sane.

I wish to thank my flatmates for a few months and friends for life: Maria and Jesse who helped me drink the wine.

Thanks to my mother, father and sister; and to Gaston LaGaffe the cat that will be missed.

Thank you for the internet conversations at the oddest hours of the night during the long thesis writing: Joao Baltazar and Lara Niny my dearest friends.

This thesis is dedicated to my grandmother.

Table of Contents

Appendices:

Digital appendices:

1. Chapter 1: Introduction

1.1. Thesis Rationale

In 2008, Chinova Resources (previously Ivanhoe Australia), discovered high grade Mo-Re mineralization during the drill out of the Cu-(Au) Mount Dore deposit in the Cloncurry District, Mt Isa Inlier. This discovery proved to be of extreme significance with the now designated Mount Dore and Merlin deposit having the highest Mo-Re grades of any orebody in the world. Besides its economic value, it also created an entirely new metalliferous exploration paradigm, since the Cloncurry District is well known for its IOCG deposits, but significant Mo-Re mineralization had not previously been found.

Another discovery of Mo-rich mineralization located 50 km north of the Mount Dore and Merlin deposit was also made in 2008 by Ivanhoe Australia. This prospect, named the Lanham's Shaft prospect, demonstrated the potential for further Mo-rich mineralization finds in the region. Furthermore, similarities between these Mo-rich occurrences and IOCG deposits in the region, such as Na-(Ca) hydrothermal alteration followed by potassic alteration accompanied by Cu-rich mineralization, indicates a possible genetic link between this new mineralization type and the IOCGs (*sensu lato*) in the region.

1.2. Thesis aims

Since both the Mount Dore and Merlin deposit and the Lanham's Shaft prospect are recent finds, very little research work has been done thus far. Therefore, the objective of this study is to create a first body of knowledge on this new mineralization and to investigate possible genetic links with the IOCG deposits in the region. The approach of this study was:

1. To characterize the hydrothermal alteration and mineralization styles at the Mount Dore and Merlin, and Lanham's Shaft.
2. To date the Mount Dore granite which overlies the metasedimentary host rocks at the Mount Dore and Merlin deposit, in order to confirm or deny a possible genetic link between the intrusive and the mineralization.
3. To date the regional Na-(Ca) hydrothermal alteration event at the Mount Dore and Merlin, and Lanham's Shaft.
4. To date the Mo-rich mineralization at the Mount Dore and Merlin, and Lanham's Shaft.

5. To define the hydrothermal fluid/s source/s for the Na-(Ca) alteration, the Cu-rich mineralization, and the Mo-rich mineralization at the Mount Dore and Merlin, and Lanham's Shaft.
6. To characterize ore precipitation mechanisms at the Mount Dore and Merlin, and Lanham's Shaft.
7. To compare and contrast the Mount Dore and Merlin, and Lanham's Shaft with the IOCG deposits in the region.
8. To create an ore genesis model for this mineralization type that can aid in the definition of exploration parameters.

1.3. Thesis Structure

This thesis adopts a classical PhD thesis format beginning with introductory chapters outlining the thesis aims, methods and regional geological setting, followed by chapters detailing the core work of the thesis, and a closing chapter that summarizes the thesis work and presents an overarching ore genesis model. Large data sets and additional information are included as appendices. Tables of the samples selected for analyses can be consulted in Appendix 2. More details on chapter contents are given below.

Chapter 1 – Introduction and methods.

Chapter 2 – Regional geology overview of the main igneous, metamorphic, tectonic and hydrothermal events with special focus on the renowned IOCG ore deposits in the area.

Chapter 3 – The local geology description, hydrothermal alteration and mineralization characterization of the Mount Dore and Merlin deposit. The geologic units in the area are described in detail as well as the ore geometry and general tectonic model. The hydrothermal alteration and mineralization styles are characterized and presented as different stages divided by their relative timing and location in the deposit. These descriptions were achieved from the core logging and sampling (Digital Appendix), petrography and electron microprobe work. Ore and hydrothermal alteration geometry was also aided by use of 3D modelling software.

Chapter 4 – Lanham's and Barnes Shafts prospects local geology mapping and description. Core logging and sampling was conducted at the Lanham's and Barnes Shafts (Digital

Appendix), and petrography at the Lanham's Shaft. The hydrothermal alteration and mineralization styles are described and compared to the Mount Dore and Merlin deposit.

Chapter 5 – Details of the geochronology conducted at the Mount Dore and Merlin deposit, and Lanham's Shaft prospect. The ages obtained are interpreted according to the regional setting and compared with other ore deposits in the area. U-Pb analyses in titanite allowed for the dating of the Na-(Ca) hydrothermal alteration stage which preceded both the Cu-rich mineralization and the subsequent Mo-rich mineralization at both the Mount Dore and Merlin and Lanham's Shaft. Re-Os dating of molybdenite in both locations was also done, taking in consideration the complexities of these ore systems and the different molybdenite mineralization styles present. The Mount Dore granite was dated by use of U-Pb systematics in zircon grains. The dating of the granite was intended to test any potential temporal and/or genetic link with the Mount Dore and Merlin mineralization.

Chapter 6 – Characterization of the fluid/s source/s and evolution of the mineralization using sulfur, molybdenum and Sm-Nd isotope studies. Sulfur isotope analyses of chalcopyrite, pyrite and molybdenite of the Mount Dore and Merlin deposit and the Lanham's and Barnes Shafts prospects allow interpretation of the sulfur source/s in these three localities. Mo isotopes of the Mount Dore and Merlin deposit were compared with other deposit types and Earth reservoirs. Sm-Nd isotope studies at the Mount Dore and Merlin deposit focused on apatite and titanite grains formed during each hydrothermal alteration stage, and compared with a regional data set, for the interpretation of fluid source/s. The isotope studies assisted in the delineation of the most likely model of fluid source/s and evolution for the defined hydrothermal alteration and mineralization stages.

Chapter 7 – Trace element geochemistry of chalcopyrite, pyrite and molybdenite of the Mount Dore and Merlin deposit, and the Lanham's Shaft prospect, with applications to characterization of mineralization stages and interpretation of ore precipitation mechanisms.

Chapter 8 – Conclusions, ore genesis model and exploration recommendations.

1.4. Methods

Electron Microprobe analysis

After detailed petrographic descriptions of thin sections under transmitted and reflected light microscope techniques, selected polished thin sections were examined by electron microprobe. Backscattered electron imaging and qualitative EDS phase analysis were conducted using a JEOL JXA8200 superprobe with 5 WD spectrometers, EDS and XCLent CL system, housed at the Advanced Analytical Centre, James Cook University (JCU), Townsville, Australia. Instrument running conditions were set to 20 nA beam current and 15 kV acceleration voltage. Cathodoluminescense (CL) wavelength mapping of apatite grains was also conducted with the superprobe.

U-Pb zircon and titanite dating

Sections of drillcore selected for U/Pb dating were crushed using a W-C plate and jaw crushed and then sieved to collect the <500 μm grainsize portion. Separates were then run through a Frantz magnetic separator and heavy liquid methods, before zircon or titanite grains were handpicked, mounted into epoxy resin blocks and polished to about half of their thickness. Prior to analysis, zircon or titanite grains were imaged using a Jeol JSM5410LV Scanning Electron Microscope with attached cathodoluminescence detector (AAC, JCU) in order to identify zonational domains and inherited cores within the grains. U–Pb isotope analyses were obtained using a GeoLas 200 Excimer Laser Ablation System in a He ablation atmosphere, coupled to a Varian ICP-MS 820 series instrument at JCU. Laser Energy at the ablation site was ~b6 J cm^{-2}. Analysis involved 30 seconds of background measurement (gas blank) followed by 35 seconds acquisition of U-Pb isotope data using either a 32 or 24 μm beam diameter. All data were processed used GLITTER^{TM} software (Jackson et al., 2004).

Zircon analysis

U–Pb fractionation was corrected using the GJ1 as the primary standard, and FC1 and Temora zircon was used as secondary running standards. A number of zircon grains were excluded from analysis due to metamictisation and small grain size. Data was processed

using the software package GLITTER™ (Jackson et al., 2004) and age calculations were made using Isoplot (Ludwig, 2003).

Titanite

U–Pb fractionation was corrected using the GJ1 zircon as the primary standard and FC1 zircon (Paces and Miller, 1993), Temora zircon. To check for any matrix-related fractionation effects we plotted the U/Pb analytical signal of the GJ1 zircon standard and titanite samples in Figure 1:1. The downhole fractionation of U from Pb (represented by time) was similar for both the GJ1 zircon and titanite samples, indicating an insignificant matrix effect during ablation, which demonstrates that the GJ1 Zircon is a suitable external standard for accurate titanite U/Pb age analysis.

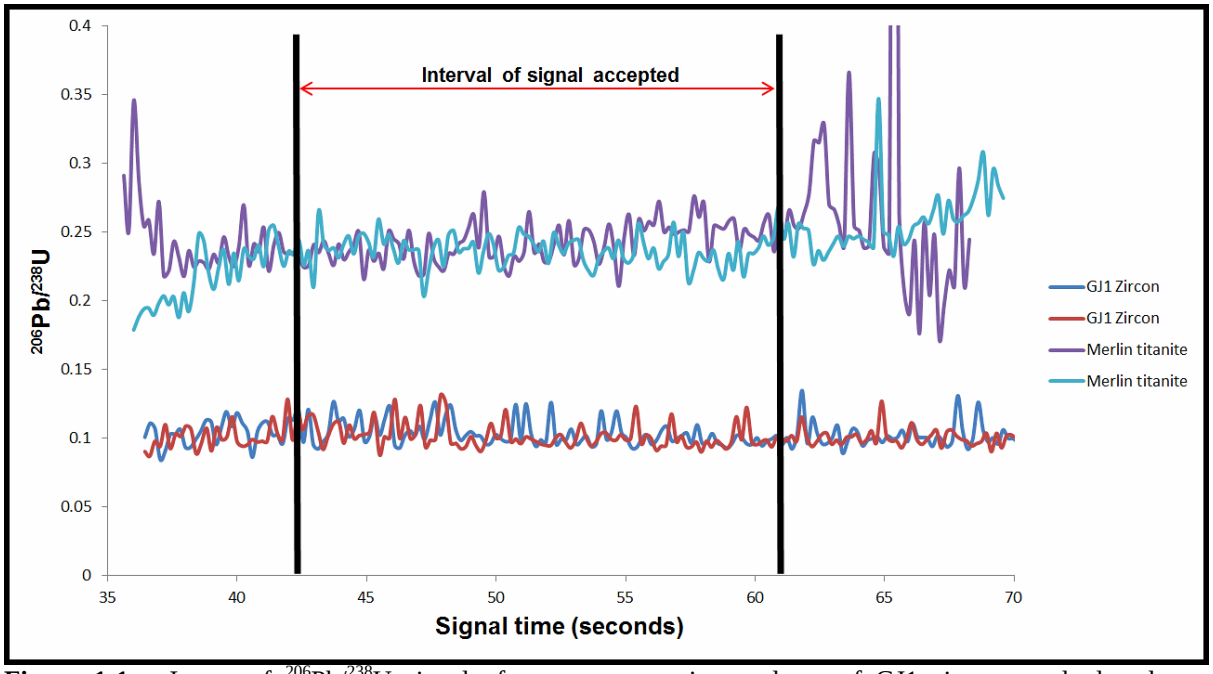

Figure 1:1 – Image of $^{206}Pb/^{238}U$ signal of two representative analyses of GJ1 zircon standard and two representative titanite grain analyses. The signals show that downhole fractionation of U from Pb is similar (over the integration interval between the two black lines) for the zircon standard and the titanite, which indicates that relaiable U/Pb ages can be obtained from titnaite using GJ1 zircon as primary standard.

Re-Os molybdenite dating

Metal-free crushing followed by gravity and magnetic concentration methods were used to obtain a molybdenite mineral separate. Methods used for molybdenite analysis were conducted by Robert Creaser at the University of Alberta, Canada, and are described in detail by Selby and Creaser (2004) and Markey et al. (2007). The ^{187}Re and ^{187}Os concentrations in

molybdenite were determined by isotope dilution mass spectrometry using Carius-tube, solvent extraction, anion chromatography and negative thermal ionization mass spectrometry techniques. A mixed double spike containing known amounts of isotopically enriched ^{185}Re, ^{190}Os, and ^{188}Os analysis is used. Isotopic analysis used a ThermoScientific Triton mass spectrometer by Faraday collector. Total procedural blanks for Re and Os are less than <3 picograms and 2 picograms, respectively, which are insignificant for the Re and Os concentrations in molybdenite. The Chinese molybdenite powder HLP-5 (Markey et al., 1998), is analyzed as a standard. For this control sample over a period of two years, an average Re-Os date of 221.56 ± 0.40 Ma (1SD uncertainty, n=10) is obtained. This Re-Os age date is identical to that reported by Markey et al. (1998) of 221.0 ± 1.0 Ma.

Sulfur isotope analyses

Sulfur isotope analyses were conducted by the GNS science laboratory in New Zealand. The samples were weighed out in duplicate in tin capsules with equal amounts of V_2O_5 and run on a EuroVector Elemental Analyser connected to a GVI IsoPrime mass spectrometer. All results are averages and standard deviations of duplicates are reported with respect to VCDT, normalized to our internal standards: R18742, R2268, and R2298 with reported values of -32.7‰, +3.3‰ and +8.6‰ respectively for $\delta^{34}S$. The analytical precision for this instrument is better than 0.2 ‰ for $\delta^{34}S$.

Molybdenite isotope analyses

All molybdenum isotope analyses were conducted on Molybdenite separates at the University of Bern, Switzerland. A ^{100}Mo-^{97}Mo double spike was used to enable corrections for mass biases induced during chemical separation and MC-ICP-MS measurement. The use of a double-spike allows for the simultaneous determination of the Mo isotope composition and the Mo concentration using isotope dilution. The $\delta^{98}Mo$ composition of all samples were analysed using a double focusing Nu Instruments TM MC-ICP-MS system (Wrexham, Wales, UK). Measurement procedure and double spike calibration are described in Greber et al. (2012), employing the double-spike mathematics outlined in Siebert et al. (2001). The precision under intermediate precision conditions is below ±0.1‰ (2SD) for both, liquid standards (see below) and the NIST SRM 610 and 612 glasses (Greber et al., 2012). The Johnson Matthey ICP standard solution (lot 602332B) was used as reference material. Its

δ^{98}Mo composition is 0.25‰ lower than the NIST SRM 3134 and 2.34‰ lower than the mean open ocean water Mo (Greber et al., 2012).

Sm-Nd isotope analyses of apatite and titanite grains

Sm-Nd isotope analyses were conducted using the methods of Hammerli et al. (2014). In situ isotopic analyses were carried out at the Advanced Analytical Centre at James Cook University (JCU) in Townsville, using a ThermoScientific NEPTUNE MC-ICP-MS coupled to a Geolas 193 nm ArF excimer laser. The faraday cup configuration is the same as that used by McFarlane and McCulloch (2007). In situ laser ablation analyses were conducted on polished thin sections over 60s with spot sizes of 60 to 120 μm, pulse rates of 4 Hz and a laser energy density at the sample site of 5–6 J/cm^2, as determined by an energy meter. Ablation was carried out in He (typical flow rate ~0.9 l/min), which was combined with Ar (~0.8 l/min, optimized daily) and N2 (~0.005 l/min) prior to transport into the torch. Interference and mass bias corrections were made according to the method of Fisher et al. (2011).

Trace element geochemistry of sulfides and apatite

Pyrite, chalcopyrite, molybdenite and apatite from polished sections and buttons were targeted for trace element analysis by laser ablation ICP-MS at JCU, using the instrumentation and tuning conditions as described above. The laser fluence was set to 6 J/cm^2 at the sample site with laser repetition rate and beam diameter set to 5 Hz, and 32 to 44 μm, respectively. Data reduction was completed using ^{95}Mo for molybdenite, ^{57}Fe for pyrite, ^{65}Cu for chalcopyrite, and ^{43}Ca for apatite, as the internal standard isotopes, and NIST SRM 612 or 610 as the bracketing external standard for molybdenite and chalcopyrite using the standard reference values of Spandler et al. (2011), MASS1 for pyrite, and NIST SRM 612 for apatite. MASS1 was used as a secondary running standard for chalcopyrite and molybdenite, NIST SRM 612 and 610 was used for pyrite and NIST SRM 610 for apatite.

2. Chapter 2: Regional Geology

2.1. Introduction

The recent discovery of the Merlin high grade Mo-Re deposit by Ivanhoe Australia and other green field exploration prospects, most notably the Lanham's Shaft prospect (Babo, 2009; Lazo and Pal, 2009; this study) has created a potential need to establish a new molybdenum mineralization style. The Merlin deposit occurs in a regional area renowned for its Iron-Oxide-Copper-Gold (IOCG) deposits but with no molybdenum-rich deposits until recently. Also the very high grades and mode of occurrence distinguish the Merlin deposit from previous recognized molybdenum rich deposits.

The deposit is hosted in Proterozoic metasedimentary rocks that are bounded by a shear-zone of intensely silicified siltstone at the footwall and an A-type quartz monzonite granite that is a thrust contact at the hanging wall. Smaller mafic and felsic sills intrude the metasedimentary units (Page and Sun, 1998; Wyborn, 1998; Mark et al. 2005a; Betts et al. 2006; Lazo and Pal, 2009; Kirkby, 2009; this study). The metasedimentary rocks host a copper-dominant mineralization above a molybdenum-dominant mineralization that partly overlap spatially (Lazo and Pal, 2009; Kirkby, 2009) the Cu-dominant mineralization that is older than the Mo-dominant one (Lazo and Pal, 2009; Kirkby, 2009; this study). The bulk of the molybdenite mineralization occurs as infill of matrix-supported breccias with rounded clasts but also in small veins (commonly stylolitic) and in disseminations (Lazo and Pal, 2009; Kirkby, 2009; this study) which indicates that the ore body geometry is structurally controlled. Although the geological trap is structural it does not explain the very high grade molybdenum mineralization, as structurally controlled deposits are widespread and abundant in the Mount Isa District, but molybdenite is rare. This requires a better understanding of the geochemical system, offering a broader understanding of this new mineralization type, regionally and globally.

The Mount Dore and Merlin deposit, and the Lanham's and Barnes Shaft prospects, are located in the Eastern Fold Belt of the Mount Isa Inlier (Carter et al., 1961; Blake, 1987 – Fig. 2:1). The Mount Isa Inlier, located in northwest Queensland Australia, is characterized by a complex protracted tectonic history of mostly Paleoproterozoic and Mesoproterozoic rocks, although rocks as young as Phanerozoic are present (Carter et al., 1961; Blake, 1987; Betts et al., 2006). The Mount Isa Inlier is sub-divided into three main regions that are roughly oriented N-S and are, from West to East: Western Fold Belt; Kalkadoon-Leichhardt

Belt, Eastern Fold Belt (Carter et al., 1961). These Belts have been further sub-divided into six zones, with the Eastern Fold Belt being comprised by the Mary Kathleen Zone, the Malbon Zone, and the Selwyn Zone (MacCready, 2006); being the Malbon and the Selwyn Zone commonly referred to as the Cloncurry District or Eastern Succession (e.g. Williams et al., 2005; Oliver et al., 2008).

The Inlier tectonic history has been divided into two main orogenies: Barramundi (~1900-1870 Ma) and Isan (~1600-1500 Ma) (Carter et al., 1961; Blake, 1987), although recent work suggests a ~1650 Ma start to the Isan Orogeny (Rubenach et al., 2008; Abu Sharib and Sanislav, 2013 – Fig. 2:2). In between these orogenic events there was crustal extension with formation of basins, and intraplate magmatism (e.g. Betts et al., 2006; Gibson et al., 2012). This tectonic regime has been described as "an inferred continental backarc setting" (Betts et al., 2006). Three Superbasin formations have been described: Leichhardt Superbasin (~1800-1750 Ma); Calvert Superbasin (~1735-1690 Ma); Isa Superbasin (~1670-1575 Ma) (Jackson and Rawlings, 2000 – Fig. 2:2). These basins show periods of sedimentation hiatus due to uplift during basin inversion (Jackson and Rawlings, 2000; Gibson et al., 2012), adding to the complexity of the geologic history in the area.

The previous stratigraphic divisions of the volcanic and sedimentary packages consists of three Cover Sequences (CS1, CS2, and CS3; Blake, 1987; Blake and Stewart, 1992), and although this model has been revised to a "Superbasin" scheme by several authors since then (e.g. Jackson and Rawlings, 2000; Southgate et al., 2000; Southgate et al., 2013), the terminology is still in use by some authors, especially in reference to the Eastern Fold Belt (e.g. Foster and Austin, 2005; Foster and Rubenach, 2006; Foster and Austin, 2008). Cover Sequence 1 is mostly composed of felsic volcanic rocks and can only be found in the Kalkadoon-Leichhardt Belt. This Cover Sequence is aged between 1870 and 1850 Ma and therefore started after the Barramundi orogeny and before the Leichhardt Superbasin formation (Blake, 1987; Jackson and Rawlings, 2000; Southgate et al., 2013). Cover Sequence 2 is dated ca. 1790-1690 Ma and comprises most of the Leichhardt and Calvert Superbasin formation (Blake, 1987; Jackson and Rawlings, 2000; Southgate et al., 2013). Cover Sequence 3 overlaps with most of the Isa Superbasin being dated in between 1680 and 1590 Ma (Blake, 1987; Foster and Austin, 2008 – Fig. 2:2).

The Barramundi Orogeny was the result of the deformation and metamorphism (from greenschist up to amphibolite facies) of Paleoproterozoic basement rocks (Carter et al., 1961; Blake, 1987). It may represent a late stage of continental growth of the North Australian

Craton, although due to subsequent superbasin formation and the Isan orogeny this event is poorly recorded in the Mount Isa Inlier (e.g. Betts et al., 2006).

The Leichhardt Superbasin is characterized by periodic E-W extensional events with formation of half-grabens and N-S normal faults (Jackson and Rawlings, 2000; Betts et al., 2006; Southgate et al., 2013). Broadly, it consists of the initial stages of intracratonic rift formation with sedimentary variation from clastic fluvial rocks to marine sediments with widespread bimodal magmatism (e.g. Jackson and Rawlings, 2000; Betts et al., 2006).

Following this event (or during its last stages, depending on the author) there is a shift in the orientation of the extensional regime from E-W to N-S and the emplacement of felsic and mafic plutons that intrude rocks from the Corella Formation and the Double Crossing Metamorphics (Holcombe et al., 1991; Betts et al., 2006; Foster and Austin, 2008; Rubenach et al., 2008). This event is commonly referred to as the Wonga Event and is best studied in the Mary Kathleen Zone where it was described as a mid-crustal (~7 Km) subhorizontal extensional décollement that was active from approximately 1755 to 1730 Ma (Holcombe et al., 1991 – Fig. 2:2). In the Eastern Fold Belt it was during the time of this event (part of Cover Sequence 2) that the Doherty and Staveley formations were deposited (Blake, 1987; Southgate et al., 2013). The Doherty Formation rocks are the host of the Lanham's and Barnes Shafts prospects (Fig. 2:1 and 2:2).

In the Western Fold Belt the Calvert Superbasin is characterized by NW-SE extension with deposition of shallow marine and clastic fluvial sediments with bimodal volcanic events intercalated (e.g. Betts et al., 2006; Southgate et al., 2013).

The Kuridala Formation, the host rocks of the Mount Dore and Merlin deposit (Fig. 2:1 and 2:2), was deposited approximately at the start of Cover Sequence 3 (Blake, 1987; Southgate et al., 2013). During this event there was deposition of fluvial and marine sediments as well as volcanic rocks, and mafic and felsic intrusives (Blake, 1987; Betts, 2006; Foster and Austin, 2008; Southgate et al., 2013).

Considering the older age of 1650 Ma for the start of the Isan Orogeny (Rubenach et al., 2008; Gibson et al., 2012; Abu Sharib and Sanislav, 2013; Southgate et al., 2013), in contrast to the 1600 Ma previously accepted (Foster and Austin, 2008), there was still sedimentation occurring in the Mount Isa Inlier, more importantly in the Western Fold Belt, at the start of the orogeny (e.g. Foster and Austin, 2008). The Isan Orogeny is characterized by several deformation stages, metamorphism, batholith emplacement, and hydrothermal alteration with formation of several ore bodies.

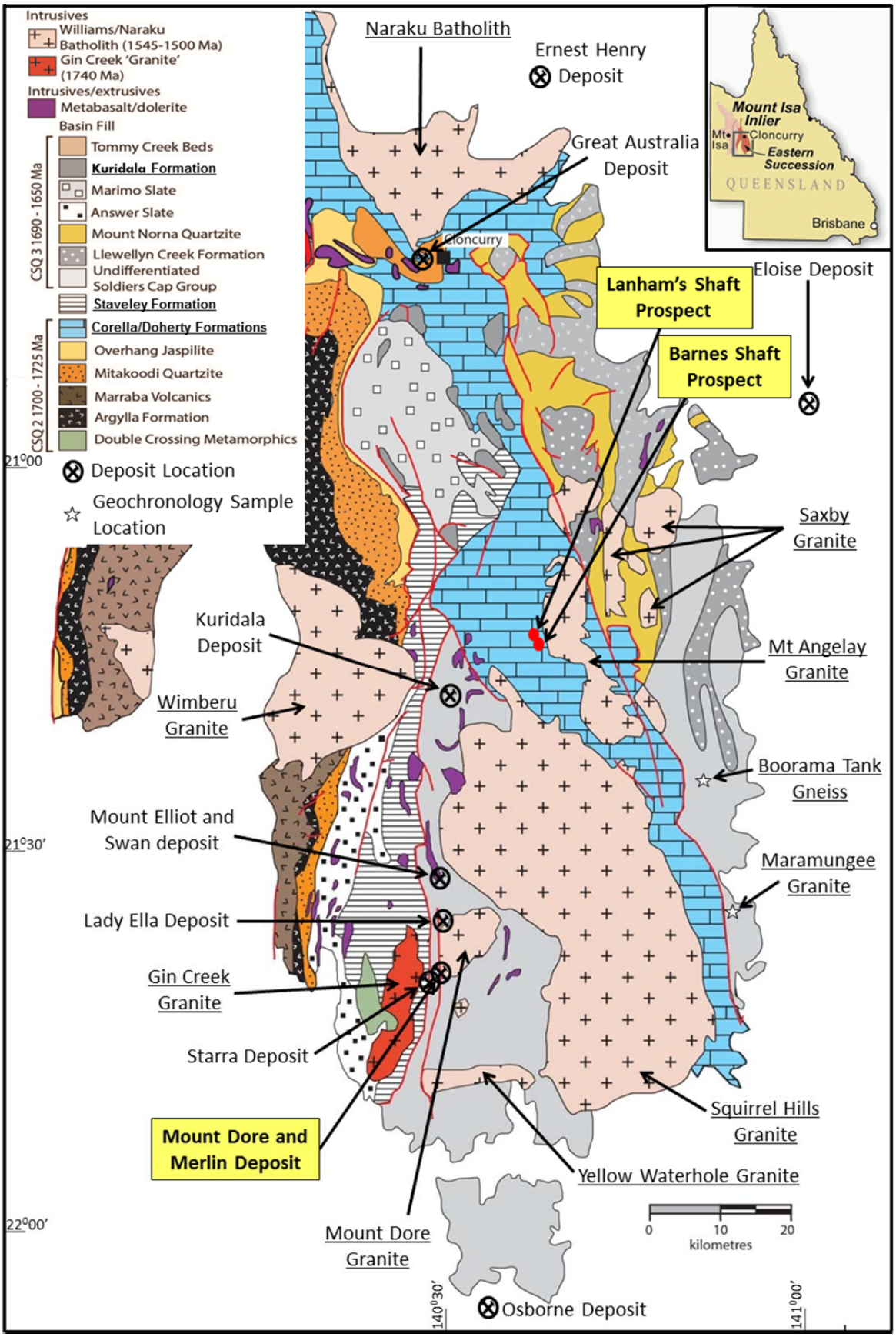

Figure 2:1 – Cloncurry District geological map adapted from Duncan et al. (2013) showing the most relevant ore deposits (including the Lanham's and Barnes Shaft prospects) and igneous intrusives. The geologic map of the Mount Dore and Merlin deposit can be seen in Chapter 3, and Lanham's and Barnes Shafts prospects in Appendix 1.

2.2. Corella and Doherty Formations

The Lanham's and Barnes Shafts prospects are located in the Doherty Formation. The Corella and Doherty Formations belong to Cover Sequence 2, being locally intruded by Wonga plutons, and they have been considered lateral facies equivalents (Blake, 1987; Williams and Phillips, 1992; Jackson and Rawlings, 2000; Foster and Austin, 2008 – Fig. 2:2).

They are characterized by thick units of thin-bedded calc-silicates and marbles with typical mineralogy consisting of mainly carbonates, K-feldspar, biotite, scapolite, amphibole, quartz, and in high grade zones clinopyroxene. Superimposed there are calc-silicate breccias with albite, clinopyroxene, and amphibole. Felspathic calcareous meta-psammite, massive calc-silicate rocks, meta-chert, metamorphosed black shales, schists, banded quartzites with tourmaline, amphibolite and metabasalt also occur in these units, although in minor abundances (Blake, 1987). The Doherty Formation has been dated at 1743 ± 11 and 1725 ± 3 Ma while the Corella Formation is ca. 1750-1740 (Page and Sun, 1998; Southgate et al., 2013). Therefore, there is evidence which indicates that the Doherty Formation may post-date by ~20 Ma the Corella Formation. The dating of these units has created some debate although it seems more reasonable to consider them as part of a similar depositional system, given their unusual chemical affinities and abundance of Cl-bearing scapolite. These units show strong variability both laterally and vertically due to highly variable deformation features and metasomatic alteration which in turn are dependent on deformation intensity, nature of the initial lithology, position in the stratigraphy, relation to thermal sources, and amount of fluid and flow pathways (e.g. Austin and Blenkinsop, 2009).

The Corella/Doherty Formation are host to several mineral deposits, besides several occurrences such as the Lanham's and Barnes Shafts, and the Ernest Henry and Great Australia Cu-Au deposits in the Cloncurry District (Fig. 2:1). In the Mary Kathleen Fold Belt the Corella/Doherty units are also the host rocks of several ore deposits, including Mary Kathleen U-REE, Tick Hill Au, and Trekelano IOCG (e.g. Oliver et al., 2004).

2.3. Kuridala and Staveley Formation

The Kuridala Formation is part of Cover Sequence 3 while the Staveley Formation has recently been allocated to Cover Sequence 2 (Blake, 1987; Southgate et al., 2013). The Kuridala Formation is the host of the Mount Dore and Merlin deposit (Fig. 2:1 and 2:2). Both the Staveley Formation and the Kuridala Formation were deposited during regional basin

extension (Blake, 1987). The deposition of this sequence probably occurred in a deep water environment resulting in turbidite sediments with carbonaceous siltstones and shales interbedded during the lower energy depositional periods (Blake, 1987).

The contact between the Stavely and Kuridala Formations consists of a steep fault at both the regional and deposit scale (e.g. Beardsmore et al., 1988; Foster and Austin, 2008), although debate on their stratigraphic setting and nature of the contact is still ongoing (e.g. Brown et al., 2009). The Staveley Formation was initially reported as younger than the Kuridala Formation (Beardsmore et al., 1988; Page and Sun, 1998; Foster and Austin, 2008), although the geochronology shows the opposite time relationship and more recent work has considered the Staveley formation as much older than the Kuridala Formation allocating it in Cover Sequence 2 (Southgate et al., 2013 – Fig. 2:2). Dating of the Kuridala Formation places it from 1690 ± 9 to 1653 ± 18 Ma. The closest dated sample to the Mount Dore and Merlin deposit (approximately 14 km to the east) consists of a tuff sample and yielded an age of 1676 ± 5 Ma (Page and Sun, 1998 – Fig. 2:2). Probably the most reliable ages for the Staveley Formation are 1746 ± 4 and 1743 ± 4 Ma (Page and Sun, 1998 – Fig. 2:2).

The Kuridala Formation is also the host of several mineral deposits and occurrences of copper and copper-gold such as Mount Elliot (Cu-Au), Lady Ella (Cu-Au), and the historical Kuridala (Cu-Au) that gives the name to the formation. The Starra (Au-Cu) and the Swan zone of the Mount Elliot and Swan deposit are hosted in the Staveley formation (Fig. 2:1 and Table 2:1).

2.4. Structural geology and deformation events

The two main regional faults recognized in the Eastern Fold Belt are the Pilgrim and Cloncurry Faults (Blake and Stewart, 1992). These structures, as well as some less pronounced brittle faults, were initially formed as normal faults during the development of the Superbasins, and have undergone several reactivation events (Austin and Blenkinsop, 2008; Blenkinsop et al., 2008).

With the use of geophysical techniques with 3D geological modelling capability new crustal structural interpretations have been produced, with three major gravity worms having been identified in the Mount Isa Inlier: The Kalkadoon-Leichhardt, the Pilgrim, and the Cloncurry worms (Austin, 2005; Blenkinsop et al., 2005a; Murphy, 2005; Lepong and Blenkinsop, 2005; Austin and Blenkinsop, 2008; Blenkinsop et al., 2008). These worms are projections of the steepest gradients of geophysical datasets and are of great importance for

the understanding of the metal endowment in the Inlier, since most recent studies indicate a strong connection between deformation and the localization of several ore deposits (Bell and Hickey, 1998; Blenkinsop et al., 2005b; McLellan and Oliver, 2005, 2008; Mustard et al., 2005; Oliver et al., 2008; Austin and Blenkinsop, 2009). The Pilgrim worm is reflected by the Mitakoodi anticlinorium while the Cloncurry worm is related to the Snake Creek anticline, where the most important studies of tectonothermal evolution of the Cloncurry District took place (e.g. Blenkinsop, 2005a; Rubenach et al., 2008). The Cloncurry fault is N-NW striking, dipping steeply towards the E, regional fault while the Cloncurry Lineament, to the E of the fault, is the surface trace of the Cloncurry worm, possibly being the margin of a rift basin, and the contact between Cover Sequence 2 and 3 (Blake, 1987; Austin and Blenkinsop, 2008). This Lineament may have acted as a pluton emplacement corridor and is speculated to be a primary pathway for magmatic-hydrothermal mineralizing fluids (Mark et al., 2004a; Mark et al., 2006a; Austin, 2005; Austin and Blenkinsop, 2008; Oliver et al., 2008). The Cloncurry Fault and Lineament is located to the East of Lanham's and Barnes Shafts prospects, and is possibly connected to the emplacement of the Mount Angeley and Saxby plutons (e.g. Austin and Blenkinsop, 2008), although its relation to the Lanham's and Barnes Shafts mineralized corridor is unclear (see details in Chapter 4).

The Mount Dore and Merlin deposit is situated on the eastern margin of the Selwyn High Strain Zone. The Starra and Selwyn High Strain Zones have been the focus of some debate, especially in the timing of its formation relative to the regional deformation stages defined (Beardsmore, 1992; Adshead-Bell, 1998; Laing, 1998; Duncan et al., 2014). These zones are oriented roughly N-S, with the Starra High Strain Zone being the discordant contact between the older Gin Creek Block and the Staveley Formation (Laing, 1998), and the Selwyn Zone is the contact between the Staveley and the Kuridala rock units (Beardsmore, 1992). There is no consensus on the formation timing of these Zones, with some authors arguing for D_1 with several subsequent reactivations (Beardsmore, 1992; Laing, 1998), while other authors defend a later formation during D_4 (see details below – Fig. 2:2).

Regional deformation events in the Mount Isa Inlier during the Isan Orogeny have been the focus of many studies with different authors proposing various deformation frameworks (e.g. Bell, 1983; Adshead-Bell, 1998; Bell and Hickey, 1998; Rubenach et al., 2008; Abu Sharib and Sanislav, Duncan et al, 2014). Some earlier studies defined 3 deformation stages (e.g. Bell, 1983), and more recently more deformation events have been added as exemplified by Rubenach et al. (2008) who defined 6 deformation stages synchronous with specific metamorphic events they define. In this study we adopt a D_1 to D_4

sequence of events compiled from several studies (Bell, 1983; Holcombe et al., 1991; Adshead-Bell, 1998; Bell and Hickey, 1998; Rubenach et al., 2008; Abu Sharif and Sanislav, 2013; Duncan et al., 2014 – Fig. 2:2).

An early deformation stage is recognized by some authors regionally, consisting of the formation of a shallow dipping, bedding-parallel foliation interpreted as extensional in origin. In the Mary Kathleen Fold Belt to the west, early extensional fabrics were dated at ~1740 Ma (Holcombe et al., 1991). To the east in the Snake Creek area, early fabrics occurred at the same time of intense albitization and low pressure-high temperature metamorphism, dated at ~1649 Ma (Abu Sharib and Sanislav, 2013). Shortly after, in the Snake Creek area, dated at ~1645 Ma, there was an N-S shortening event with the formation of E-W folds with steep axial planes (Rubenach et al., 2008; Abu Sharib and Sanislav, 2013). The absolute age of early fabrics in the Selwyn Corridor is not directly constrained, and whether they are extensional in origin or not is also not clear. The Gin Creek Pluton immediately west of the Selwyn corridor has an emplacement age of ~1740 Ma (Page and Sun, 1998), similar to intrusions in the Mary Kathleen Fold Belt dated as syn-extensional (Holcombe et al., 1991). However, early fabrics also appear to affect the Kuridala Formation near the study area, which was deposited at ~1675 Ma. For convenience, and as the details do not appear to impact on the understanding of the later mineralization, early fabric(s) here are referred to as “D1”.

The second deformation event (D_2) was separated by some authors into two events (e.g. Adshead-Bell, 1998; Rubenach et al., 2008), and is characterized by upright folds, trending N to NE with steep axial planes and steep to easterly-dipping axial plane foliation, followed by local rotation of the previous formed folds resulting in shallow axial planes with top-to-the west shear folds. This deformation event has been dated between ~1590 and 1580 Ma in the Snake Creek area, corresponding to the metamorphic peak (Rubenach et al., 2008; Abu Sharib and Sanislav, 2013 – Fig. 2:2).

The D_3 event produced NNW-oriented folds and steeply east-dipping crenulations (e.g. Rubenach et al., 2008). The timing of this event is reasoned at ~1550-1540 Ma on field observations in the Maramungee area, because the Maramungee granite (1545 ± 11 Ma) display D_3 foliations (e.g. Page and Sun, 1998; Mark, 2001).

The D_4 event resulted in N-E oriented folds with steep axial planes (e.g. Adshead-Bell, 1998; Rubenach et al., 2008). The timing of this event (~1530-1500 Ma) is broadly synchronous with most of the Williams-Naraku pluton emplacement, like the Mount Dore and the Mount Angeley granites. The brittle structures formed during this event, which

probably post-date most fold formation, host the majority of the younger Cu and Cu-Au deposits of the Eastern Succession, with some of these mineralized structures displaying strike-slip movement (McLellan and Oliver, 2008). This event has also been connected to the formation of fluidized discordant breccias that are an important feature of the Lanham's and Barnes Shafts prospects area (see Chapter 4 for details).

2.5. Metamorphism

The metamorphism in the Mount Isa Inlier is characterized by dominantly low pressure-high temperature multiple events from lower greenschist to upper amphibolite facies, with complex anticlockwise and clockwise P-T-t paths (Rubenach, 1992; Rubenach, 2005b; Foster and Rubenach., 2006; Rubenach et al., 2008). The Proterozoic metamorphism is not restricted to the Mount Isa Inlier being also present in Eastern and Central Australia (e.g. Foster and Rubenach, 2006). In the Mount Isa Inlier the metamorphism created roughly N-S oriented belts that are divided into greenschist and amphibolite facies (Foster and Rubenach, 2006).

Several metamorphic events were defined in the Snake Creek Anticline, many of which appear applicable in the Selwyn Corridor. These span from ~1680 to ~1520 Ma (Foster and Rubenach, 2006; Rubenach et al., 2008; Abu Sharib and Sanislav, 2013). The oldest metamorphic event may relate to extension rather than contraction, and later stages appear to overlap with contact metamorphism, with the regional metamorphic peak occurring in between ~1600 and 1580 Ma (Rubenach et al., 2008 – Fig. 2:2).

There are three models that have attempted to explain the heat source responsible for the protracted low-pressure, high-temperature metamorphism, which requires a long-lived thermal anomaly. The models are: 1) High abundance of radioactive isotopes (McLaren et al., 1999); 2) Mantle upwelling and lithospheric delamination (e.g. Oliver et al., 1991; 2008); and 3) Igneous intrusions (e.g. Rubenach, 2005a; Foster and Rubenach, 2006; Rubenach et al., 2008), although all of these may have acted in tandem. Oliver et al. (2008) argued that mantle delamination was an unlikely explanation for the protracted metamorphism present being only a suitable explanation for more time restricted events. The most current accepted model emphasises mafic intrusives as the main heat source with granitic magmas causing heat advection into the upper crust, although the contribution of radioactive isotopes are considered as an important factor in the thermal budget (McLaren et al., 1999; Foster and Rubenach, 2006; Rubenach et al., 2008). Geophysical data interpretation have suggested the presence of great abundances of deep crustal mafic to ultramafic (Blenkinsop et al., 2008),

and Oliver et al. (2008) suggested back arc extension, anomalous mantle geochemistry and greatly thinned crust as the igneous material source.

There is limited dating on the mafic intrusives and further work will be essential to better understand their nature, nevertheless the Snake Creek sill complex (~1686 Ma), the Toole Creek Volcanics (~1658 Ma), and the gabbros and dolerites that intruded with the Williams-Naraku batholiths show that there was mafic igneous activity from shortly before and throughout the Isan Orogeny (e.g. Rubenach et al., 2008 – Fig. 2:2). The metamorphic peak (syn-D_2, ~1580 Ma) was a period of strong crustal shortening and the intrusives that may have been responsible for the heat transfer to upper crustal depths at this time are pegmatites and small felsic intrusive bodies (Rubenach et al., 2008 – Fig. 2:2).

The Williams-Naraku Batholith emplacement was accompanied by thermal/regional metamorphism. Rocks of the Corella/Doherty Formation developed extensive brecciation and metasomatism, and rocks of the Soldiers Cap Group display 675°C at 285 MPa immediately adjacent to the Saxby Granite due to contact metamorphism (e.g. Oliver et al., 2006). The brecciation is also important in the ore deposit formation with Ernest Henry deposit mineralization being hosted by such breccias (Mark et al., 2000; Mark et al., 2006b; Oliver et al., 2006 – Table 2:1).

2.6. Magmatism

The Mount Isa Inlier is characterized by several igneous events, with two events being pre-Isan Orogeny and three events occurring during the orogenic event.

The oldest igneous intrusives, post Cover Sequence 1, are from the Wonga event which is dated in between ~1755 and ~1730 Ma (Fig. 2:2). The granite intrusives that typify this event are strongly deformed in the Mary Kathleen Zone, where the Wonga Batholith is located, but also appear in the Cloncurry District, with the Gin Creek and Levian granites (Holcombe et al., 1991; Oliver et al., 1991; Beardsmore, 1992; Page and Sun, 1998; Davis et al., 2001; Foster and Austin, 2008 – Fig. 2:1). These granites display evidence of strong fractionation with silica abundance related to K_2O, F, Th, U, Rb, K/Rb enrichment (Holcombe et al., 1991; Wyborn et al., 1992).

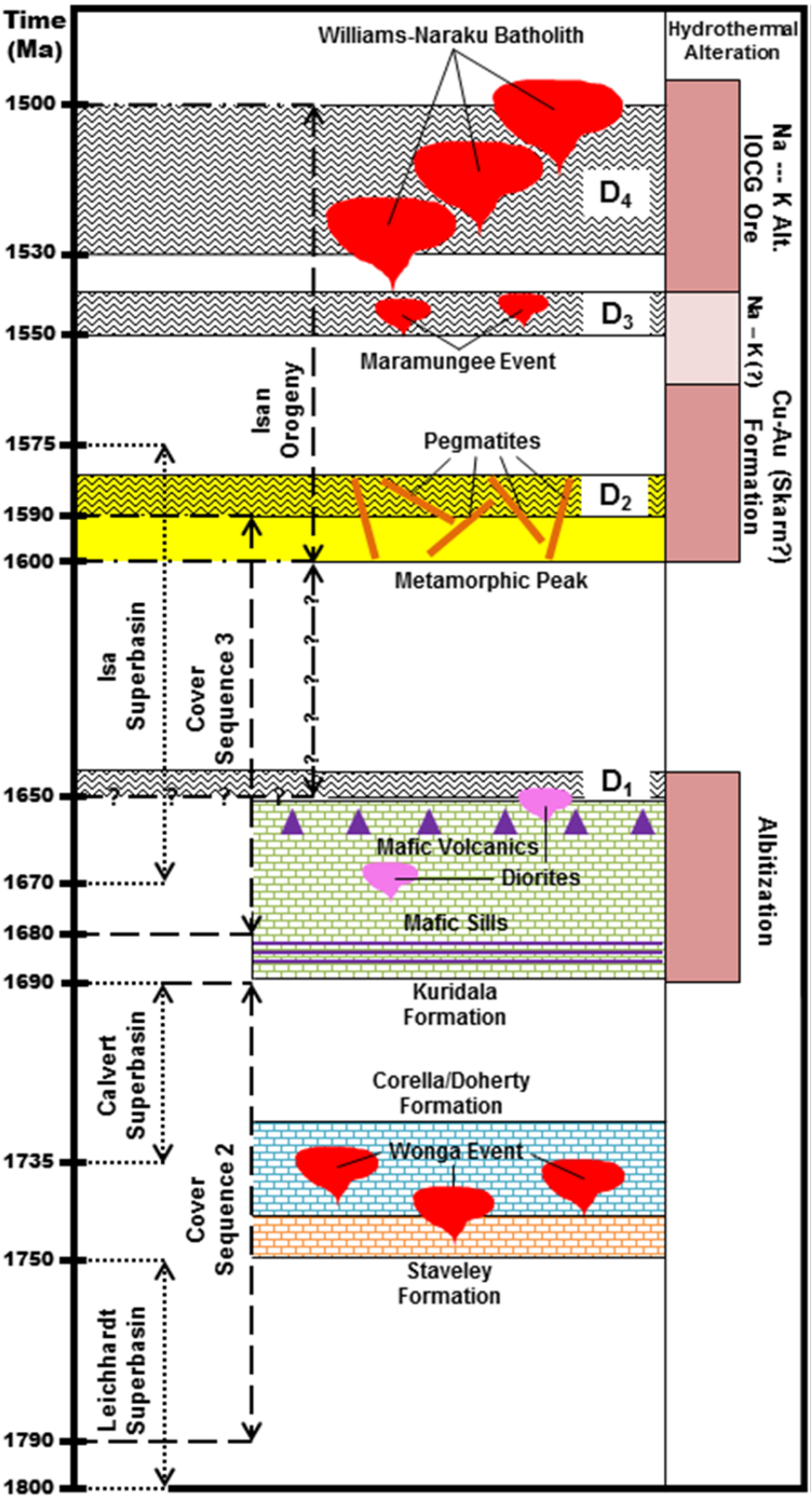

Figure 2:2 – Diagram showing timing of the main tectonostratigraphic divisions, lithological formations relevant to the Mount Dore and Merlin deposit and the Lanham's and Barnes Shafts prospects, main igneous events, deformation events, metamorphic peak and main metasomatic events. References in text.

The second pre-Isan Orogeny igneous event consists of mostly mafic intrusives and extrusives that were formed between ~1690 and ~1640 Ma, having some overlap with the early stages of the Isan Orogeny (Rubenach et al., 2008; Gibson et al., 2012; Abu Sharib and Sanislav, 2013 – Fig. 2:2). The Toole Creek Volcanics are the most abundant mafic volcanic rocks in this stage being composed of metamorphosed basalt and dolerite underlain by fluvial and marine metasediments (e.g. Betts et al., 2006). A mafic sill complex was also recognized in the Snake Creek Anticline, with dating of a trondhjemite intrusion at ~1686 Ma (Rubenach et al., 2008). Another important igneous intrusive of this event is the Ernest Henry diorite (~1673-1647 Ma) (Pollard and McNaughton, 1997; Mark et al., 2004b – Fig. 2:2). These intrusive igneous rocks have been connected to a major metasomatic event, characterized predominantly by albitization, with dating of monazite in cordierite yielding the age of 1649 ± 12 Ma (Rubenach, 2005a; Rubenach et al., 2008; Abu Sharib and Sanislav, 2013 – Fig. 2:2).

During the metamorphic peak (~1600-1580 Ma), defined in the Cloncurry District, there is an igneous event that is characterized by the intrusion of pegmatites and small felsic bodies, part of the tectonothermal system responsible for the metamorphism (Rubenach et al., 2008 – Fig. 2:2). These pegmatites intrude up to the levels of the sillimanite zone and are best recognized in the Snake Creek Anticline and around the Osborne and Cannington mines (Adshead, 1995; Giles and Nutman, 2003; Rubenach et al., 2008).

In the Cloncurry District, at ca. 1550 Ma, there was the emplacement of the Maramungee intrusives (Fig. 2:2). These intrusives are considered to be of the trondhjemites-tonalite-granodiorite (TTG) series, and are I-type with high field strength trace elements and Y, Nb, Ta, Sc- depleted, and Sr-undepleted (Williams and Phillips, 1992; Williams and Heinemann, 1993; Mark, 2001). The Maramungee Granite (1545 Ma) and the Boorama Tank Gneiss (1547 Ma) are the representatives of this igneous event and outcrop along the Cloncurry Fault (Page and Sun, 1998 – Fig. 2:1). These granites display D_3 foliation (Blake et al., 1983; Williams and Phillips, 1990; Mark, 2001).

The most voluminous igneous event consists of the Williams-Naraku Batholiths and occurred between ~1540 and ~1490 Ma (e.g. Pollard and McNaughton, 1997; Page and Sun, 1998 – Fig. 2:2). These intrusive rocks originated by partial melting of the lower crust due to introduction of mantle mafic material into the crust (Pollard et al., 1998; Mark, 2001; Blenkinsop et al., 2008). They display geochemistry of A-type granites with high-K, Y-undepleted, and Sr-depleted, and have been correlated to a global Proterozoic A-type, K-rich, igneous event (Collins et al., 1982; Wyborn, 1998; Pollard and McNaughton, 1997; Pollard et

al., 1998; Mark, 2001; Mark et al., 2005a). Concomitant with the granites there are less voluminous (but common) gabbro and dolerite intrusions, and although dating is absent there are mixing and mingling textural and geochemical evidences that prove that at least some mafic activity is synchronous with the Williams-Naraku granites (e.g. Jacob, 2009). The granitic intrusives commonly display compositional diversity that has also been connected to mixing and mingling resulting in magma hybridization (e.g. Pollard et al., 1998; Mark, 2001; Mark et al., 2005b). The Mount Margaret granite (~1530 Ma) represents Na-rich, Y-undepleted alkaline intrusions that are rare but clearly show the geochemical variations which exist in these granitoids (e.g. Page and Sun, 1998; Pollard et al., 1998; Mark, 2001; Mark et al., 2005a).

The Williams-Naraku batholith has been implicated as the fluid source and/or fluid flow heat engine responsible for the younger regional Na-(Ca) hydrothermal alteration and most of the IOCG deposits in the region (e.g. Oliver et al., 2008; Kendrick et al., 2008), although the mafic rocks may have been more important as copper sources (Oliver et al., 2008).

2.7. Economic Geology

The Mount Isa Inlier is renowned for its metal endowment with several world class ore deposits rendering it a highly prospective area. In the Cloncurry District there are two main types of ore deposits: IOCG deposits, and Ag-Pb-Zn which share similarities with the Broken Hill world class deposits and are therefore commonly grouped in the ‘Broken Hill Type’ deposits (e.g. Williams, 1998; Hutton et al., 2012). The Mount Isa Inlier is also host of another deposit type that consists of U-REE, of which the skarn hosted Mary Kathleen deposit, located in the Fold Belt of the same name, is its best representative (e.g. Oliver et al., 1993; Oliver et al., 1999; Williams, 1998; Hutton et al., 2012).

The Cannington Ag-Pb-Zn deposit is the most important deposit of this type in the Cloncurry District (e.g. Hutton et al., 2012 and references therein). This deposit has been argued to have been formed from pre-metamorphic mineralization which was reworked and refined in the subsequent metamorphism, deformation and extensive retrograde alteration (e.g. Bodon, 1998). More recently this model has been challenged, considering that the Cannington deposit has more in common with a metasomatic skarn deposit than the ‘Broken Hill Type’ deposits, by arguing that the deposit has a metasomatic, late-metamorphic origin (e.g. Chapman and Williams, 1998).

The most abundant ore deposits in the Cloncurry District are commonly typified as IOCGs although this broad view of what qualifies as an IOCG type deposit has been criticized by some authors (e.g. Groves et al., 2010). The IOCG type *sensu stricto* classification consists of the following characteristics (Hitzman et al., 1992; Groves et al., 2010): 1) Formed in rocks dated in between 1.1 and 1.8 Ga, early to mid-Proterozoic host rocks; 2) They are structurally controlled, located in areas that have been cratonic or continental margin environments during Archean or Paleoproterozoic time, and formed from 100 to 200 Ma after supercontinent assembly; 3) Dominated by low Ti iron oxides (magnetite and/or hematite), that are associated but commonly older than the Cu-Fe sulfides. The ore deposits contain enrichment in REE, commonly in apatite, as well as frequently abundant P, F, Ba and CO_3 rich minerals; 4) The deposits are temporally connected to voluminous igneous intrusives although they are not spatially connected. They are also magmatic-hydrothermal deposits with economic Cu-Au mineralization; 5) The host rocks display intense hydrothermal alteration that generally is characterized by sodic alteration which is overprinted by potassic alteration.

The previous characterization does not account for the great variability of ore deposits that although have several affinities with IOCG style deposit *sensu stricto* do not completely conform to its definition. Geoscientists have been since then grouping all those deposits as IOCG style deposits *sensu lato*, which has created some confusion and several attempts to create sub-divisions. For example, Groves et al. (2010) created 5 sub-groups in an attempt to preserve the IOCG *sensu stricto* definition. Despite the value of such debate it is readily apparent that IOCG ore deposits *sensu lato* in the Andes show very important differences relative to the IOCG ore deposits *sensu lato* in the Mount Isa Inlier (e.g. Sillitoe, 2003; Oliver et al., 2008). It is therefore, at the current level of understanding of these deposits, better to focus on specific ore deposit districts settings, such as the Cloncurry District.

In the Cloncurry District there are several important ore deposits that have been given the classification of IOCG, such as: Mount Dore (and Merlin), Starra, Mount Elliot and Swan, Osborne, Eloise, and Ernest Henry, to mention the most important.

Table 2:1 – Cloncurry District main IOCG ore deposits characteristics. Further information and references on the age of the deposits can be consulted in Chapter 5 and Digital Appendix.

Deposit	Age	Iron Oxides relation with mineralization	Resources (Measure & Indicated)	Host Formation	Host lithology	Metasomatic alteration	Structure	References
Starra	1594 – 1503 (Accepted as Post-metamorphic peak)	Fe oxide-hosted	7.6 Mt; 1.1g/t Au, 0.99% Cu	Staveley Formation	Magnetite and hematite ironstones hosted by metasediments and calc-silicate rocks (hanging-wall); and albite-chlorite-magnetite schists (footwall)	Sodic » Potassic » Au-Cu	Formed by metasomatism of the metasedimentary rocks and ironstones in a brittle-ductile shear zone	Rotherdam (1997a and b); Rotherham et al. (1998); Williams et al. (2001)
Osborne	1667 - 1465 (Accepted as pre to syn-metamorphic peak)	Fe oxide associated	12 Mt; 1.4% Cu, 0.88g/t Au	Referred as resembling Mount Norna Formation (and it's the same age group as Mount Norna and Kuridala)	Feldspathic psammite and pelite, banded ironstone and associated schist, metabasic intrusions, and pegmatitic intrusions	Sodic » Silica flooding » Qtz-Cu-Au	Localised near the crest of a D2 fold that overprints a strong shear fabric contained in mylonitic siliceous rocks of the ore halo	Fisher (2007); Oliver et al. (2008); Kendrick et al. (2008)
Mount Elliot and Swan	1540 - 1496 (Accepted as Williams-Naraku time)	Fe oxide associated (Skarn?)	Mount Elliot - 210 Mt; 0.52% Cu, 0.32g/t Au & Swan - 2.3 Mt Cu, 4.3 Moz Au.	Mount Elliot - Kuridala Formation; Swan - Staveley Formation	Mount Elliot - Phyllites, schist, and metadolerites; Swan - Calc-silicates and calcareous metasediments	Sodic » Ca-Fe-Cu-Au-rich skarn (?)	Mount Elliot and Swan are separated by a steep strike-slip fault. Swan is hosted in crackle to matrix-supported breccias. Mount Elliot mineralization is in open spaces of breccias surrounded by skarn alteration	Wang and Williams (2001); Brown et al. (2009)
Ernest Henry	1651 - 1476 (Accepted as Williams-Naraku time ~1525 Ma)	Fe oxide associated	Underground mining resources: 73 Mt; 0.97% Cu, 0.5g/t Au	Argylla and/or Corella/Doherty Formations (?)	Meta-andesite, graphitic schist, calc-silicate rocks, and metadiorites	Sodic » Potassic » Potassic-Cu-Au	Localized in a pronounced bend in a regional shear zone which hosts a SSE-plunging breccia pipe in which ore grades are systematically related to the intensity of brecciation	Mustard et al. (2005); Mark et al. (2006b); Marshall and Oliver (2008)
Eloise	1555 - 1514 (Argued to be of pre to syn-metamorphic peak ?)	Fe oxide poor	Indicated resources - 1.5 Mt; 2.8% Cu, 0.7ppm Au, 7.8ppm Ag	Mount Norna Formation (similar age to the Kuridala Formation)	Amphibolite, meta-arkose, and quartz-biotite schist	Sodic » Cu » Potassic	Mineralization is hosted in ductile shear zones, stockworks and faults. These structures were formed in a local jog from anastomosing shear zones belonging to the regional Levuka Shear Zone	Baker and Laing (1998); Baker et al. (2001); Oliver et al. (2008)
Mount Dore and Merlin	1552 - 1497 (Extensive discussion in Chapter 5)	Fe oxide poor, although footwall rocks are moderately rich	Mount Dore - 70 Mt; 0.58% Cu, 0.08g/t Au & Merlin (indicated) - 6.7 Mt; 1.4% Mo, 13ppm Re	Kuridala Formation	Phyllites, carbonaceous slates, and calc-silicate rocks	Sodic » Potassic-Cu-polymetallic » Potassic-Mo-Re	Cu-dominated mineralization is hosted in angular clast-supported breccias and veins & Mo-dominated mineralization is hosted matrix-supported breccias with rounded clasts, veins (commonly stylolitic), and disseminations. The breccias follow the stratigraphy	This Study

2.7.1. Cloncurry District main IOCG deposits characterization

The interrelationships between the IOCG deposits in this district are complex with important variations in Cu:Au ratios, timing of iron oxides relative to sulfides, host rocks nature, tectonic structures, metasomatic alteration, and age.

Relatively to the age, there is at present a distinction between two groups: 1) Pre to syn-metamorphic peak deposits (Osborne, and possibly Eloise); 2) Williams-Naraku Batholith age IOCGs (Mount Elliot and Swan, and Ernest Henry). Further details and references on these deposits geochronology can be seen in Chapter 5, Figs. 5:13, 5:14 and Appendix 3.

All major IOCGs in the Cloncurry District are structurally controlled although the variation in the tectonic setting and structure formation age is complex, variable, and in some cases uncertain (Bell and Hickey, 1998; Blenkinsop et al., 2005b; McLellan and Oliver, 2005, 2008; Mustard et al., 2005; Oliver et al., 2008; Austin and Blenkinsop, 2009). Despite the complexities, efforts to use the district tectonic structures at different scales as a prospection tool has proven to have some success For example, McLellan and Oliver (2005 and 2008) demonstrated that most occurrences of copper mineralization in the Eastern Succession could be predicted by use of numerical models for fault-related fluid flow. Other authors have also suggested large scale temporal connections between the various deposits based on structural data interpretation. For example, Austin and Blenkinsop (2009) considered the possibility of a continuum between Pb-Zn-Ag and Cu-Au mineralization formed by structural controls (e.g. unit contacts, permeable units, faults). These efforts to model the structural components of the Cloncurry District as a prospective tool are of merit and have produced promising results. However, a detailed characterization of the various geologic aspects of the different ore deposits in the region is necessary in order to continue to improve large scale tectonic modelling, due to the simple fact that there is a need for a tectonic trap to form an ore deposit but not all suitable traps are mineralized. Structural details of the main ore deposits in the Cloncurry District can be seen in Table 2:1.

Based on the variations of the Cu:Au ratios, timing of iron oxides relative to sulfides, and host rocks nature, Mark et al. (2006a) proposed 4 sub-divisions: 1) Sulfide barren magnetite and/or hematite ironstones; 2) Fe oxide-hosted Cu-Au deposits (Starra); 3) Fe oxide Cu-Au deposits (Osborne, Mount Elliot and Swan, Ernest Henry); and 4) Fe oxide-poor Cu-Au deposits (Eloise); details on these ore deposits are in Table 2:1. As it can be readily seen this classification does not include the ore deposits geochronology as a parameter.

2.7.2. Ore forming fluids and metasomatic alteration

There are many controversies about the source of the metal bearing fluids that formed these deposits (e.g. Oliver and Wall, 1987; Oliver, 1988; Davidson and Garner, 1997; Davidson, 1998; Fu et al., 2003; Mark et al., 2004c; Mark et al., 2006a; Marshall and Oliver, 2006; Oliver et al., 2006; Pollard, 2001, 2006; Oliver et al., 2008; Oliver and Rubenach, 2009). The most commonly accepted theory consists of a direct link between the emplacement of the Williams-Naraku Batholith and ore deposit formation where the intrusive rocks would provide the metal rich fluids and/or heat engine for fluid flow (e.g. Williams, 1998; Mustard et al., 2005; Pollard, 2006). This theory was more recently revised due to new geochronology data, and noble gas and halogen fluid inclusion studies, in particular on the Osborne deposit (Perkins and Wyborn, 1998; Gauthier et al., 2001; Fisher, 2007; Fisher and Kendrick, 2008; Kendrick et al., 2008; Rubenach et al., 2008). These studies updated the model to include both early 'basinal' or 'metamorphic' varieties including Osborne and possibly Eloise, and later deposits (most notably Ernest Henry) that are related to the release of fluids from the Williams-Naraku Batholith (Butera et al., 2005; Fisher and Kendrick, 2008; Oliver et al., 2008; Rubenach et al., 2008).

The older deposits, which are metamorphic and/or basinal fluid-derived, are characterized by mainly sodic-calcic (Na-(Ca)) alteration (e.g. Oliver et al., 1992; Oliver et al., 2004; Rubenach, 2005b; Fisher, 2007; Oliver et al., 2008; Oliver and Rubenach, 2009). The younger deposits, such as the Ernest Henry, are also characterized by albite rich, Na-(Ca) alteration that is locally overprinted by potassic-iron (K-Fe) alteration, which hosts most of the IOCGs in the Cloncurry District (e.g. Oliver et al., 1992; De Jong and Williams, 1995; Mark et al., 2000; Oliver et al. 2004; Mark et al. 2006b; Marshall and Oliver, 2008; Oliver and Rubenach, 2009).

De Jong and Williams (1995) defined the Na-(Ca) alteration as fluid buffered with several stages, which are divided into several styles based on different factors such as variations in (P-T) conditions, fluid pressures, pressure-temperature, strain rates, and rock competences. According to the same authors the Na-(Ca) alteration was formed in pressures >200 Mpa, with temperatures between 400 and 500^{o}C, which are similar to the temperatures obtained in other studies (Oliver et al., 2004; Mark et al., 2006a).

An integrated progression linking the Na-(Ca) and K-Fe metasomatic alteration has been suggested by several authors. The main minerals that are formed during the Na-(Ca) alteration consist of: actinolite, magnetite, albite ± titanite, calcite, and apatite. The formation

of these minerals involves the loss of K, Fe, Ba and, in some cases Cu (Oliver et al., 2004; Mark et al., 2006a, Marshall and Oliver, 2006). Based on these considerations it has been argued that the subsequent localized K-Fe alteration is, at least in part, due to the previous Na-(Ca) geochemical evolution (Oliver et al., 2004; Mark et al., 2006b).

The most important deposit in the Cloncurry District that can be used to typify the younger IOCG deposits, which are synchronous with the Williams-Naraku Batholith emplacement, is the Ernest Henry deposit (e.g. Oliver and Rubenach, 2009). This deposit hydrothermal alteration is characterized by, from older to younger: 1) Na-(Ca) alteration that formed albite and minor diopside, actinolite, scapolite, magnetite, and pyrite; 2) K-(Mn,Ba) alteration that formed biotite and magnetite proximal to the ore minerals; 3) K-feldspar dominated alteration which is closely associated to the ore minerals (Mark et al., 2006b). Based on geochemistry studies of the deposit these authors considered that a diversely metal bearing fluid, probably magmatic, had to be crucial in the mineralized system.

Concerning the origin of the fluids that resulted in the Na-(Ca) alteration and subsequently in the formation of ore deposits, Fisher (2007) and Fisher and Kendrick (2008) suggested a sedimentary, and/or possibly metamorphic, derived origin of the mineralizing fluids for the Osborne deposit. These findings were taken further by Kendrick et al. (2008) who expanded the model to encompass not only older deposits, such as Osborne, but also younger deposits, such as Ernest Henry. They suggested that the fluids associated with the Na-(Ca) alteration were thermally driven by the Williams-Nakaru Batholith, but were sedimentary formation waters in origin with minor contribution of magmatic fluids. This model argues that these sedimentary derived fluids are from the upper crust, which reached high levels of salinity by dissolving halite or scapolite (Kendrick et al., 2008). This model works well with older pre to syn-metamorphic ore deposits as Osborne but it is less likely for younger post-metamorphic deposits due to the metamorphization of halite-rich evaporates into scapolite during the metamorphic peak (Oliver, 1995; Oliver et al., 2004; Foster and Rubenach, 2006). This issue is reinforced by the similarity in composition between fluid inclusions associated with mineralization at Ernest Henry and mantle-derived igneous rocks. Addressing this issue, Kendrick et al. (2008), suggested: either, that the ratios I/Cl and Br/Cl of the evaporites would be preserved by the scapolites and therefore its break-down during metasomatism would result in a similar fluid chemical signature; or, younger post-metamorphic sediments were the source of the high-salinity fluids and are now eroded. The main critique to this model arises from stable isotope studies (e.g. Marshall et al., 2006) which are interpreted to indicate that magmatic derived fluids play an important role in the

formation of, at least, the younger deposits (e.g. Oliver et al., 2008). These arguments lead to the model in which the younger deposits mineralizing fluids are mostly magmatic-hydrothermal in origin while for the older deposits a basinal derived fluid is most likely (Oliver et al., 2008; Oliver and Rubenach, 2009). The defenders of the mainly sedimentary derived fluids consider that up-temperature fluid flow can readily explain the stable isotope signatures; therefore the debate is still ongoing.

3. Chapter 3: Merlin local geology and petrography

3.1. Introduction

The Merlin deposit is located approximately 90km southwest of Cloncurry in the Cloncurry District (e.g. Williams et al., 2005), of the Eastern fold belt (Carter et al., 1961). The deposit is hosted in the Kuridala Formation (e.g. Foster and Austin, 2008).

The Proterozoic metasediments of the Kuridala Formation were thrust above the Staveley Formation with the Mount Dore Shear Zone separating them. The Mount Dore A-type quartz monzonite granite was thrust above the Kuridala formation and smaller mafic and felsic sills intrude the metasedimentary units (Page and Sun, 1998; Wyborn, 1998; Mark et al., 2005a; Betts et al., 2006; Lazo and Pal, 2009). The Staveley and Kuridala Formations strike roughly N-S, and dip to the east in the study area. The thrust contact between the Kuridala Formation and the overlying Mount Dore granite also dips towards the east (Fig 3:1). At the deposit scale the metasedimentary rocks of the Kuridala Formation are, from top to bottom, interbedded phyllite and carbonaceous slates, followed by banded calc-silicate rocks (Fig. 3:1).

The composite Mount Dore and Merlin deposits consist of Cu – polymetallic mineralization (Mount Dore), which overlies and is locally cut by the recent discovery of the high grade Mo-Re mineralization (Merlin) (Fig. 3:1). The copper mineralization is more extensive to the north and south than the Mo-Re mineralization (Fig. 3:1). This study was mostly focused in the zone of the deposit where both copper and molybdenum mineralization occur. The copper dominated mineralization is mostly hosted by the carbonaceous slates, occurring mostly in breccias, but also within phyllites and calc-silicate rocks. The Mo-Re mineralization occurs mostly in breccias that follow the contact zone between the carbonaceous slates and the calc-silicates (Fig. 3:1).

The main geological units, hydrothermal alteration and mineralization styles of the Mount Dore and Merlin deposit will be described in this chapter. These studies are based on the fieldwork conducted and subsequent microscopy, using both standard petrological microscope and electron microprobe (see Chapter 1 for details).

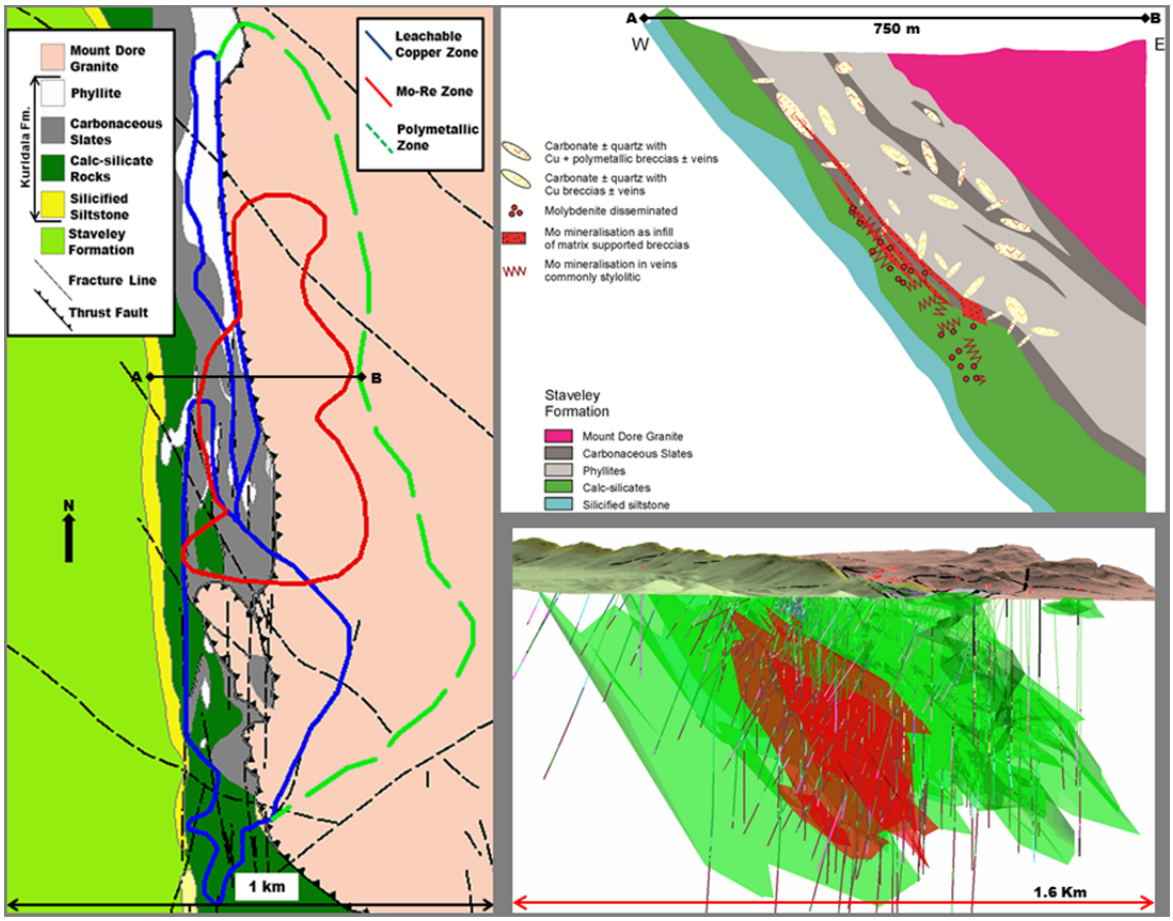

Figure 3:1 – At the left: Geologic map of the Mount Dore and Merlin deposit, adapted from Ivanhoe Australia LTD, showing the schematic contour of the copper and molybdenite mineralization. At the top right: Schematic cross-section of the Merlin deposit showing the main rock units and the copper and molybdenite mineralization. At the bottom right: 3D MicroMine software image showing a NW-SE cross-section of the Mount Dore and Merlin deposit with the geologic map surface and the copper (green) and molybdenite (red) ore shells.

3.2. Rock type description

The petrography of the main rock units in the Mount Dore and Merlin deposit is complex due to several hydrothermal alteration stages that overprint, partially to completely, the metamorphic mineral assemblages. The main rock types are from top to bottom, and east to west: Mount Dore granite, phyllites, carbonaceous slates, calc-silicates, and silicified siltstone (Figs. 3:1 and 3:2). Intruding the main rock types are dikes/sills of intermediate to mafic, and locally felsic composition.

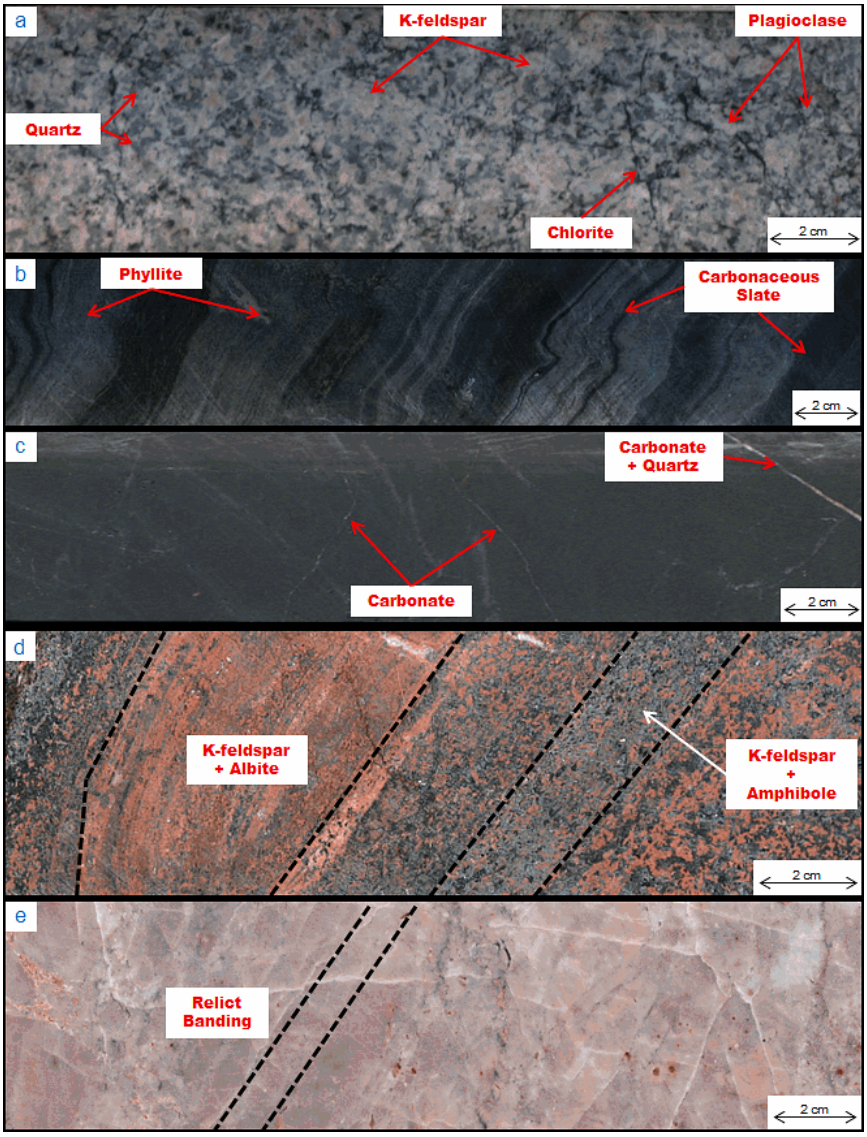

Figure 3:2 – Showing the appearance in drillcore of the 5 main units, from structural top to bottom: – **a)** Drillhole MDQ0252 at ~180 metres depth showing Mount Dore granite with moderate alteration. **b)** Drillhole MDQ0252 at ~236.70 metres depth showing banded and folded phyllite with bedding parallel laminations. **c)** Drillhole MDQ0112 at ~340.30 metres depth showing carbonaceous slate with minor veinlets of carbonates and quartz. **d)** Drillhole MDQ0149 at ~272.90 metres depth showing a strongly altered banded calc-silicate sample. **e)** Drillhole MDQ0120 at ~379.30 metres depth showing silicified siltstone with weak relict banding.

3.2.1. Mount Dore Granite

The A-type Mount Dore granite, of roughly 100 km^2 exposure, shows uniform composition of mostly equigranular K-feldspar + quartz + plagioclase + biotite ± zircon ± hornblende (Fig 3:2). Biotite and titanite are common minor minerals, whereas hornblende is rare. Core samples display moderate to strong alteration with colour variations from white to red, with widespread replacement of biotite (± hornblende) by chlorite and

replacement of titanite by mostly rutile ± ilmenite. The different alteration colours are due to chloritization and hematite staining that seems locally connected in proximity to the lower contact but is variable and apparently random throughout the unit. Altered titanite still preserve their former crystal shape with small unidentified oxides and ilmenite grains forming the former crystal boundaries as well as dispersed in the grains. Small disseminated pyrite grains are common, whereas chalcopyrite is rarely observed. The deformation is weak but observable as undulose extinction in quartz. Locally it is possible to see patches of pyrite with minor chalcopyrite close to the lower contact. The bottom contact with the carbonaceous slates and the phyllites is sharp and commonly brecciated due to the thrust nature of the contact and the competence difference between the granite and the metasediments (Fig 3:1 a and 3:3).

3.2.2. Phyllites

This unit shows intense foliation with weaker folding and crenulations. The mineralogy is relatively simple, consisting of mostly quartz and muscovite of similar size crystals, and varies from muscovite (sericite) rich with a silky lustre, to darker quartz + muscovite (Fig. 3:2 b). The phyllites are interbedded with carbonaceous slates that can appear as carbonaceous millimetric bands within the phyllites (Fig. 3:2 b) or are homogenous metric wide units as described below. The foliation is observed as aligned, lamellar muscovite and elongated quartz aggregates. Primary metamorphic carbonates appear locally in veins and also in the matrix texturally interlocked with quartz and muscovite indicating that these phases co-crystalized. Rare biotite and amphibole, and chlorite formed after amphibole, are also present. The interbedded millimetric bands of carbonaceous slates contain minor graphite and strongly altered andalusite that in most cases is completely replaced by a later carbonate phase and chlorite with minor opaques. Also in the darker bands, it is possible to find tourmaline, which is an important vein infill and alteration mineral in the thicker beds of the carbonaceous slates (see below).

3.2.3. Carbonaceous slates

The carbonaceous slates are the most important unit as they are the main host of the Cu-polymetallic mineralization and they represent the main rheological boundary with the calc-silicate rocks along which molybdenite matrix-supported breccias occur. The unit is interbedded with the phyllites and most of the primary metamorphic mineral assemblage

has been altered by subsequent hydrothermal alteration. The metamorphic minerals remaining are quartz, muscovite and graphite. The mineral assemblage now is composed of very fine grains of K-feldspar + muscovite (sericite) + quartz + albite + carbonates ± graphite ± tourmaline ± chalcopyrite ± galena ± rutile. Cross-cutting small veins and wider foliation-parallel veins show quartz + K-feldspar + tourmaline ± albite ± apatite. These veins are mineralized with small crystals of mostly sphalerite + galena. Although there is some galena + sphalerite mineralization in the phyllites, the carbonaceous slates unit is the host of the bulk of the Cu-polymetallic mineralization. In the matrix, there are also disseminated crystals of chalcopyrite + tourmaline ± galena ± rutile. The unit shows intense foliation with sericite, albite, K-feldspar grains and graphite lamellae strongly aligned (Fig. 3:2 c). In the mixed unit of banded phyllites and carbonaceous slates, the foliation is weakly to moderately folded and crenulated (Fig. 3:2 b).

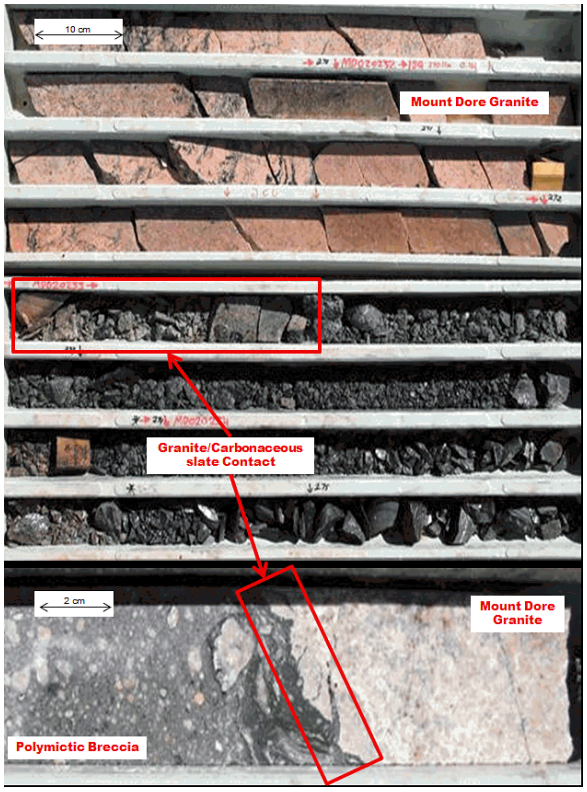

Figure 3:3 – Drillhole MDQ0222 from ~268.80 to ~273.80 metres depth showing the thrust contact between the Mount Dore granite and the carbonaceous slates, and drillhole MDQ0145 at ~226 metres depth showing detail of polymictic contact breccia between the same units.

3.2.4. Calc-silicates

This unit is composed of banded fine to medium grained metasediments that intercalate between finer grained red colour and medium grained dark green bands (Fig 3:2 d). The mineral association is dominated by amphibole (tremolite-actinolite, commonly zoned) + K-feldspar + quartz + albite + carbonate ± apatite ± titanite ± magnetite ± epidote ± zircon. The

finer grained bands are K-feldspar + albite dominated with strong hematite dusting while the coarser grained bands are amphibole + K-feldspar dominated. It is intensely hydrothermally altered rendering features of the protolith unrecognisable although the banding and mineralogy indicates that it likely represents a layered limestone and impure marl. The relation between K-feldspar, albite, carbonates and quartz is complex with all of these minerals appearing as vein infill and as replacive minerals. This unit also shows great variation from top to bottom, partly due to protolith variations but more importantly due to hydrothermal alteration. In the top part of this unit, albite + K-feldspar + quartz alteration is dominant and it is where the bulk of the Mo-Re mineralization is hosted. In this mineralized zone, the hydrothermal alteration can locally obliterate the banding, and lighter colours are prevalent. Breccias and veins, which host most of the molybdenite, are also common and the banding displays complex fold geometries. Towards the bottom of the unit, K-feldspar alteration with hematite dust becomes stronger with locally important amounts of magnetite and apatite. The bottom contact zone displays intense silicification that is related to the silicified siltstone below.

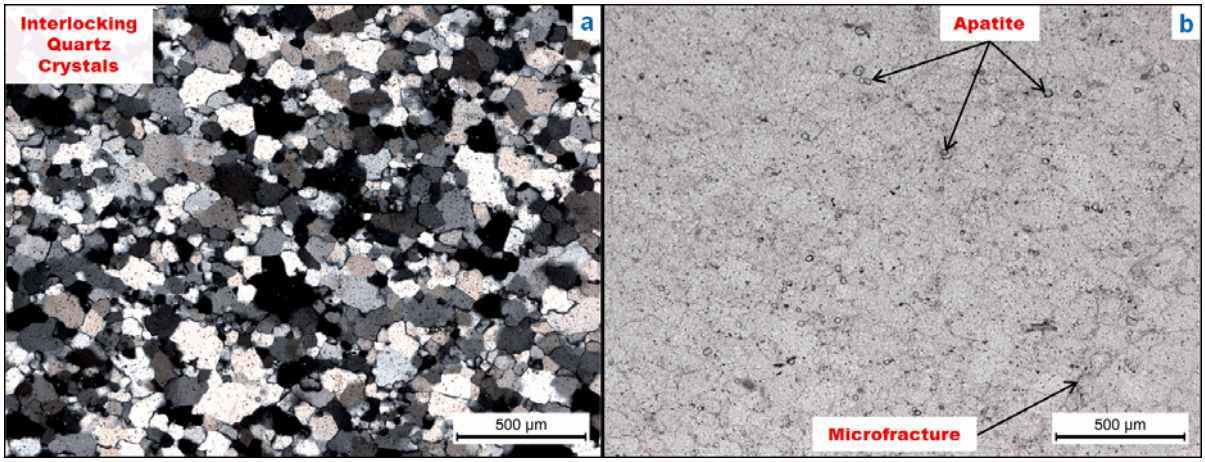

Figure 3:4 – Photomicrographs of a silicified siltstone core sample from drillhole MDQ0252 at ~550.60 metres depth. **a)** Photomicrograph taken in cross-polarized light showing interlocking fine to medium grained crystals of quartz. **b)** Photomicrograph taken in plane-polarized light showing small apatite crystals and microfractures.

3.2.5. Silicified siltstone

This unit is very homogeneous due to the intense pervasive silicification. The quartz crystals display a preferred orientation, which is visible in hand samples and lower magnification microscopy, possibly reflecting relict metasedimentary banding (Fig. 3:2 e). The silicified siltstone is composed of fine to medium size interlocking quartz crystals with minor small dispersed crystals of apatite (Fig. 3:4). There are also quartz veins that can be recognised as

such due to displaying slightly larger crystal sizes. Discontinuous microfractures are common and are locally filled with chlorite and in wider small pods, have hematite filling. Also locally, there is a later low temperature alteration dominated by sericite.

3.2.6. Dikes and Sills

Several felsic and intermediate to mafic dikes/sills intrude the previously described units. The dikes/sills are commonly a few metres wide. These intrusions are sometimes difficult to recognize due to similar mineralogy and/or alteration to the surrounding rocks, and their importance might be underestimated at the deposit scale. The intermediate to mafic intrusives display apatite and magnetite that seem to be primary igneous minerals and there is an absence of other minerals that typify the regional Na-(Ca) hydrothermal alteration stage. However, there is strong hydrothermal carbonate ± sulfides alteration associated with these intermediate intrusions. Given these alteration signals, it is likely that these intrusions are younger than the regional alteration and older or synchronous with the Cu-polymetallic hydrothermal alteration stage (see more details below). The felsic dikes/sills display intense Na-(Ca) hydrothermal alteration, which makes them much more difficult to recognize, and are therefore considered as pre-hydrothermal alteration intrusives.

The sills/dikes that are the easiest to identify are of intermediate to mafic composition. Two good examples of these intermediate to mafic intrusions were identified and described (Fig. 3:5). The first is a fine grained dolerite mostly composed of fine to medium grained plagioclase, with very minor small crystals of pyrite in a very fine grained matrix, within which the mineral assemblage is difficult to ascertain. This intrusion has chilled margins on the contacts with the calc-silicate rocks it intrudes. The zone of the chilled margin has disseminated small to medium crystals of chalcopyrite with small associated crystals of pyrite and locally carbonate veins (Fig. 3:5 b, e, and f). The second representative sill/dike of intermediate to mafic composition consists of equigranular plagioclase + biotite with rare larger phenocrysts of plagioclase. A minor quantity of magnetite and apatite, and rare, fine grained pyrite is also present. The biotite is moderately to intensely altered to chlorite (Fig. 3:5 a, c, and d).

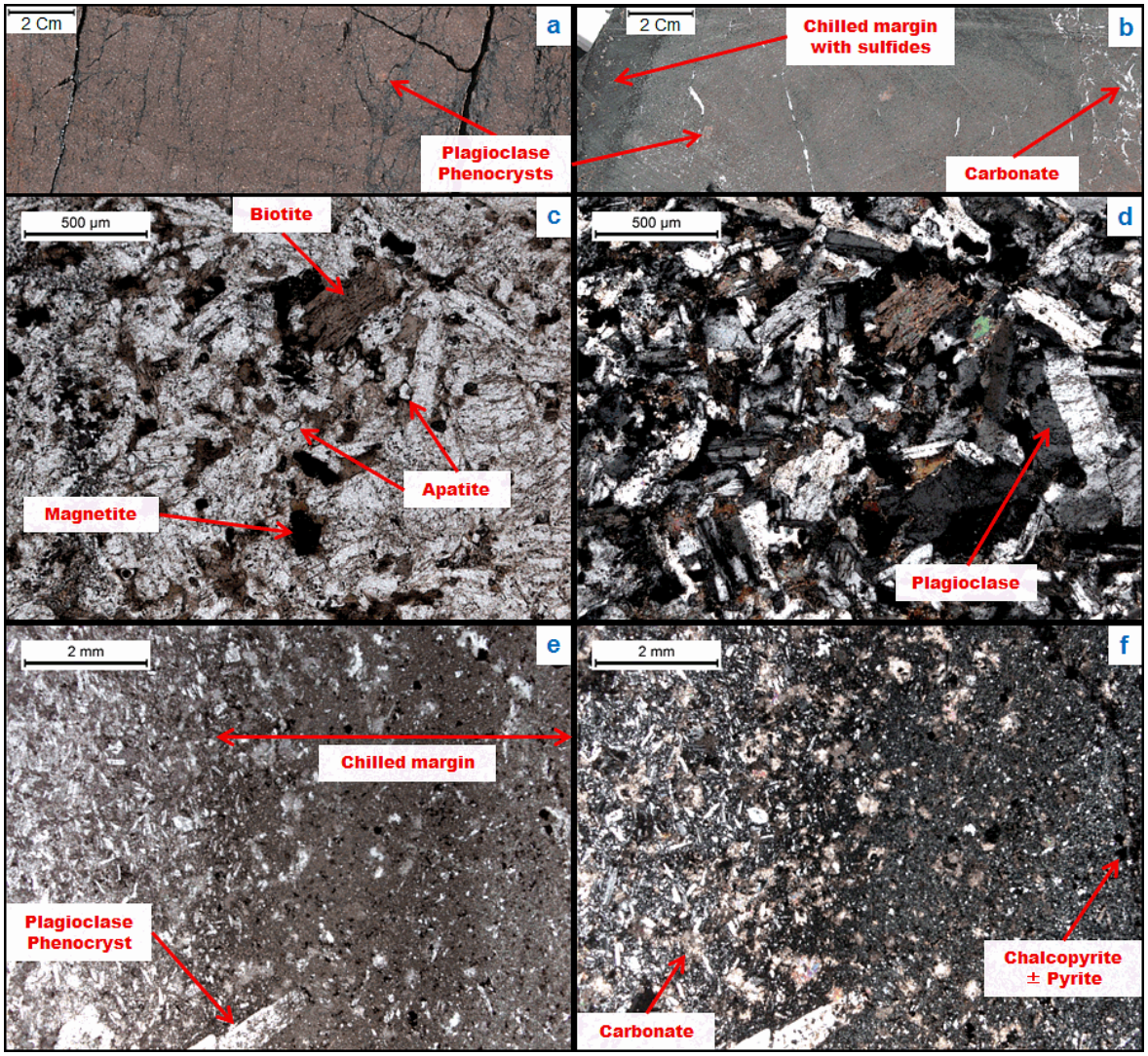

Figure 3:5 – **a)** Drillhole MDQ0129 at ~166.45 metres depth showing a fine grained intermediate sill/dike core sample. **b)** Drillhole MDQ0120 at ~360.00 metres depth showing a very fine grained mafic dike/sill with a chilled margin contact in calc-silicate rocks. **c)** Photomicrograph of sample a) taken in plane-polarized light showing intermediate intrusion with equigranular fine grained plagioclase + biotite (chlorite altered) ± magnetite ± apatite (small crystals). **d)** Photomicrograph of the previous taken in cross-polarized light. **e)** Photomicrograph of sample b) taken in plane-polarized light showing detail of the chilled margin. **f)** Photomicrograph of the previous taken in cross-polarized light.

The major mineralogy of the felsic sills/dikes is medium grained quartz + K-feldspar ± apatite (small crystals) ± titanite (small crystals) (Fig. 3:6 a and b). These rocks are intensely altered with hematite dusted albite + carbonates ± tourmaline ± chlorite ± sericite (Fig. 3:6 c and d). The hematite dusted albite is the first hydrothermal alteration mineral followed by the carbonates associated with tourmaline, then followed by veinlets of chlorite (see below for details). The sericite alteration is a later low temperature event. It is important to note that the tourmaline in this sample is strongly pleochroic from clear to olive green in contrast to the tourmaline found commonly associated with the Cu-polymetallic mineralization that is pleochroic with yellow, which may reflect different contents of Fe.

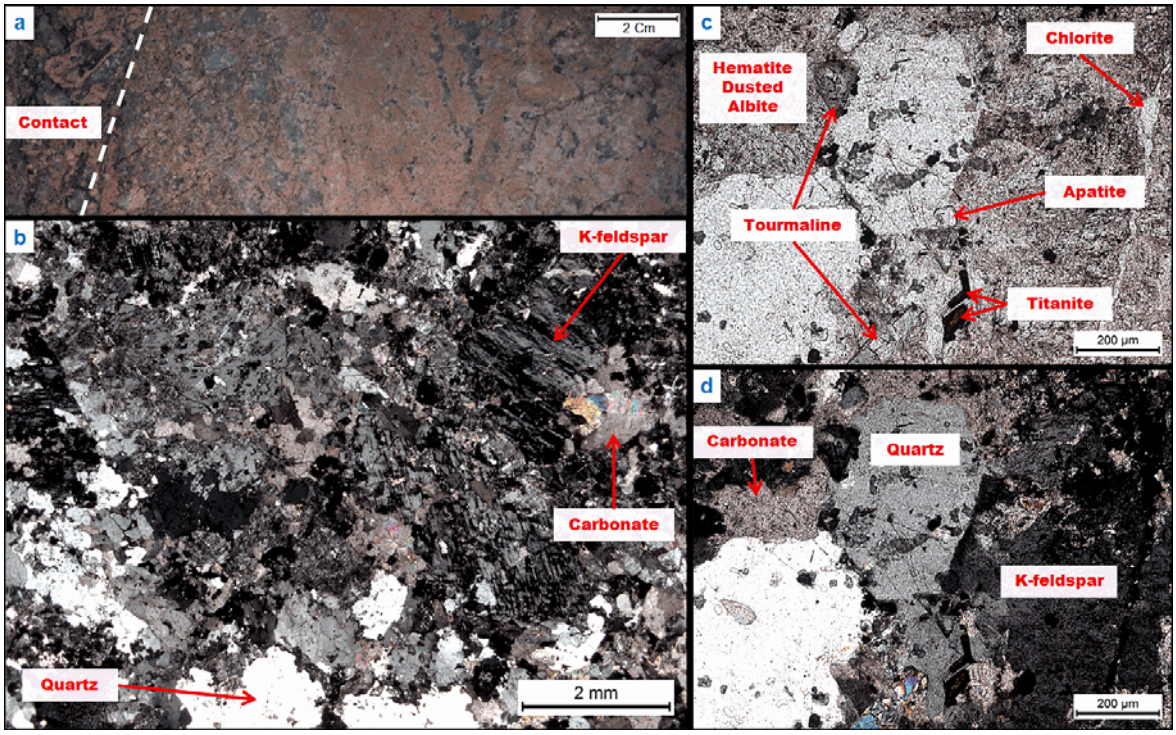

Figure 3:6 – **a)** Drillhole MDQ0120 at ~324.80 metres depth showing felsic dike/sill core sample, with quartz and K-feldspar, and weakly brecciated contact with calc-silicate rocks. **b)** Photomicrograph taken in cross-polarized light of the previous sample showing K-feldspar + quartz + carbonates. **c)** Photomicrograph taken in plane-polarized light of drillhole MDQ0120 at ~324.80 metres showing example of a felsic sill/dike mineral assemblage with quartz + K-feldspar ± apatite ± titanite, and the hydrothermal alteration minerals: Hematite dusted albite + carbonate + tourmaline. **d)** Photomicrograph of the previous taken in cross-polarized light.

3.3. Hydrothermal alteration and mineralization of the Merlin deposit

The designation of each stage is based on the main mineral assemblage and their relative timing of formation. This division should not be seen as completely dissociated from each other, since there are minerals that appear in more than one alteration stage and there are temporal and spatial overlaps. Routine microprobe mineral identification was used to complement the petrography studies.

3.3.1. Na-(Ca) stage

The first hydrothermal alteration stage in the Mount Dore and Merlin deposit is related to the regional Na-(Ca) hydrothermal event that is widespread in the Cloncurry district. This alteration is possibly concomitant with the emplacement of felsic intrusives of the Williams-Naraku Batholiths (see Chapter 5 for details), the most important igneous event in the Eastern Fold Belt (e.g. Oliver et al., 2004). This alteration stage is best observed in the central part of the calc-silicate unit, between the overlying black slates and the underlying silicified siltstone.

This association is preferentially preserved here, as subsequent alteration stages are only weakly developed. The mineral assemblage that defines the Na-(Ca) stage in the calc-silicates is mostly composed of albite + amphibole with important amounts of apatite (Fig. 3:7 a and b). Most of this mineral assemblage in the calc-silicate rocks occurs as replacement, although there are albite ± quartz veins that can parallel or cross-cut the banding, and there is also evidence of amphibole growth into veins (Fig 3:7 d).

The albite displays locally strong hematite dusting and the amphiboles show complex zoning. Both minerals are frequently intensely to moderately altered by carbonates, chlorite and sericite (Fig. 3:7 c). The apatite is quite abundant in the calc-silicate rocks and appears as either dispersed isolated crystals or in clusters (Fig. 3:7 a and b). Apatite grain size is on average ~100µm, and contains several complex growth zones, as imaged by cathodoluminence and microprobe SEM (see Chapters 2 and 6 for more details).

There are zones of strong silicification that are associated with the albite alteration (Fig. 3:7 d). The upper and lower contact zones that bound the calc-silicate unit are strongly silicified. This silicification results in zones where the calc-silicate banding and the carbonaceous slates are largely replaced by a fine mesh of quartz and albite. This alteration in the carbonaceous slates can be very intense, making recognition of the protolith difficult. Although there is albite ± quartz veining the albitization and silicification during this hydrothermal alteration stage, it is mostly ductily deformed, while the formation of quartz that is associated with the Cu-polymetallic stage is mostly controlled by brittle deformation structures (veins, faults, breccias). There are zones of silicification in the phyllites and upper units of the carbonaceous slates that were also formed during this alteration stage although it is less pervasive and more complicated to distinguish from the quartz formation associated with the Cu-polymetallic alteration stage.

The most important secondary minerals that are formed during this stage in the calc-silicate rocks are magnetite, epidote, titanite, clinopyroxene, and possibly rutile. The apatite and magnetite are found in direct association, although apatite is more abundant than magnetite (Fig 3:7 e and f). It is important to note that, in the calc-silicate unit below the mineralization, there are occurrences of chalcopyrite and pyrite in banding-parallel veins, “patches” and disseminations that are commonly associated with magnetite-bearing calc-silicate zones. The epidote is present as euhedral grains that appear infrequently in the calc-silicates. The timing of epidote formation was defined to be during the later stages of the Na-(Ca) stage due to spatial associations with the main sodic stages and local apatite inclusions in epidote. Clinopyroxene might have been a more abundant mineral during this stage but is

now intensely altered by amphibole and albite, and is very difficult to recognize. The rutile may have been formed during regional metamorphism or earlier, and its relation with the hydrothermal alteration is difficult to ascertain. Titanite forms euhedral crystals that, as with rutile, may be partly inherited from the metamorphic mineral assemblage. Unlike rutile though, the titanite displays a textural relationship with the Na-(Ca) mineral assemblage, indicating that at least part of the titanite is hydrothermal (Fig. 3:7 c).

The Na-(Ca) hydrothermal stage in the carbonaceous slates and phyllites is less pervasive; it manifests mostly as an assemblage of albite + quartz ± apatite ± rutile. The albite appears as mostly alteration in bands parallel to the foliation, and less commonly as vein infill. The apatite in these units is smaller than in other units, and is easily recognized in the foliation-parallel veins. Again the rutile in these units may be of metamorphic origin. It is difficult to further characterize the Na-(Ca) hydrothermal stage in the carbonaceous slates and phyllites due to the very fine to fine grain textures, the less intense alteration of this stage in these units, and strong overprint by subsequent alteration.

3.3.2. Cu-polymetallic stage

The second hydrothermal stage was responsible for the copper and polymetallic mineralization. It was adopted by Ivanhoe Australia (with special emphasis on the south zone; Fig. 3:1, plan view), to designate and distinguish the Mount Dore Cu-polymetallic mineralization from the Merlin Mo-Re deposit, even though the Merlin deposit also contains Cu-polymetallic mineralization. The copper dominated mineralization can be sub-divided into two zones: The Mount Dore leachable copper zone (oxide and transitional) and the Mount Dore polymetallic zone (primary sulfides) (Fig. 3:1). The indicated resources consist of 70 Mt with 0.58% Cu and 0.08g/t Au and 38 Mt with 0.51% Cu and 0.13g/t Au of inferred resources (Ivanhoe Australia LTD technical report, 2012).

The Mount Dore leachable copper zone is the top-most weathered and supergene altered section of the deposit, and consists of intensely weathered metasedimentary rocks with secondary copper mineralization characterized by chrysocolla, cuprite, chalcotrichite, pseudomalachite, native copper, and trace azurite and malachite (Lazo and Pal, 2009) (Fig. 3:8 a). This changes gradationally into the primary polymetallic zone with chalcocite, native copper and trace covellite (Lazo and Pal, 2009). The starting depth of the primary polymetallic zones is dependent on faults and the zone of the deposit, i.e. slope of the host units and whether or not the Mount Dore granite caps them (Fig. 3:1).

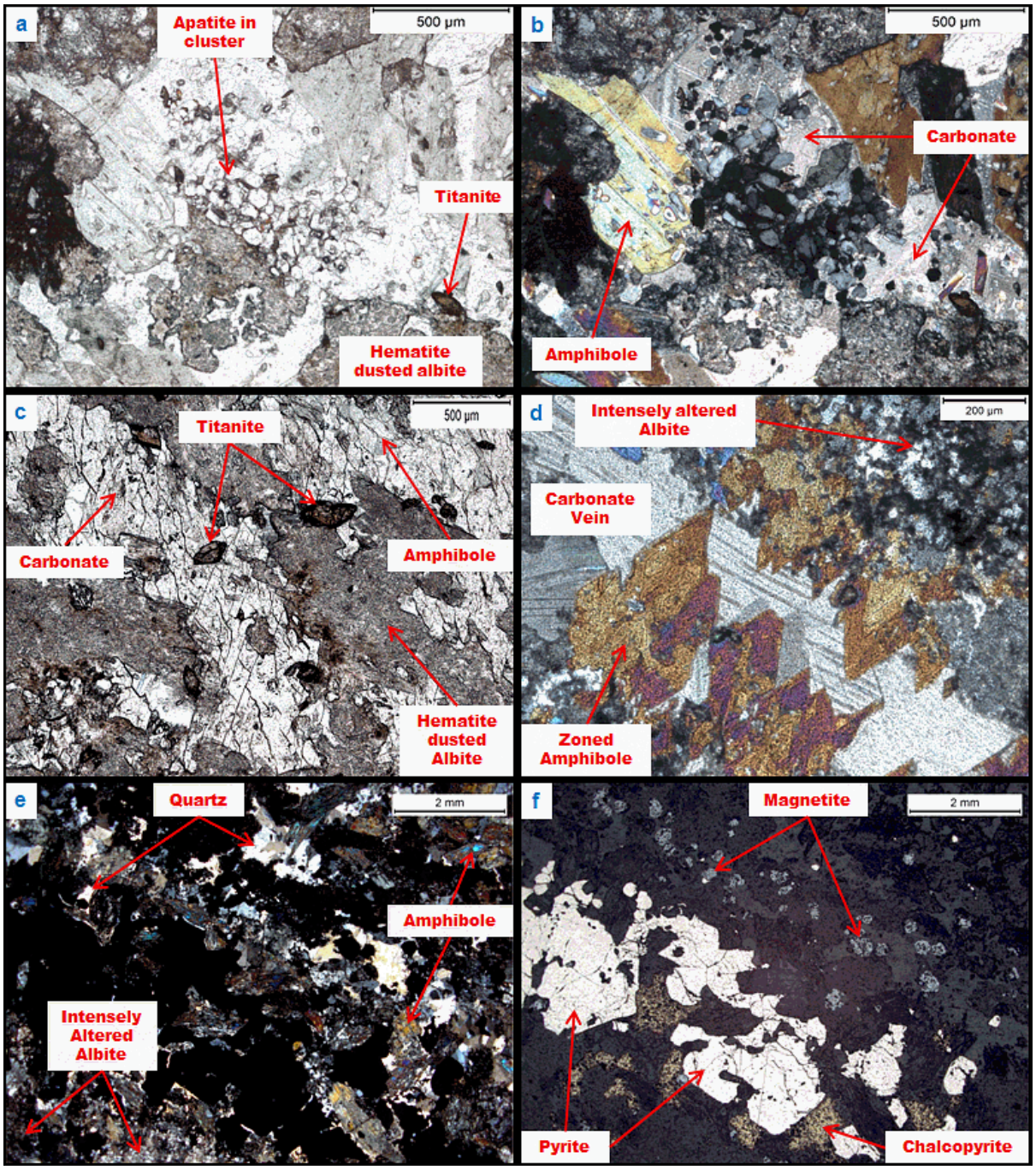

Figure 3:7 – **a)** Photomicrograph taken in plane-polarized light of drillhole MDQ112 at ~381.85 metres depth showing Na-(Ca) hydrothermal alteration mineral assemblage in calc-silicate rocks characterized by apatite arranged in a cluster, amphibole, hematite dusted albite and carbonate. **b)** Photomicrograph of the previous taken in cross-polarized light. **c)** Photomicrograph taken in plane-polarized light of drillhole MDQ112 at ~381.85 metres depth showing textural relation of titanite crystals with hematite dusted albite, amphiboles (tremolite-actinolite) and carbonate in Na-(Ca) hydrothermal alteration mineral assemblage in calc-silicate rocks. **d)** Photomicrograph taken in plane-polarized light of drillhole MDQ0112 at ~381.85 metres depth showing Na-(Ca) hydrothermal alteration in calc-silicate rocks with zoned amphiboles growing into a vein of carbonates that cut intensely altered and hematite dusted albite. **e)** Photomicrograph taken in plane-polarized light of drillhole MDQ0252 at ~537.85 metres depth in calc-silicate rocks, showing intensely altered albites and amphiboles with magnetite crystals and quartz in bands parallel to vein infill with pyrite and chalcopyrite. The pyrite and chalcopyrite crystals show thin rims of quartz. **f)** Photomicrograph of the previous taken in transmitted light.

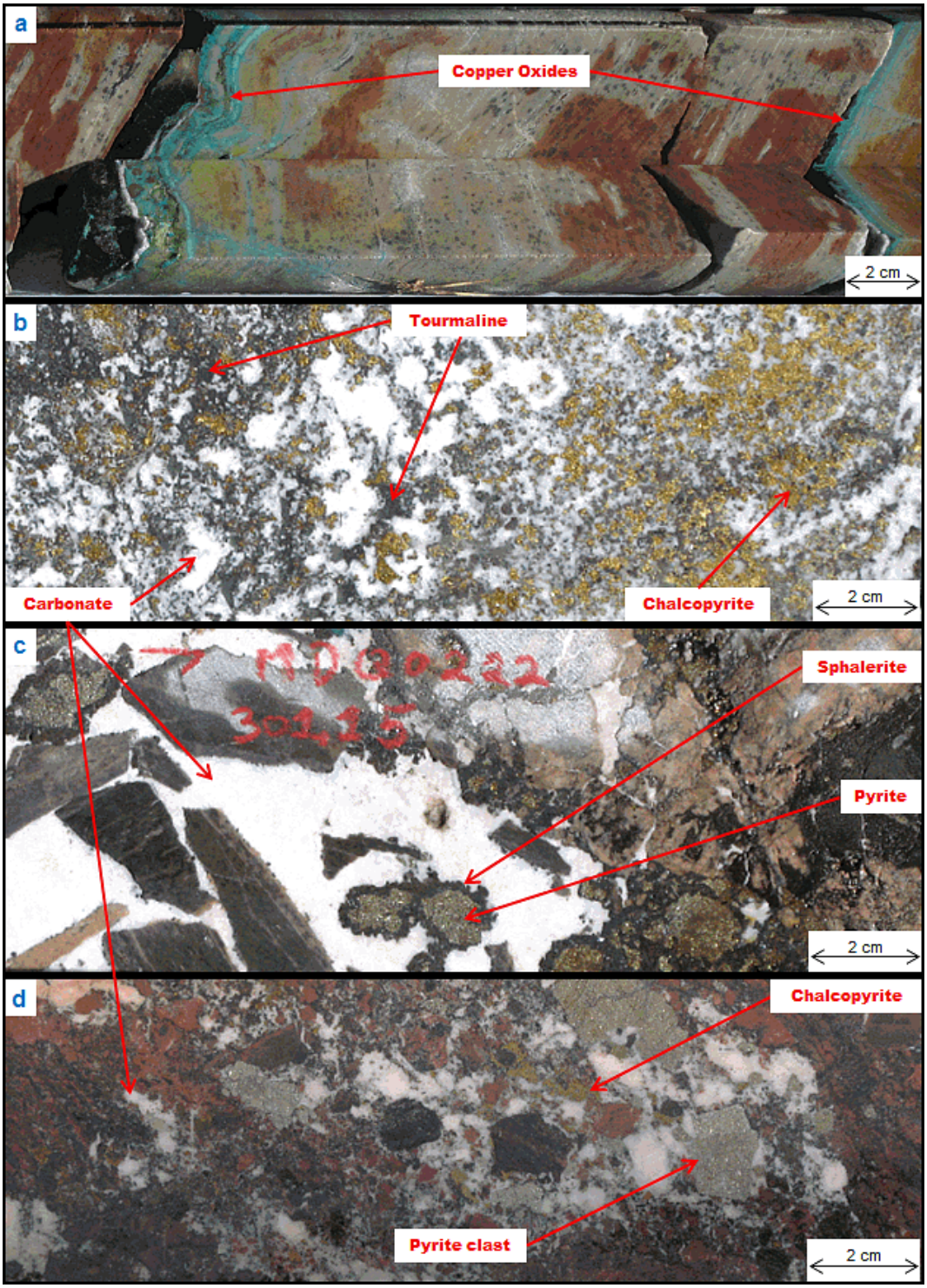

Figure 3:8 – a) Drillhole MDQ0129 at ~53.85 metres depth showing intensely weathered carbonaceous slates / phyllites core sample with oxidized copper minerals in veins parallel to foliation. **b)** Drillhole MDQ0133 at ~373.75 metres showing carbonate vein/breccia core sample with tourmaline + chalcopyrite + pyrite. **c)** Drillhole MDQ0222 at ~301.05 metres depth showing jigsaw clast-supported breccia core sample in carbonaceous slates with infill of sphalerite surrounding chalcopyrite + pyrite in carbonates. **d)** Drillhole MDQ0222 at ~403.10 metres depth showing clast-supported breccia core sample in calc-silicate rocks with pyrite + K-feldspar altered clasts with carbonate ± chalcopyrite infill.

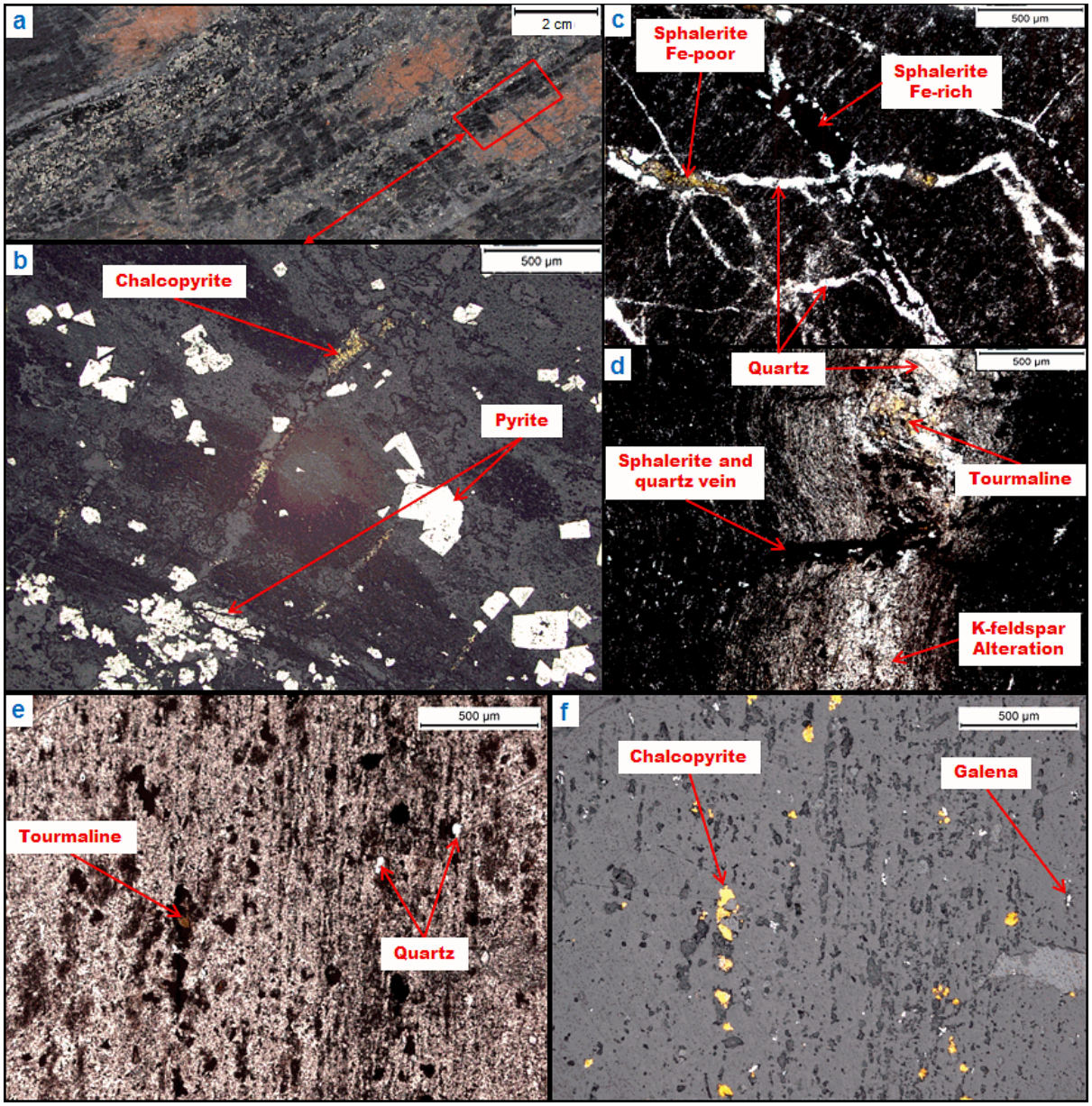

Figure 3:9 – **a)** Drillhole MDQ0133 at ~193.0 metres depth showing altered carbonaceous slate with quartz + albite/K-feldspar + chlorite + pyrite ± chalcopyrite. **b)** Photomicrograph taken in reflected light showing detail of the previous with pyrite composed of euhedral crystals disseminated and as ragged crystals arranged in banding-parallel veins, following the foliation orientation. The textural differences of the pyrite indicate different pyrite formation stages. The chalcopyrite appears in veins that cut the foliation. **c)** Photomicrograph taken in plane-polarized light of drillhole MDQ0221 at ~244.10 metres depth of carbonaceous slate with quartz + sphalerite in veins cross-cutting the foliation. The vein with dark (Fe-rich) sphalerite is cut by the yellow coloured (Fe-poor) sphalerite vein. **d)** Photomicrograph taken in plane-polarized light of the previous sample showing another quartz + sphalerite vein cutting a parallel to foliation vein with tourmaline + K-feldspar ± sphalerite ± galena. **e)** Photomicrograph taken in plane-polarized light of drillhole MDQ0252 at ~362.70 metres depth of phyllite with foliated muscovite + K-feldspar/albite ± quartz ± tourmaline ± chalcopyrite ± galena. **f)** Photomicrograph taken in reflected light of the previous.

The Cu-polymetallic alteration and associated mineralization occurs mostly in the carbonaceous slates and in lesser abundances in the phyllites and calc-silicate rocks. It is dominated by chalcopyrite although galena, sphalerite, bornite, cobaltite and arsenopyrite are also found (Brown et al., 2010; this study). After chalcopyrite, sphalerite and galena are the

most abundant sulfides and all three commonly appear associated (Fig. 3:10 d and e). Bornite, cobaltite and arsenopyrite appear in very minor amounts. The bulk of the Cu-polymetallic mineralization occurs in angular clast-supported breccias with carbonate infill, which is frequently dolomitic (Fig. 3:8 c and b). The Cu-polymetallic sulfides that were formed in the breccias are mostly infill but there can be pyrite clasts in the breccias, although not frequently, which is indicative of multiple pyrite forming phases (Fig. 3:8 d).

The mineralization also appears in lesser quantities in veins that cross-cut the foliation and as foliation-parallel veins. These mineralized veins display complex cross-cutting relations, indicating several vein formation events (Fig. 3:9). The mineralization of the earlier veins consists of chalcopyrite + pyrite that are cut by iron rich sphalerite that in turn are cut by iron-poor sphalerite veins. Small crystals of chalcopyrite ± galena occur aligned with the foliation in the carbonaceous slates, forming a small quantity of the Cu-polymetallic mineralization (Fig. 3:9 e and f). Chalcopyrite + pyrite also appear without other sulfides, in the phyllites, in intensely altered carbonaceous slates, and in the calc-silicate rocks. This mineralization type occurs in breccias and veins but also as disseminations that are commonly arranged in patches (Fig. 3:9 a and b). This style of mineralization is locally coincident with the Mo-Re mineralization (Fig. 3:10 f).

The minerals that are found with the sulfides in this hydrothermal alteration stage are K-feldspar, carbonates, tourmaline, quartz and minor apatite. The K-feldspar appears mostly as a replacive mineral and locally, in lesser amounts, as vein infill (Fig. 3:10 a). The carbonates are a very important mineral during this alteration stage appearing in veins and, most commonly, as breccia infill (Fig. 3:10 a and c). In the Mount Dore and Merlin hydrothermal system there are different carbonate compositions, typically dolomite and calcite, as observed in routine microprobe work, although their overlapping textures and the difficulty of their identification under the microscope does not allow for their complete distinction. Nevertheless, most of the carbonates that are associated with the Cu-polymetallic stage are pink coloured dolomitic and lesser, but still important, calcite. Most of the sulfides formed during this stage are associated with the carbonate formation. The tourmaline that occurs in the carbonaceous slates, and rarely in the phyllites, is also associated with this mineralizing stage, appearing in three main settings:

- Small crystals aligned with the foliation together with small crystals of chalcopyrite ± galena ± apatite in carbonaceous slates (Fig. 3:9 e and f).
- In the same unit there are also larger crystals of tourmaline in foliation-parallel veins with K-feldspar ± quartz ± fine galena ± sphalerite ± apatite (Fig. 3:9 d).

- With the bulk of the Cu-polymetallic mineralization in the carbonate breccias (Fig. 3:10 a, b, and c). The tourmaline that is associated with these breccias is both alteration and infill. Alteration-related tourmaline occurs as centimetric alteration halos in the clasts and host rock adjacent to the breccia infill and when infill it crystalizes at the edges of the clasts and host rocks (Fig. 3:10 a, b, and c).

The quartz formation during this stage is complicated by the intense silicification of the previous hydrothermal stage but seems to be mostly infill. The quartz appears as the main mineral in cross-cutting veins in the carbonaceous slates, and in lesser amounts in the phyllites, with sphalerite. It also appears in the carbonate mineralized breccias where it crystalizes in the edges between the carbonate infill and the sulfides (Fig. 3:10 c).

3.3.3. Mo-Re stage

The third major hydrothermal alteration stage was responsible for producing the unique Mo-Re mineralization, with indicated mineral resources estimates of 6.7 Mt at 1.4% Mo and 23 ppm Re, and inferred mineral resources with 0.2 Mt at 0.8% Mo and 13 ppm Re, at a 0.3% Mo cut-off (Ivanhoe Australia LTD technical report, 2012). One of the most striking finds by Ivanhoe Australia is the Little Wizard ore body, which is a massive molybdenite body still open towards the east. An important observation is that although the surrounding metasedimentary rocks are extremely weathered this ore body is mainly composed of molybdenite instead of ferrimolybdite and other molybdenum oxides that can be found in the southwest area of the deposit in the oxide zone.

The Mo-Re mineralization has four main styles of occurrence: Breccia infill, veins, stylolitic veins, and disseminated (Fig. 3:11). These different styles show some spatial overlap, with the mineralized matrix-supported breccias with rounded clasts being mostly located in the carbonaceous slate and calc-silicate contact zone. The breccias gradually change downwards, at the top part of the calc-silicates, into mineralized veins, commonly stylolitic, and disseminations. There is also a smaller part of the Mo-Re mineralized breccias in the contact between the phyllites and the carbonaceous slates, which is due to the ore geometry that will be discussed below.

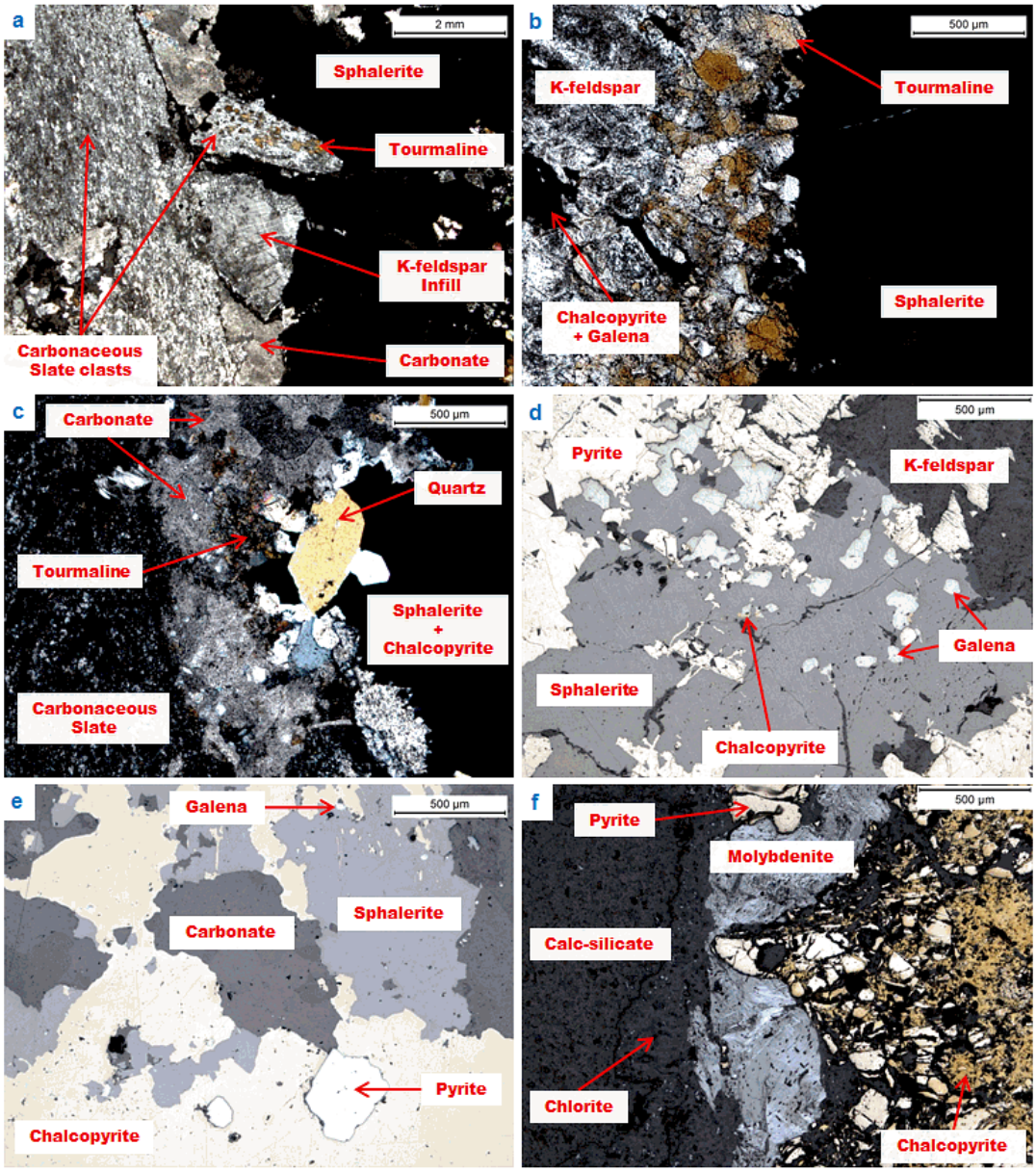

Figure 3:10 – **a)** Photomicrograph taken in plane-polarized light of drillhole MDQ0222 at ~301.10 metres depth of a breccia in carbonaceous slates with sphalerite ± chalcopyrite and carbonate and K-feldspar associated, as infill. The fine grained clasts are intensely K-feldspar altered carbonaceous slates with locally strong tourmaline alteration. **b)** Photomicrograph taken in plane-polarized light of drillhole MDQ0222 at ~301.10 metres depth showing breccia clast edge in carbonaceous slates with sphalerite + chalcopyrite mineralization infill with tourmaline crystalizing at the clast edge and K-feldspar altering the breccia clast. In the clast there is also chalcopyrite + galena mineralization. **c)** Photomicrograph taken in cross-polarized light of drillhole MDQ0252 at ~362.70 metres depth showing a mineralized vein in carbonaceous slates with carbonates + tourmaline + quartz infill. **d)** Photomicrograph taken in transmitted light of drillhole MDQ0222 at ~381.50 metres depth showing galena in close association with pyrite, chalcopyrite and sphalerite infill in brecciated carbonaceous slate with strong K-feldspar alteration. Galena displays textures indicative of coeval precipitation with pyrite and chalcopyrite and earlier formation relative to sphalerite. **e)** Photomicrograph taken in transmitted light of drillhole MDQ0133 at ~373.75 metres depth of mineralized carbonate breccia with sphalerite + chalcopyrite ± pyrite ± galena in close association. Textural relations indicate co-precipitation of chalcopyrite and sphalerite. Sphalerite also displays characteristic micrometric exolutions of chalcopyrite. **f)** Photomicrograph taken in cross-polarized light of drillhole MDQ0252 at ~532.00 metres depth showing a banding parallel chlorite + molybdenite vein in banded calc-silicates with moderate to intense alteration overlapping a vein/patch of chalcopyrite + pyrite. The chalcopyrite displays textures that indicate partly co-precipitation and partly later formation relative to the pyrite.

The change in Mo-Re mineralization styles is reflected by the hydrothermal alteration mineral assemblage that gradually changes depending on the degree of fracturing and the nature of the host rocks. The most abundant and the highest grades of Mo-Re mineralization are found as matrix-supported breccias with rounded clasts where molybdenite occurs as infill. These breccias are commonly polymictic and the nature and relative abundance of the different clast types is dependent on the location of these breccias relative to the wallrocks (i.e. phyllite/carbonaceous slate, carbonaceous slate/calc-silicate contact), although it is not always possible to ascertain the clast origin due to the intense alteration. The clasts in these breccias are rounded and vary from millimetric to a few centimetres in size and commonly have small molybdenite disseminations. The Mo-Re mineralized breccias are associated with intense K-feldspar alteration, where the clasts are mostly composed of K-feldspar, and lesser amounts of chlorite (Fig. 3:11 a and 3:12 a and b).

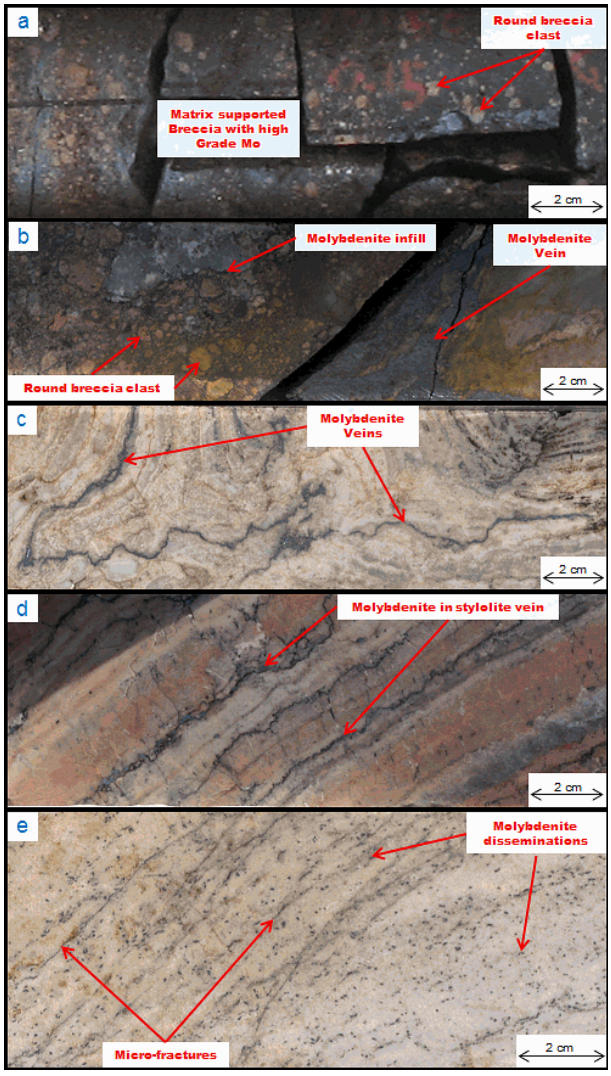

Figure 3:11 – **a)** Drillhole MDQ0119 at ~416.6 metres depth showing core sample with high grade Mo-Re mineralization as infill of matrix-supported breccias with rounded clasts in the contact zone between carbonaceous slates and calc-silicates. **b)** Drillhole MDQ0252 at ~393.3 metres depth showing core sample with matrix-supported breccias with rounded clasts with molybdenite infill and in veins in calc-silicate rocks. **c)** Drillhole MDQ0252 at ~487.8 metres depth showing core sample with banding-subparallel stylolitic veins with molybdenite in intensely altered calc-silicate rocks. **d)** Drillhole MDQ0132 at ~388.75 metres depth showing core sample of molybdenite veins with weak stylolitic textures following the banding in calc-silicate rocks. **e)** Drillhole MDQ0132 at ~364.70 metres depth showing disseminated molybdenite weakly arranged in preferential orientation parallel to relict banding in intensely altered calc-silicates. The disseminations of molybdenite are controlled by microfractures filled with chlorite.

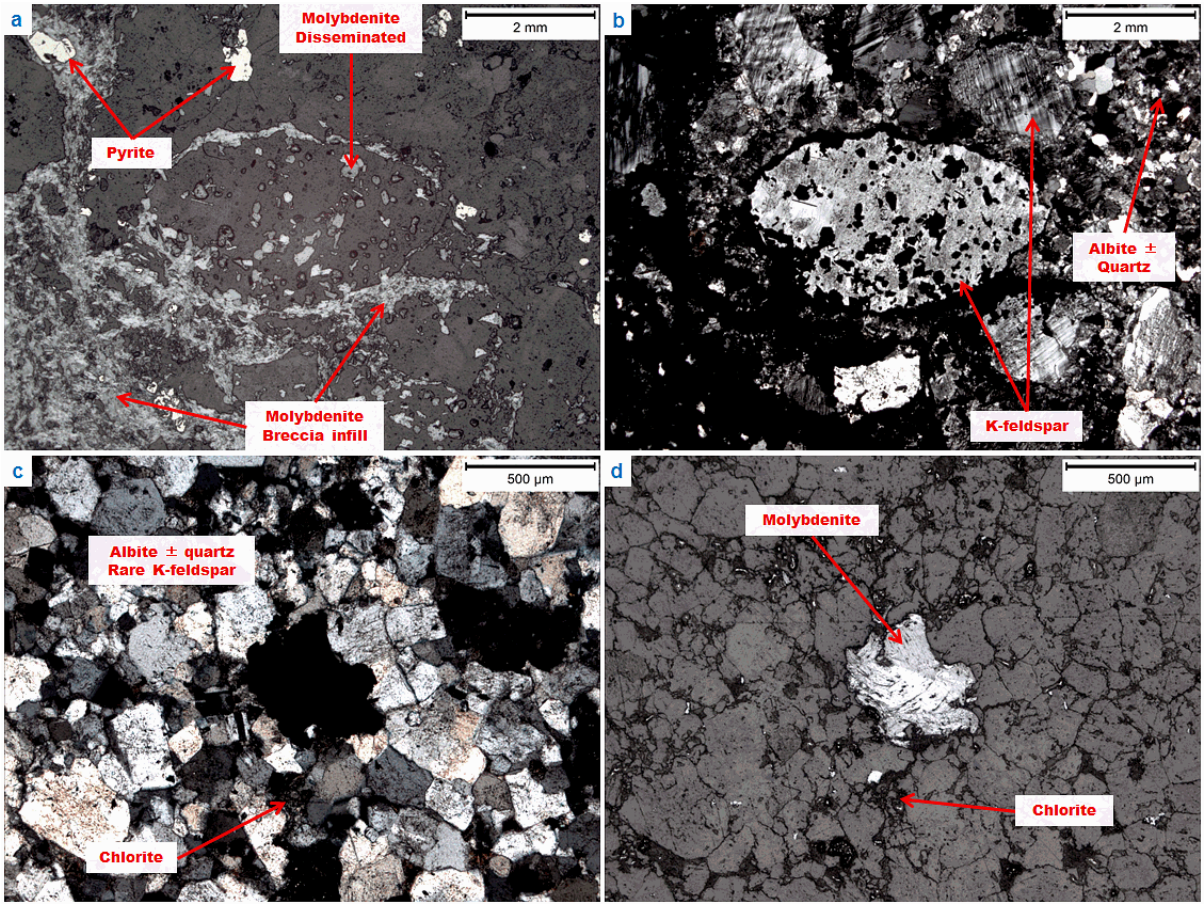

Figure 3:12 –Photomicrograph taken in (a) transmitted light, and (b) cross-polarised light of drillhole MDQ0150 at ~170.80 metres depth showing detail of the edge of a matrix-supported breccia with rounded clasts with molybdenite infill, and disseminated in clasts of K-feldspar, in calc-silicate rocks. The presence of albite ± quartz reflects the Na-(Ca) hydrothermal alteration assemblage of the calc-silicate host rock and K-feldspar characterizes the potassic hydrothermal alteration associated with Mo-Re mineralization. Photomicrograph taken in (c) cross-polarized and (d) transmitted light of drillhole MDQ0132 at ~364.70 metres depth showing disseminated molybdenite mineralization controlled by micro-fracturing with chlorite infill. This mineralization is hosted by intensely altered calc-silicates with strong albitization and silicification with minor K-feldspar alteration.

Around the breccias are Mo-Re mineralized veins that are more extensive at depth in the calc-silicate rocks, in comparison to the intensely altered carbonaceous slates and phyllites above (Fig. 3:11 b). They are mostly parallel to the banding even when the banding is intensely folded and disrupted, and less commonly appear cutting relict banding (Fig. 3:11 c). Many of the veins of molybdenite have stylolitic textures indicating pressure dissolution processes and some likelihood for remobilization of molybdenite at the scale of the core samples or broader (Fig. 3:11 d). The abundance and molybdenite content of the mineralized veining decreases with distance from the main Mo-Re breccias, becoming more frequently stylolitic and locally controlled by micro-fractures with disseminated molybdenite. These disseminations may be related to the veining since the molybdenite crystals are normally connected to each other by a small network of micro-veins that show a weak banding-parallel orientation (Fig. 3:11 e and

3:12 c and d). K-feldspar alteration intensity is directly proportional with the degree of brecciation/fracturing. This observation is supported by electron probe semi-quantitative analyses that allowed the identification of albite and K-feldspar in mineralized samples, when it was not feasible to efficiently distinguish between those minerals with the petrographic microscope.

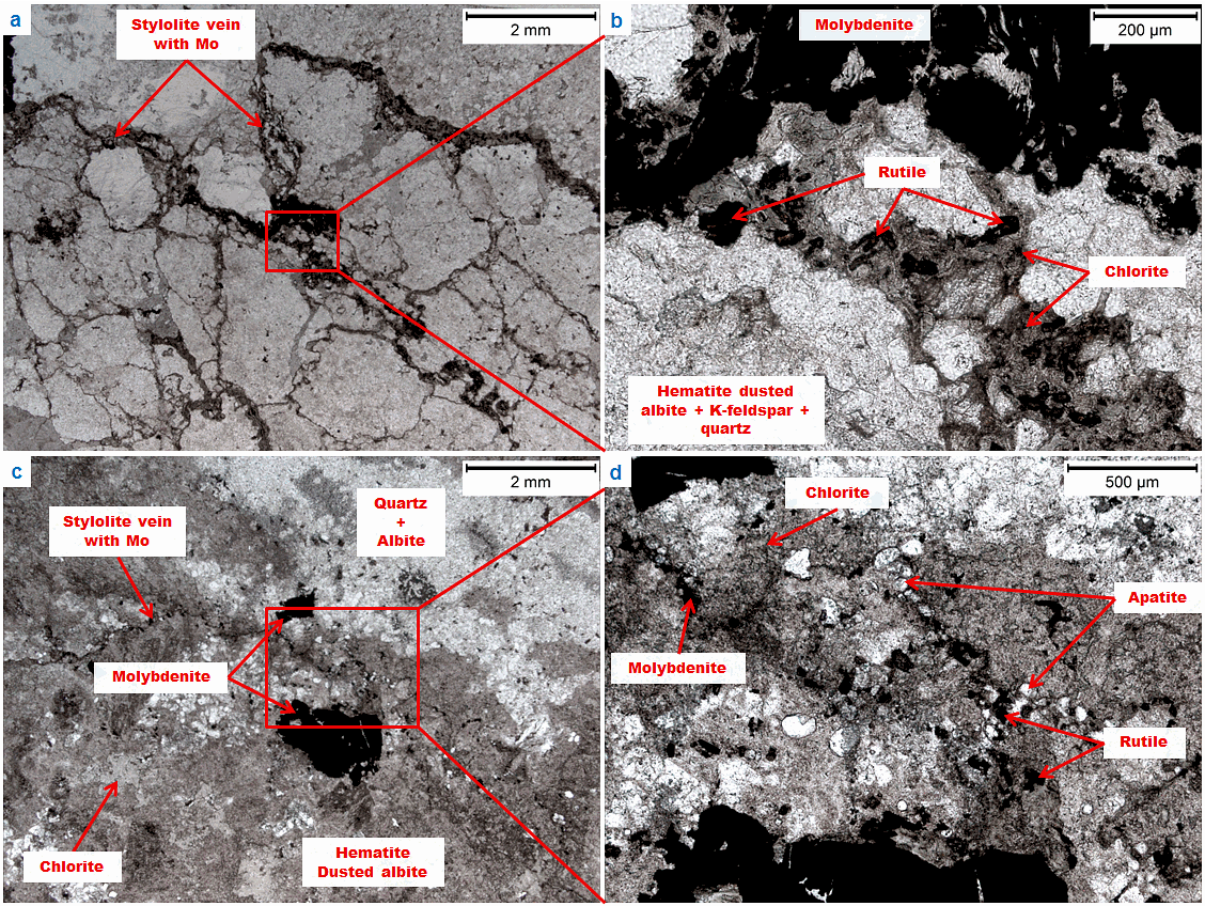

Figure 3:13 – **a)** Photomicrograph taken in plane-polarized light of drillhole MDQ0252 at ~487.90 metres depth showing a sample of calc-silicate rock with stylolitic vein with Mo-Re mineralization. **b)** Photomicrograph taken in plane-polarized light showing detail of the previous with molybdenite + chlorite ± rutile infilling the stylolitic vein. **c)** Photomicrograph taken in plane-polarized light of drillhole MDQ0132 at ~376.30 metres depth showing a sample of calc-silicate rock with stylolitic vein with Mo-Re mineralization associated. **d)** Photomicrograph taken in plane-polarized light showing detail of the previous with molybdenite + chlorite ± rutile ± apatite infilling the stylolitic vein.

Significant amounts of rutile and apatite occur with the chlorite in the Mo-Re veins, stylolitic veins and disseminations in the calc-silicate rocks. There are also rutile and apatite associated with the Mo-Re mineralized veins in the carbonaceous slates, but their quantity is much less and the relation with the Mo-Re mineralization is also less certain. It is important to note that both the rutile and apatite that are associated with chlorite and Mo-Re veins are more abundant when the veins display stylolitic textures. The rutile that can be found in these veins

is typically small, commonly 20 to 30 µm to a rare maximum of 50 to 70 µm, although locally very abundant (Fig. 3:13). There is strong textural evidence for apatite formation in chlorite + molybdenite ± rutile veins and stylolitic veins (Fig. 3:13). Electron probe semi-quantitative mineral analyses were used to identify minute amounts of micrometre-sized zircon and monazite grains associated with molybdenite mineralization. These more refractory accessory minerals may have been concentrated to higher abundances than elsewhere by dissolution of other more soluble components associated with the formation, or stylolitization, of the Mo-Re veins.

3.4. Discussion

The hydrothermal alteration and mineralization in the Mount Dore and Merlin deposit is very complex since multiple hydrothermal stages occurred with different intensities and/or alteration textures and/or at different location(s) in different geologic unit(s) (Fig. 3:14 and 3:15). Therefore the understanding of the complex deformation history is necessary although a detail structural analysis was beyond the scope of this study.

3.4.1. Previous structural interpretations

The phyllites and carbonaceous slates show penetrative foliation that is parallel to bedding and the calc-silicates show banding with moderate parallel to bedding foliation. The foliation was formed during regional D_2 deformation, which is synchronous with the peak of regional metamorphism (Bell, 1983; Adshead-Bell, 1998; Bell and Hickey, 1998; Betts et al. 2006; Rubenach et al. 2008; Marjoribanks, 2008). Regional D_2 (Duncan et al., 2014) or D_3 deformation (Marjoribanks, 2008) formed the Mount Dore Ductile Shear Zone, which marks the contact between the younger Staveley and the older Kuridala Formations and is dominated by the silicified siltstone. The Williams and Naraku Batholiths, which includes the Mount Dore Granite, intruded during the regional D_4 deformation stage and the thrust of the granite above the metasedimentary package occurred late or post D_4 (Rubenach et al., 2008; Marjoribanks, 2008, Duncan et al., 2014).

According to Marjoribanks (2008) the thrusting of the Mount Dore granite created a duplex structure that was responsible for the dilational structures that host the Cu-polymetallic mineralization. The deformation model proposed an E-W compressional regime with formation of folding and tectonic brecciation in phyllite/carbonaceous slates and

carbonaceous slates/calc-silicate contacts. The common fold limbs are zones of dilation that accommodated part of the Mount Dore and Merlin mineralization zones (Marjoribanks, 2008; Duncan et al., 2014). Differences in competence of the rock units in this compressional regime are thought to have resulted in tectonic brecciation along lithological contacts. The Mount Dore Ductile Shear Zone served has an impermeable barrier in the footwall and the Mount Dore granite in the hangingwall (Marjoribanks, 2008).

Hinman (*pers comm.*) improved the former structural interpretation by including brecciation zones in the contacts between the calc-silicates and carbonaceous slates, and carbonaceous slates and phyllites, which were formed due to reverse faults that dip towards the northeast. These reverse faults were formed during a compressive regime, as were the folds. The reverse fault structures did not create brecciation in the phyllites due to their mostly micaceous mineralogy that accommodated the strain by ductile behaviour, and therefore have lower levels of mineralization and hydrothermal alteration.

3.4.2. Key observations leading towards a new model

This structural model combined with the body of knowledge of hydrothermal alteration events and mineralization in the region led to the assumption that the structures that host the mineralization and the mineralization are formed upon the emplacement and thrusting of the Mount Dore granite. Although the general structural controls of the mineralization geometry from Marjoribanks (2008) and Hinman (*pers comm.*) are adapted to this study, the geochronological data (see Chapter 5 for details) do not agree with a synchronicity between the emplacement and thrusting of the Mount Dore granite and the mineralization. The main differences between the previous structural models and this study are:

- The tectonic faulting is the precursor structure for the formation of the hydrothermal brecciation. The tectonic brecciation was formed due to early regional deformations events (D_1 and D_2). These breccias were later used by the hydrothermal fluids that formed the Cu-dominated mineralization resulting in the angular clast mineralized breccias located in the carbonaceous slates. At a later event, similar tectonic breccias, located between the carbonaceous slates and the calc-silicate rocks, were used by the Mo-rich hydrothermal fluids which were magmatic in origin (see Chapters 5, 6, 7 and 8 for details), creating the matrix-supported magmatic-hydrothermal breccias with rounded clasts (Sillitoe, 1985), that host the bulk of the Mo-Re mineralization.

- The phyllites have acted as less permeable units in the hangingwall, instead of the Mount Dore granite as previously argued (Marjoribanks, 2008). Therefore the flow of mineralizing hydrothermal fluids would have been mostly contained within the carbonaceous slates and calc-silicate rocks, resulting in their spatial concentration and metal content upgrade.
- The emplacement of the Mount Dore granite (D_4) and subsequent thrusting (late or post D_4) occurred after the main Mo-Re mineralization stage (see Chapters 5 for details). Nevertheless, the Mount Dore granite emplacement had mineralization remobilization and deformational effects, and the Mo-Re stylolitic veins (Fig. 3:11 and 3:13) are interpreted to be a reflection of the Mount Dore granite thrust.

3.4.3. Hydrothermal alteration mineral assemblages

The first hydrothermal alteration stage characterized is similar to the Na-(Ca) widespread alteration found in the Eastern Fold Belt (Oliver et al., 2004; Mark et al., 2006a; Marshall and Oliver, 2006). This regional alteration event has been connected to the emplacement of the Williams-Naraku Batholiths (e.g. Pollard, 2001), of which the Mount Dore granite is the closest to the Mount Dore and Merlin deposit (albeit younger than the main mineralization at Merlin; see Chapter 5 for details). This chronology of events indicates that there is no causality effect between the Na-(Ca) hydrothermal alteration stage at the Mount Dore and Merlin and the intrusion of the Mount Dore granite. This does not preclude concomitance between the Na-(Ca) hydrothermal alteration at Mount Dore and Merlin and other Williams-Naraku aged intrusive, as the intrusive episode is known to be rather protracted, spanning approximately from 1540 to 1480 Ma (Pollard and McNaughton, 1997; Page and Sun, 1998; Mark et al., 2006a; Oliver et al., 2008; Rubenach et al., 2008).

The Na-(Ca) hydrothermal alteration stage is best characterized in the middle part of the altered calc-silicate unit, where there is less overprinting by subsequent hydrothermal alteration (Fig. 3:14 and 3:15). Nevertheless, this alteration stage has strongly altered the rocks in the contact zone between the carbonaceous slates and calc-silicate rocks where the bulk of the Mo-Re mineralization occurs. In the carbonaceous slates this hydrothermal alteration is less pervasive, and is especially weak in the phyllites. The intensity of the Na-(Ca) hydrothermal alteration is connected with the nature of the host rocks, where the calc-silicates are the most chemically reactive rocks, and with fractures and veins (Fig. 3:15 A 1).

The connection between this alteration and fracturing is clearly displayed by the rocks in the brecciated contact zone between the carbonaceous slates and calc-silicate rocks, in comparison to the weak alteration displayed by the ductily deformed and little-veined phyllites.

The silicification that is interpreted as part of this hydrothermal alteration stage is also intense in the contact zone between the carbonaceous slates and calc-silicate rocks, indicating a similar connection between the degree of fracturing and intensity of alteration. The contact zone between the calc-silicates and the silicified siltstones is also strongly silicified, which is explained by the proximity to the intense silicification of the Mount Dore Ductile Shear Zone. The middle part of the calc-silicate rocks is weakly silicified, because the intensity of fractures and veins is lesser, due to the deformation being more focussed along the boundaries (Fig. 3:15 A 2).

In the calc-silicate rocks there are also abundant carbonates associated with the Na-(Ca) mineral assemblage. Some of the carbonates were formed during this stage in the calc-silicate rocks (Fig. 3:7 a, b, c, and d), as it is common in the Cloncurry area (e.g. Oliver et al., 2004), although the bulk of the carbonates found in the hydrothermal system were formed during the Cu-polymetallic alteration stage.

During the Na-(Ca) stage there was formation of magnetite and/or hematite and apatite in the calc-silicate rocks. Commonly associated with these minerals are pyrite and chalcopyrite. While this mineral assemblage displays similarities to the IOCG style of mineralization (e.g. Hitzman et al., 1992; Williams and Pollard, 2002; Groves et al., 2010) the sulfides are interpreted to form after the magnetite (Fig.3:8 e and f), although it is possible that there is very minor formation of sulfides during this hydrothermal stage.

The second hydrothermal alteration stage overprints the Na-(Ca) alteration and is characterized by the formation of the Cu-polymetallic mineralization (Fig. 3:14 and 3:15). This mineralization can be sub-divided based on mineral assemblage, the style of occurrence and its location in the deposit, and although relative timing can be put forward between the following styles, the hydrothermal alteration as a whole is considered one stage:

1 – Chalcopyrite occurs as small crystals associated with galena in the carbonaceous slates and locally in the phyllites. These minerals are associated with tourmaline and small apatite crystals and appear aligned with the foliation of the host rocks (Fig. 3:9 e and f).

2 – In the mineralized carbonate breccias, the chalcopyrite is associated with pyrite, galena and sphalerite. It displays co-precipitation textures with sphalerite and locally with galena, but mostly post-dating pyrite (Fig. 3:10 d and e).

3 – Chalcopyrite also appears in veins, associated with pyrite, in calc-silicate rocks, carbonaceous slates, and locally in contact with Mo-Re mineralization (Fig. 3:10 f). It mostly displays later formation textures relative to pyrite but with some co-precipitation also occurring (Fig. 3:9 a and b).

By careful observation of the textural relationships it was possible to define a temporal sequence between the sulfide minerals. Pyrite and chalcopyrite are present in all of the styles of copper dominated mineralization. Pyrite displays strong evidence for formation before, and with, the other sulfides, but it does not appear to have formed after the precipitation of the other sulfides. For example, in the mineralized carbonate breccias the pyrite can appear as breccia clasts and also intergrown with the other sulfides (Fig. 3:8 c and d). Galena is formed early in the Cu-polymetallic system, appearing associated and locally intergrown with chalcopyrite in the first and second style (Fig. 3:9 e and f, and 3:10 d and e). In the mineralized carbonate breccias it shows textural evidence of having been formed before the sphalerite although with some temporal overlap (Fig. 3:10 d). The sphalerite textural relationship with the chalcopyrite is clearly synchronous although the chalcopyrite locally shows textures indicating some precipitation occurring before the sphalerite formation (Fig. 3:10 d and e). Textural evidence which indicates that the sphalerite continued to be precipitated after the chalcopyrite stopped forming is weak but is nevertheless present. The evidence referred to is the existence of quartz + sphalerite centimetric veins, in carbonaceous slates and less frequently in phyllites, that show a cross-cutting sequence going from iron-rich sphalerite to iron-poor sphalerite, which is interpreted as the last stage of sphalerite formation (Fig. 3:9 c and d). In these veins other sulfides are absent or occur in minute amounts, which indicate that sphalerite formation might be the last mineralizing pulse in this hydrothermal alteration stage. In all the mineralization styles, the infill sulfide minerals are associated with carbonates and/or minor quartz. The quartz is formed later relative to the carbonates, which can be observed in the wider veins and breccias (Fig. 3:10 c). Minor apatite was formed during this hydrothermal stage, with apatite crystals appearing in close association with the Cu-polymetallic mineralization. The best evidence for interpreting these apatite crystals as formed with the mineralization is their presence in carbonaceous slates where they can be recognized as small crystals in the parallel to foliation veins that display typical mineral assemblages of the Cu – polymetallic hydrothermal stage.

All of the three mineralization styles defined are associated with strong potassic alteration with formation of K-feldspar. This potassic alteration is common in the Cloncurry District where localized potassic alteration overprints the more widespread regional Na-(Ca)

alteration and hosts many of the IOCG deposits in the district (De Jong and Williams, 1995; Oliver et al., 2004; Mark et al., 2006b; Marshall and Oliver, 2008).

The copper mineralization is locally in contact with the Mo-Re mineralization. A number of features including Mo-Re minerals cross-cutting Cu mineralization, molybdenite precipitation around chalcopyrite and pyrite crystals, and also overprinting of the Cu-polymetallic hydrothermal alteration by the Mo-Re hydrothermal alteration (Fig. 3:10 f) make it clear that the copper mineralization is older relative to the Mo-Re.

The third hydrothermal alteration stage defined, which is responsible for the Mo-Re mineralization, has a relatively less complex mineral assemblage (Fig. 3:14 and 3:15). This mineralized system consists of high grade Mo-Re hosted in matrix supported breccias located in the contact zone between the carbonaceous slates and calc-silicates, and also localized in zones at the contact between phyllites and carbonaceous slates (Fig. 3:15 A 4). These high grade breccia zones are associated with intense potassic alteration with formation of K-feldspar. The system gradually changes around those breccias, more extensively at depth in the calc-silicates, into Mo-Re bearing veins, commonly stylolitic, and disseminations. The potassic alteration also gradually becomes less intense and chlorite vein infill and alteration becomes dominant with distance from the high grade breccias. Therefore, the amount and pervasiveness of the K-feldspar alteration is related to the amount of brecciation/fracturing, which also appears to relate to the amount of mineralizing fluid that percolated the host rocks. The mineralized veins, in particular the stylolitic ones, display chlorite infill and alteration that is also associated with relatively abundant rutile and apatite crystals (Fig. 3:13). Three mechanisms can be put forward on the basis of the vein textures, host rock and amount of rutile present in those Mo-Re mineralized veins. 1. There is the possibility of concentration of rutile in the stylolitic veins due to pressure dissolution. Although this is put forward as a mechanism that can account for part of the rutile abundance in those structures, it cannot justify all of the rutile present, taking into account the weak mobility of titanium and the trace to minor amounts of rutile in the host rocks. 2. Scavenging of titanium from the titanite in the calc-silicate host rock and re-precipitation in the mineralized veins is another possible contributing factor and it might account for the amounts of rutile found associated with the Mo-Re mineralization. 3. The third possible mechanism consists of hydrothermal formation of rutile directly from the mineralizing fluid. The same three mechanisms of formation that were put forward for the formation of the rutile can also account for the apatite formation, although scavenging of apatite from the host rocks is more feasible, due to its abundance in the previous hydrothermal alteration stages.

The mineral assemblage of the Na-(Ca) hydrothermal alteration stage is indicative of temperatures between 450-580°C (e.g. Rubenach et al., 2008). Also, Ti/Zr thermometry conducted in rutile grains associated with the Mo-Re mineralization has yielded temperatures of ~500°C (Kirkby, 2009).

The hydrothermal alteration system in Merlin is very complex with three main hydrothermal alteration stages defined which are controlled by tectonic deformation structures and host rock nature. These hydrothermal stages overlap with each other in many parts of the system adding to the complexity of their understanding (Fig. 3:15). Even though this deposit is unique, (the high grade Mo-Re mineralization being the utmost expression of that) the pre-mineralization Na-(Ca) alteration followed by local overprinting by potassic alteration that is associated to the mineralization stages is a common feature of the IOCG deposits in the region, and in many worldwide IOCG (e.g. Hitzman et al., 1992; Oliver et al., 2004; Mark et al., 2006a; Oliver et al., 2008; Rubenach et al., 2008), although with notable exceptions (e.g. Sillitoe, 2003). These hydrothermal alteration similarities with IOCG systems are important to consider but should not be interpreted as saying that the Mount Dore and Merlin deposit should be classified as an IOCG deposit (*sensu strictu* – see Chapters 2 and 8 for details). The only area of the deposit that could be classified as an IOCG (*sensu strictu*) is the bottom part of the calc-silicate unit where magnetite and/or hematite appears associated with apatite, and chalcopyrite and pyrite is commonly present, although in unimportant economic amounts.

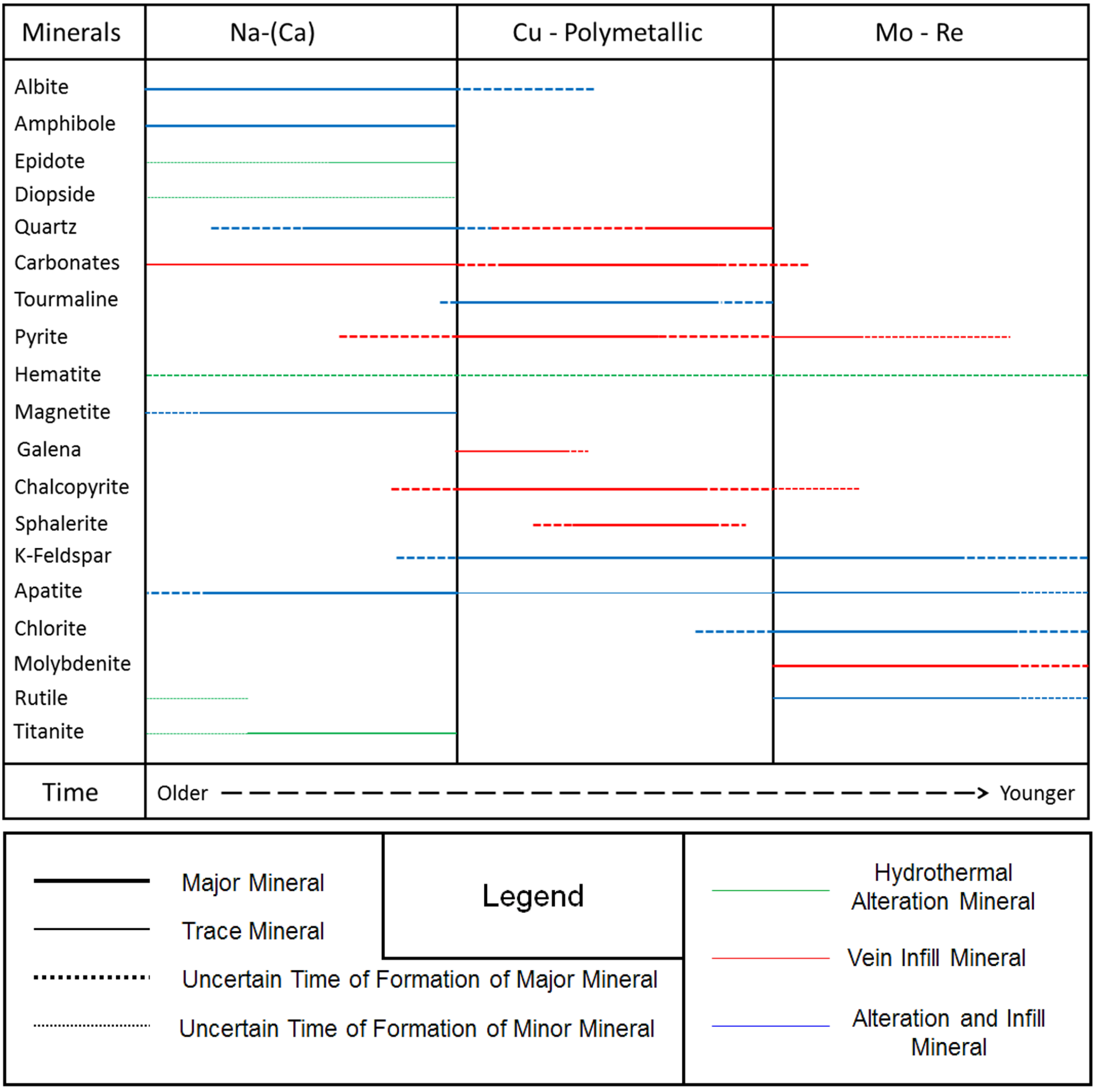

Figure 3:14 – Hydrothermal alteration mineral assemblages of the Merlin deposit. Variation in thickness of lines represents relative abundances.

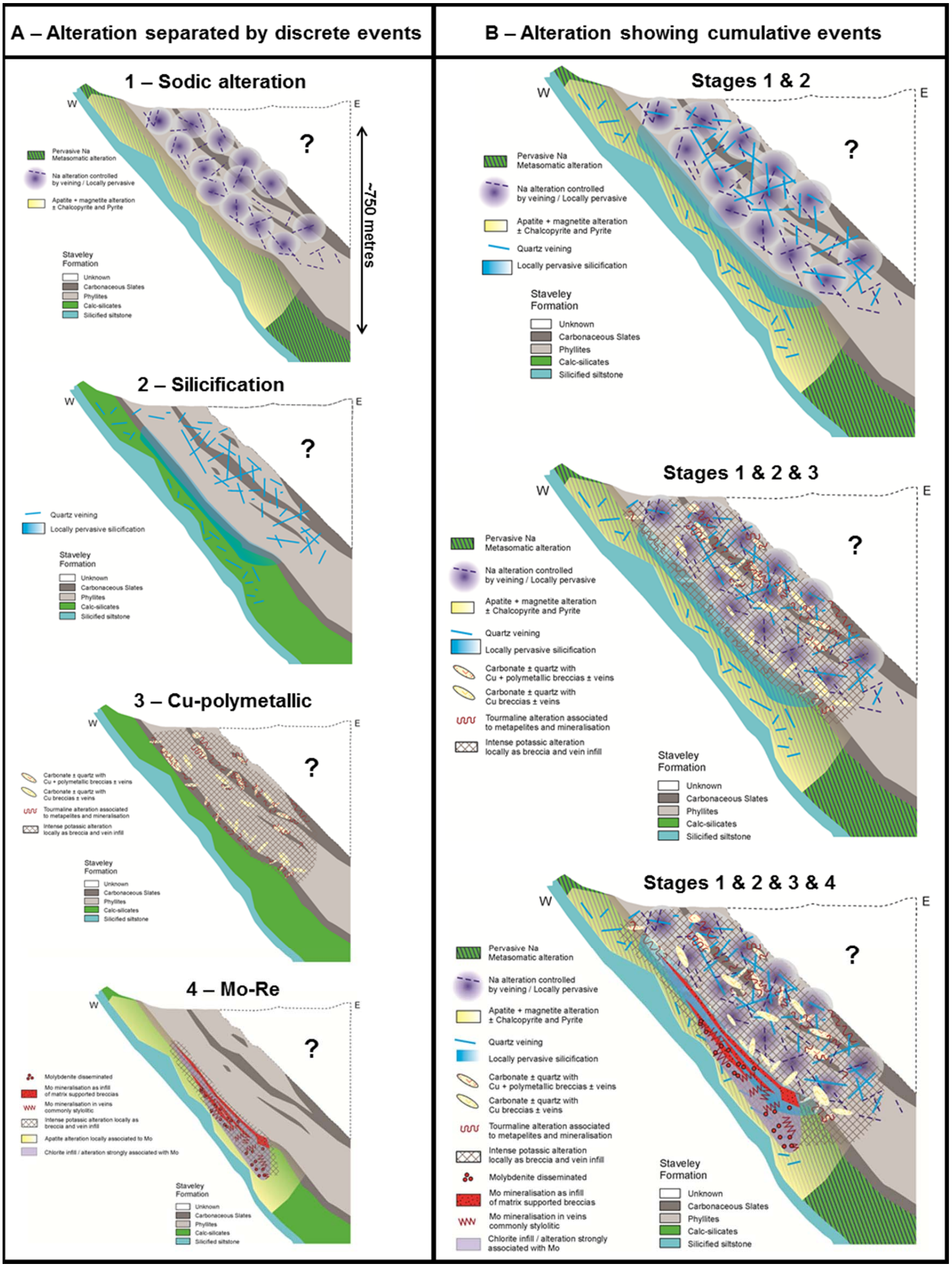

Figure 3:15 – Mount Dore and Merlin deposit hydrothermal alteration on idealized cross-section. Sodic alteration and silicification are interpreted as concomitant but separated here for better understanding and visualization: 1 – Sodic alteration; 2 – Silicification; 3 – Cu-polymetallic mineralization; 4 – Mo-Re mineralization. Red arrows show the four stages separated. Blue arrows show the cumulative effect over time of the four stages. The Mount Dore granite was thrust above the metasedimentary package after the hydrothermal alteration stages. The unit/s that was above the metasediments at the time of the hydrothermal alteration is unknown and therefore represented by the question mark. *Scale in the first cross-section.*

4. Chapter 4: Geology and petrography of the Lanham's and Barnes Shafts prospects

4.1. Introduction

The Lanham's Shaft and Barnes Shaft prospects are located approximately 55km southwest of Cloncurry, in the Eastern fold belt (Carter et al., 1961), and approximately 50km NNE of the Mount Dore and Merlin deposit (Fig. 3:1). They are hosted by the Doherty Formation (1725 ± 3 and 1743 ± 11 Ma; Southgate et al., 2013), which is part of the Cover Sequence 2 (Blake et al., 1983). The Lanham's Shaft prospect consists of molybdenum ± copper ± uranium mineralization, and the Barnes Shaft prospect (1km to the south of Lanham's Shaft) of copper ± cobalt. The importance of these prospects lies with the comparison potential with the Mount Dore and Merlin deposit due to the similar mineralization present in the Lanham's Shaft and the absence of molybdenum mineralization in Barnes Shaft prospect, even though it shares many similarities to the nearby Lanham's Shaft. The Lanham's Shaft prospect was the focus of study of an honours project by this same author (Babo, 2009). The Barnes Shaft prospect was discovered in 2010 by Ivanhoe Australia. For the work presented here, three more drillholes from Lanham's Shaft were logged and sampled, and geological mapping was extended to the south to include the Barnes Shaft prospect (Appendix 1). Drillcore from 5 holes of the Barnes Shaft prospect were also logged and sampled. In this chapter a short description of the local geology, mineralization and hydrothermal alteration is provided, essentially reviewing the work of Babo (2009) and adding the new Barnes Shaft and detailed Lanham's shaft work, as a means to compare and contrast these prospects with the Merlin deposit.

4.2. Local geology of Lanham's Shaft and Barnes Shaft

The Doherty Formation is mostly comprised of thinly-bedded calc-silicate rocks and breccias, but also contains marble, schists, metamorphosed black shales, feldspathic calcareous meta-psammite and banded quartzites (Blake, 1987). It has endured strong deformation and hydrothermal alteration, creating a highly variable unit that differs laterally and vertically (e.g. Austin and Blenkinsop, 2009). This formation has been interpreted by Foster and Austin (2008) as a lateral facies equivalent to the Corella Formation although geochronological data

put the Doherty Formation as 20 Ma younger than the Corella Formation (Carter et al., 1961; Blake, 1987; Blake and Stewart, 1992).

In the mapping area the main rock units are: Calc-silicate rocks, carbonaceous slates, and mafic and felsic intrusions. Four deformational stages were defined in the area and tentatively correlated with regional deformational events (Table 4:1).

Table 4:1 – General description and correlation of deformation events, defined in the Lanham's and Barnes Shafts prospects area and the regional deformation events (see Chapter 2 for details).

Local deformation events	Regional deformation events	General description of events in mapping area.
D_1	D_1	Foliation parallel to bedding
D_2	D_2	Regional open folds
D_3	D_2 - D_3	Dip-slip NW-SE trending faults followed by strike-slip SW-NE trending faults.
D_4	D_4	Mafic and Felsic intrusive bodies Minor NW-SE and NE-SW trending faults Discordant calc-silicate breccias

The timing of the deformation stages is put forward based on ductile and brittle cutting relationships, although a detailed structural study was beyond the scope of this analysis and therefore such timing considerations are only tentative:

- D_1 in the area produced the bedding-parallel foliation that is observable in the calc-silicate and carbonaceous slate rocks.
- D_2 was inferred from ductile folding that produced the NW-SE flexures best observed in the general trend of the carbonaceous slate units (Fig. 4:2). Lanham's Shaft and Barnes Shaft prospects are hosted in calc-silicate rocks proximal to the carbonaceous slate unit (Fig. 4:2), and appear to be spatially associated with open fold flexures (Appendix 1). Small copper occurrences have also been recognized in the calc-silicate rocks to the north and south along strike of the carbonaceous slates. The metamorphic peak is interpreted to have occurred during the D_2 event.
- D_3 is characterised by the formation of NE striking steep dip-slip faults, and steep NW-SE trending and later sinistral SW-NE trending faults, which display apparent Riedel shear relationships to the shallow dip-slip faults (Tchalenko and Ambraseys, 1970; Babo, 2009). This deformation event is interpreted as resulting from a SSW-NNE compressional regime that is most apparent along rheological

contacts, especially the dip-slip faults. This event has been noted as an important structural control in most of the ore deposits in the region (e.g. Adshead-Bell, 1998; Mark et al., 2000).

- D_4 consisted in the formation of NW-SE and NE-SW trending faults, possibly during E-W shortening. This deformation stage my also be responsible for the formation of the upright, N-S trending, isoclinal folds, that plunge steeply N and occur to the NE of Barnes Shaft prospect (Appendix 1). During this deformation stage there was the emplacement of the felsic and mafic intrusives in the area, which are considered as part of the Williams Batholith (e.g. Jacob, 2009). Concomitant with the formation of the intrusives was the formation of matrix-supported breccias with rounded clasts that are discordant relative to the metasedimentary package. These breccias are widespread and mappable as an independent unit (Appendix 1) and locally display clasts of carbonaceous slates and, when in close proximity to the mafic bodies, dolerite clasts. The forceful formation of these breccias is interpreted to be due to mixing and mingling of the felsic and mafic melts, rapid volatile release and development of very high fluid pressures in the contact aureole, leading to dramatic release of the contained volatiles, forming the discordant breccias (Oliver et al., 2006; Jacob, 2009; Bertelli and Baker, 2010). These breccias locally overprinted previously formed faults (Appendix 1).

The field relationships of the calc-silicate rocks are complex, with three different sub-types defined in the mapping area according to their level of brecciation:

- Banded calc-silicate rocks that consist of thinly, well-bedded rocks. Small discontinuous layers of marbles are commonly present (Fig. 4:2 a).
- Clast-supported crackled breccias (Fig. 4:2 c).
- Matrix-supported breccias (Fig. 4:2 b) where contacts with the other calc-silicate rocks and the carbonaceous slates are sharp. These breccias have more abundant clasts of the unit they are cutting and are clearly latter - and discordant to - other metamorphic sedimentary units and crackle breccias.

The banded calc-silicate rocks are arranged in thin bands that are either; 1. scapolite dominated; 2. scapolite + hornblende + clinopyroxene; 3. K-feldspar + hornblende + biotite, or; 4. calcite + K-feldspar + quartz. The foliation parallel to banding is readily seen in the K-feldspar dominated bands that typically have small, elongated grains of biotite with preferred orientation. There are also small amounts of magnetite + apatite + titanite. These banded

calc-silicate rocks display the metamorphic assemblage that is consistent with rock buffered alteration conditions (i.e. without significant infiltration by externally derived fluids) (Oliver et al., 1992).

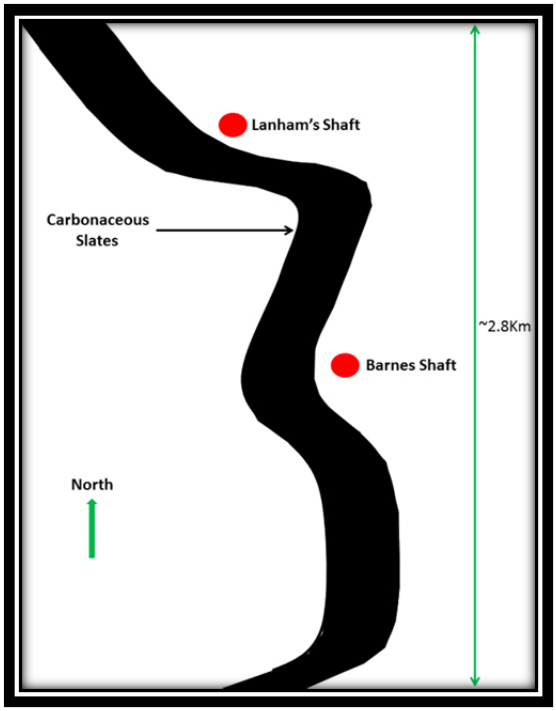

Figure 4:1 – Schematic drawing of the general trend of the carbonaceous slates unit 1 in the mapped area (Appendix 1).

The clast-supported crackle breccias are the main host of the Lanham's and Barnes Shafts mineralization. These breccias resulted from poly-stage deformation and hydrothermal alteration of the banded calc-silicate rocks.

The matrix-supported breccias only contain U mineralization and locally cut the Lanham's Shaft Cu and Mo mineralization. There is also textural evidence that the rounded nature of the clasts is at least partly due to chemical dissolution. These observations indicate that these breccias are post Cu and Mo mineralization at Lanham's Shaft. The matrix of these breccias is composed of coarser grains compared to the minerals that comprise the clasts, and also have more abundant pyrite and fine grained hematite ("dust") than the clasts. Besides these differences, the mineralogy of the matrix and the clasts are both composed of hematite stained albite + zoned tremolite/actinolite ± titanite ± apatite ± pyrite ± epidote. The matrix-supported breccias at Barnes Shaft are similar to those of Lanham's Shaft, although the Barnes Shaft breccias contain a relatively high proportion of polymictic clasts of carbonaceous slates and dolerite (Fig. 4:2 d and 4:3 b).

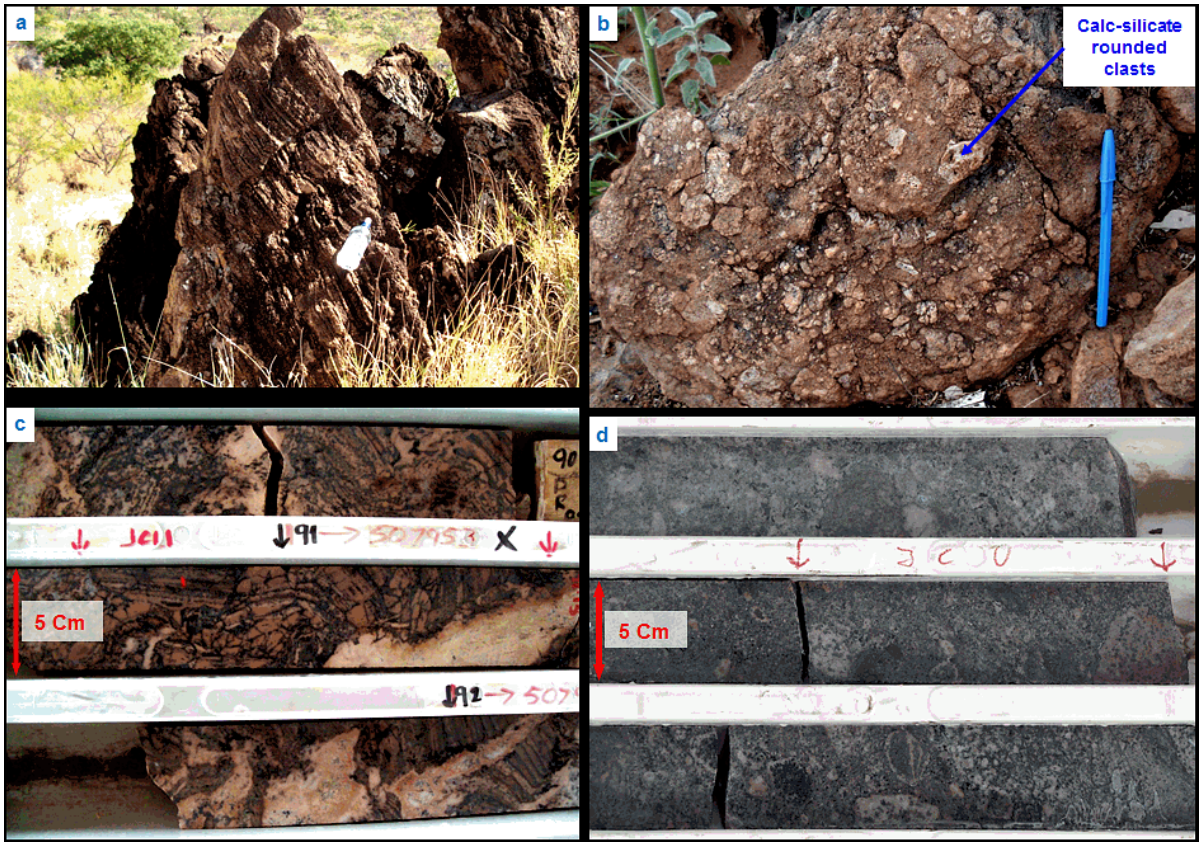

Figure 4:2 – **a)** Representative outcrop of banded calc-silicate rocks. **b)** Representative outcrop of matrix-supported with rounded clasts discordant breccia. **c)** Drill core LAD0002 at ~91 meters depth showing calc-silicate dominant, clast-supported, crackle breccia. **d)** Drill core BAD0001 at 246.50 meters depth showing matrix-supported with rounded clasts discordant breccia in calc-silicate rocks.

The carbonaceous slate units are characterized by thin bedded layers with pervasive bedding-parallel foliation. These units are interlayered within the calc-silicate rocks with conformable contacts, with the exception of the contacts with the discordant breccias and igneous intrusives (Fig. 4:3 b). These units can be divided into unaltered carbonaceous slates and intensely altered bleached slates (Fig. 4:3 a). The carbonaceous slates are composed of very fine grained graphite + plagioclase + quartz ± biotite ± apatite ± calcite ± epidote with ellipsoid pods of medium sized (1-3 mm) plagioclase grains. These pods are possibly replacements of scapolite by plagioclase since they display pseudomorphic textures and displacement of graphite towards the edges of the plagioclase grains. In the Lanham's Shaft prospect there is locally abundant albite or K-feldspar, and/or quartz veining with minor calcite (mm to dm width). There are also minor disseminations and smaller veins of pyrite and very rare chalcopyrite. The carbonaceous slates in the vicinity of Barnes Shaft are more commonly brecciated and fractured.

The intense bleaching of the carbonaceous slates is connected to the hydrothermal mineralizing system and will be discussed further below.

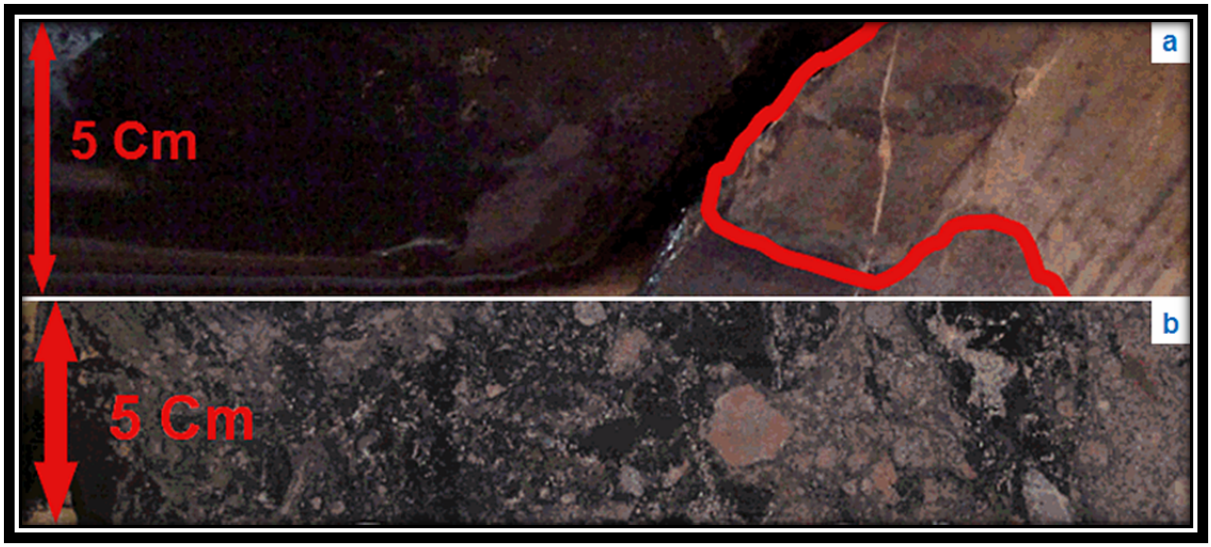

Figure 4:3 – **a)** Drillhole LAD0001 at ~217 metres depth showing core sample with the contact between the carbonaceous slates and the leached carbonaceous slates. **b)** Drillhole BAD0006 at ~292.95 metres depth showing core sample of matrix-supported with rounded clasts discordant breccia. The clasts are composed of carbonaceous slates and calc-silicate rock.

Gabbros and dolerites crop out in the area as semi-rounded bodies. The outcrop size varies from a few metres to ~500 m in diameter. The smaller bodies may be surrounded by matrix-supported discordant calc-silicate breccias locally with clasts of the mafic intrusives (common at Barnes Shaft), indicating that the formation of the breccias was syn- to post-emplacement of the intrusive rocks. The grain size varies from 1 to 4 mm within individual bodies, making the distinction between gabbro and dolerite designations difficult. The main mineralogy of these intrusive bodies consists of subophitic grains of plagioclase, clinopyroxene and amphibole with lesser amounts of magnetite, ilmenite, titanite, pyrite and chalcopyrite, and trace amounts of quartz and biotite. The amphiboles and clinopyroxenes display chlorite alteration, and magnetite is locally exsolved into ilmenite. The pyrite and chalcopyrite are commonly associated with, or included in, large magnetite grains.

In the area of Lanham's and Barnes Shafts, the mafic intrusives are more abundant than the felsic intrusives and significant dolerite with Py + Cpy mineralization in breccias, veins, patches and more weakly in disseminations was intersected in the Barnes Shaft drill core.

The felsic intrusions are phaneritic micro-granite to granite that mainly consist of medium grained quartz and moderately hematite-stained K-feldspar, with trace amounts of epidote with possibly some allanite replacement, and trace amounts of titanite. These intrusions are less abundant than the mafic intrusions in the area and the contacts between the felsic and mafic intrusions are not always clear, although there is field evidence to support mixing and mingling of both rock types (Jacob, 2009; this study; Appendix 1).

Within the mapping area there are a few small surface occurrences of malachite and azurite, and there are several gossanous ironstones of several metres in outcrop dimension. The ironstones appear to be replacing calc-silicate rocks and/or marbles. These ironstone bodies are associated with fault zones, and are interpreted to be post metamorphic peak and hydrothermally derived (e.g. Mark et al., 2006a).

4.3. Lanham's Shaft and Barnes Shafts mineralization

The main mineralization of the Lanham's Shaft prospect consists of molybdenum, copper-gold, and uranium. The highest grades of Mo mineralization at Lanham's Shaft are around 0.5 to 3 % in 1 metre sample assays, rarely going up to 8-9 %. The high grade intercepts are normally around 5 to 10 metres thick. There are also high grade copper intercepts of around 5 to 10 metres thick with the grades commonly between 1 to 3 % in 1 metre sample assays, rarely going up to 8 %. Gold is associated with the copper, with the high grade 1 metre intercepts containing 1 to 2 g/t, rarely going up to 5 g/t. The uranium mineralization, 1 metre, high grade intercepts are around 500 to 750 ppm, rarely going up to 0.2 %. The uranium mineralization shows less consistency with high grade intercepts of variable thicknesses from 3 metres up to 10 metres.

Copper and molybdenite mineralization occurs in the clast-supported breccias adjacent to the carbonaceous slates and in lesser amounts in leached slates, while the U mineralization also occurs in matrix-supported breccias. The mineralization was formed in three different events (Babo, 2009, this study) that were defined on textural evidence for relative timing and ore body geometry.

The first mineralizing event produced the Cu-Au mineralization that occurs in fractured and clast-supported breccias in calc-silicates as both disseminations and vein infill. When it occurs as vein infill it is accompanied by quartz (Fig. 4:4 b). Textural evidence places the Mo mineralizing event as forming after the Cu-Au, although both mineralization styles occur locally in the same vein system and are hosted by clast-supported, calc-silicate crackle breccias (Fig. 4:4 a).

The Mo mineralization occurs as vein infill and as rare disseminations. The mineralized veins are commonly composed of calcite with lesser amounts of amphibole and rare clinopyroxene. Intense phlogopite alteration appears along the borders of the mineralized veins. The carbonates display textural evidence of multiple fracturing, or progressive opening of fractures, or dissolution/re-precipitation. This observation coupled with the existence of

stylolite veins (pressure dissolution) composed of calcite with molybdenite in the centre indicate that the Mo mineralization was formed during deformation (Fig. 4:4 c). The molybdenite veins commonly comprise multiple small platy molybdenite grains, which appear as a dark mass in reflected light under a petrographic microscope. Only coarse well-developed bladed or platy grains have a bright metallic grey reflectance. Although uncommon, there are also rare occurrences of molybdenite as rounded patches with elongated grains arranged in radial aggregates.

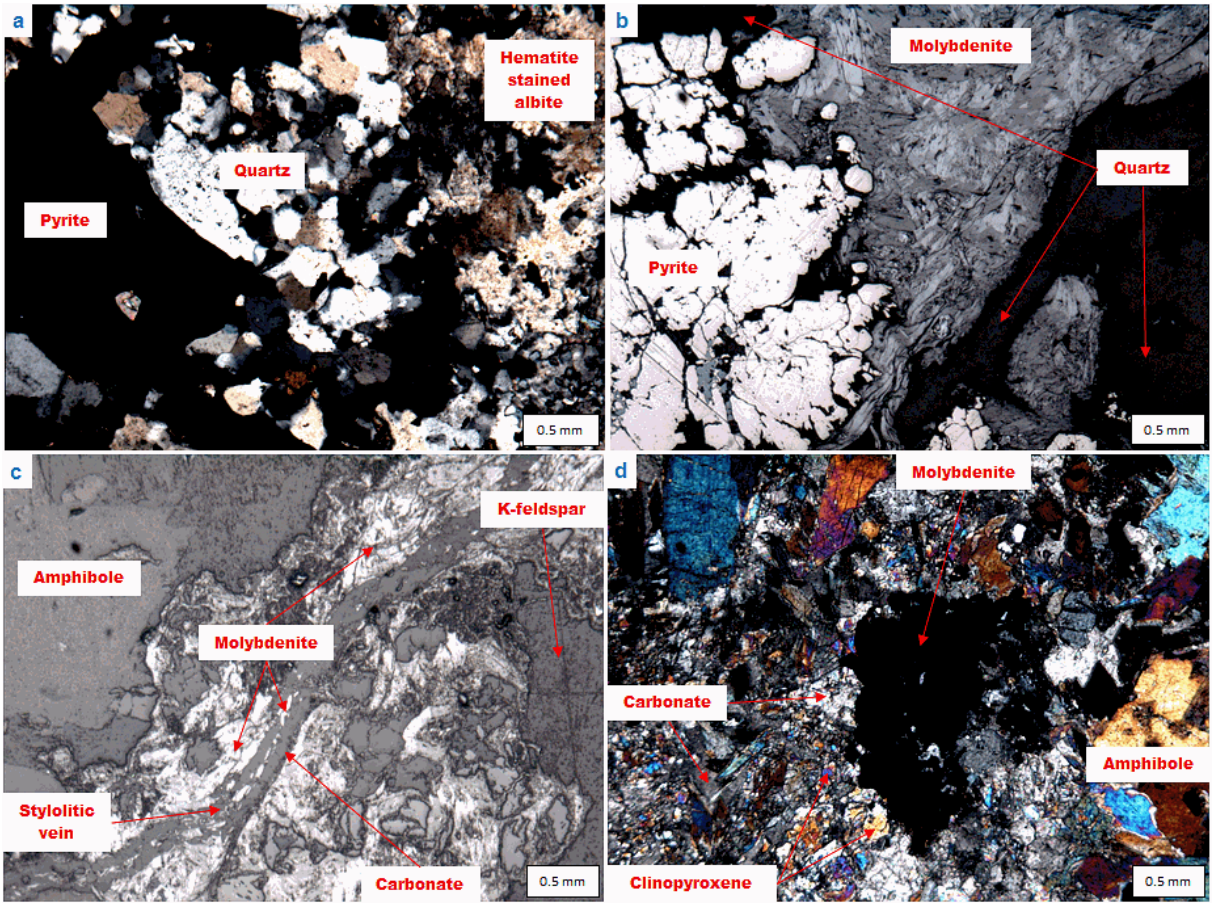

Figure 4:4 –**a)** Cross-polarized light photomicrograph of drillhole LAD0001 at ~164.95 metres depth of hydrothermally-altered calc-silicate with hematite stained albite, quartz and pyrite (alteration Stage 2). **b)** Transmitted-light photomicrograph of drillhole LAD0002 at ~143.75 metres depth of hydrothermally-altered calc-silicate sample with molybdenite, pyrite and quartz. Molybdenite is overlapping pyrite with textures showing the later Mo formation (alteration Stages 2 and 3). Later quartz veins cut the molybdenite vein mineralization (alteration Stage 4). **c)** Transmitted-light Photomicrograph of drillhole LAD0001 at ~81.80 metres depth of hydrothermally-altered calc-silicate with molybdenite, calcite, amphibole and K-feldspar (alteration Stage 3). Also shows calcite + molybdenite stylolitic vein that cuts the thicker molybdenite vein indicating pressure dissolution features. **d)** Cross-polarized light photomicrograph of drillhole LAD0002 at ~122.60 metres depth of a molybdenite patch associated to carbonate, amphibole and clinopyroxene (alteration Stage 3). See below for details on the alteration stages.

The relative timing of the third (uranium rich) mineralizing event is based on the matrix-supported discordant breccias. The logging of Lanham's drillholes coupled with geochemical

assays and in situ scintillometer readings show that these breccias contain uranium mineralization. It is proposed that the formation of these breccias was synchronous with the U-rich mineralization. In all of the drillholes logged these discordant breccias have very minor sulfide disseminations with no molybdenite. In some zones it is even possible to observe Cu and Mo mineralization being cut by these breccias. Therefore, it is reasonable to conclude that the U-rich mineralization stage postdates the Cu and Mo mineralization.

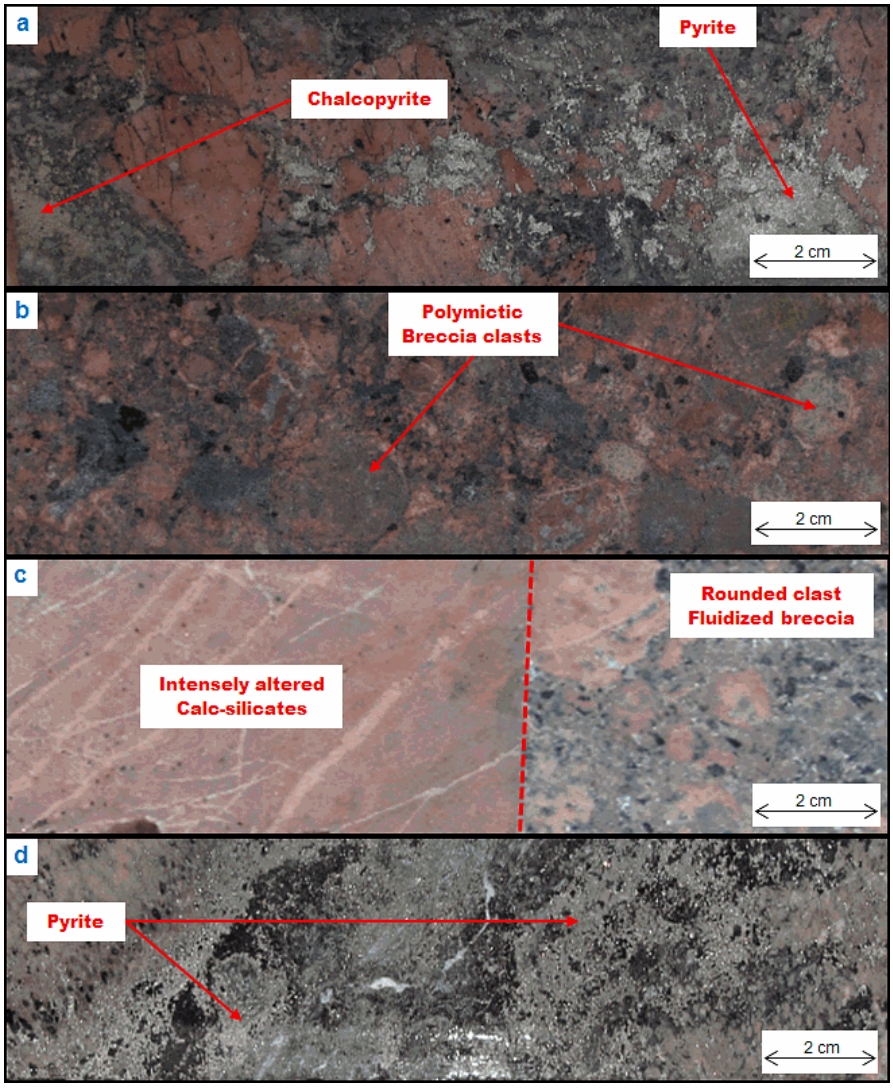

Figure 4:5 – a) Drillhole BAD0006 at ~37.55 metres depth of a core sample showing clast-supported calc-silicate breccia with chalcopyrite and pyrite infill. b) Drillhole BAD0006 at ~16.70 metres depth showing polymictic rounded clast fluidized breccia core sample. c) Drillhole BAD0010 at ~136.75 metres depth of a core sample showing sharp contact between intensely altered calc-silicates and rounded clast, fluidized breccia. d) Drillhole BAD0007 at ~103.75 metres depth of a core sample showing strong pyrite mineralization coincident with high cobalt values in intensely altered calc-silicate rocks.

Another notable difference of the U-rich mineralization is that besides being present in the matrix-supported and clast-supported breccias, it is also present (albeit in lesser amounts) in the leached slates that occur both above and below the unaltered carbonaceous slates.

The description of the Barnes Shaft mineralization is based on core logging only, as no detailed petrographic study was conducted. The main sulfides present are pyrite and chalcopyrite that are mostly associated with intensely hydrothermally-altered calc-silicate rock but also appears locally in the carbonaceous slates (Fig. 4:5 a and d). The mineralization appears as veins and tectonic breccia infill that are commonly more intense in the contact zones between the carbonaceous slates and the calc-silicate rocks, indicating that the fracturing was facilitated by the rheological differences between the rock units. The mineralized breccias and fractures consist mostly of angular clast-supported breccias that are locally cut by the polymictic rounded clast- and matrix-supported breccias that are weakly mineralized with pyrite (Fig. 4:5 b and c). As in the Lanham's Shaft prospect, these fluidized breccias are interpreted as a later event relative to the Cu-Co main mineralization.

Chalcopyrite is commonly associated with the pyrite mineralization, although it is not as extensive as the pyrite. A most striking feature of this prospect is the presence of a several-metre thick dolerite intrusion that is locally mineralized with vein infill and disseminations of mostly pyrite. The connection between the dolerite intrusion and the mineralization is difficult to ascertain without detailed petrographic and geochemical studies, although the fact that it displays mineralization does indicate a potential genetic link between this intrusive and the mineralization.

4.4. Lanham's and Barnes Shafts hydrothermal alteration

By the petrographic observation of rock sections in the Lanham's Shaft prospect it was possible to identify 4 hydrothermal alteration stages. These 4 stages are best observed in the clast-supported calc-silicate breccias and are composed of several major and minor mineral assemblages that can occur as vein infill and/or replacive minerals (Fig. 4:7). The hydrothermal alteration stages can be broadly summarized by:

1. Regional Na-(Ca) hydrothermal alteration;
2. Cu-Au mineralization with early K-Fe hydrothermal alteration;
3. Mo mineralization with potassic hydrothermal alteration;
4. Late-stage, low temperature alteration.

The first metamorphic mineral to be replaced is the hornblende followed by the replacement of the metamorphic clinopyroxene, K-feldspar and scapolite. These minerals are largely

replaced by actinolite and hematite stained albite with lesser amounts of pyrite, apatite, tourmaline, clinozoisite, and clinopyroxene. In the waning stage of this alteration stage there is also formation of hydrothermal scapolite with higher content of sodium and silica (on the side of marialite end member) relative to the metamorphic calcium rich scapolites (on the meionite end member side). Actinolite and hematite stained albite also appear as vein infill during this alteration stage with minor clinopyroxene, biotite and calcite. Titanite is minor but present in important amounts with textural evidence of having been formed during this hydrothermal stage, although some titanite crystals may be inherited from previous hydrothermal or metamorphic stages.

The second alteration stage is characterized by the coeval formation of chalcopyrite and pyrite as vein infill with discontinuous vein border growth of quartz in moderate quantities. There was also formation of minor quantities of magnetite, tourmaline and apatite, which was more important in this stage than the previous. K-feldspar formation is associated with this stage and overprints the regional Na-(Ca) alteration.

The Mo mineralization occurred during the third hydrothermal alteration stage as vein infill, commonly in the borders of calcite veins. The molybdenite can also appear in a network of small veins where calcite is minor or absent. The other mineral that is strongly connected to this mineralization is phlogopite that appears to be replacing other minerals along the borders of the mineralized veins. The mineralization appears in textural equilibrium with actinolite, K-feldspar and rarer clinopyroxenes. There is also formation of minor apatite, tourmaline and rare quartz.

The timing of the uranium mineralization stage occurred between alteration stage 3 and 4 and it is characterized by the formation of epidote with locally allanite substitution.

The fourth and lower temperature alteration stage is sub-divided into three mineral assemblages, and it is of minor importance to the mineralized system. The three assemblages are; (1) quartz + pyrite veins that cross-cut the Mo mineralized veins; (2) chloritic alteration of biotite and actinolite, and lesser sericitization of the biotite and actinolite, and; (3) formation of clay minerals.

The Barnes Shaft prospect displays similar features to the Lanham's Shaft hydrothermal alteration, although hand samples description is very limited when interpreting complex multistage hydrothermal alteration. Nevertheless it is reasonable to state that in general the Barnes Shaft rocks underwent Na-(Ca) hydrothermal alteration that was subsequently locally overprinted by potassic alteration that is likely associated with the

mineralization. Detailed petrographic study of the Barnes Shaft prospect is required to better understand the similarities and differences between the two prospects.

4.5. Discussion

Comparison between the Merlin deposit and the Lanham's and Barnes Shafts prospects is intended to shed light on the regional potential for Mo mineralization. In this section the similarities and differences of the local geology, mineralization styles and hydrothermal alteration will be discussed. Sulfur isotope analyses, Re-Os geochronology and Laser ablation ICP-MS analyses of sulfides from both the Lanham's Shaft prospect and the Merlin deposit are outlined in subsequent chapters (Table 8:1 – Chapter 8).

The Merlin deposit is hosted by the Kuridala formation while the Lanham's and Barnes Shaft are hosted by the Doherty Formation. Even though there is a considerable time difference between their depositions and in styles of hydrothermal alteration, the interpreted protoliths of the calc-silicate rocks and the carbonaceous slates which hosts these three ore mineral occurrences are very similar. The main lithological differences between these mineralization styles are the presence of relatively carbonaceous-poor phyllites at the Merlin deposit and the greater abundance of mafic intrusives in the Lanham's and Barnes Shafts prospects area. The phyllites at Merlin have an important role in the deformation and hydrothermal history, acting as a less permeable unit at the hangingwall of the deposit.

There are several significant differences in the style of the copper mineralization in the three localities studied:

- Copper dominated mineralization in the Mount Dore and Merlin Deposit is hosted mainly in the carbonaceous slates and is accompanied by polymetallic mineralization with important amounts of sphalerite and galena.
- The copper mineralization at Lanham's Shaft is hosted in the calc-silicate rocks with low levels of gold.
- In the Barnes Shaft prospect the copper mineralization is accompanied by pyrite mineralization that is linked to high values of cobalt and is mainly hosted in calc-silicate rocks.

Despite these important differences the copper dominated mineralization in the three localities is hosted in fractures and breccias that are tectonically derived and locally controlled by rheological competence differences of lithology.

The main difference between the Mo-rich mineralization textures at Lanham's Shaft prospect and the Merlin deposit (besides the outstanding high grades) is the molybdenite-dominated matrix supported, rounded clast breccias at Merlin. The molybdenite rich breccias at Merlin display similar textures to the discordant breccias that occur in the area of the Lanham's and Barnes Shaft prospects. However at Mount Dore and Merlin they are not widespread and are mainly restricted to lithological contact areas, and are superimposed on earlier fault breccias. Despite the similarity in breccia style, a genetic or even temporal connection between the Mo-rich breccias at Merlin and the unmineralized discordant breccias at Lanham's and Barnes Shafts cannot be confidently ascertained, as indicated also by the geochronology (Chapter 5).

The Mo-rich mineralization at the Lanham's Shaft prospect is hosted in fractures and crackle breccias. These structures at Lanham's Shaft are also the host of the Cu-rich mineralization that is locally cut by the Mo-rich mineralization, similar to the Mount Dore and Merlin deposit.

The molybdenite veins and disseminations at Merlin and Lanham's Shaft are very similar texturally, including the existence of stylolitic veins in both localities. The stylolitic veins present in both Merlin and Lanham's Shaft, and their distribution relative to other styles of molybdenum mineralization, indicate that veins with molybdenite infill are prone to form pressure dissolution features during subsequent deformation stage/s; these stylolites can be regarded as evidence for remobilization.

Another important difference between this prospect and the Mount Dore and Merlin deposit relative to the Mo veins is the distance of the carbonaceous slates. In the Merlin deposit the bulk of the Mo mineralization is located in the contact zone between the carbonaceous slates and the calc-silicate rocks. By contrast, at Lanham's Shaft the mineralization is in calc-silicate rocks commonly a few metres distant from the carbonaceous slates, which is probably related to the specific structural controls present at the Lanham's Shaft prospect.

To date, no molybdenum rich mineralization has been discovered at Barnes Shaft despite being only 1km southeast of the Lanham's Shaft prospect. This may be due to several factors, such as difference in fluid source, fluid evolution, fluid pathways, and mineralization host lithology, but these aspects can only be further resolved with more detailed petrographic studies.

Based on the detailed petrographic studies at Lanham's Shaft prospect (Babo, 2009, this study), at the Merlin deposit, and the diamond drillhole core logging at Barnes Shaft

prospect, it is apparent that these localities share similarities relative to the hydrothermal alteration in a broad view but have important differences when observed in greater detail. The similarities in broad view are:

1- They have apparently undergone the same regional Na-(Ca) alteration that was formed either by fluids exsolved from the Williams-Naraku Batholiths (e.g. Pollard, 2001) or by earlier basinal hydrothermal systems that are thought of as the mechanism for this alteration at older IOCG systems such as Osborne and parts of Starra (Rubenach et al., 2008; Oliver et al., 2008; Fisher and Kendrick, 2008). Considering that the Na-(Ca) hydrothermal alteration results in the typical loss of iron, potassium, barium and, frequently, copper and carbonate (Oliver et al., 2004; Mark et al., 2006a, Marshall and Oliver, 2006), it is reasonable to argue that the mineralizing fluid/s had these elements available in the subsequent hydrothermal alteration stages.

2- The second hydrothermal alteration stage that is shared by the two prospects and the deposit is the subsequent local potassic alteration overprint of the sodic alteration. The first potassic alteration stage is responsible in all cases for the formation of the copper dominated mineralization with associated K-feldspar formation.

3- At the Mount Dore and Merlin deposit and at Lanham's Shaft prospect the potassic alteration continues, and is an integral part of the Mo-rich mineralization, also with K-feldspar associated.

Although in broad view the hydrothermal alteration is similar, in detail the mineral assemblages display many differences:

- The copper dominated hydrothermal stage in the Mount Dore and Merlin deposit is associated with carbonates with some quartz and tourmaline, besides the K-feldspar.
- At the Lanham's Shaft prospect the copper mineralization is associated with quartz and minor tourmaline, besides the K-feldspar.
- The Mo-rich mineralization at the Lanham's prospect is associated mainly with carbonates, biotite and K-feldspar.
- At the Mount Dore and Merlin deposit the Mo-rich mineralization is associated with K-feldspar and chlorite with minor amounts of apatite and rutile.

The carbonates association with the Cu-rich mineralization at the Mount Dore and Merlin and with the Mo-rich mineralization at the Lanham's Shaft might be due to the relative timing of the sulfide precipitation in the host rock relative to the general hydrothermal sequence (Fig. 4:6).

The association of quartz with the Cu-rich stage in both localities is considered to be connected to the nature of the Cu-rich mineralizing fluids and not to the host rocks or the previous Na-(Ca) alteration (Fig. 4:6).

Lanham's and Barnes Shafts prospects, together with other regional occurrences of Cu-Au mineralization, follow the carbonaceous slates general trend both to the north and to the south (Appendix 1 and Fig. 4:1). The south extension of this trend is in particular highly prospective, as there has been very little previous work in this area. This trend can be considered as a mineralized corridor in the region of interest for economic deposit/s discoveries. Since both Lanham's and Barnes Shafts are part of this corridor, prospectivity can be either or both Cu-dominated and Mo-dominated mineralization.

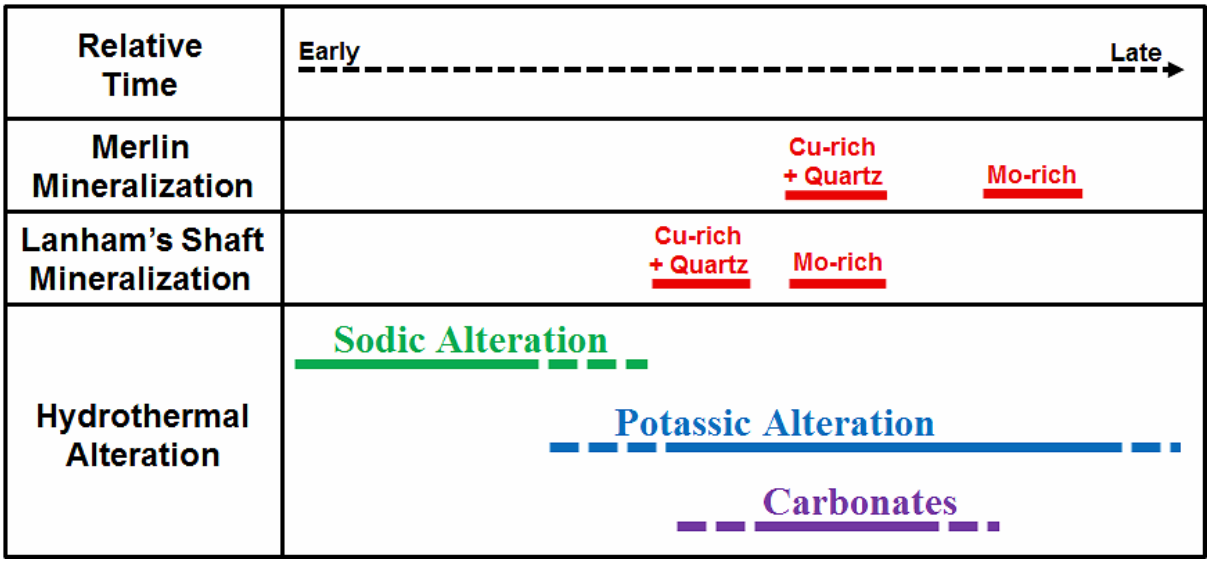

Figure 4:6 – Simplified diagram showing relative timing of host rock controlled hydrothermal alteration stages and mineralization at the Merlin deposit and the Lanham's Shaft prospect. The relative time relates hydrothermal alteration and the mineralization in each deposit, and does not relate the deposits to each other.

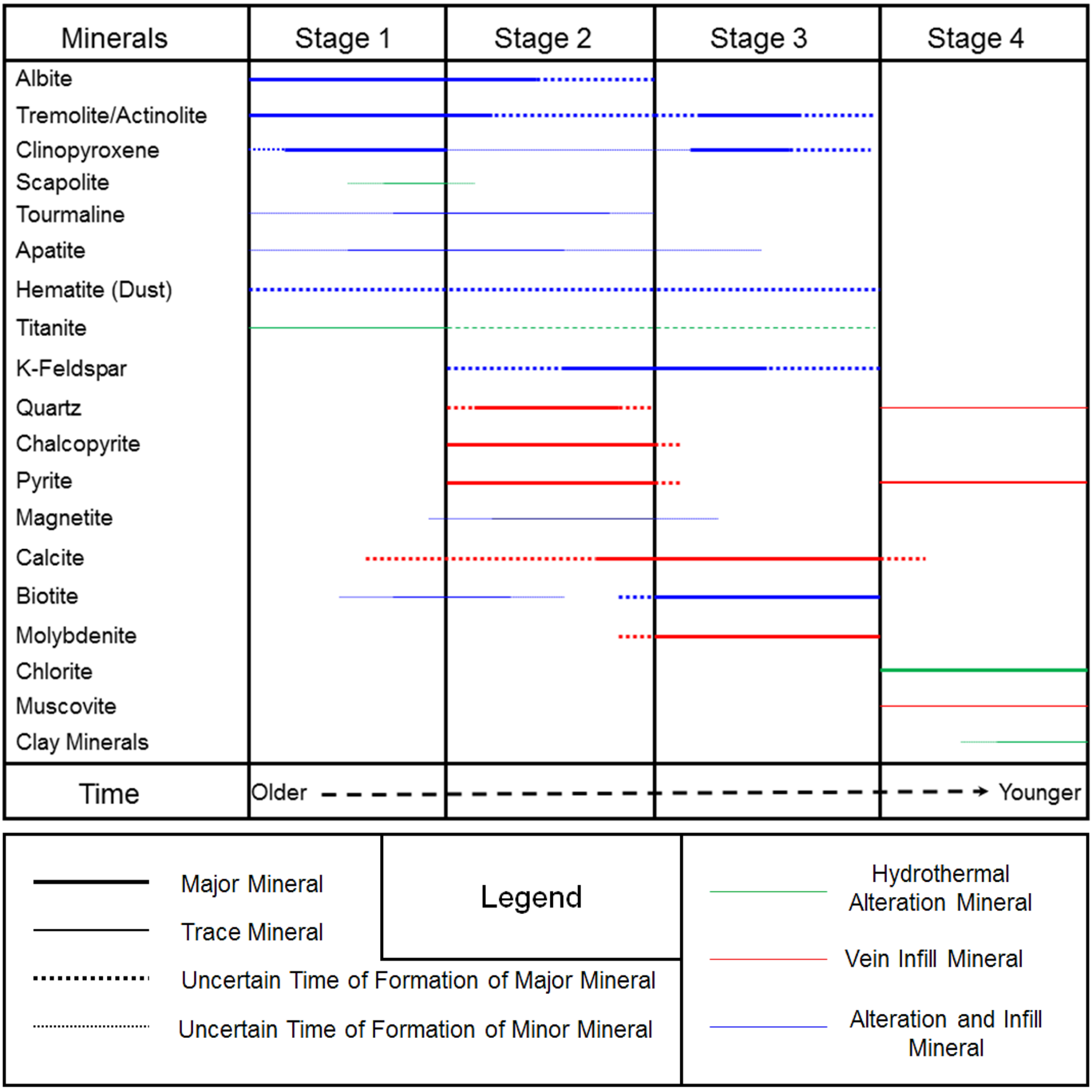

Figure 4:7 – Hydrothermal alteration mineral assemblages of the Lanham's Shaft prospect modified from Babo (2009). Variations in thickness of lines represent relative abundances.

5. Chapter 5: Geochronology

5.1. Introduction

5.1.1. Regional geochronology

Early models for genesis of Cu-Au ore deposits in the Eastern Fold Belt reasoned that the Williams-Naraku batholiths were the most likely source of the metals for IOCG deposits in the region (e.g. Pollard, 2006; Mark et al. 2006a. and references therein), since formation of the majority of the ore deposits were apparently synchronous with emplacement of most of the granitic intrusions (~1540 and 1480 Ma; Fig. 5:13 and 5:14; Wyborn et al., 1988; Perkins and Wyborn, 1998; Mark et al., 2005; Mark et al., 2006a). However, this model does not fit well with the data obtained for the Osborne deposit, which indicate ore formation at between 1595 and 1600 Ma (Gauthier et al., 2001; Rubenach et al., 2001), which lies within the 1600-1580 Ma window for metamorphic peak (Fisher and Kendrick, 2008; Rubenach et al., 2008 – Fig. 5:13 and 5:14). The fact that there is at least one Cu-Au deposit that is not related to the Williams-Naraku Batholiths implies a more complex ore genesis history for this region (Oliver et al., 2008).

There is much debate on the ore forming processes in the region (see Chapter 2 for details). Nevertheless there is consensus on a temporal connection between IOCG ore genesis and igneous events, at least for the younger parts of the thermal history. Another characteristic of the Proterozoic IOCG deposits in the region and worldwide (albeit with notable exceptions; Sillitoe, 2003), is the Na or Na-Ca hydrothermal alteration that precedes the mineralization, and subsequent localized potassic alteration (e.g. Hitzman et al., 1992; Sillitoe, 2003; Oliver et al., 2004; Williams et al., 2005; Mark et al., 2006a; Oliver et al., 2008; Rubenach et al., 2008). Accurate geochronological studies of both igneous intrusive rocks and ore deposits are essential for unravelling the timing and processes responsible for mineralization.

The oldest igneous event in the Eastern Fold Belt is represented by the ~1743 Ma Gin Creek and Levin granites, which respectively lie ~3 km to west, and over 100 km to the north of the Mount Dore and Merlin deposit (Fig. 5:13). These intrusives are temporally equivalent to the Wonga Batholith granites of the Mary Kathleen Fold Belt to the west (Holcombe et al., 1991; Page and Sun, 1998; Davis et al., 2001).

The igneous rocks that were formed between 1690 and 1640 Ma (Fig. 5:14) consists of mafic sills, and trondhjemite and diorite intrusives (Rubenach and Oliver, 2005; Rubenach et al., 2008). The diorites that are found in the Ernest Henry deposit were also formed during this igneous event, with ages that span from 1673 to 1647 Ma (Pollard and McNaughton, 1997). In a sample from the Saxby granite both granite and xenocrysts were dated giving the ages of 1536 ± 20 and 1666 ± 24 Ma respectively (Pollard and McNaughton, 1997). The xenocrysts age probably reflect the depositional ages of the intruded rocks, which are part of the Cover Sequence 3 (Blake, 1987; Blake and Stewart, 1992). The Toole Creek volcanics, 1658 ± 8 Ma, were also formed during this time period (Page and Sun, 1998; Foster and Austin, 2008).

At around 1550 Ma, possibly having started by the end of the metamorphic-peak, there is an igneous event commonly denominated by the Maramungee intrusives (Fig. 5:14). These intrusives have been described as trondhjemitic and display foliation that has been interpreted as D_3 stage (Blake et al., 1983; Williams and Phillips, 1990; Mark, 2001 – Fig. 5:14), and therefore are considered to have been formed late to post metamorphic peak time (Mark, 2001). The timing relation between these intrusives and the remainder of the Williams-Naraku is unclear in relation to a possible time overlap between both igneous events; nevertheless they show clear textural and geochemical differences. In the Eastern Fold Belt the dated intrusives of this igneous event are: the Maramungee Granite (1545 ± 11 Ma), the Boorama Tank Gneiss (1547 ± 5 Ma), and the Mount Angeley Tonalite (1552 ± 42) (Page and Sun, 1998; Pollard and McNaughton, 1997; Mark et al., 2005 – Fig. 5:13 and 5:14). The Maramungee Zn prospect is spatially associated with the Maramungee granite, although there are no geochronology studies conducted in the prospect (Williams and Heinemann, 1993).

The most important igneous event in the Eastern Fold Belt consists of the main Williams-Naraku intrusions that formed approximately from 1540 to 1480 Ma (e.g. Pollard and McNaughton, 1997; Page and Sun, 1998). Mafic intrusives are less voluminous but common during this igneous event (e.g. Jacob, 2009). The Mount Dore and the Mount Angeley granite belong to the Williams-Naraku igneous event, and they are the closest batholiths to the Mount Dore and Merlin deposit and the Lanham's and Barnes Shafts prospects, respectively (Fig. 5:11), although the older 1743 Ma Gin Creek pluton is also close to Mount Dore and Merlin. Further details can be seen in Chapter 2, and Fig. 5:13 and 5:14.

The Mount Dore and Merlin deposit fall within a mineralized corridor that is aligned with the Selwyn High Strain Zone (Beardsmore, 1992; Adshead-Bell, 1998; Laing, 1998). This corridor hosts several IOCG deposits that are proximal to the Mount Dore and Merlin;

the Starra deposit; Lady Ella deposit; Mount Elliot and Swan deposit; and further north the Kuridala deposit (Fig. 5:13 and 5:14).

The closest deposit to Merlin is the Au-Cu Starra deposit that has three dates reported (Perkins and Wyborn, 1998; Duncan et al., 2011 – Fig. 5:13 and 5:14):

1. The oldest age is 1594 ± 8 Ma and was obtained by U-Pb SHRIMP in a titanite (Duncan et al., 2011). Some researchers proposed the mineralization at the Starra deposit as post metamorphic peak, with minor hydrothermal titanite formation during Na-(Ca) alteration (Rotherham, 1997a and b; Rotherham et al., 1998; Williams et al., 2001). Since titanite formation is common during syn-regional metamorphism Na-(Ca) alteration elsewhere in the district it is reasonable to argue that the age of 1594 ± 8 Ma dates the metamorphic-peak (Rubenach et al., 2008). However, other researchers suggest at least some mineralization pre-dates or was synchronous with the regional metamorphism (Davidson and Large, 1989), noting that this titanate age is similar to that found at Osborne (Rubenach et al., 2001; Oliver et al., 2008).

2. The youngest age of 1503 Ma was obtained from $^{40}Ar/^{39}Ar$ hydrothermal biotite (Perkins and Wyborn, 1998). The $^{40}Ar/^{39}Ar$ geochronology technique reflects mineral closure temperatures and therefore its relevance is connected to the specific mineral being analysed, its relationship to the ore assemblage, and the temperature of ore formation (Dodson, 1973; Harrison et al., 1985; Scaillet, 2000; Kelley, 2002; Harrison et al., 2009). Although previous authors consider that the $^{40}Ar/^{39}Ar$ age is reasonable for the Au-Cu mineralization (e.g. Rotherham et al., 1998; Williams et al., 2001) it can be argued that the Starra deposit displays a protracted hydrothermal history and therefore the $^{40}Ar/^{39}Ar$ are reflective of the end of the hydrothermal activity and not necessarily the mineralization formation age (Fig. 5:14).

3. Possibly most robust age is at 1568 ± 7 Ma, obtained with Re-Os geochronology from molybdenite associated with mineralized ironstone (Duncan et al., 2011). This is the oldest post-metamorphic age reported in a deposit in the Cloncurry District (Fig. 5:13 and 5:14).

The Lady Ella deposit was also dated by use of Re-Os geochronology in molybdenite which gave 1487 ± 5 Ma (Duncan et al., 2011 – Fig. 5:14). This Cu-Au deposit is located approximately 10 km north of Merlin proximal to the Mount Dore granite (Fig. 5:14). The molybdenite sample dated was associated with pyrite and chalcopyrite in the supergene alteration zone of the deposit (Duncan et al., 2011), and possibly represents a later alteration/remobilization in the system.

Mount Elliot and Swan is the dated deposit in the corridor that is furthest away from the Mount Dore and Merlin deposit (Fig. 5:13). This deposit consists of two different mineralized zones, the Mount Elliot deposit hosted by the Kuridala formation and the Swan deposit hosted by the Staveley formation (e.g. Brown et al., 2009). The two deposits are now considered as one mineralized system, separated by a steep strike-slip fault, with different mineralization styles due to the different nature of their host rocks (Brown et al., 2009). This deposit has been dated by several geochronology techniques: U-Pb in zircons and titanite, Re-Os in molybdenite, and $^{40}Ar/^{39}Ar$ in biotite and actinolite:

1. The dated zircon was obtained from a dike sample, although it was considered hydrothermal in origin, with an age of 1549 Ma (Duncan et al., 2011).
2. Titanite grains dated are considered to have been formed during Na-(Ca) hydrothermal alteration with an age of 1530 ± 11 Ma (Duncan et al., 2011).
3. Two molybdenite samples dated from Mount Elliot – Swan returned Re-Os ages of 1513 ± 5 Ma and 1515 ± 6 Ma, respectively (Duncan et al., 2011).
4. The youngest dates reported are 1510 ± 3 Ma (actinolite) and 1496 Ma (biotite), by $^{40}Ar/^{39}Ar$ (Perkins and Wyborn, 1998; Wang and Williams, 2001).

In this case it is reasonable to consider the age obtained from the titanite grains is a reflection of a younger Na-(Ca) alteration association, which is close to the zircon age (unfortunately there are no errors reported for the zircon age) (Wang and Williams, 2001; Oliver et al., 2004; Mark et al., 2006a; Oliver et al., 2008; Rubenach et al., 2008; Duncan et al., 2011). The 1510 ± 3 Ma age probably reflects a cooling of the terrane during the waning of the regional hydrothermal activity.

The ages of the Starra, Lady Ella, and Mount Elliot and Swan deposits are similar to other IOCG deposits in the region, most notably to the Ernest Henry and to the Eloise deposits (Twyerould, 1997; Perkins and Wyborn, 1998; Baker et al., 2001; Mark et al., 2004b; Mark et al., 2006b; Duncan et al., 2011 – Fig. 5:13 and 5:14), and are further supported by the dating of the Na-(Ca) hydrothermal alteration in the Ernest Henry deposit which was dated between 1541 and 1519 Ma (Twyerould, 1997; Perkins and Wyborn, 1998; Mark et al., 2006b).

The Eloise deposit was dated by use of $^{40}Ar/^{39}Ar$ on biotite, hornblende and muscovite in different hydrothermal alteration stages defined (Baker et al., 2001). Although there are several limitations with the $^{40}Ar/^{39}Ar$ technique as previously mentioned, the five age clusters obtained by this method could reflect early cooling after syn- to late regional metamorphic Na-(Ca) alteration age (1555 ± 4 Ma), followed by subsequent stages related to

cooling during syn-Williams Batholith Cu-Au mineralization (1533 – 1511 Ma). If this interpretation is correct, then the mineralization at the Eloise deposit would be of similar age to the Mount Elliot and Swan, and the Ernest Henry deposits, as originally interpreted by Baker et al. (2001). There is also the possibility that the Eloise deposit is of similar age to the Osborne deposit, being either metamorphic-peak time or during the ~1650 Ma albitization event (Oliver et al., 2008; Rubenach et al., 2008). The most accepted age for the mineralization of the Ernest Henry deposit is ~1514 Ma, and 1529 ± 11 Ma for the pre-mineralization Na-(Ca) hydrothermal alteration (e.g. Mark et al., 2004b; Mark et al., 2006b). However, Re-Os whole rock geochronology conducted in mineralized samples of the Ernest Henry deposit yielded ages around 1650 Ma (Mark et al., 2004b). These ages were interpreted to be indicative of an early genetic connection between the Ernest Henry diorites and a stage of the mineralization, which in this case would be have been formed in two separate events (Mark et al., 2004b).

5.1.2. Geochronology conducted in this study

The complexity of igneous and hydrothermal events in the area is reflected in the substantial geochronology work conducted in the region (Fig. 5:11 and 5:12). Due to the complexity of hydrothermal events observed at the Mount Dore and Merlin deposit and at the Lanham's Shaft prospect, and the significance and uniqueness of Mo-rich mineralization in the region there is the need for further geochronology studies in these two localities.

The geochronology studies conducted in this study are threefold; U-Pb dating of zircons from the Mount Dore granite, Re-Os dating of molybdenite and U-Pb dating of titanite grains, formed during the Na-(Ca) hydrothermal alteration, from the Merlin deposit and the Lanham's Shaft prospect.

The Mount Dore granite has been previously dated at 1516 ± 10 Ma, by U-Pb in zircons with use of the SHRIMP technique (Pollard and McNaughton, 1997). This granite sample was collected approximately 2 km from the Mount Dore and Merlin deposit. The rationale for further dating of the Mount Dore granite was based on dating granite samples that are located in close proximity to the mineralizing system (Fig. 5:1) and therefore to ascertain if the granite was constructed by multiple intrusive events over an extended time period or formed by one single igneous event. The U-Pb geochronology was done by use of Laser Ablation ICP-MS, and zircon was the mineral chosen because it is the most reliable

mineral in the dating of igneous intrusives, and is not readily affected by alteration (see details on methods in Chapter 1).

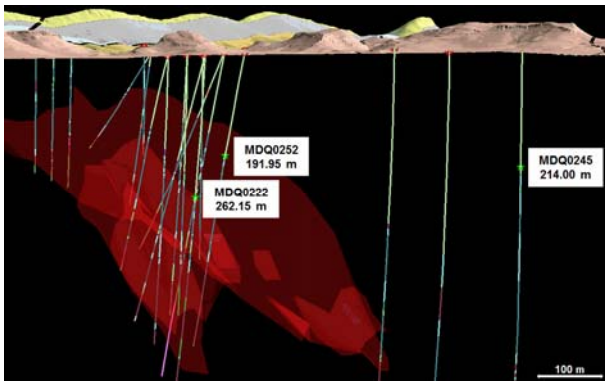

Figure 5:1 – 3D image of MicroMine software program showing a Merlin deposit cross-section oriented SW-NE (looking towards NW). It displays the surface with geologic map, Mo-Re mineralization ore shell, and most of the sampled and re-logged drillholes with location, drillhole name and depth of the Mount Dore granite samples collected for U-Pb zircon geochronology.

Dating of molybdenite from the Mount Dore and Merlin deposit has also been conducted by Duncan et al. (2011) and Duncan et al. (2013). The necessity of further Re-Os dating is due to the detailed petrographic work conducted in this study, which defined four Mo-Re mineralization styles and the characterization of the mineralizing hydrothermal system evolution (see Chapter 3 for details). This work allowed for better sampling collection, based on Mo-Re mineralization styles and sample location relative to the ore body geometry (Fig. 5:2). The robustness of the Re-Os geochronology has been well established as the Re-Os system in molybdenite has a high closure temperature and is resistant to disturbance from events such as high-grade metamorphism and deformation (Foster et al., 1996; Stein et al., 1998; Stein et al., 2001; Bingen and Stein, 2003). Therefore Re-Os dating can provide accurate dating of molybdenite formation provided that the proper care in sampling preparation and analyses is taken (e.g. Markey et al., 1998; Selby and Creaser, 2004; Markey et al., 2007).

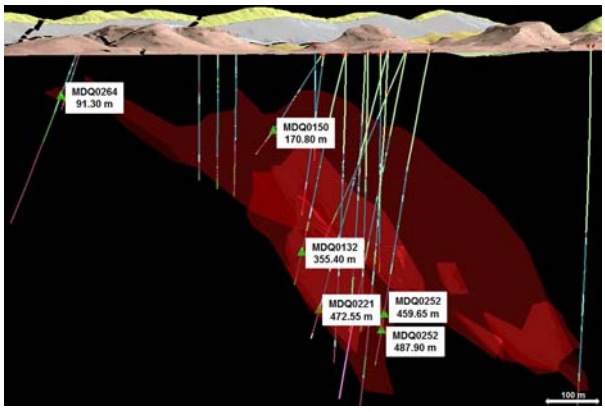

Figure 5:2 – 3D image of MicroMine software program showing a Merlin deposit cross-section oriented SW-NE (looking towards NW). It displays the surface with geologic map, Mo-Re mineralization ore shell, and most of the sampled drillholes with location, drillhole name and depth of the Mo-Re mineralized samples collected for Re-Os geochronology.

Re-Os dating of molybdenite was also done in the Lanham's Shaft prospect, which, in general, has comparable hydrothermal alteration and mineralization histories to the Mount Dore and Merlin deposits (see Chapter 4 for details). The dating of this prospect was intended to ascertain if the molybdenite rich mineralization in the region is constrain to a particular time event or otherwise. The sample collection represents the main molybdenite mineralization styles located in the central part of the mineralized system at Lanham's Shaft.

Titanite U-Pb dating was conducted on one representative sample of Na-(Ca) hydrothermal alteration of the Mount Dore and Merlin deposit, and of the Lanham's Shaft prospect. The titanite grains in each sample were formed during the Na-(Ca) hydrothermal alteration, which was the first characterized alteration stage in both systems. This dating coupled with the molybdenite dating can better define the time span of the hydrothermal activity and bracket the Cu-rich stage.

5.2. Sample Description

5.2.1. Mount Dore granite sample selection

Three core samples of the Mount Dore granite were selected from three drillholes for Laser Ablation ICP-MS zircon U-Pb geochronology (Fig. 5:3). The samples were selected with respect to their proximity to the mineralization, with two samples sourced from two drillholes that intercept the central molybdenite mineralization and a third sample from a relatively distal drillhole that does not intercept significant mineralization (Fig. 5:1). The other criterion used in the sample selection is rock colour that can reflect minor weathering and/or later low temperature hydrothermal alteration. All three samples consist of equigranular K-feldspar + quartz + plagioclase with minor amounts of biotite + titanite ± zircon ± hornblende.

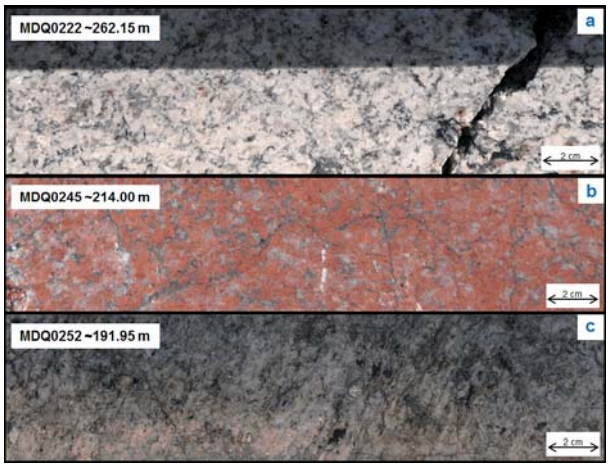

Figure 5:3 – Mount Dore granite samples chosen for U-Pb zircon geochronology. Samples **a)** and **c)** are relatively unaltered and were collected in close proximity to the Mo-Re mineralization central zone, while sample **b)** is most altered and was collected from a relatively distal drillhole to the central mineralization zone.

The sample from drillhole MDQ0222 at ~262.15 metres depth is located in close proximity to the central part of the Mo-Re mineralization and is representative of the least altered granite with light colours and minor chlorite veining. The sample from drillhole MDQ0245 at ~214.00 metres depth is a relatively distal sample to the Mo-Re mineralized zone and shows a red colour alteration with moderate abundance of quartz + chlorite veins. The red colours are possibly due to the sericitization of the feldspars controlled by the proximity to the thrust contact with the black slates below. The sample collected in drillhole MDQ0252 at ~191.95 metres depth is the most altered and is located in close proximity to the central part of the Mo-Re mineralization. The sample is moderately deformed with intense chlorite and sericite veining. The deformation and alteration is controlled by the proximity of the lower thrust contact with the black stales. In all samples the low temperature alteration was formed after the main hydrothermal stages, during the thrusting of the Mount Dore granite, or as an even later weathering effect, or a conjunction of both (see Chapter 3 for details).

The processing of the three granite samples resulted in between 25 to 30 zircon grains per sample. Subsequent SEM catholuminescence revealed abundant oscillatory zoning and hydrothermal textures in some grains rims (Fig. 5:4 a). Twenty Laser Ablation ICP-MS analyses were conducted for each sample, with several grains subject to two analyses spots in order to obtain data for cores and rims where possible (Fig. 5:4 b). Details on the methods used can be seen in Chapter 1.

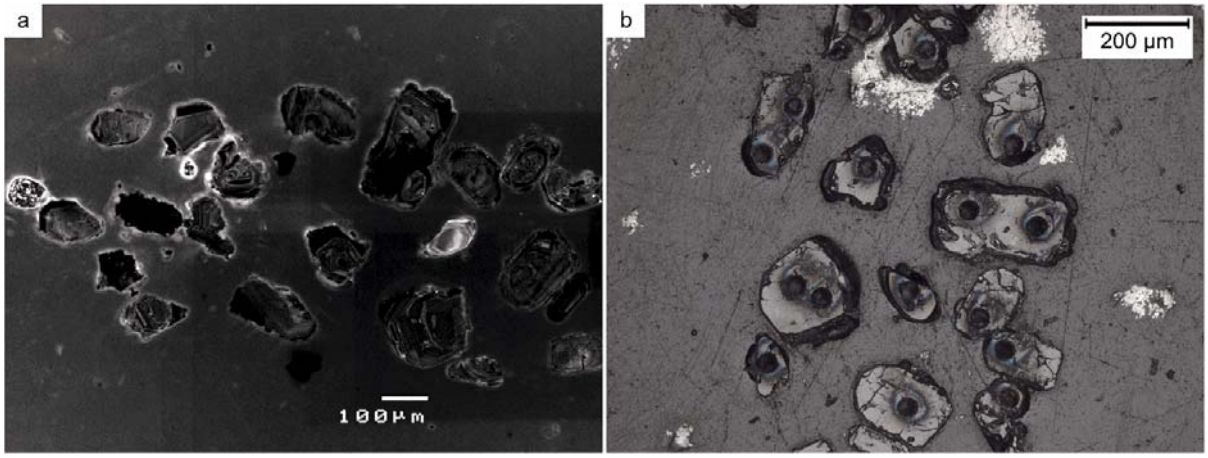

Figure 5:4 – **a)** SEM catholuminescence photo showing example of zircon grains from drillhole MDQ0252 at ~262.15 metres depth. **b)** Microphotograph of previous in transmitted light with detail of LA-ICP-MS spot analyses.

5.2.2. Molybdenite sample selection

In the Merlin deposit six core samples with molybdenite mineralization were selected from 5 drillholes for Re-Os geochronology. The selection of the samples was based on the

mineralization style (Fig. 5:5) and their localization in the deposit (Fig. 5:2). The Merlin deposit samples chosen are:

- The sample from drillhole MDQ0264 at 91.30 metres depth consists of massive molybdenite mineralization of the Little Wizard 'pod'. The mineralization is surrounded by intensely weathered rocks in which the protolith is difficult to ascertain (Fig. 5:5 a).
- The sample from drillhole MDQ0150 at ~170.80 metres depth consists of matrix-supported with rounded clasts breccia, in which the matrix is composed of almost 100% molybdenite (Fig. 5:5 b and 5:12). This style of molybdenite mineralization comprises the bulk of the Mo-Re mineralization and displays the highest grades in the deposit. These mineralized breccias typically occur in the contact zone between the carbonaceous slates and the altered calc-silicate rocks, and less commonly between phyllites and the carbonaceous slates. This sample originates from the carbonaceous slates. There is intense potassic alteration associated with this mineralization style where the rounded clasts consist of K-feldspar with small molybdenite disseminations.
- The sample from drillhole MDQ0132 at ~355.40 metres depth consists of calc-silicate breccia, as above, with intense potassic alteration in the contact zone between the carbonaceous slates and altered calc-silicate rocks (Fig. 5:5 c and 5:12). The sample was collected as a ~5 cm fragment of massive molybdenite (Fig. 5:5 c). These veins and breccias extend for ~15 metres in intensely hydrothermally altered and mineralized calc-silicates becoming gradually less mineralized downwards. Although the mineralized breccia is strongly broken they are not weathered, simply disaggregated by normal drill core handling due to the mechanical weakness of molybdenite.
- The sample from drillhole MDQ0221 at a depth of ~472.55 metres was collected from banded calc-silicate rocks with moderate hydrothermal potassic alteration that is overprinting hydrothermal Na-(Ca) alteration. The molybdenite mineralization appears as disseminations that are controlled by small fractures that are parallel to banding and also cross-cutting the bands (Fig. 5:5 d). This mineralization is located ~7 metres from the contact between the carbonaceous slates and calc-silicate rocks.
- Two samples were collected from drillhole MDQ0252 at ~459.65 and ~487.90 metres. The first sample is representative of the molybdenite veins with incipient

brecciation style (Fig. 5:5 e). This mineralized sample has potassic hydrothermal alteration, which accompanies the molybdenite, and overprints the earlier Na-(Ca) hydrothermal alteration. These mineralized veins also display weak to moderate stylolitic features. The deeper sample obtained in this drillhole are from banded calc-silicate rocks that display less intense potassic and Na-(Ca) hydrothermal alteration, although the Na-(Ca) alteration is still strong. The Mo-Re mineralization is concentrated in stylolitic small veins that mostly follow the banding contacts but can also cut the banding (Fig. 5:5 f). Both samples derive from the calc-silicate unit and are almost 100 metres distance from the upper contact with the carbonaceous slates.

These samples represent the various molybdenite mineralization styles of the Merlin deposit and it covers the vertical and, in part, the east-west lateral extension of the mineralization (Fig. 5:2).

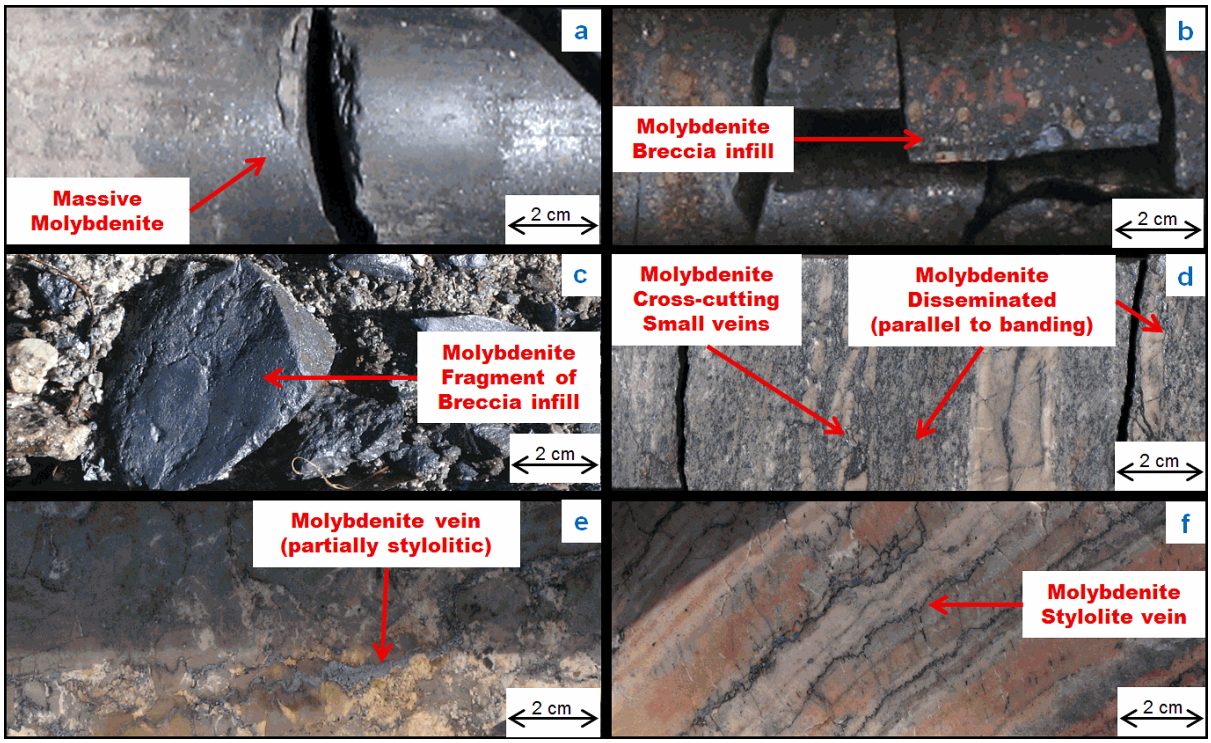

Figure 5:5 – **a)** Drillhole MDQ0264 at ~91.30 metres depth showing core sample of massive molybdenite from the Little Wizard 'pod', which is surrounded by intense weathering. **b)** Drillhole MDQ0150 at ~170.80 metres depth showing core sample of matrix-supported with rounded clasts Mo-Re mineralized breccias. This particular sample was collected from the contact zone between phyllites and carbonaceous slates. **c)** Drillhole MDQ0132 at ~355.40 metres depth showing core sample of similar breccia as previous, although collected from the contact zone between the carbonaceous slates and calc-silicate rocks. These breccias are easily broken-up due to molybdenite weakness; therefore the picture displays fragments of massive molybdenite which was breccia infill. **d)** Drillhole MDQ0221 at ~472.55 metres depth showing core sample of disseminated Mo-Re mineralization that follows the calc-silicate host rock banding with locally cross-cutting mineralized small veins. **e)** Drillhole MDQ0252 at ~459.65 metres depth showing core sample of Mo-Re mineralized veins, locally stylolitic, with incipient brecciation in calc-silicate rocks. **f)** Drillhole MDQ0252 at ~487.90 metres depth showing core sample of Mo-Re mineralized stylolitic veins that follow the calc-silicate host rock banding.

The two core samples from Lanham's Shaft prospect are (Fig. 5:6):

- Sample from drillhole LAD0001 at ~158.50 metres depth consists in a mineralized vein with angular clasts brecciation in calc-silicate rocks (Fig. 5:6 a). The molybdenite mineralization is associated with carbonate and phlogopite infill/alteration, and K-feldspar alteration, which is the typical potassic hydrothermal overprint of the earlier Na-(Ca) hydrothermal alteration at the Lanham's prospect (see Chapter 4 for details).
- The sample collected from drillhole LAD0002 at ~119.30 metres depth displays molybdenite mineralization arranged in small veins, with potassic alteration associated, hosted in calc-silicate rocks (Fig. 5:6 b). These veins are thinner than the previous sample with less carbonate infill and phlogopite infill/alteration.

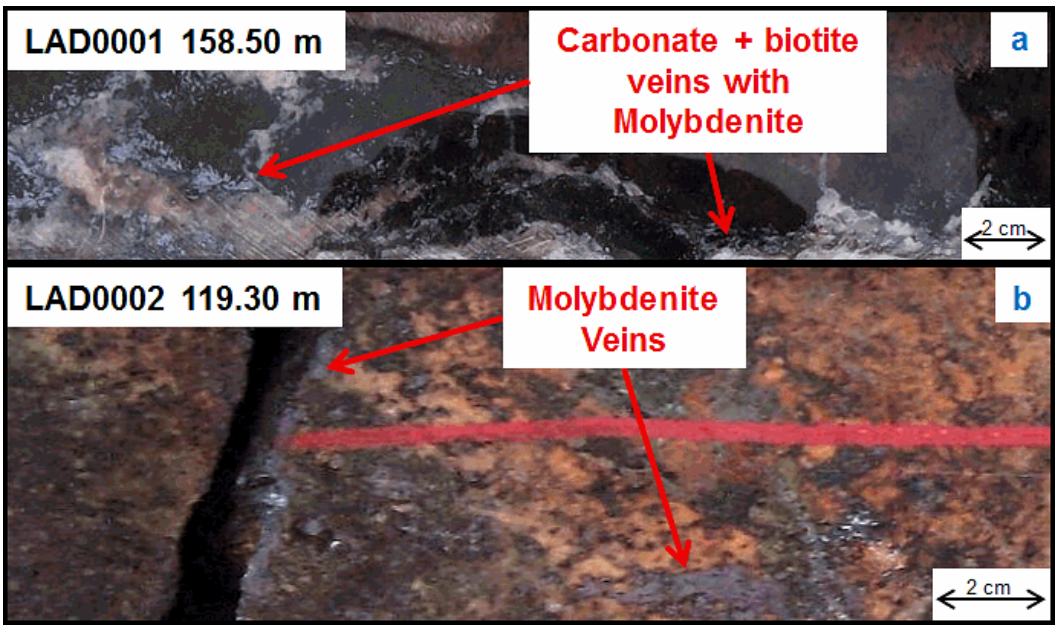

Figure 5:6 - **a)** Drillhole LAD0001 at ~ 158.50 metres showing core sample with carbonate + biotite + molybdenite infill of crackled breccia in potassic altered calc-silicate rocks. **b)** Drillhole LAD0002 at ~ 119.30 metres depth showing core sample with molybdenite veins ± carbonate ± phlogopite in potassic altered calc-silicate rocks.

5.2.3. Titanite sample selection

The Na-(Ca) altered representative sample from the Mount Dore and Merlin deposit and the Lanham Shaft prospect were selected from calc-silicate rocks that display titanite grains with textural evidence of being formed during that hydrothermal stage, with little or no overprinting by the subsequent hydrothermal associations, and unmineralized (Fig. 5:7).

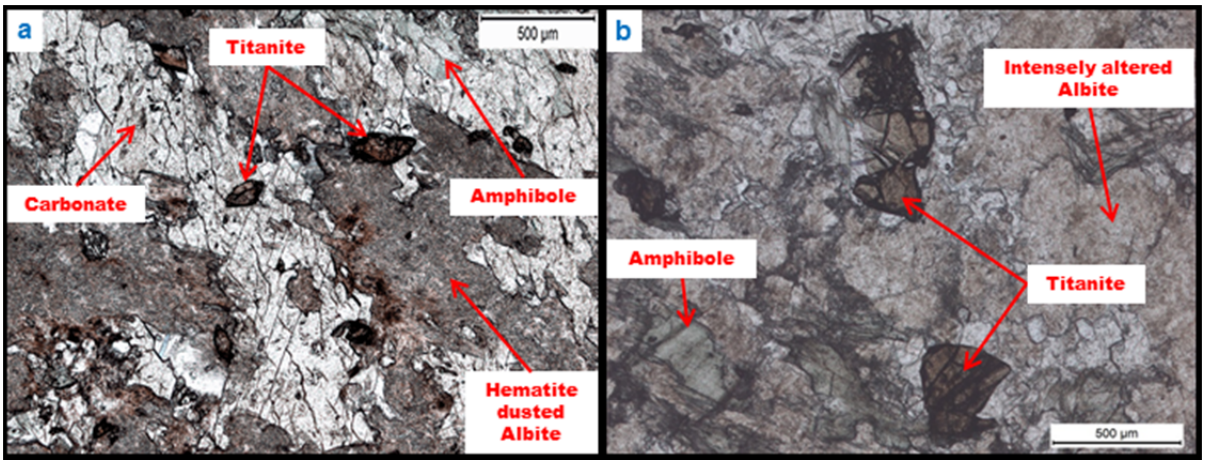

Figure 5:7 – a) Photomicrograph taken in plane-polarized light of drillhole MDQ112 (Mount Dore and Merlin) at ~381.85 metres depth showing textural relation of titanite grains with hematite dusted albite, amphiboles and carbonate in Na-(Ca) hydrothermal alteration mineral assemblage in calc-silicate rocks. **b)** Photomicrograph taken in plane-polarized light of drillhole LAD0001 (Lanham's Shaft) at ~173.30 metres depth showing textural relation of titanite grains with hematite dusted albite and amphiboles in Na-(Ca) hydrothermal alteration mineral assemblage in calc-silicate rocks.

5.3. Results

5.3.1. Mount Dore granite geochronology

The detailed methods used in U-Pb zircon geochronology can be consulted in Chapter 1. The Laser Ablation ICP-MS data was reduced with the Glitter software (Van Achterbergh., 2001) and the time-resolved single isotope signals from the samples and standards were selected taken into account ^{204}Pb signals, discordancy, and micrometric inclusions. The statistical method adopted for data presentation is the Concordia plots (Fig. 5:8). The $^{206}Pb/^{238}U$ ages therefore obtained are: 1516 ± 12 Ma for drillhole MDQ0222 at ~262.15 metres depth; 1513 ± 13 Ma for drillhole MDQ0245 at ~214.00 metres depth; and 1521 ± 10 Ma for drillhole MDQ0252 at ~191.95 metres depth (Table 5:1). The MSWD are between 1.2 and 3.2 and the analyses chosen have <30% discordancy. The three ages obtained are in between 1526 and 1500 Ma, with an average of 1517 Ma, which is similar to the 1516 ± 10 Ma age obtained by Pollard and McNaughton (1997).

Table 5:1 – U-Pb zircon ages for the three Mount Dore granite samples dated.

Drillhole	Depth	Age
MDQ0222	262.15	1516 ± 12
MDQ0252	191.95	1521 ± 10
MDQ0245	214.00	1513 ± 13

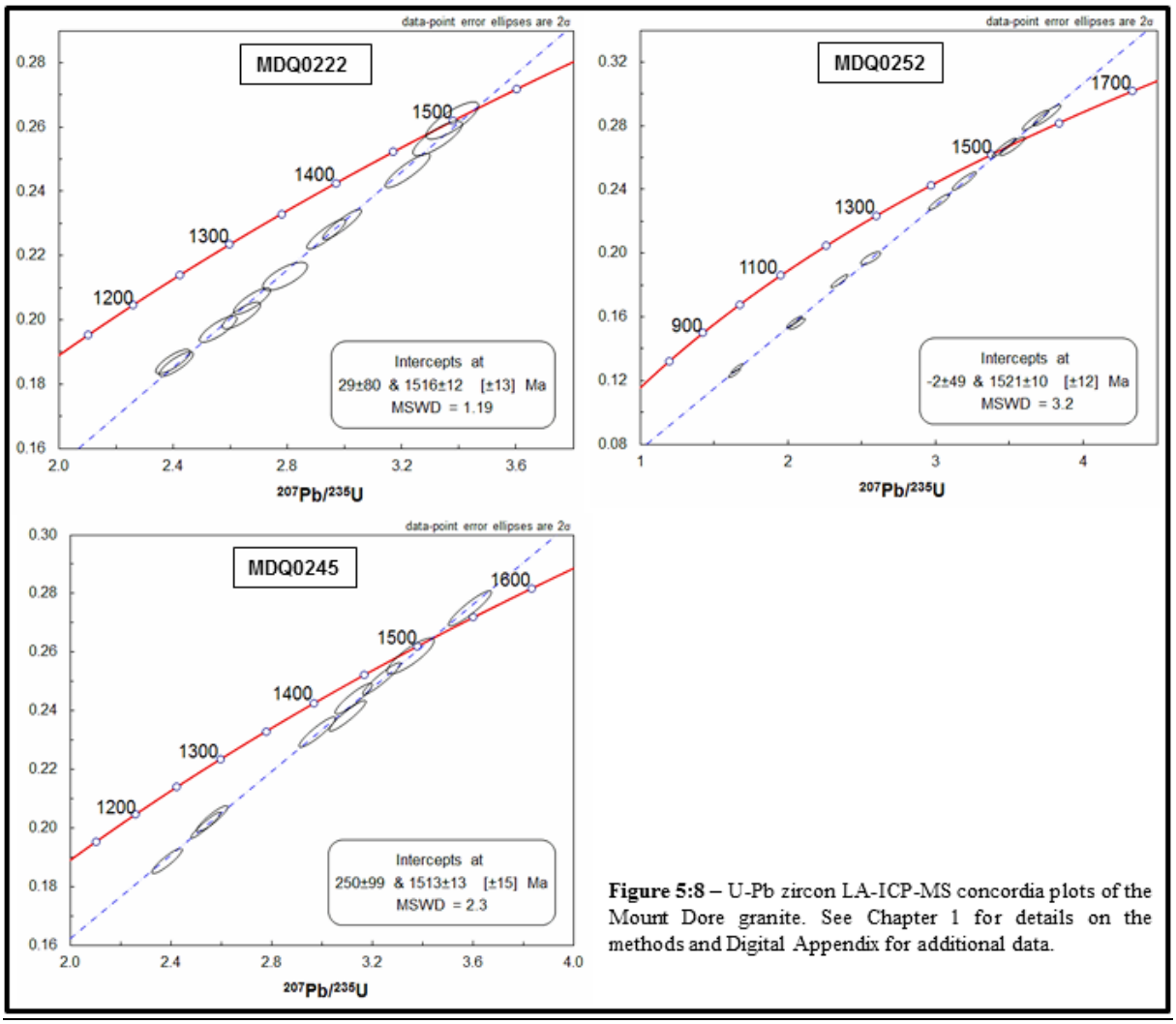

Figure 5:8 – U-Pb zircon LA-ICP-MS concordia plots of the Mount Dore granite. See Chapter 1 for details on the methods and Digital Appendix for additional data.

5.3.2. Molybdenite geochronology

The Re-Os geochronology detailed methods can be seen in Chapter 1. The results of the six molybdenite samples used from the Mount Dore and Merlin deposit and the two sample ages from Lanham's Shaft prospect are presented in Table 5:2.

At the Mount Dore and Merlin deposit three different ages were found:

- The sample from drillhole MDQ0264 at 91.30 metres depth yielded two ages of 1591 and 1802 ± 7 Ma.
- The sample from drillhole MDQ0150 at ~170.80 metres depth was analysed three times resulting in similar ages of 1541, 1539 and 1533 ± 6 Ma. From drillhole MDQ0132 at ~355.40 metres depth the ages 1534 and 1529 ± 6 Ma were obtained. These two samples have an average age of 1535 Ma.
- The sample collected from drillhole MDQ0221 at a depth of ~472.55 gave the age of 1523 ± 6 Ma. Two samples were collected from drillhole MDQ0252 at ~459.65

and ~487.90 metres depths which yielded the ages of 1521 and 1520 ± 6 Ma, respectively. These three samples have an average age of 1521 Ma.

The two molybdenite samples from Lanham's Shaft prospect returned similar ages of 1559 ± 6 Ma and of 1560 ± 7 Ma (Table 5:2).

Table 5:2 – Re-Os geochronology in molybdenite of the Mount Dore and Merlin deposit and the Lanham's Shaft Prospect. Also, Re-Os geochronology in molybdenite of the Mount Dore and Merlin deposit compiled from Duncan et al. (2011) and Duncan et al. (2013).

Location and study	Drillhole	Depth (m)	Age (Ma)	Mineralization style
Mount Dore and Merlin (This study)	MDQ0221	472.55	1523 ± 6	Disseminated and milimetric veins
	MDQ0252	459.65	1521 ± 6	Stylolitic veins
	MDQ0252	487.90	1520 ± 6	Stylolitic veins
	MDQ0150	170.80	1539 ± 6	Breccia infill
	MDQ0150	170.80 Repeat	1541 ± 6	
	MDQ0150	170.80 Repeat	1533 ± 6	
	MDQ0132	355.40	1529 ± 6	Breccia infill
	MDQ0132	355.40 Repeat	1534 ± 6	
	MDQ0264	91.30	1591 ± 7	Massive; Little Wizard 'pod'
	MDQ0264	91.30 Repeat	1802 ± 7	
Lanham's Shaft (This study)	LAD0001	158.50	1559 ± 6	Wide vein
	LAD0002	119.30	1560 ± 7	Thin veins
Mount Dore and Merlin (Duncan et al., 2011, 2013)	MDHQ-07-82	269.07	1497 ± 6	Carbonate veins with milimetric Mo veinlets
	MDHQ-07-82	269.07 Repeat	1501 ± 5	
	MDHQ-07-86	305.05	1508 ± 5	
	MDHQ-07-86	305.05 Repeat	1503 ± 5	
	MDQ0218	440.70	1503 ± 5	
	MDQ0119	413.30	1502 ± 7	Breccia infill (unclear distinction between samples)
	MDQ0119	413.30	1552 ± 6	

5.3.3. Titanite geochronology

The U-Pb titanite dating was processed similarly to the U-Pb zircon data (see above). Three statistical methods plots are presented (Fig. 5:8) and the results can be consulted in Table 5:3.

The weighted average is the method that shows the greater consistency with the lowest MSWD values, highest probability, and smallest errors. The three statistical methods vary in precision but are consistent between themselves with the exception of the Pb/Pb ages of the Lanham's Shaft prospect. The Pb/Pb age at the prospect shows the highest MSWD

value of all plots and very low probability (0.51). The detailed methods can be consulted in Chapter 1.

The Mount Dore and Merlin deposit yielded an age of 1557 ± 18 Ma, and the Lanham's Shaft prospect the age of 1575 ± 24 Ma (weighted averages).

Table 5:3 – U-Pb titanite ages for the Mount Dore and Merlin deposit and Lanham's Shaft prospect samples.

Location	Drillhole	Depth (m)	Age (Ma)	Statistical method
Mount Dore and Merlin	MDQ0112	381.95	1558 ± 60	Concordia
			1557 ± 18	Weighted average
Lanham's Shaft	LAD0001	173.30	1575 ± 71	Concordia
			1575 ± 24	Weighted average

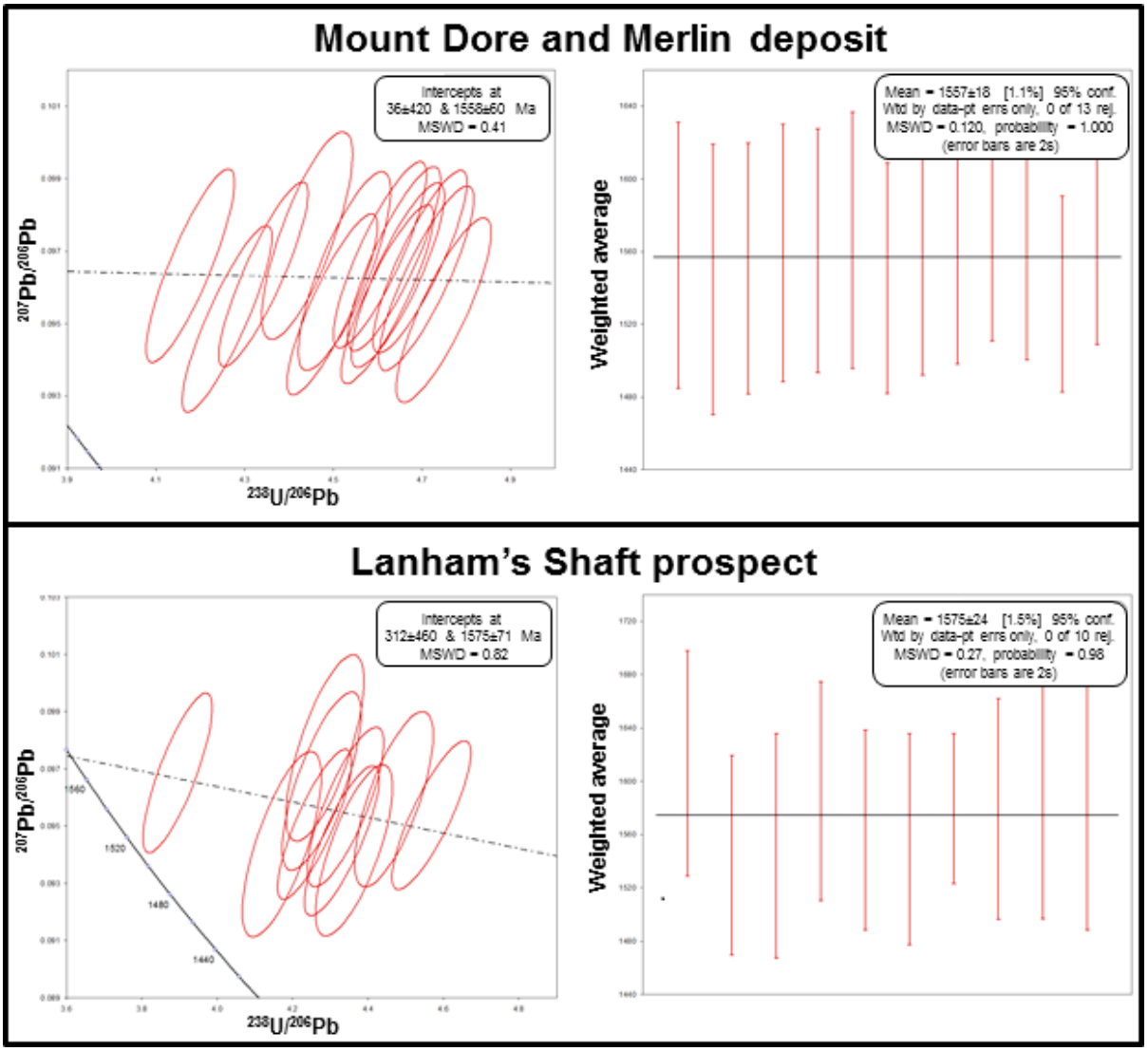

Figure 5:9 – U-Pb titanite LA-ICP-MS Concordia, Pb/Pb ages, and weighted average plots of the Mount Dore and Merlin deposit and the Lanham's Shaft prospect. See Chapter 1 for details on the methods and Digital Appendix for additional data.

5.4. Discussion

5.4.1. Mount Dore and Merlin deposit age dating

The new U-Pb zircon ages of the Mount Dore granite are similar to the previously published zircon age from Pollard and McNaughton (1997). Collectively the data suggest that the whole of the Mount Dore granite formed as a single intrusion between ~1525 to 1510 Ma.

The Na-(Ca) hydrothermal alteration at the Mount Dore and Merlin deposit is dated at 1557 ± 18 Ma by use of U-Pb in titanite grains. This age overlaps with the oldest Mo-Re mineralization ages obtained in this study, and is similar also to the Re-Os age obtained from one sample of mineralized ironstone from Starra (1568 ± 7 Ma – Duncan et al., 2011); and of a zircon from a dike (1549 Ma – Duncan et al., 2001) and Na-(Ca) hydrothermal titanite (1530 ± 11 Ma – Duncan et al., 2011) from the Mount Elliot and Swan deposit.

The Re-Os results for Merlin molybdenite (discounting MDQ0264, as discussed below) indicate an age range for mineralization of between ~1520 and 1535 Ma, with only the youngest samples possibly overlapping in age the emplacement of the Mount Dore granite (~1517 Ma) (Fig. 5:13 and 5:14). This means that a significant portion of the mineralization predates granite emplacement. Therefore, the compressive deformation event responsible for the thrust of the Mount Dore granite over the metasedimentary host rocks (that occurred after cooling of the granite), cannot also be the causative event for the main mineralized structures in the deposit (see Chapter 3 for details).

The two ages from the Little Wizard ‘pod’ (sample MDQ026) are interpreted to be inaccurate because they differ by ~200 Ma (Table 5:2), are older than all the other samples analysed, and the older age is older than the plausible age of the host rocks (See Chapter 2 for details). The reason for the erroneous analytical results is probably connected with the intense weathering present in that location, which is the closest to surface drillhole interval sampled, and previous studies have shown this results in the rapid loss of Re (Fig. 5:2 and 5:5 a - Peucker-Ehrenbrink and Hanningan, 2000; Jaffe et al., 2002; Georgiev et al., 2012). Little Wizard is completely enclosed in intensely weathered rocks.

The oldest ages for mineralization in fresh, unweathered material (MDQ0150, 1539 – 1535 Ma; MDQ0132, 1535 - 1528 Ma) come from the two samples that represent the Mo-Re mineralization in the matrix-supported breccias with rounded clasts that host the bulk of the Mo-Re mineralization at the Mount Dore and Merlin deposit (Fig. 5:5, Table 5:2). The average age of this mineralization style is 1535 Ma.

The other three samples that consist of veins, commonly stylolitic, and disseminations yield usable ages that are significantly younger, with an average of 1521 Ma. The ages of the two molybdenite styles do not overlap within uncertainty, so these mineralization styles are considered to be temporally distinct events. These data indicate that formation and/or remobilization of the Mount Dore and Merlin orebody was protracted.

5.4.2. Comparison with Duncan et al. (2011, 2013)

The samples from drillholes MDHQ-07-82 and MDHQ-07-86 that returned ages of ~1510 - 1495 Ma are approximately 700 metres distance from the other samples studied by Duncan et al. (2013), and from the samples studied here. These two drillholes sampled by Duncan et al. (2011) did not intercept significant molybdenite mineralization; instead they penetrate the outer edge of the shell of the copper-dominated mineralization. The other two samples dated by Duncan et al. (2013) also returned ages around 1500 Ma and do come from within the zone of significant molybdenite mineralization (Fig. 5:10) and are located relatively close to the majority of the older samples that returned older ages as reported above (Table 5:2).

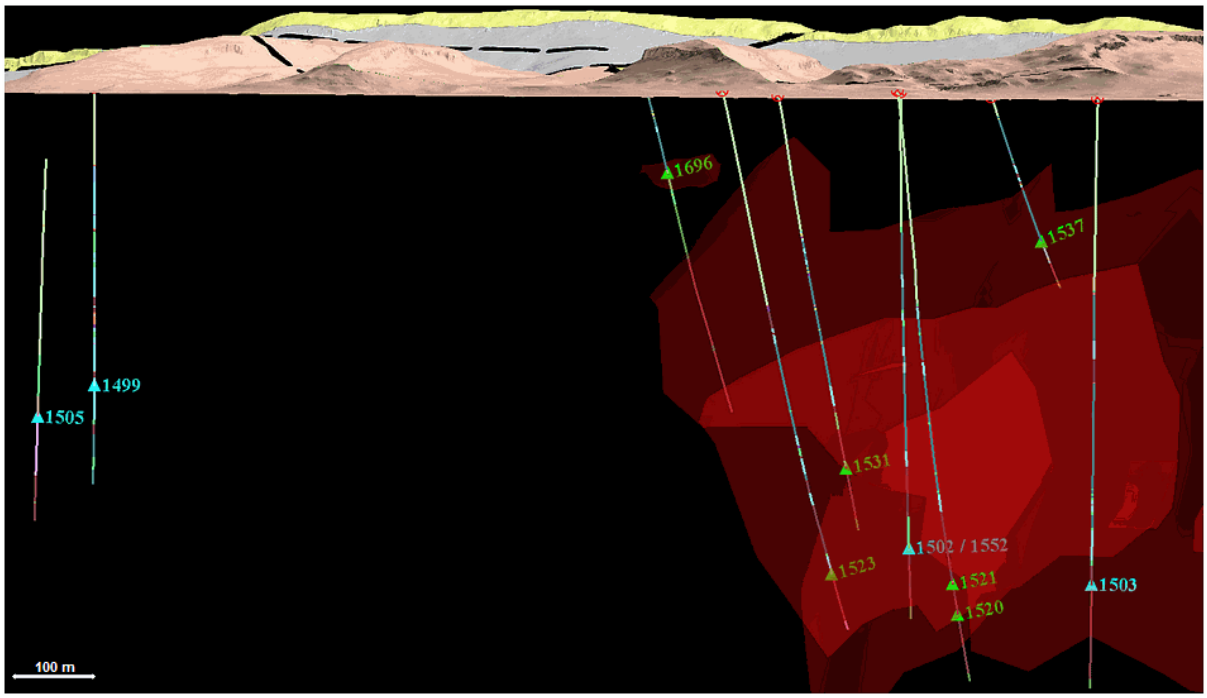

Figure 5:10 – 3D image of MicroMine software program showing a Merlin deposit cross-section oriented NNE-SSW (looking towards WNW). It displays the surface with geologic map, part of the Mo-Re mineralization ore shell, and some of the sampled drillholes with location and ages of the Mo-Re mineralized samples. The green triangles mark the sample location and ages from this study and the blue triangles mark the samples reported in Duncan et al. (2011) and Duncan et al. (2013).

Using the visual and descriptive database of core samples provided by Ivanhoe Australia LTD and the data gathered in this study, it is possible to conclude that the samples reported by Duncan et al. (2011) and Duncan et al. (2013), with the exception of the two samples collected from drillhole MDQ0119, consist of small centrimetric carbonate veins with small millimetric veins of probably chlorite with minor Mo-Re mineralization associated (Fig. 5:11). These veins are hosted in calc-silicate rocks, locally with angular clast brecciation. The mineral paragenesis derived from the hydrothermal mineral assemblages places carbonate formation predominantly with the Cu-polymetallic mineralization, while the Mo-Re mineralization is associated with chlorite (see chapter 3 for details). Therefore it is possible to argue that these centimetric veins of carbonates were formed during the Cu – polymetallic hydrothermal stage. If this is true then the chlorite veinlets that host the Mo-Re mineralization formed later relative to the carbonate veins. Another possibility is that these carbonate veins are in fact concomitant with the Mo-Re mineralization. If this is true they must represent a minor stage that is distal to the main Mo-Re mineralization, in consideration to the hydrothermal mineral assemblages defined in Chapter 3. The third possibility is that these veins represent a later, minor hydrothermal stage that was not detected in the core of the deposit in this study. In either case, these Mo-Re occurrences represent a very minor Mo-Re mineralization style (Fig. 5:11).

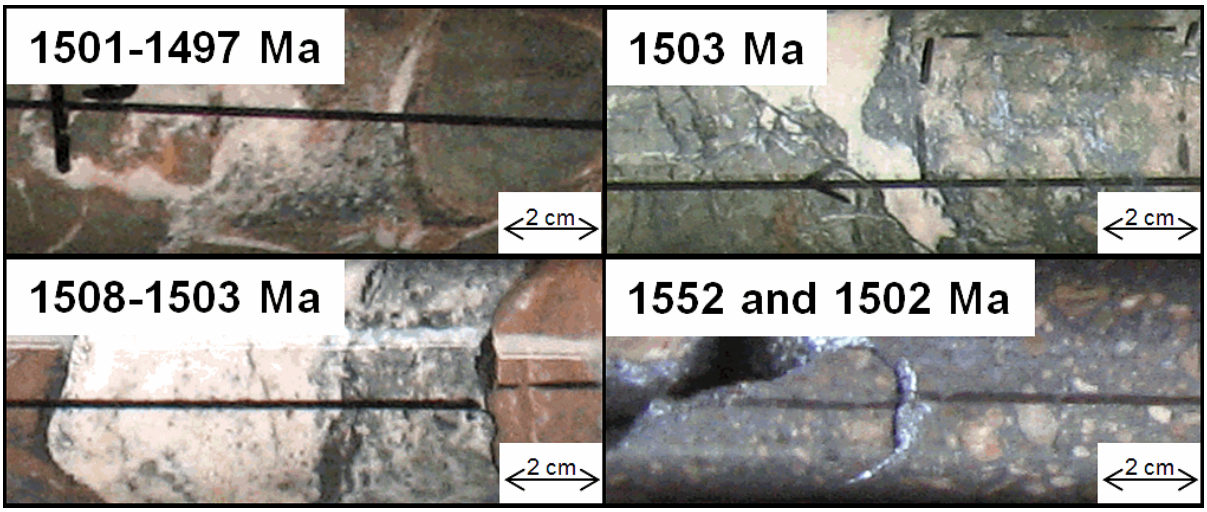

Figure 5:11 – Drillhole core sample pictures from the reported drillholes designations, depths, and ages by Duncan et al. (2011) and Duncan et al. (2013), which compilation can be seen in the table above.

The sample analysed by Duncan et al. (2013) from drillhole MDQ0119 at 413.30 metres depth, which yielded two ages (1502 ± 7; 1552 ± 6 Ma), consists of high grade Mo-Re mineralization in matrix-supported with rounded clasts calc-silicate breccia, which is the mineralization style that hosts the bulk of the Mo-Re mineralization (Fig. 5:11). Duncan et al.

(2013) describes two different Mo-Re mineralization styles in this sample, although the description is difficult to reconcile with the mineralization stages in this study. A sample from the same drillhole at ~411.10 metres depth was collected in this study and a polished button was made with subsequent molybdenite sulfur isotope analyses (Fig. 5:12). Although it is difficult to ascertain the nature of those different molybdenite 'stages' collected by Duncan et al. (2013) it is important to note that at least one of the molybdenite samples that was analysed for a mineralized matrix-supported with rounded clasts calc-silicate breccia yielded an older age of 1552 ± 6 Ma (Table 5:2), which overlaps with the oldest analyses of the Mount Dore and Merlin deposit and with the results obtained for the Lanham's Shaft prospect (Table 5:2 and Fig. 5:14).

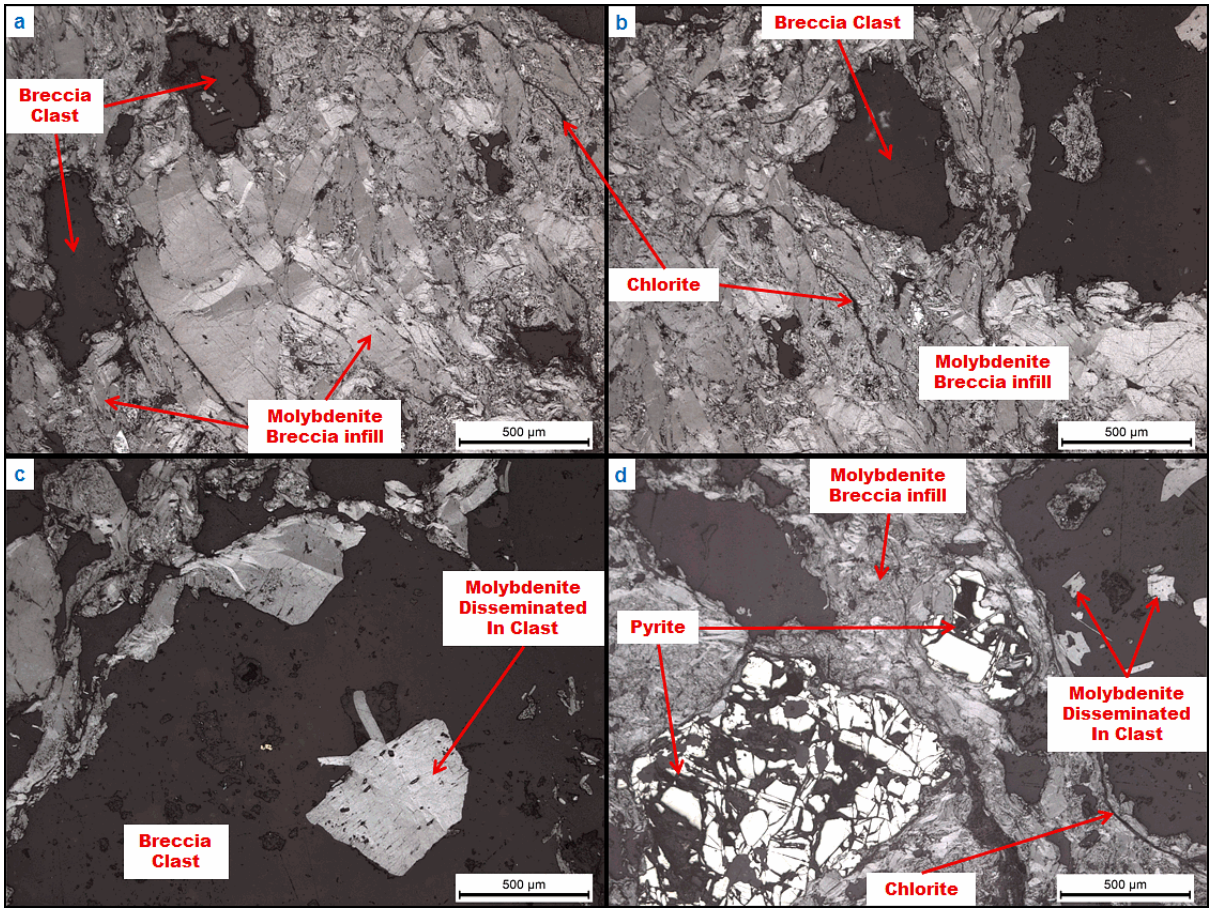

Figure 5:12 – Microphotographs taken in transmitted light of Mo-Re mineralized matrix-supported with rounded clasts calc-silicate breccia from drillhole MDQ0119 at ~411.10 metres depth. Mo-Re mineralization breccia infill textures consist of molybdenite crystals that depending on size and cut effects can be elongated, well-formed grains or smaller grains with indistinct crystal faces. The infill molybdenite is frequently associated to small veins of chlorite **(a, b and c)**. Breccia clast size varies from a few micrometers to 2-5 cm and commonly contains molybdenite disseminations **(c and d)**. Infrequently pyrite crystals can be found in the breccia matrix (possibly as clasts?) showing earlier formation timing relative to the molybdenite and moderate to strong alteration textures **(d)**.

Excluding this older age analysis, Duncan et al. (2011) and Duncan et al. (2013) ages range from 1508 to 1497 ± 5/7 Ma. In consideration of the characterization and interpretation of the geochronology conducted by Duncan et al. (2011) and Duncan et al. (2013), and the sample locations, it is my interpretation that the young ages reported, at around 1502 Ma, consist of minor remobilizations of Mo-Re mineralization, possibly due to thrusting of the Mount Dore granite, and therefore does not reflect the Mo-Re main mineralizing event at the Merlin deposit.

The new Re-Os ages in this study, together with the comparison of the previously reported ages (Duncan et al., 2011; Duncan et al., 2013) require reinterpretation of the formation time of the Mount Dore and Merlin deposit. Considering the younger ages of Duncan et al. (2011) and Duncan et al. (2013), we are left with two possibilities for the main Mo-Re mineralization timing of the Merlin deposit. One possibility consists of two Mo-Re mineralizing stages and the other is a long lived mineralizing system possibly spanning ~15 to 20 Ma. The age averages of the matrix-supported Mo-Re mineralization style and the Mo-Re mineralized (stylolitic) veins are 1539-1528 and 1526-1517 Ma, respectively. The first average age may reflect the first mineralizing stage that formed the high grade matrix-supported breccias with rounded clasts. This mineralizing stage would be responsible for the bulk of the Mo-Re mineralization. The later average age, would then belong to a secondary mineralizing stage that formed the Mo-Re mineralization in the vein system and disseminations. This second stage could be due to remobilization of the previously Mo-Re mineralization, or a secondary, less intense, mineralizing pulse. It is important to note that the intrusion of the Mount Dore granite is approximately of this age (1526 to 1511 Ma), therefore its involvement in in at least part of the Mo-Re mineralizing history cannot be discarded. The other possibility is a continuous mineralizing system evolution with the main portion of the Mo-Re mineralization being formed earlier in the system followed by the Mo-Re vein precipitation that would represent a gradational waning of the mineralizing hydrothermal activity. In both cases the mineralized breccias and veins underwent a later (~1502 Ma) age resetting. This was probably caused by the deformation involved with the thrusting of the Mount Dore granite that created minor molybdenite remobilization or a minor mineralizing fluid pulse, reflected by the younger ages of Duncan et al. (2011) and Duncan et al. (2013). These ages are also consistent with $^{40}Ar/^{39}Ar$ ages of ore deposits in the region (Fig. 5:13) possibly reflecting the waning of hydrothermal activity.

5.4.3. Regional considerations

The Na-(Ca) alteration and Mo-Re mineralization at the Mount Dore and Merlin deposit overlap with the Williams-Naraku batholith formation activity in the region (~1540-1480 Ma). The absence of a specific felsic igneous intrusive of exactly the same timing is the main stage mineralization in the immediate vicinity of Mount Dore and Merlin is not inconsistent with other studies of IOCG deposits, none of which lie immediately adjacent to intrusions of the same age as mineralization (e.g. Mark et al., 2005a; Rubenach et al., 2008). Although the age dating overlaps with the Williams-Naraku batholith the Na-(Ca) alteration and the older Mo-Re ages also overlap with the Maramungee type intrusives ages, and therefore a connection between that earlier igneous event and the mineralization at Mount Dore and Merlin deposit also cannot be excluded (Fig. 5:14). In any case, there is an abundance of regional intrusions emplaced at ~ 1530 Ma (the age of main Mo mineralization).

The Cu-polymetallic mineralization stage was formed after the Na-(Ca) alteration and before the Mo-Re mineralization. Since the age of the Na-(Ca) alteration at the Mount Dore and Merlin (1557 ± 18 Ma) overlaps with the Starra mineralization, that consists of ironstone hosted Au-Cu mineralization, it is possible that the mineralization age of Starra (1568 ± 7 Ma) was formed at the same time as the Cu – polymetallic mineralization at the Mount Dore and Merlin deposit (Fig. 5:14). It is important to note that fluid inclusions studies have argued that the Starra deposit consists of two mineralizing stages with different fluid sources (Williams et al., 2001), Davidson et al. (1989) proposed a syngenetic or pre-metamorphic origin for the ironstones and some sulfides, and Oliver et al. (2008) have also argued a two stage history for Starra, including an earlier stage formed before emplacement of the Williams Batholith. The connection here made between the Mount Dore and Merlin deposit Cu-dominant mineralization and the Starra deposit mineralization is speculative but worth mentioning due to the spatial proximity of the deposits (Fig. 5:13).

5.4.4. Lanham Shaft

The Lanham's Shaft prospect, where the Na-(Ca) alteration association is dated at 1575 ± 24 Ma and the Mo-rich mineralization at 1560 ± 7 Ma, is older than the Williams-Naraku granites, with the ~1525 Ma Mount Angelay granite being the closest (Fig. 5:13). It is also older than the Mount Dore and Merlin deposit ages with exception of the oldest age of Duncan et al. (2013) (Fig. 5:14). The Lanham's Shaft prospect Re-Os ages overlap with the

Maramungee type igneous activity in the region (Page and Sun, 1998; Pollard and McNaughton, 1997; Mark et al., 2005b – Fig. 5:13 and 5:1) and a genetic connection between the Na-(Ca) alteration association and the regional metamorphic peak cannot be discarded. The Mo-rich mineralization on the other hand cannot be connected to the metamorphic peak due to its younger ages. In the prospect area small to medium size igneous bodies are abundant (see Chapter 4 for details). Although, at least some, of these intrusives are concomitant with the Williams-Naraku batholiths (e.g. Jacob, 2009) the lack of age dating does not preclude the existence of some older intrusive/s that could be genetically linked to this older mineral occurrence.

5.5. Conclusions

1 – The Na-(Ca) (1557 ± 18 Ma) and the bulk of the Mo-Re mineralization (1539-1528 Ma) ages overlap with each other. These ages also overlap with both the Maramungee (1545 ± 11 Ma) and Williams-Naraku (1540-1480 Ma) igneous events.

2 – The Mo-Re mineralization in veins, commonly stylolitic, and disseminations ages (1526-1517 Ma) do not overlap with the above ages but are synchronous with the emplacement of the Mount Dore granite (1525 to 1510 Ma) .

3 – The other reported ages for molybdenite mineralization (1508 to 1497 ± 5/7 Ma - Duncan et al., 2011) are the youngest and do not overlap with the previous ages. They display similar ages to $^{40}Ar/^{39}Ar$ dating of other deposits in the region, possibly reflecting the waning of the hydrothermal activity (Fig. 5:13 and 5:14). This mineralization style is very minor and possibly synchronous with the thrusting of the Mount Dore granite above the metasedimentary host rocks.

The Lanham's Shaft prospect Na-(Ca) (1575 ± 24 Ma) and Mo-rich (1560 ± 7 Ma) stages also display age overlap. The two sets of ages do not overlap with the Williams-Naraku igneous event although their age range partly overlaps the Maramungee igneous event. The Na-(Ca) alteration also shows age overlap with the regional metamorphic peak (1600 to 1580 Ma) although the molybdenite mineralization does not. There are several undated small to medium igneous bodies in the prospect area that can be related to the formation of the ore deposit.

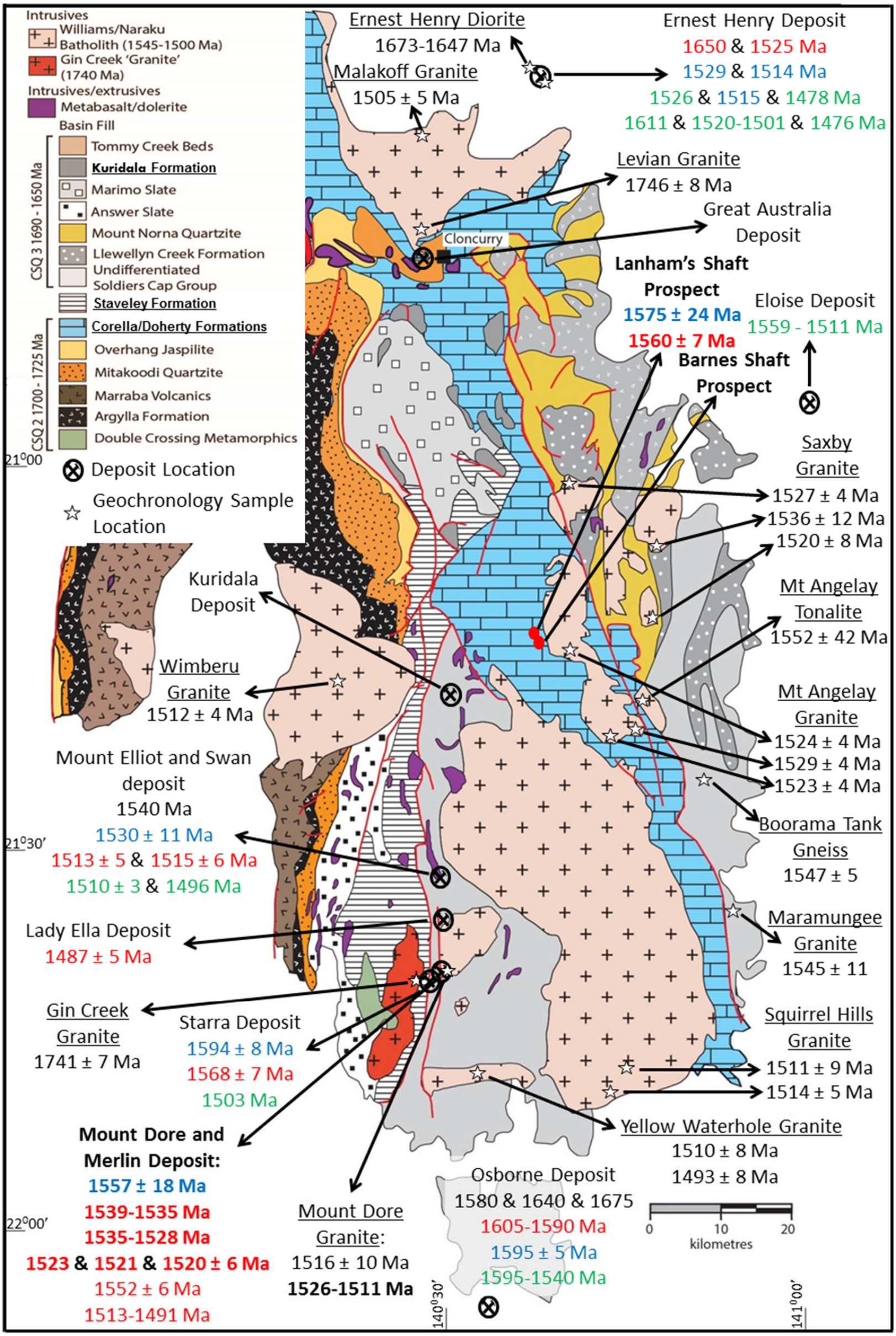

Figure 5:13 – Eastern Fold Belt geologic map, adapted from Duncan et al. (2011), showing location and geochronology of igneous intrusive bodies and the most important ore deposits, including the Mount Dore and Merlin deposit and the Lanham's prospect (this study). The ages are shown with the errors when possible or as an age range in the cases where more than one age data exists. The color coding of the ages represent the different geochronology methods used: Black – U-Pb Zircon; Red – Re-Os molybdenite; Blue – U-Pb Titanite; Green – Ar-Ar or K-Ar in various minerals. These dates and references are provided in Table 1 and 2. Tables with references can be consulted in Appendix 3.

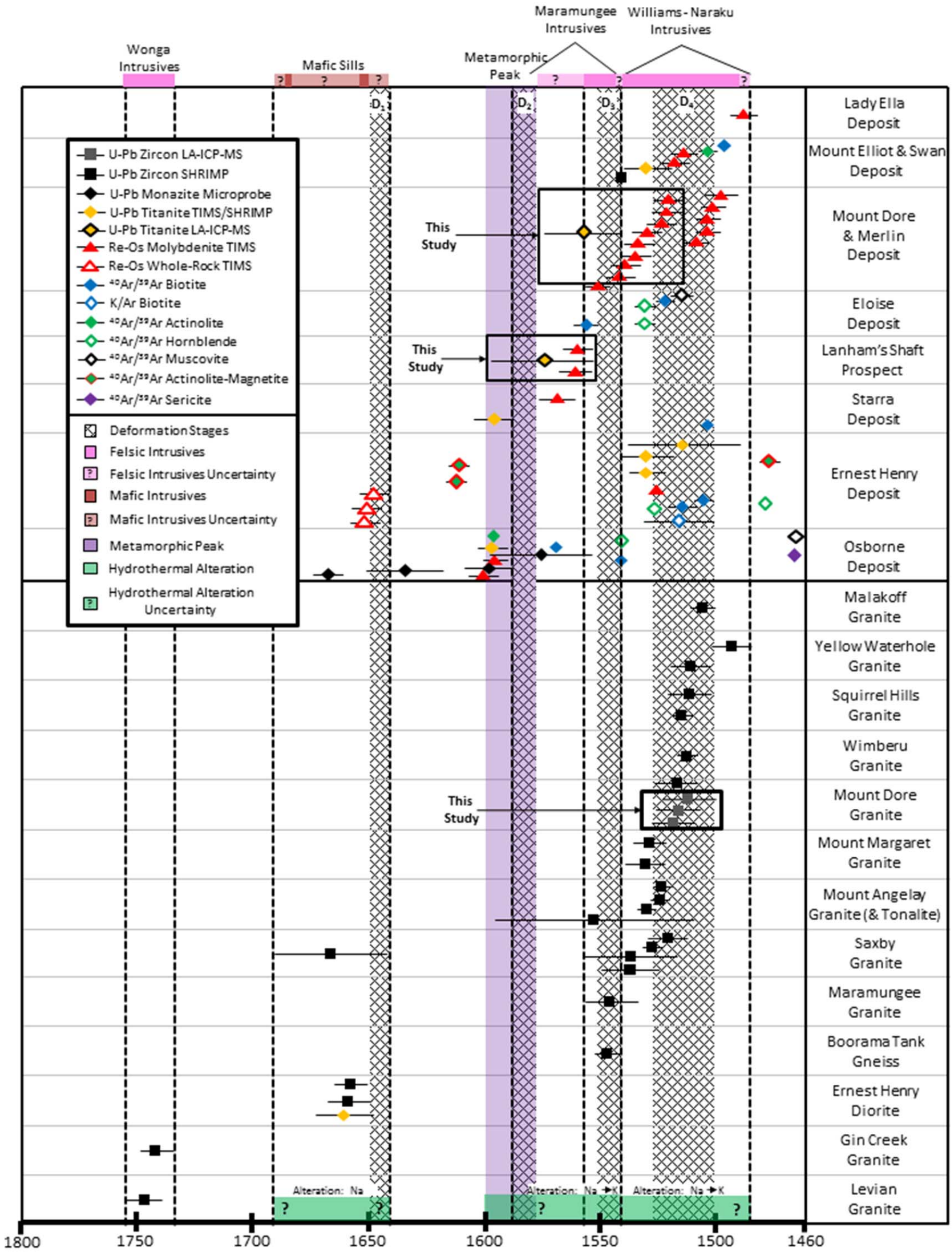

Figure 5:14 – Diagram showing Eastern Fold Belt ages of igneous intrusives and most important ore bodies in relation to the main regional igneous, metamorphic, and deformation events. The igneous intrusives and ore bodies' ages can be seen in Table 1 and 2. See text and Chapter 2 for details in the regional events. Tables with references can be consulted in Appendix 3.

6. Chapter 6: Isotopes

6.1. Introduction

Sulfur isotope studies are used in ore deposits research to determine the sulfur source/s of the mineralization. The sulfur isotopic signatures can be compared with Earth's main sulfur reservoirs (Fig. 6:1) and other ore deposits in order to determine fluid source/s. The Sm-Nd isotope system was originally used as a geochronology tool but is now mostly used in provenance studies. Similar to the sulfur isotopes it can be used to determine fluid/s origin in both bulk rock samples and in minerals. The Mo isotope studies relating to ore deposit studies are scarce but have the potential to identify ore deposit types and fluid/s sources.

In this chapter multi-set isotope data will be presented and discussed. The isotope techniques used were: Sulfur isotopes of molybdenite, chalcopyrite and pyrite; Sm-Nd isotopes in apatite and titanite crystals; and molybdenum isotopes on molybdenite.

The sulfur isotope studies were conducted at the Mount Dore and Merlin deposit as well as at the Lanham's and Barnes Shafts prospects. The $\delta^{34}S$ values in these localities allow for: 1. The investigation of potential differences between the Cu-dominated mineralization and Mo-dominated mineralization in respect to the sulfur source/s; 2. comparison of the Mount Dore and Merlin deposit Mo-rich and Cu-rich mineralization with the similar Lanham's Shaft prospect mineralization, and; 3. comparison of the Cu-dominated mineralization of the Barnes Shaft, that has no molybdenite mineralization, with the Lanham's Shaft prospect. The data gathered is also interpreted relative to sulfur isotope studies of other ore deposits in the Cloncurry District.

Sulfur isotope studies for IOCG deposits in the Cloncurry District (i.e. Ernest Henry, Eloise, Starra, Osborne, among others) display values for chalcopyrite that vary from approximately $\delta^{34}S$ -7 to 5‰ (Scott et al., 1985; Andrew et al., 1989; Davidson and Dixon, 1992; Davidson and Garner, 1997; Rotherham et al., 1998; Mark et al., 2006a). These $\delta^{34}S$ values overlap with the $\delta^{34}S$ ranges of several natural reservoirs (e.g. Thode et al., 1961; Coleman, 1977) (Fig. 6:1).

In this region the sulfur isotope studies have been coupled with oxygen and carbon stable isotopes studies (Rotherham et al., 1998; Mark et al., 2006a; Marshall and Oliver, 2006; Marshall et al., 2006; Babo, 2009). Based on these stable isotopes studies, and regional geology considerations, such as ore deposit age dating, most authors have argued for an igneous source for the hydrothermal fluids that, from deposit to deposit, would vary in its

interaction with the host rocks, either to change the $\delta^{34}S$, or the $\delta^{18}O$ and $\delta^{13}C$ (e.g. Mark et al., 2006a; Marshall and Oliver, 2006; Marshall et al., 2006). Although this interpretation is reasonable there are some data conflicts with, for instance, the Mount Elliot deposit $\delta^{18}O$ and $\delta^{13}C$ signatures being interpreted as indicative of low fluid-wallrock interaction (Marshall et al., 2006), while its $\delta^{34}S$ signatures have been interpreted to be indicative of wallrock sulfur contribution to the mineralizing system (Mark et al., 2006b). These interpretations are still possible considering the high complexity of these systems and other parameters that can change these stable isotopes signatures, such as: fO_2, pH, temperature, pressure, fluid mixing, and isotopic fractionation between sulfides (e.g. Ohmoto, 1972; Rye and Ohmoto, 1974; Friedman and O'Neil, 1977; Mark et al., 2006a). At the Lanham's Shaft prospect the reported $\delta^{18}O$ and $\delta^{13}C$ values of carbonates associated with molybdenite mineralization are similar to the Mount Elliot signatures which would indicate an igneous fluid source in a fluid buffered system (Alt et al., 1986; Criss and Taylor, 1986; Deines, 2002; Babo, 2009).

More recently, fluid inclusion studies have modified the previous interpretations with evidence of sedimentary formation waters as a component of the hydrothermal fluid in most IOCG deposits in the Eastern Fold Belt (Kendrick et al., 2006; Fisher, 2007; Kendrick et al., 2007; Kendrick et al. 2008; Fisher and Kendrick, 2008). Older deposits such as Osborne are almost completely dominated by these fluids while Ernest Henry, which main mineralizing stage is one of the youngest in the area, shows mixing between bittern brine fluids and igneous fluid (Kendrick et al., 2006; Fisher, 2007; Kendrick et al., 2007; Kendrick et al. 2008; Fisher and Kendrick, 2008; Oliver and Rubenach, 2009).

$\delta^{18}O$ and $\delta^{13}C$ analysis of carbonate at the Mount Dore and Merlin deposit was not conducted during this study due to the existence of several different carbonates, the high complexity of the textural relationships between them, and the general lack of carbonates associated with the Mo-dominated mineralization.

Sm-Nd isotope studies have been used for provenance studies in the better understanding of crustal processes (e.g. McCulloch, 1987; Maas and McCulloch, 1991). The Sm-Nd isotopic system in these provenance studies is used in conjunction with age dating techniques. This processing of results has, for example, been used to show that certain suite of granites have an older crustal component when another suite has a younger crustal component (e.g. Pollard and McNaughton, 1997; Page and Sun, 1998; Mark, 2001). The ability to retrace the εNd of rock samples through time also allows comparing between different aged samples, which has also been used to investigate ore deposit genesis (e.g. Maas et al., 1987; Oliver et al., 1999; Skirrow et al., 2007). New technical advancements have very recently created the

opportunity to conduct single grain *in situ* analyses of Sm-Nd using LA Multicollector-ICP-MS (e.g. Hammerli et al., 2014), while most of the previous studies were based on whole rock Sm-Nd isotope data. A very comprehensive database of Sm-Nd and age dating from collations of all available data has been used in this study (Pollard and McNaughton, 1997; Champion, 2013).

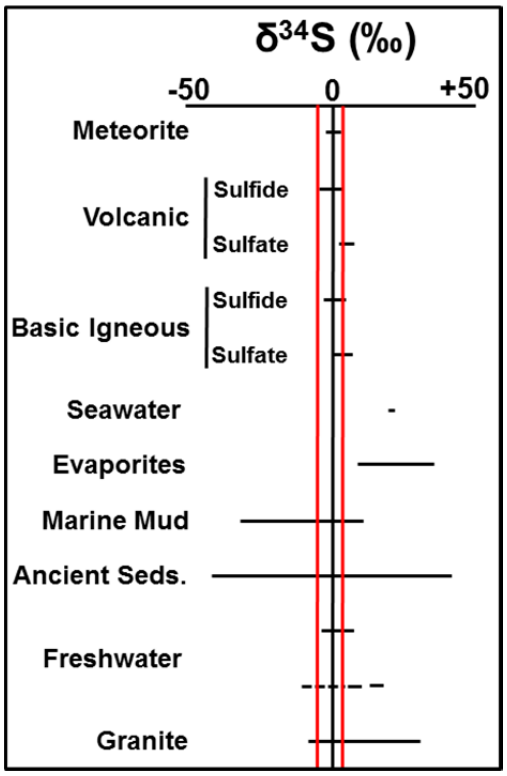

Figure 6:1 – $\delta^{34}S$ (‰) values range for the main sulfur reservoirs adapted from Coleman (1977). The red lines displays the $\delta^{34}S$ isotopic range found at the Mount Dore and Merlin pyrite, chalcopyrite and molybdenite.

Most molybdenum isotopes studies have concentrated in the geochemical reservoirs related to the ocean sedimentary cycle due to its potential as a paleoceanography proxy (Barling et al., 2001; McManus et al., 2002; Siebert et al., 2003; Barling and Anbar, 2004; Arnold et al., 2005; Tossel, 2005; Siebert et al., 2006; Archer and Vance, 2008; Poulson et al., 2009; Voegelin et al., 2009; Nagler et al., 2011; Neubert et al., 2011; Goldberg et al., 2012), which has given support, for instance, to studies of past global cycles of anoxia (e.g. Arnold et al., 2004; Siebert et al., 2004). There is also interest in the study of molybdenum isotopes in ore systems and, although these studies are still developing, indications of their potential uses have been shown (Hannah et al., 2007; Mathur et al., 2010; Greber et al., 2011). Despite these advances, laboratory comparison is complex due to the lack of an internationally accepted standard (e.g. Hannah et al., 2007; Greber et al., 2011, 2012), which makes the data available difficult to cross-reference.

Hannah et al. (2007) considered her extensive analyses of ore deposits molybdenite to be similar to the crustal average values despite differences in geographic and geologic setting, age and temperature. Other studies of molybdenum isotopes in different deposit types have argued that there is the possibility of identifying distinct hydrothermal deposits and even different mineralization events based on the molybdenum isotopic signatures (Malinovsky et al., 2005; Mathur et al., 2010; Greber et al., 2011; ShiMing et al., 2011; Song et al., 2011; Hannah et al., 2007) as well as a potential framework to identify molybdenite samples not suitable for Re-Os dating (Mathur et al., 2010).

6.2. Sample description and results

6.2.1. Sulfur isotopes sampling and results

Molybdenite, chalcopyrite and pyrite were analyzed for $\delta^{34}S$ in both the Mount Dore and Merlin deposit and the Lanham's Shaft prospect. At the Barnes Shaft prospect chalcopyrite and pyrite was also analyzed. An additional 14 analyses of sulfides at the Lanham's Shaft prospect from Babo (2009) were included in this study (Table 6:1). Details on the methods can be consulted in Chapter 1 and tables with the results in Digital Appendix.

Table 6:1 – Number of sulfur isotope analyses by sulfide mineral in each case study. Analyses conducted by Babo (2009) for the Lanham's Shaft Prospect are indicated in brackets.

Locality	Pyrite	Chalcopyrite	Molybdenite	Total
Mount Dore and Merlin	19	14	39	72
Lanham's Shaft	6 (+ 5)	4 (+ 3)	5 (+ 6)	15 (+ 14)
Barnes Shaft	14	4	-	18

The sulfur isotope results were also analyzed with respect to their spatial position in the mineralizing system, with special attention to the Mount Dore and Merlin deposit due to greater abundance of data and the complexity of the system (Fig. 6:2).

Most (~90%) of the $\delta^{34}S_{Mo}$ from the Mount Dore and Merlin deposit cluster in between -4 and 0‰, with a large proportion of samples (22 of 39) between -3 and -2‰ (Fig. 6:3). Only three samples fall outside this range, and these are between 0 and 3‰ (Fig. 6:2 e). The $\delta^{34}S_{Cpy}$ clusters between 1 and 6‰, with only one analysis lying outside this range with the value of -5.4‰ (Fig. 6:2 d). The sulfur isotope values from pyrite show greater complexity. The heavier sulfur signatures cluster between 0 and 5‰. There is another cluster between -3 and -1‰, which lies in the middle of the $\delta^{34}S_{Mo}$ cluster. The remaining three values range between -8 and -4‰.

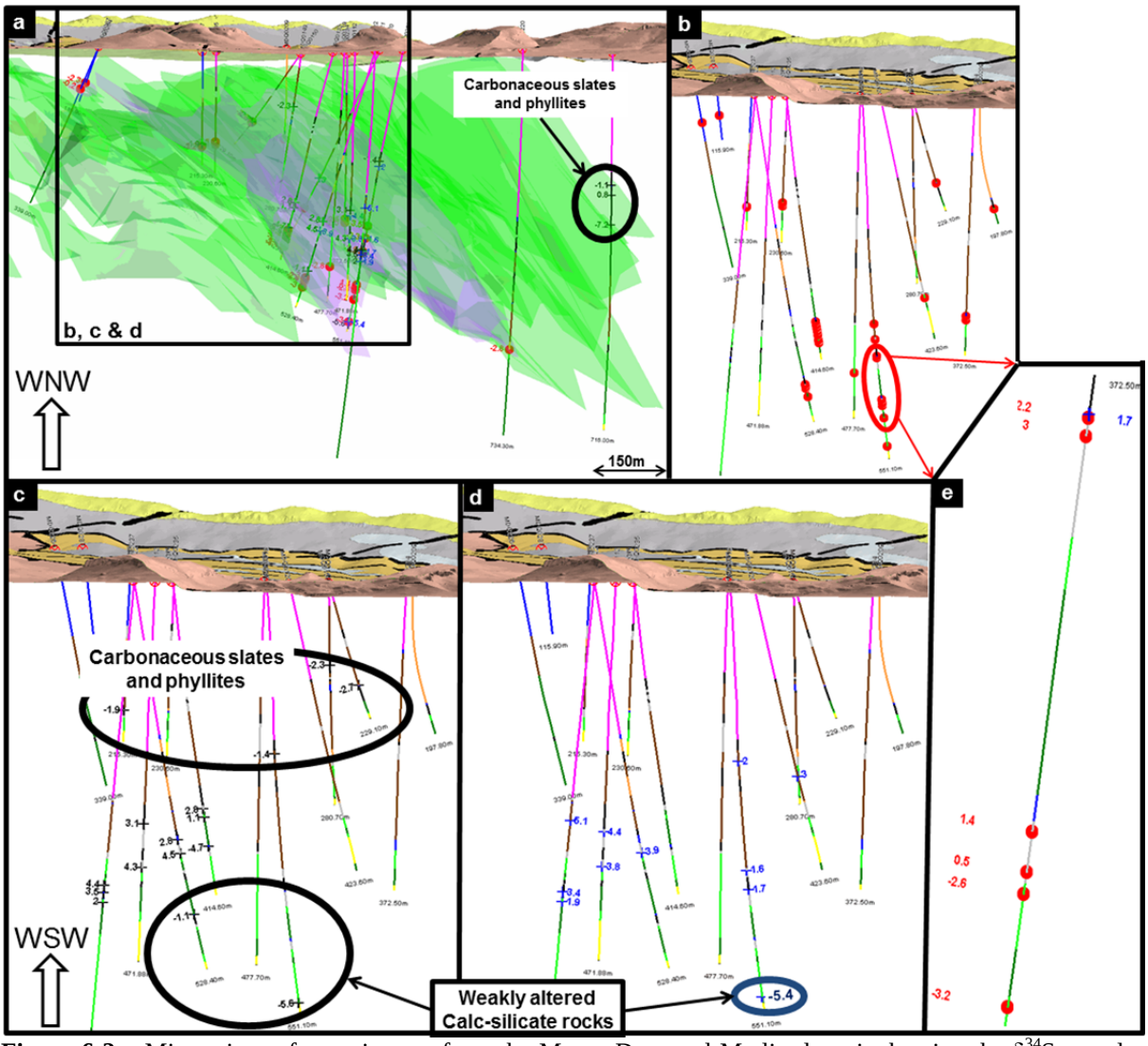

Figure 6:2 – Micromine software images from the Mount Dore and Merlin deposit showing the $\delta^{34}S$ samples location. In red are the $\delta^{34}S_{Mo}$, in blue the $\delta^{34}S_{Cpy}$, and in black the $\delta^{34}S_{py}$. **a)** Image showing geologic map surface, sampled drillholes, Cu-rich mineralization (green) and Mo-rich mineralization (purple) ore shells. **b)** Image showing $\delta^{34}S_{Mo}$ sample locations and **e)** is detail image of drillhole section with $\delta^{34}S_{Mo}$ outlier values. **c)** Image showing $\delta^{34}S_{py}$ sample locations, highlighting the outlier values locations and host rocks. **d)** Image showing $\delta^{34}S_{py}$ sample locations, highlighting the outlier value location and host rocks.

The Lanham's Shaft prospect displays strong similarities with the Mount Dore and Merlin deposit, with $\delta^{34}S_{Py}$ and $\delta^{34}S_{Cpy}$ concentrating between -1 and 5‰ and a peak in both sulfides at around 3-4‰ (Fig. 6:4). There is only a single outlier analysis of $\delta^{34}S_{Cpy}$ which has the value of -3.3‰. Comparatively, the $\delta^{34}S_{Mo}$ values show a more complex spread. The majority (57%) of values clusters between -7 and -4‰. There are two samples that are between -3 and -1‰, another sample is 1.7‰, and the last sample is 3.6‰ (Fig. 6:4).

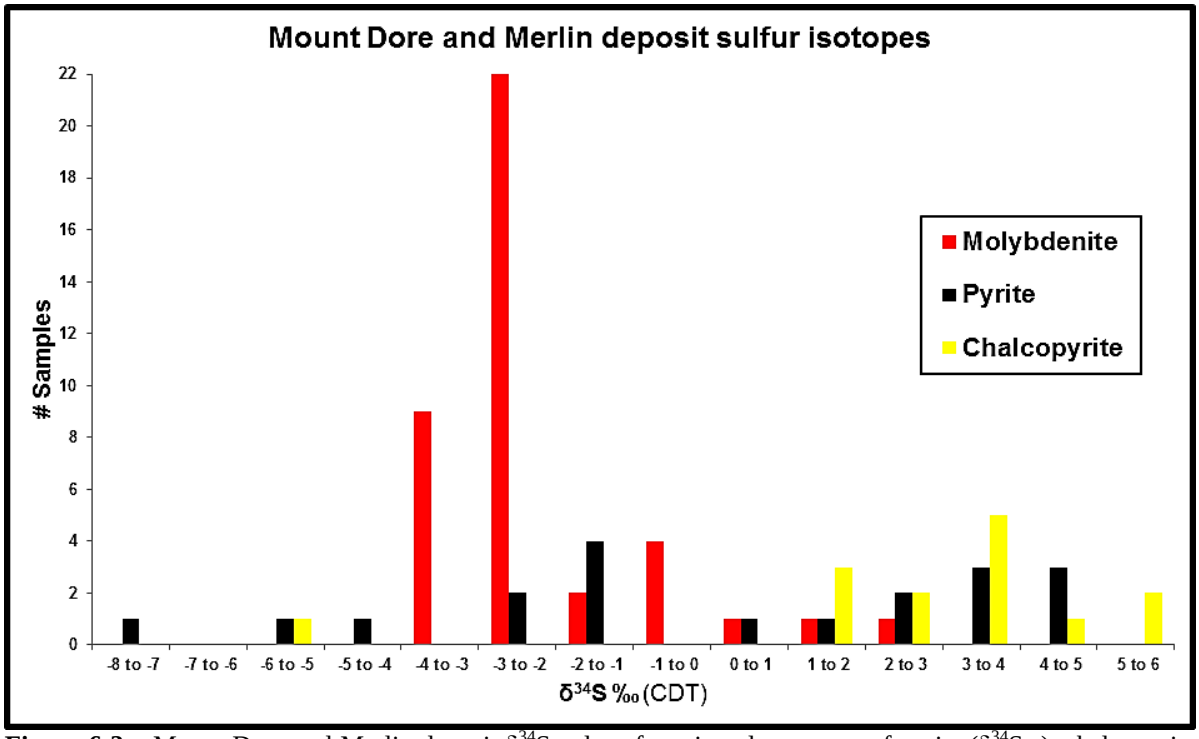

Figure 6:3 – Mount Dore and Merlin deposit $\delta^{34}S$ values for mineral separates of pyrite ($\delta^{34}S_{Py}$), chalcopyrite ($\delta^{34}S_{Cpy}$) and molybdenite ($\delta^{34}S_{Mo}$) plotted against frequency.

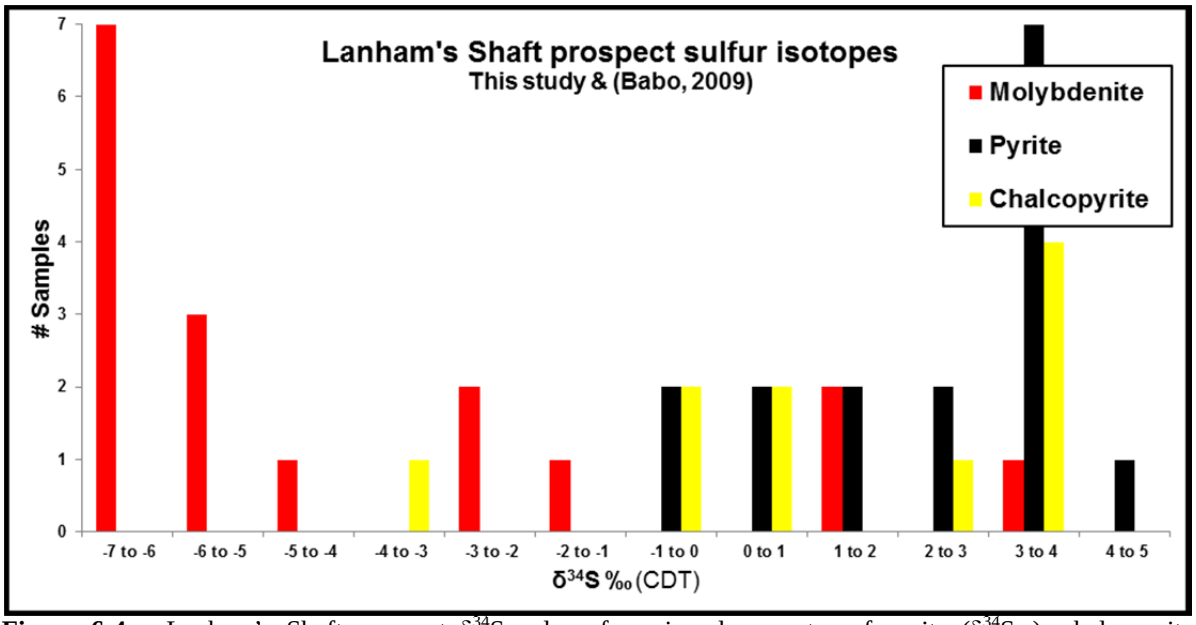

Figure 6:4 – Lanham's Shaft prospect $\delta^{34}S$ values for mineral separates of pyrite ($\delta^{34}S_{Py}$), chalcopyrite ($\delta^{34}S_{Cpy}$) and molybdenite ($\delta^{34}S_{Mo}$) plotted against frequency.

At the Barnes Shaft prospect only pyrite and chalcopyrite were analyzed, due to the lack of molybdenite in that prospect (Fig. 6:5). The $\delta^{34}S_{Py}$ and $\delta^{34}S_{Cpy}$ show similarities to the Lanham's Shaft prospect and the Mount Dore and Merlin deposit chalcopyrite and pyrite signatures. The $\delta^{34}S_{Py}$ values cluster between 2 and 8‰ with more samples towards the

heavier sulfur values. There is one pyrite sample outlier with the value of -1.6‰. There are only 4 samples analyzed for $\delta^{34}S_{Cpy}$ and they are between 1 and 5‰ (Fig. 6:5).

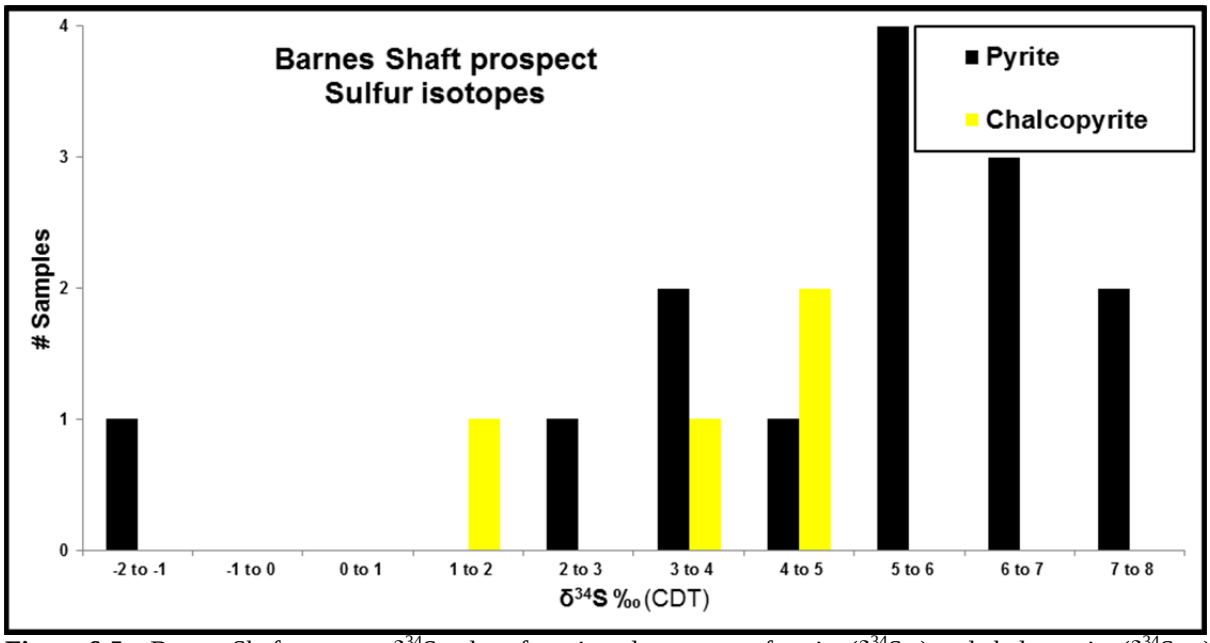

Figure 6:5 – Barnes Shaft prospect $\delta^{34}S$ values for mineral separates of pyrite ($\delta^{34}S_{Py}$) and chalcopyrite ($\delta^{34}S_{Cpy}$) plotted against frequency.

The comparison of the three graphs shows that (Fig. 6:6): 1) The $\delta^{34}S_{Mo}$ and $\delta^{34}S_{Py+Cpy}$ form mainly two distinct populations. 2) The majority of the $\delta^{34}S_{Mo}$ are negative, with peaks at -3 to -2‰ at the Mount Dore and Merlin deposit, and at -7 to -6‰ at the Lanham's Shaft prospect. 2) The $\delta^{34}S_{Py}$ and $\delta^{34}S_{Cpy}$ is positive in the three cases with most samples at 3 to 4‰, although Barnes Shaft has slightly broader values for $\delta^{34}S_{Cpy}$ and $\delta^{34}S_{Py}$ between -1 and 8‰. 3) There is a smaller cluster of $\delta^{34}S_{Py}$ values between -3 and -1‰, coincidental with the main population of $\delta^{34}S_{Mo}$ of the Mount Dore and Merlin deposit. 4) There are a few samples of $\delta^{34}S_{Mo}$ which overlap with the highest cluster values of $\delta^{34}S_{Py}$ and $\delta^{34}S_{Cpy,}$ and vice-versa. 5) There are very few values that are outliers relative to the two main clusters, which represent the Cu-rich and the Mo-rich mineralization.

The samples used for the sulfur isotope analyses cover the mineralization styles and host rocks present in the three localities (see Chapters 3 and 4 for details). At the Mount Dore and Merlin deposit and at the Lanham's Shaft prospect examples of the outlier $\delta^{34}S$ samples textures are presented in more detail in figure 6:7.

The representative sample with positive values of $\delta^{34}S_{Mo}$ in the Mount Dore and Merlin deposit shows fragmented pyrite grains in molybdenite veins that were formed later relative to the pyrite (Fig. 6:7a). At the Lanham's Shaft prospect a representative sample also

with positive $\delta^{34}S_{Mo}$ shows abundant pyrite being cut by molybdenite mineralization in a vein (Fig. 6:7b). The representative sample with pyrite that gave similar $\delta^{34}S_{py}$ values to the main molybdenite mineralization shows co-precipitation textures of the two sulfides (Fig. 6:7c).

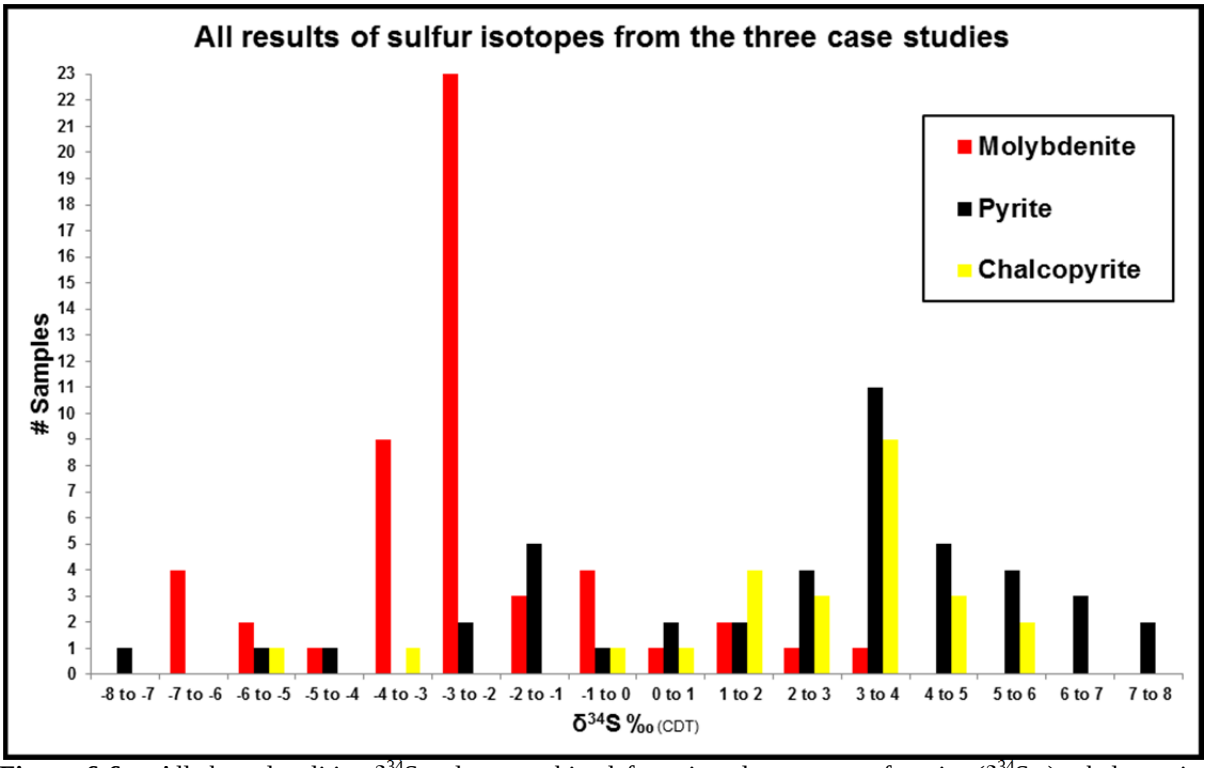

Figure 6:6 – All three localities $\delta^{34}S$ values combined for mineral separates of pyrite ($\delta^{34}S_{Py}$), chalcopyrite ($\delta^{34}S_{Cpy}$) and molybdenite ($\delta^{34}S_{Mo}$) plotted against frequency.

6.2.2. LA-MC-ICP-MS in apatite and titanite grains: Sampling and results

Apatite trace element composition and Sm-Nd isotopes studies were very useful due to the existence of apatite crystals associated with the three different hydrothermal alteration stages (Fig. 6:8 c, d, and f). The Sm-Nd analysis of titanite was conducted in typical euhedral crystals associated with the Na-(Ca) hydrothermal alteration stage (Fig. 6:8 c). The samples selected as best representative of each hydrothermal stage consist of; a sample of Na-(Ca) hydrothermally altered calc-silicate rock (Fig 6:8 a); an angular-clast carbonate breccia with Cu-polymetallic mineralization in carbonaceous slate (Fig. 6:8 b), and; a moderate to intensely altered, banded carbonaceous slate sample with small stylolitic veins and disseminations of molybdenite (Fig. 6:8 e). The last sample was selected due to the very good textural relationship between the apatite crystals and the hydrothermal mineral assemblage representative of the molybdenite mineralization (Fig. 6:8 f). This carbonaceous slate sample shows moderate to intense alteration that does not completely destroy the graphitic dark

colours of some of the bands (Fig. 6:8 e). In most other cases, these bands are completely overprinted adding to the complexity of rock identification.

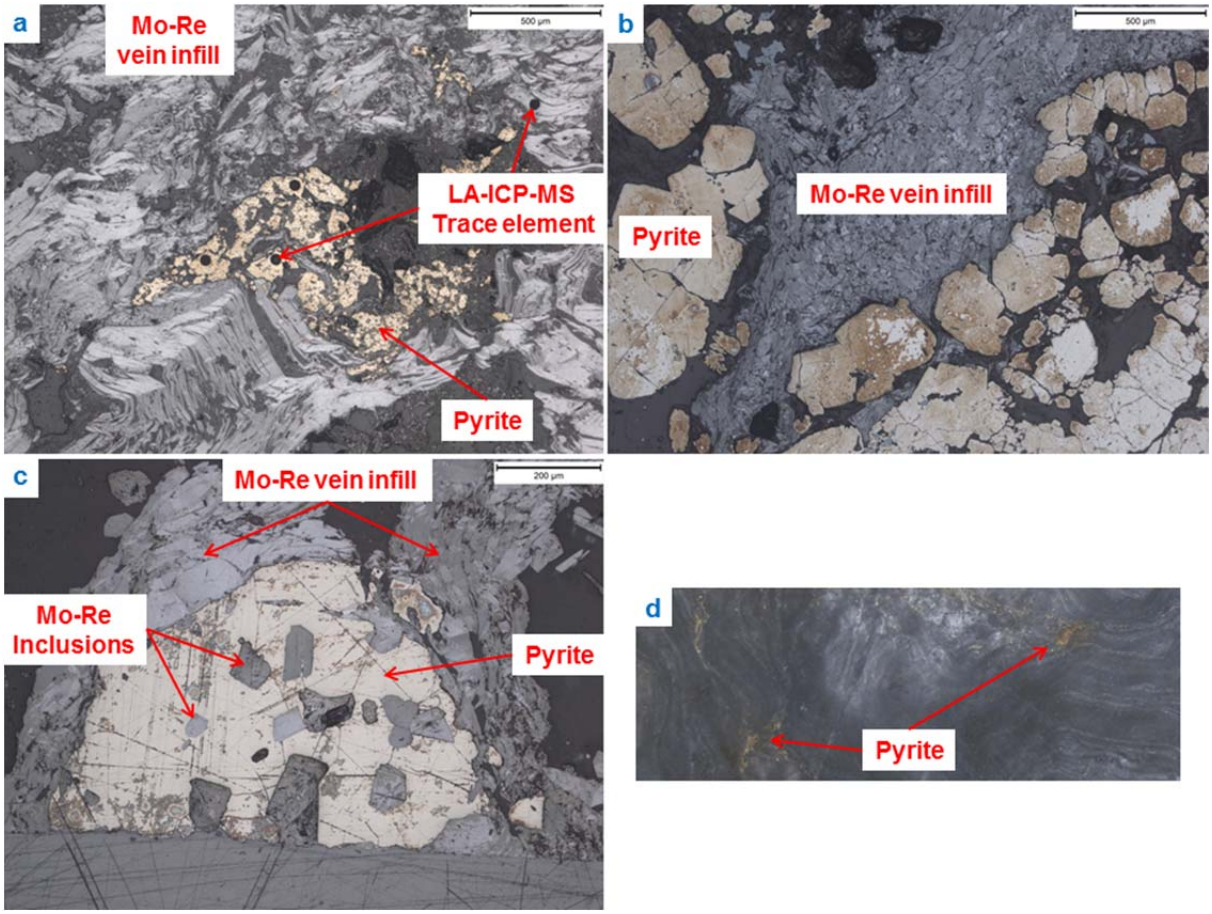

Figure 6:7 – **a)** Photomicrograph taken in transmitted light of drillhole MDQ0252 at ~459.65 metres depth showing molybdenite mineralization reacting with pyrite crystals with fragmented textures. Also LA-ICP-MS spot analyses in both sulfides. **b)** Photomicrograph taken in transmitted light of drillhole LAD0001 (Lanham's Shaft) at ~143.75 metres depth showing molybdenite mineralization cutting abundant pyrite crystals. **c)** Photomicrograph taken in transmitted light of drillhole MDQ0150 at ~170.80 metres depth showing a pyrite crystal with inclusions and also surrounded by molybdenite mineralization. Drillhole MDQ0245 at ~326.55 metres depth showing a phyllite core sample with pyrite following the convoluted folding of the penetrative foliation present.

The apatite crystals in each sample were characterized by petrographic microscope and CL imagery to establish textural relationship with the mineral assemblage and determine crystal zonation (Fig. 6:9). These apatite crystals were then analysed in situ for trace elements (Fig. 6:10) and Sm-Nd isotopes (Fig. 6:11). The elements analysed were: Si, P, K, Ca, Ti, V, Cu, As, Sr, Y, Zr, Mo, Sb, Ba, La, Ce, Nd, Sm, Eu, Gd, Dy, Er, Yb, Lu, W, Pb, Th, U, Dy. Calcium was used as the internal standard and several elements were typically below detection limit (i.e. Si, K, Ti, Cu, Zr, Mo, Sb).

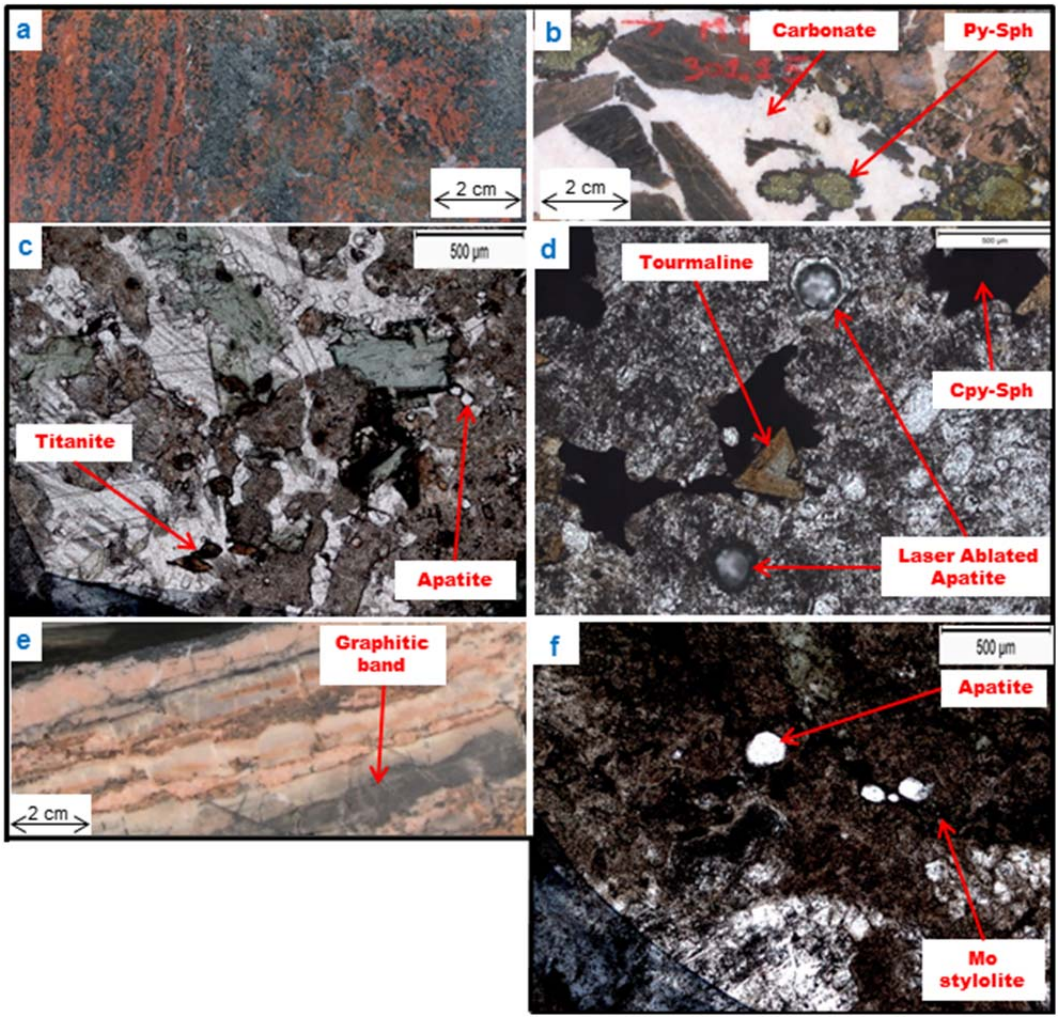

Figure 6:8 – **a)** Drillhole MDQ0112 at ~381.95 metres depth showing calc-silicate rock core sample with Na-(Ca) hydrothermal alteration. **b)** Drillhole MDQ0222 at ~301.15 metres depth showing angular clast breccia with carbonate and Cu-polymetallic mineralization hosted in carbonaceous slates core sample. **c)** Photomicrograph taken in plane-polarized light of **a)** showing apatite and titanite crystals associated with typical Na-(Ca) hydrothermal alteration minerals. **d)** Photomicrograph taken in plane-polarized light of **b)** showing apatite crystals associated with Cu-polymetallic mineralization and; **g)** higher magnification of the same with ablated spot analyses in apatite crystals. **e)** Drillhole MDQ0132 at ~376.30 metres depth showing moderate to intensely altered banded carbonaceous slates core sample. **f)** Photomicrograph taken in plane-polarized light of **e)** showing apatite crystals associated with stylolitic vein of molybdenite.

The processing of the trace element results obtained displayed a good correlation between apatite crystal zonation and several elements, from which Y, Ce, and Pb were chosen as the best (Fig. 6:10). The REE elements display distinct populations in all three samples that correspond to apatite grains cores and rims. Y was chosen due to its affinity with REE and Ce as a light REE element. Pb was the element used as indicative of co-precipitation of mineralization with the apatite grains, where the sample representative of Na-(Ca) alteration, that has no mineralization, displays the highest Pb values.

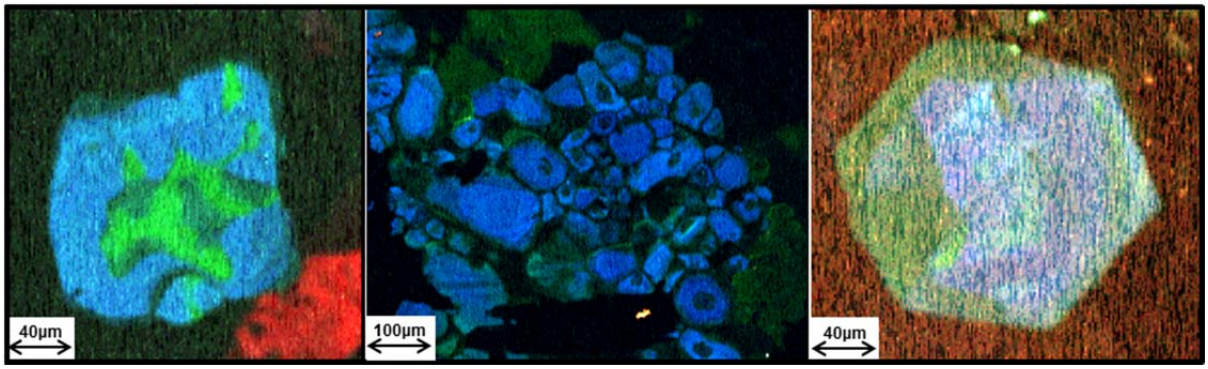

Figure 6:9 - Three pictures taken in CL showing apatite zoned crystals of the three rock samples: Apatite associated with molybdenite mineralization; cluster of apatite in calc-silicate rocks with Na-(Ca) alteration; euhedral apatite associated with Cu-polymetallic alteration. The crystal zones are defined by the natural color spectrum.

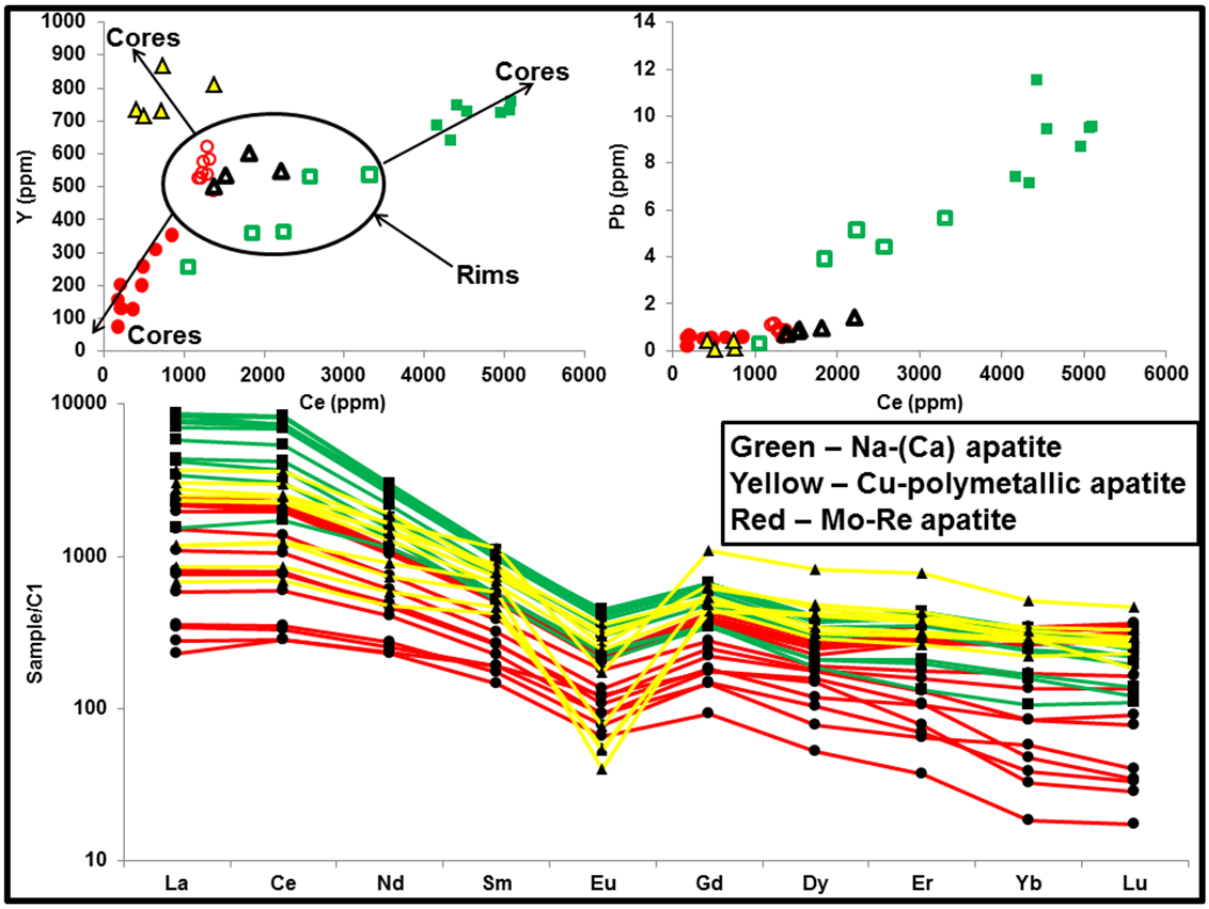

Figure 6:10 – LA-ICP-MS apatite crystals trace elements geochemistry of three samples representative of each hydrothermal alteration stage defined. Bottom plot show REE patterns of the three samples normalised to chondrite (Sun and McDonough, 1995).

The Sm-Nd isotopic values obtained were recalculated to the age of formation with respect to the Re-Os ages discussed on Chapter 5. The sample where the apatite is associated with molybdenite mineralized stylolites and disseminations, the age of 1521 Ma was adopted in concordance with the three ages obtained in similar mineralized samples. The age of 1557 Ma was used for the remaining samples based on the titanite dating of the Na-(Ca) hydrothermal

alteration (see Chapter 5 for details). The εNd values of the three samples have in several cases large errors due to either low counts or shooting through the grain, and the analyses that yielded errors above the value of 2 with respect to 2σ error are not presented here. Further details on the methods can be consulted in Chapter 1; the complete Sm-Nd isotope data can also be consulted in Digital Appendix. The εNd average of values and ages used for its calculation are presented in Table 6:2.

The results of the three samples representative of the hydrothermal stages characterized were calculated and plotted according to their assigned age and compared with the whole rock εNd reported values and respective age dating for igneous intrusives and metasedimentary rocks of the Eastern Fold Belt (Fig. 6:11). The whole rock εNd values and age dating was sourced from Pollard and McNaughton, (1997) and Champion (2013).

Table 6:2 – LA-ICP-MS εNd results by assigned age from apatite and titanite crystals, representative of the three characterized hydrothermal alteration stages at the Mount Dore and Merlin deposit.

Drillhole	Depth	εNd	2σ error	Age	Hydrothermal Stage
MDQ0132	376.30	-3.22	1.25	1521	Molybdenite mineralization stage - Apatite
MDQ0222	301.15	-4.08	1.15	1557	Cu-polymetallic mineralization stage - Apatite
MDQ0112	381.95	-3.51	1.30	1557	Na-(Ca) hydrothermal alteration stage - Apatite
MDQ0112	381.95	-4.14	1.13	1557	Na-(Ca) hydrothermal alteration stage - Titanite

6.2.3. Molybdenite isotopes sample description and results

Six samples of molybdenite mineralization were collected for the molybdenite isotope study. One sample corresponds to the Little Wizard ‘pod’; two samples consist of molybdenite in infill of matrix-supported breccias with rounded clasts; two samples are from stylolitic veins and disseminations; and the last sample occurs in carbonate veins as ‘patches’ and disseminations (Table 6:3). Three samples were analysed twice and yielded consistent results within analytical error (Digital Appendix). Further details on analytical methods can be consulted in Chapter 1.

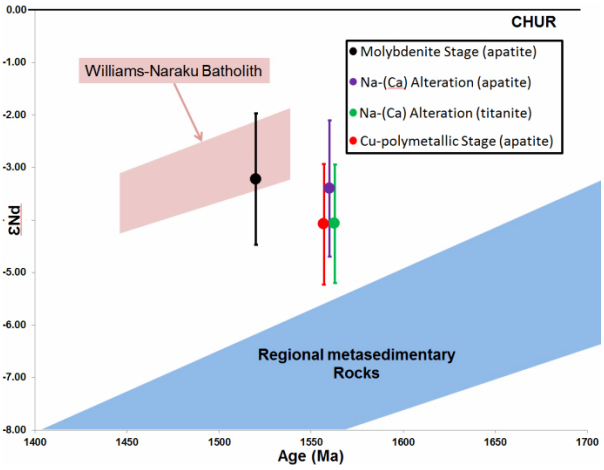

Figure 6:11 – LA-ICP-MS Sm-Nd isotopes of apatite and titanite crystals of the three hydrothermal stage's characterized, plotted using εNd and assigned age (see text for discussion). Regional values fields calculated from Pollard and McNaughton (1997) Champion (2013). The ages of Na-(Ca) and Cu-polymetallic samples is slightly displaced for better visualization of the results.

Table 6:3 - δ^{97}Mo results of the six samples selected by mineralization type. Also $\delta^{34}S_{Mo}$ values obtain from the same samples is presented here. Further details on Digital Appendix.

Drillhole	Depth (m)	δ^{97}Mo	Uncertainty (2SD)	Mineralization Type	δ^{34}S (‰)
MDQ0287	77.40	-0.13	0.10	Little Wizard	-2.3
MDQ0132	355.40	-0.12	0.03	Breccia infill	-2.3
MDQ0209	174.70	-0.14	0.09	Breccia infill	-1.4
MDQ0252	487.90	-0.28	0.10	Stylolite	-3.2
MDQ0221	472.55	-0.16	0.10	Disseminated	-2.9
MDQ0252	343.85	0.05	0.08	Carbonate vein	-3.5

The molybdenum results from the six samples analysed show a well constrained spread of values in between -0.28 and 0.05‰ in δ^{97}Mo (Fig. 6:12). These values partly overlap with the previously reported values for 3 samples (each analysed twice) from the Mount Dore and Merlin deposit (Kirkby, 2009), although those analyses tend to lighter values. The one outlier of the previously reported values is only one of two repeat analyses conducted in the same sample (Kirkby, 2009), and therefore might be an analytical error.

The δ^{97}Mo values were compared with other studies done in different deposit types (Fig. 6:12 - Mathur et al., 2010; Barling et al., 2001) and with other natural materials signatures (Barling et al., 2001; McManus et al., 2002; Siebert et al., 2003; Arnold et al., 2004; Barling and Anbar, 2004).

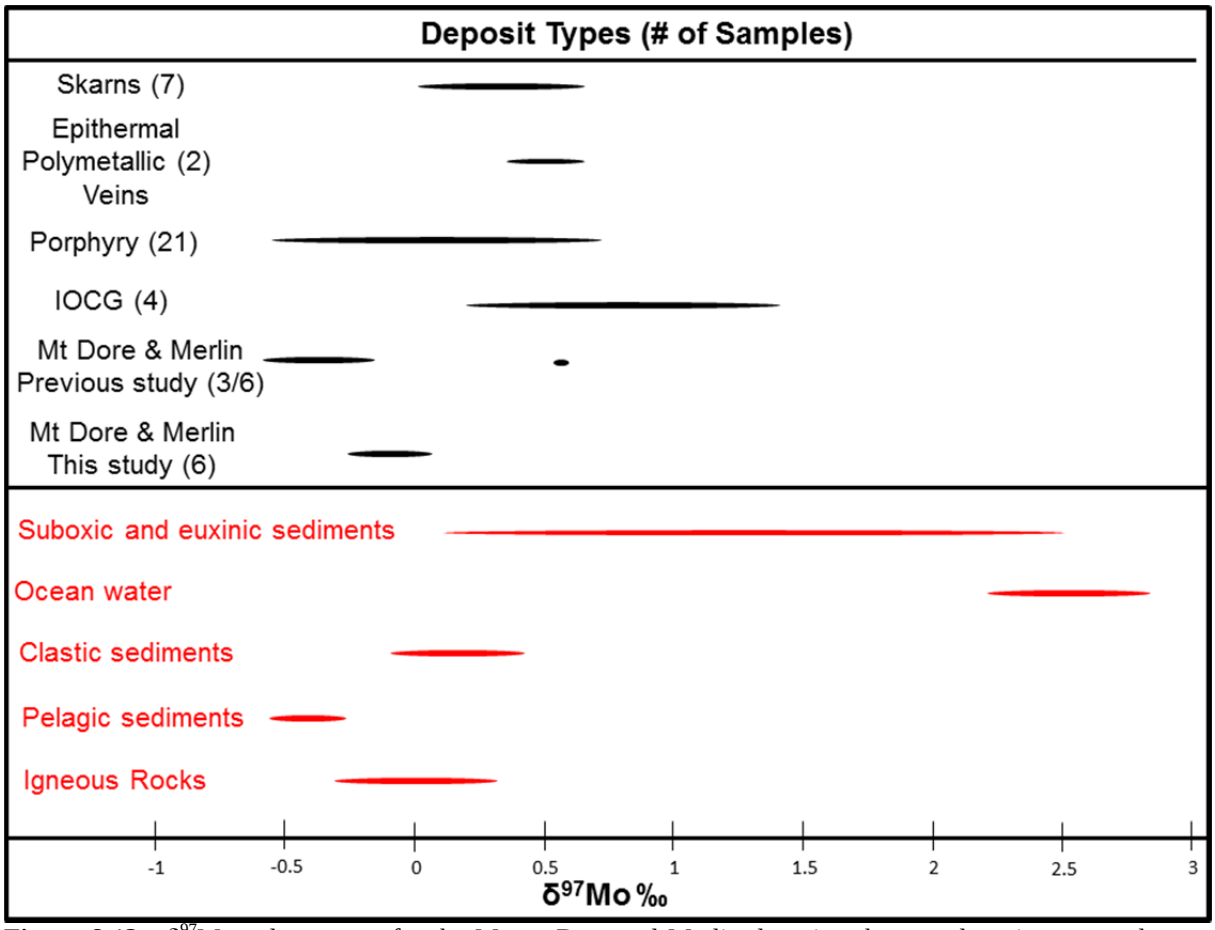

Figure 6:12 - δ^{97}Mo value ranges for the Mount Dore and Merlin deposit, other ore deposit types and some natural materials. See text for references.

6.3. Discussion

6.3.1. Sulfur isotopes

The sulfur isotope results of the three localities display positive values for Cu-rich mineralization and negative values for Mo-rich mineralization. Nevertheless, there are a few values that are inconsistent with the main clusters that need to be understood.

At the Mount Dore and Merlin deposit there are three groups of outlier values. The three $\delta^{34}S_{Mo}$ analyses that overlap with the general range of $\delta^{34}S_{Py}$ and $\delta^{34}S_{Cpy}$ are all from one particular section of drillhole MDQ0252 (Fig. 6:2 e). This section consists of an intensely altered rock unit that is difficult to classify, but has been logged as altered carbonaceous slates. Also, in one of those samples the molybdenite has reacted strongly with previously formed pyrite crystals that show fragmented textures (Fig. 6:7 a). These molybdenite/pyrite reaction textures are uncommon. Although it is difficult to be certain of the reason why this particular drillhole interval (Fig. 6:2) is displaying anomalies, it can be argued that the anomalous sulfur isotope values are due to the particular nature of the host rock and/or a

higher degree of interaction with previously formed pyrite. This sample was also used for Re-Os dating and trace element geochemistry in both molybdenite and pyrite, and it will be further referred to in the next chapter. Nevertheless, the fact that these three particular sulfur isotope values represent a minor proportion of the entire dataset testifies to the low frequency of sulfur exchange between sulfides of the Cu-rich stage and Mo-rich stage.

At the Lanham's Shaft prospect there are also two samples which have positive $\delta^{34}S_{Mo}$ values. In this case, these values are proposed to be due to sample contamination because of its high pyrite content (Fig. 6:7 b). The fact that these positive $\delta^{34}S_{Mo}$ values are only found in two samples also indicates that sulfur exchange between Mo-rich and Cu-rich mineralization was low at the Lanham's Shaft prospect.

One of the three Mount Dore and Merlin deposit pyrite samples that have $\delta^{34}S$ values that overlap with the typical $\delta^{34}S_{Mo}$ was characterized in more detail. This sample has texture indicative of co-precipitation between the molybdenite and the minor pyrite present (Fig. 6:7 c). This clearly indicates a direct link between the textures observed and the $\delta^{34}S_{Py}$ and $\delta^{34}S_{Mo}$ values measured. As in the above case, this sample was analyzed for trace elements in both pyrite and molybdenite; and also dated by Re-Os. It is important to note that such occurrences of pyrite co-precipitated with molybdenite are infrequent due to the very minor quantity of pyrite formation during the Mo-rich stage.

The three $\delta^{34}S_{Py}$ and one $\delta^{34}S_{Cpy}$ that tend to lighter values at the Mount Dore and Merlin deposit, as well the one negative value of $\delta^{34}S_{Cpy}$ at the Lanham's Shaft prospect were sampled from phyllites (Fig. 6:12 d), carbonaceous slates, or from weakly hydrothermally altered calc-silicate rocks that are a few metres from both the main Cu-rich and Mo-rich mineralization. The $\delta^{34}S_{Cpy}$ in both cases is from calc-silicate rock samples. In these few cases the sulfides are in zones of low hydrothermal alteration and minor mineralization. The negative values are therefore interpreted as reflecting the metasedimentary reservoir of sulfur which would be then relatively light in $\delta^{34}S$. It is important to note that the lighter $\delta^{34}S_{Mo}$ values at the Lanham's Shaft deposit are similar to the more negative $\delta^{34}S_{Py}$ values at the Mount Dore and Merlin deposit, which can indicate higher host rock sulfur inheritance by the Mo-rich mineralization at the Lanham's Shaft prospect.

The $\delta^{34}S_{Py}$ and $\delta^{34}S_{Cpy}$ values of the Barnes Shaft prospect are similar and slightly heavier that the Cu-rich mineralization values of both the Mount Dore and Merlin deposit and the Lanham's Shaft prospect. One single outlier sample of pyrite, with moderate contamination by chalcopyrite, gave the value of -1.6‰. This sample was taken from the mineralized dolerite intersection (see Chapter 4 for details) and although the reason why this

mineralization is displaying a different sulfur isotopic signature is not understood it is put forward that it is directly related to the mafic intrusive.

In summary, the Cu-rich mineralization shows a different isotopic signature to the Mo-rich mineralization; both signals are well defined and are consistent in all three localities; the isotopic signatures of the metamorphic host rocks prior to the hydrothermal alteration shows good indications of being more negative than the hydrothermal sulfur of both mineralization types. These results can be due to either: 1. Change of physicochemical conditions between mineralization types; 2. Spatial and/or temporal changes in the composition and degree of host rock reaction to the hydrothermal fluid(s), or; 3. Variable degrees of mixing between two different sulfur-bearing fluids with or without sulfur exchange with the host rock sulfur and variations in physicochemical conditions.

There are two likely mechanisms to change the positive sulfur isotopic values of the Cu-rich mineralization to the negative Mo-rich mineralization from one single sulfur source: Isotopic fractionation between different sulfides at a given temperature (e.g. Friedman and O'Neil, 1977); and/or oxygen fugacity and/or pH change (e.g. Ohmoto, 1972; Rye and Ohmoto, 1974). The temperature of mineralization was estimated based on the mineral association to be between 450-580 $^{\circ}$C and 400-500 $^{\circ}$C, for the Mount Dore and Merlin deposit (see Chapter 3 for details) and for the Lanham's Shaft prospect (see Chapter 4 for details), respectively. At the lowest estimated temperatures the fractionation between molybdenite and pyrite is less than 0.5‰, and the fractionation between molybdenite and chalcopyrite is less than 1.0‰, becoming even smaller with higher temperatures (Friedman and O'Neil, 1977). These values are too small to explain the difference between the δ^{34}S values of the Mo-rich mineralization and Cu-rich mineralization.

It is feasible that a change to lower pH and/or higher fO_2 during the precipitation of the Mo-rich mineralization relative to the Cu-rich mineralization can account for the sulfur isotopic signatures obtained at the deposits (e.g. Ohmoto, 1972; Rye and Ohmoto, 1974). This mechanism can only be directly used to justify the sulfur isotopic signature change between mineralization types if the sulfur source is common to both. This is not the case as is clearly indicated by the Sm-Nd isotope study (see below) and the trace elements in sulfides (see Chapter 7). At least two different sulfur sources are thus implied for the Cu and Mo mineralization.

6.3.2. Apatite LA-ICP-MS trace elements and Sm-Nd isotopes

The trace element analysis was conducted in the apatite grains which are associated with the three hydrothermal alteration stages characterized. The interpretation of the results obtained is complex due to several parameters that need to be considered. The different host rocks, mineral assemblages, and crystal zonation influence in the results are difficult to compare. The sample that represents the Na-(Ca) hydrothermal alteration stage has, for instance, titanite in its mineral assemblage which can be a strong factor in the REE abundances of co-precipitating apatite. Also, tourmaline associated with the Cu-polymetallic stage and monazite crystals with the Mo-Re stage are important to consider. Nevertheless, the trace element geochemistry work done in these apatite grains agree with the textural observations and hydrothermal alteration stages defined.

The trace element results show a clear indication that the apatite cores of each sample are geochemically distinct while the composition of the apatite rims are similar between samples (Fig. 6:10). The similar rim compositions can be due to a later hydrothermal stage that formed those apatite rims or, the rims reflect host rock signatures.

The two mineralized samples (Cu- and Mo-rich) show much lower abundances in Pb relative to the Na-(Ca) stage sample, which is a clear indication that there was co-precipitation of apatite crystals with sulfides that preferentially sequester Pb. The REE patterns, normalised to chondrite (Sun and McDonough, 1995), show similar trends between the samples with the exception of the cores of the apatite crystals associated with the Cu-polymetallic hydrothermal alteration stage, which are relatively Eu depleted (Fig. 6:9). It is possible that such Eu anomalies are related to the host rock, which is a moderately altered carbonaceous slate and contains Eu-loving plagioclase in equilibrium with the mineralization. The lower values in Y displayed by the apatite cores of the Mo-Re stage are possibly connected to formation of monazite.

The characterization of these apatite grains as being formed during each hydrothermal stage defined had been done qualitatively by petrographic observations. The trace element data shows quantitatively that those observations were in fact correct and can thus serve as a basis for the interpretation of the Sm-Nd study.

The average εNd results for apatite crystals representative of the younger Mo-Re mineralization stage overlaps with the Williams-Naraku Batholith field (Fig. 6:11). In this sample there was also one analysis that overlaps with the metasedimentary rocks field in the region, but that was not plotted due to having a large error, possibly due to either analytical

problems or an inherited, older apatite crystal that reflects the metasedimentary host rocks isotopic signature.

The apatite crystals associated with the Na-(Ca) alteration and the Cu-polymetallic mineralization display an average result in between the Williams-Naraku Batholith field and the regional metasedimentary rocks field (Fig. 6:11).

From the observation of these results it can be put forward that the ~1520 Ma Mo-rich mineralization (second Mo-Re mineralizing event; Chapter 3 for details) has Sm-Nd isotopic signatures typical of the Williams-Naraku intrusives. Both the Na-(Ca) hydrothermal stage and Cu-polymetallic mineralization are neither completely controlled by the metasedimentary rocks nor by the Williams-Naraku intrusives.

6.3.3. Molybdenum isotopes

The Mount Dore and Merlin δ^{97}Mo signatures overlap with some of the porphyry type deposit signatures which might indicate that the Mo bearing hydrothermal fluid is of felsic igneous origin, which is in acceptance with other data, such as the Sm-Nd isotopes and the sulfides trace elements (see next chapter for details).

Relative to the larger scale δ^{97}Mo reservoirs (Fig. 6:12) the values obtained in this study overlap with igneous rocks values that cluster tightly around 0‰ (Siebert et al., 2003). Besides the igneous rocks the overlaps are small lying between the oxic sediments and the suboxic to euxinic sediments δ^{97}Mo ranges (Barling et al., 2001; McManus et al., 2002; Siebert et al., 2003; Arnold et al., 2004; Barling and Anbar, 2004). It also partly overlaps with the clastic sediments values (Siebert et al., 2003).

Due to the variety of possible source reservoirs it can only be noted that the δ^{97}Mo values of the Mo-dominated mineralization at the Mount Dore and Merlin deposit display fluid/s source/s consistent with igneous signatures, probably felsic. It is difficult to further the comparison of these results with the values obtained in this study.

6.3.4. Comparison of different isotopic data sets

The main consideration that can be drawn from the isotope studies coupled with the textural characterization of the hydrothermal alteration stages and the age dating is that the Cu-polymetallic mineralization was formed by a different hydrothermal fluid than the Mo-Re mineralization. The Sm-Nd isotope signatures of both Na-(Ca) alteration and Cu-polymetallic

alteration indicate a different from Williams-Naraku Batholith and metasedimentary rocks component present in those hydrothermal stages.

In view of other sulfur isotope work and fluid inclusion studies done on IOCG deposits in Cloncurry district (Scott et al., 1985; Andrew et al., 1989; Davidson and Dixon, 1992; Davidson and Garner, 1997; Rotherham et al., 1998; Kendrick et al., 2006; Mark et al., 2006a; Fisher, 2007; Kendrick et al., 2007; Kendrick et al. 2008; Fisher and Kendrick, 2008), the age dating conducted in this study, the isotope data presented, and the textural evidence that shows that the Cu-dominated mineralization pre-dates the Mo-dominated mineralization, the proposed sulfur and fluid source/s model is (Table 6:4):

- The Na-(Ca) hydrothermal alteration and subsequent Cu-polymetallic mineralization were formed by a bittern brine fluid which reacted with the metasedimentary host rocks. In this scenario the sulfur isotope signatures would be a reflection of the mixing of the typical evaporite values (10 to 20‰) and metasedimentary host rocks values (≤ -8‰ – Fig. 6:6). The regional source of the bittern brine fluids is still in debate (Kendrick et al., 2006; Fisher, 2007; Kendrick et al., 2007; Kendrick et al. 2008; Fisher and Kendrick, 2008).
- The main and first Mo-Re mineralizing event is argued to be formed from a hydrothermal fluid derived from an igneous felsic intrusion. A similar dual sulfur source is put forward as the preferred model with mixing of felsic igneous sulfur , which are typically around 0 to 3‰ in $\delta^{34}S$ (e.g. Coleman, 1977), and metasedimentary host rocks sulfur (≤ -8‰). For this event a connection with the Mount Dore granite emplacement is not possible due to the older age of the mineralization although a connection with the broader and somewhat older main Williams-Naraku Batholith is reasonable.
- The second Mo-Re mineralizing event consists of a relatively minor remobilization of the first Mo-Re mineralization event with maintenance of the $\delta^{34}S_{Mo}$ signatures. This remobilization is argued to have occurred due to the emplacement of the Mount Dore granite. The fact that the sulfur signatures do not change between the two events indicates that the hydrothermal fluids added to the system during the second mineralizing event are either sulfur poor; and/or not abundant enough to impact sulfur isotopic signature of the Mo-Re remobilized mineralization.

The processes discussed for the Na-(Ca), Cu-polymetallic, and for the first Mo-Re mineralizing event at the Mount Dore and Merlin deposit are considered as essentially the

same for the Lanham's Shaft prospect ore genesis model, except that the age of the mineralization is older than the known Williams-Naraku batholiths (see Chapter 5 for details). The more negative sulfur isotope signatures in most molybdenite sulfur at the Lanham's Shaft prospect are possibly due to higher exchange with the metasedimentary host rocks and/or a smaller component of magmatic-hydrothermal fluid, which seems reasonable considering the less intense mineralization present; and/or a lighter sulfur isotope signature of the host rocks and/or igneous fluid; and/or variation of the physicochemical conditions. These possibilities will be further discussed in the next chapter.

The Barnes Shaft prospect Cu-Co mineralization is not as well understood due to the low amount of information obtained. It is possible that the Cu-Co mineralization is formed by a similar fluid evolution as the Na-(Ca) and Cu-rich mineralization in the other two localities, or was formed at a different time by other processes, although the similarity of sulfur isotopic signatures with the Cu-rich signatures of Mount Dore and Merlin deposit and Lanham's Shaft prospect do indicate a likely similar fluid source and host rock interaction during the formation of its mineralization.

Table 6:4 – Summary table of hydrothermal fluids types, and sulfur and ƐNd sources in respect to the isotope studies conducted and age dating for the Mount Dore and Merlin deposit.

Hydrothermal phases Mount Dore and Merlin		Age (Ma)	$\delta^{34}S$ (‰)	εNd	Hydrothermal Fluid/s	Sulfur and εNd source/s
Na-(Ca)		1557	n.d.	-3.51 and -4.14	Bittern brine (?)	n.d.
Cu-polymetallic		1557 - 1535	+1 to +6	-4.08	Bittern brine	Bittern brine ($\delta^{34}S$ 10 to 20‰) + Metasedimentary host rocks ($\delta^{34}S$ < -8‰) (εNd -8.3 to -6.3)
Mo-Re	Stage 1	1535	-4 to 0	n.d.	Felsic Igneous (Williams-Naraku)	Felsic Igneous ($\delta^{34}S$ 0 to 3‰) (εNd -3.7 to -2.1) + metasedimentary host rocks ($\delta^{34}S$ < -8‰) (εNd -8.3 to -6.3)
	Stage 2	1521	-4 to 0	-3.22	Felsic Igneous (Williams-Naraku)	Remobilization of Phase 1 Mo-Re mineralization ($\delta^{34}S$ -0 to 4‰)

6.4. Conclusions

Although these are highly complex systems the overall interpretation of the isotope studies coupled with the petrographic characterization and age dating studies allow for the delineation of a preferred model of fluid/s sources and evolution by reaction with the host rocks. The three systems studied display strong similarities with interpreted similar fluid source and evolution for the Cu-rich mineralization and Mo-rich mineralization.

The Cu-rich mineralization consists of a bittern brine fluid which exchanged sulfur with the host rocks and therefore formed sulfides with mixed sulfur isotopic signatures between the heavier fluid sulfur and the lighter metasedimentary sulfur.

At the Mount Dore and Merlin deposit and the Lanham's Shaft prospect the Cu-rich mineralization was followed by the adding of a Mo-rich igneous felsic derived fluid which also reacted with the host rocks and therefore also displays a mix sulfur isotopic signature between igneous sulfur values and the metasedimentary host rocks values.

At the Mount Dore and Merlin deposit a secondary event occurred, due to the emplacement of the Mount Dore granite, which consisted of the minor remobilization of previously formed Mo-Re mineralization with maintenance of the molybdenite sulfur isotopic signatures.

7. Chapter 7: Sulfide trace element geochemistry

7.1. Introduction

The use of trace elements in sulfide minerals for understanding ore genesis processes is a field that is still in its infancy, as relevant analytical techniques have only recently been developed and ore systems are often highly complex. The most frequent use in sulfides has been to distinguish different crystal zones, and/or mineralization stages in order to characterize different generations or possibly connect the mineralization stages to geologic events (e.g. Large et al., 2009).

The understanding of trace element geochemistry of sulfides varies from species to species, with pyrite being the most well understood sulfide, as it is ubiquitous in most ore systems (e.g. Huston et al., 1995; Large et al., 2009). On the other hand, the understanding of trace element geochemistry of molybdenite is very limited, being mostly concerned with rhenium (e.g. Berzina et al., 2005). When dealing with trace elements geochemistry in ore deposit sulfides, there are several parameters that need to be addressed. The first concern is the common presence of micrometric inclusions. Since ore systems commonly have co-existing sulfide species, it is very common to have inclusions of other sulfides, as well as the inclusions of gangue minerals (e.g., silicates, oxides). Laser ablation ICP-MS recording of significant levels of Cu, Zn, Pb, Ba, Bi, Ag, Sb in pyrite crystals and Pb, Bi, Zn, and Ba in chalcopyrite commonly represents sampling of micro-inclusions (Huston et al., 1995). Due to the co-existence of sphalerite, galena, chalcopyrite, pyrite, and molybdenite in the Mount Dore and Merlin deposit, all the composing elements of these minerals and their common inclusions can appear in each of the three sulfides (pyrite, chalcopyrite, and molybdenite) analysed. The presence of inclusions can in itself be of scientific importance in distinguishing mineralization stages (e.g. Large et al., 2009).

The other reason for significant concentrations of certain elements in the sulfide species are as substitutes for major elements. There are a range of parameters that influence element substitution into crystal lattices, including physicochemical conditions of the sulfide formation, and charge, size, and availability of the ions. In general the main element substitutions are: Ag can substitute for Cu in chalcopyrite; In and Sn for Fe in chalcopyrite; Co and Ni for Fe in pyrite; Re (and W) for Mo in molybdenite; and Se and Te for S in all three minerals (e.g. Huston et al., 1995).

Rhenium is an obviously important element to consider in a deposit such as the Mount Dore and Merlin since Re and Mo are considered to be geochemical twin elements (i.e., they share very similar ionic charge and radius; Shannon, 1976). Most studies have been done on porphyry type deposits, and the classical view holds that Re concentrations in these deposits are controlled by the relative amounts of molybdenite in the deposit (Giles and Shilling, 1972; Newberry, 1979; Stein et al., 2001). Although this view seems to hold true for porphyry deposits, other factors such as the metal source, Re concentration of the mineralizing fluid, composition of the igneous melt, temperature, pressure, $fO2$, pH, Cl activity, should not be ignored (e.g. Berzina et al., 2005, and references therein).

Selenium and tellurium are very useful and important elements in sulfide geochemistry studies since Se is a geochemical twin element of S, and Te also frequently substitutes for S in sulfides (Shannon, 1976; McPhail, 1995; Helmy et al., 2007; Barnes et al., 2009). There is strong correlation between Se, Te, and S in Primitive mantle estimates, upper mantle rocks, basalts and sulfides (Hattori et al., 2002; Rose-Weston et al., 2009; Jenner and O'Neill, 2012), which means that the Se and Te display similar behaviour and follow the S content in natural materials. Therefore the variation in the ratios of S/Se and S/Te in natural materials, and therefore also in sulfides, is mostly dependent of the physicochemical conditions of the mineralizing fluid from the source to precipitation (Yamamoto, 1976; Howard, 1977; Huston et al., 1995; Hattori et al., 2002; Xiong et al., 2003; Fitzpatrick, 2008; Layton-Matthews et al., 2008; Rose-Weston et al., 2009; Helmy et al., 2010; Jenner et al., 2010), and in the possible preferential incorporation of S, Se, and Te from the host rocks to mineralization (e.g. Queffurus and Barnes, 2014). If the conditions of a fluid do not change from source to sink, the S/Se and S/Te ratios will be maintained and the minerals that precipitate from that fluid will have the same ratios to the initial fluid. In all cases, the physicochemical conditions of a fluid changes from source to sink, which may modify the S/Se and S/Te ratios. Sulfur, Se, and Te have been used in several studies such as: Earth differentiation (e.g. Rose-Weston et al., 2009), igneous processes often connected to ore deposit generation (e.g. Metrich and Clocchiatti, 1996; Hattori et al., 2002; Helmy et al., 2010; Jenner et al., 2010), experimental and natural studies of ore genesis (e.g. Yamamoto, 1976; Howard, 1977; McPhail, 1995; Huston et al., 1995; Xiong et al., 2003; Helmy et al., 2007; Fitzpatrick, 2008; Layton-Matthews et al., 2008; Barnes et al., 2009), and even as protolith pathfinders in weathered profiles (Malisa, 2001) and as indicators of paleoredox conditions of marine systems (Johnson and Bullen, 2004). In ore systems these ratios have not been greatly explored due to the analytical difficulty of obtaining accurate values of Se

and Te (e.g. Fitzpatrick, 2008). The recent ability of using LA-ICP-MS in sulfide geochemistry is rapidly enhancing our understanding of these processes (e.g. Fitzpatrick, 2008).

Selenium and tellurium concentrations in pyrite are higher with decreasing temperature, and higher pH and fO_2 (Hsu, 1977; McPhail, 1995; Huston et al., 1995; Metrich and Clocchiatti, 1996; Johnson and Bullen, 2004; Jenner et al., 2010). The temperature is able to strongly vary the content of Se in pyrite at temperatures from 300° to 50°C (Huston et al., 1995). Unfortunately, thermodynamic calculations on the effect of temperature in ore deposits have been mostly done in VMS type deposits which are typically formed at temperatures $<350^{0}$C and it is therefore difficult to estimate the temperature effect at higher temperatures (e.g. McPhail, 1995; Huston et al., 1995; Fitzpatrick, 2008).

Both the Se and Te contents in sulfides decrease with increasing pH at low temperatures (150^{0}C – 250^{0}C) (McPhail, 1995; Huston et al., 1995). This increase can be of an order of magnitude for higher pH conditions but it is mostly negligible for neutral and more acidic fluids (McPhail, 1995; Huston et al., 1995).

Assimilation of sulfur from metasedimentary wall rocks by the mineralizing fluid can also change the S/Se and Te/Se ratios of the systems, and hence the precipitated sulfides (e.g. Queffurus and Barnes, 2014). High S/Se values typically reflect basinal or evaporitic sources while low S/Se ratios are typical of magmatic sources (e.g. Fitzpatrick, 2008). It is important to note that the granitic rocks have typically much lower contents of Se relative to sedimentary rocks. The reason for the high S/Se ratios of basinal or evaporitic derived fluids is due to the fractionation of the S/Se during sedimentary processes, with the evaporites and rich in organic matter sediments sequestering S preferentially (e.g. Malisa, 2001).

Oxygen fugacity is considered the most important parameter affecting S/Se ratios of sulfides (Metrich and Clocchiatti, 1996; Jenner et al., 2010). The S/Se ratio in pyrite decreases with increasing fO_2 (McPhail, 1995; Huston et al., 1995; Metrich and Clocchiatti, 1996; Johnson and Bullen, 2004; Jenner et al., 2010).

Tungsten is another important element that appears associated with molybdenite mineralization in several ore deposits (e.g., skarns), which, depending on the oxidation state, can substitute for Mo (e.g. Hsu, 1977; O'Neill et al., 2008). Molybdenum and tungsten are high field strength elements and thus tend to be incompatible during igneous fractionation processes (e.g. Mutschler et al., 1981).

7.1.1. S/Se and W/Mo ratios variation as a function of fO_2

Sulfur, Se, Mo, and W change their valence state as a function of fO_2, and since the valence state determines their compatible or incompatible behaviour, the fO_2 conditions during ore genesis processes will determine the amount being transported in the fluid and their precipitation. Most authors assume Mo^{4+} and W^{4+} in sulfide and Mo^{6+} and W^{6+} when transported in the fluid (Hsu, 1977; Rempel et al., 2009). Sulfur and selenium behave similarly with variation of their valence state for the fO_2 range of natural rocks, from S^{2-} and Se^{2-} in sulfides and S^{6+} and Se^{6+} when transported in the fluid (e.g. Jenner et al., 2010). Therefore, the S/Se and W/Mo ratios in ore minerals have the potential to monitor the fO_2 conditions in ore genesis processes.

Therefore, the fractionation between S/Se and W/Mo can be evaluated for fO_2 and represented schematically (Fig. 7:1). The schematic illustration of S/Se and W/Mo are based on thermodynamic calculations at different temperatures (Hsu, 1977; McPhail, 1995; Huston et al., 1995; Metrich and Clocchiatti, 1996) and re-calculated for fO_2 relative to fayalite-magnetite-quartz buffer (FMQ). These calculations are translated into the schematic drawing (Fig. 7:1) where the behaviour of S/Se and W/Mo can be interpreted relative to the oxidation state of the hydrothermal fluid during ore genesis. The Y-axis shows the amount of selenate and sulfate over the total of selenium and sulfur from 0, where all the selenium and sulfur are in the form of selenide and sulfide, to 1, where the formers are on the form of selenate and sulfate. The X-axis shows the values of fO_2 relative to (FMQ). This schematic representation shows the curved line that separates the stability fields between both sulfate/sulfide and selenate/selenide in respect to fO_2. The change in oxidation state of sulfur and selenium occur at different relative fO_2 (FMQ), which means that for constant pH and temperature:

- A theoretical fluid with S/Se that is formed at relative fO_2 FMQ +6 and precipitates a sulfide at relative fO_2 FMQ -2 will maintain the initial S/Se ratio.
- If the same fluid precipitates a sulfide at relative fO_2 FMQ +2 the S/Se ratio of the sulfide will be lower since S is still mostly in the sulfate stability field while the Se is mostly in the selenide field.
- If a different theoretical fluid is formed at relative fO_2 FMQ +2 and precipitates a sulfide at relative fO_2 FMQ-0 the S/Se ratio of the sulfide will be higher than the initial fluid ratio because the fluid when formed was mostly in the stability field of selenide and sulfate.

Figure 7:1 is interpreted in the same manner as for S/Se except that the fO_2 curves are at higher values of relative fO_2 (FMQ).

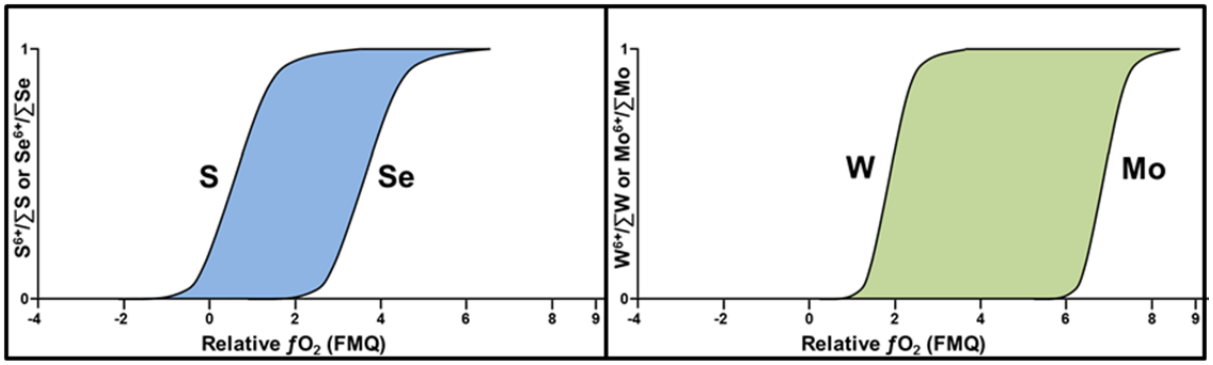

Figure 7:1 – Schematic diagrams showing the predicted lower Se6+/ΣSe and Mo6+/ΣMo with increasing $fO2$ relative to FMQ. Diagrams adapted and calculated based on the work by Hsu (1977); Cygan and Chou (1987); Metrich and Clocchiatti (1996); Jenner et al. (2010).

The trace element geochemistry in sulfides of both the Mount Dore and Merlin deposits and the Lanham's Shaft prospect was conducted to determine: 1. The geochemical characterization and distinction of mineralization stages, and 2. The physicochemical conditions of the mineralizing fluid during ore genesis processes.

7.2. Sample description and results

7.2.1. Trace element geochemistry of sulfides: sampling and results

In this study, trace elements analyses were conducted in chalcopyrite, pyrite and molybdenite of the Mount Dore and Merlin deposit and in pyrite and molybdenite of the Lanham's Shaft prospect. All analyses were conducted *in situ* from polished thin sections by laser ablation ICP-MS, as described in Chapter 1. Representative samples of both Cu-rich and Mo-rich mineralization stages from the Mount Dore and Merlin were analyzed. In both mineralization stages the samples selected were intended to cover the different mineralization styles of each stage in different host rocks and ore deposit zones. For instance, the chosen samples with Mo-Rich mineralization comprise the spread of mineralization styles: infill of matrix-supported breccias with rounded clasts; veins; stylolitic veins; and disseminations (Table 7:1). Overlap between the trace element analyses and other data sets was also partly achieved, in particular with sulfur isotope, Re-Os age dating, and the Mo-rich sample used for Sm-Nd isotope studies in apatite crystals (Table 7:1).

At the Lanham's Shaft prospect the same reasoning was applied although with less complexity due to the Cu-rich and Mo-rich mineralization being located in the same lithology. These studies were intended to determine the geochemical characteristics of the different mineralization stages and styles, to compare the similar mineralization between the deposit and the prospect, and also to better understand ore precipitation mechanisms.

Seven polished sections and two 'buttons' from different drillhole core samples were selected from the Mount Dore and Merlin deposit for laser ablation analyses of sulfides. In addition, six polished sections were also selected from the Lanham's Shaft prospect for the same purpose. The analytical procedure spanned a three year period with a total of 193 separate analyses for the Mount Dore and Merlin deposit and 99 for the Lanham's Shaft prospect. More than one sulfide was analysed in the same sample wherever possible (Table 7:1).

The comprehensive trace element suite that was analysed in the sulfides includes, Si, P, Ti, V, Cr, Mn, Fe, Co, Ni, Cu, Zn, As, Se, Sr, Zr, Nb, Mo^{95}, Mo^{97}, Ag, Cd, In, Sn, Sb, Te, Ba, W, Re, Pt, Au, Tl, Pb, and Bi. Elements such as Sr, Zr, Ti, P, and Si were included to monitor mineral inclusions. Further details on the LA-ICP-MS trace element analysis can be consulted in Chapter 1 and the tables with the results are in Digital Appendix.

The results were interpreted cautiously due to analytical complexities such as ablating through the crystal into other mineral and micrometric inclusions. All elements were considered and graphically analysed.

The pyrite grains show high contents of Co and As, and moderate to high contents of Pb, Cu, Zn, and Ni. Se and Te contents are variable between samples. The pyrite of the Lanham's Shaft prospect displays higher values in Se, Te, W, and Ni relative to pyrite from the Mount Dore and Merlin deposit. Molybdenite of both localities has low to high values of W, Se, and Te, dependent on sample and case study, with the Lanham's Shaft prospect displaying higher values in all three elements. The chalcopyrite of the Mount Dore and Merlin deposit shows low contents of Co, As, Ni, and moderate amounts of Zn, Ag, Pb.

The elements of focus for presentation and discussion are Se, Te, W, Ag, Zn, Pb, and Re. Selenium and Te are relevant in molybdenite and pyrite, W was used for molybdenite, and the remaining elements are particularly relevant in chalcopyrite. Selenium data are presented as S/Se ratios, where the sulfur was calculated by mineral stoichiometry. The Re and W concentrations in molybdenite were used to differentiate the Mo-rich mineralization between the Mount Dore and Merlin deposit and the Lanham's Shaft prospect. The S and Te in pyrite, and W in molybdenite, were chosen because their concentrations in sulfides is

controlled by the physicochemical conditions of the fluid, in particular the fO_2, (e.g. Hsu, 1977; Jenner et al., 2010) and can therefore be used to interpret fluid evolution and ore precipitation mechanisms. The reason for the relevance of Ag, Zn, and Pb in the chalcopyrite of the Mount Dore and Merlin deposit, besides the already mentioned frequent substitution of Cu by Ag (e.g. Huston et al., 1995; Large et al., 2009), is the common association of chalcopyrite with galena and sphalerite, especially in the Cu-polymetallic mineralization zone.

Table 7:1 – Drillholes codes and depths of samples analysed by LA-ICP-MS for trace elements geochemistry in sulfide minerals with the number of spot analyses and sulfide species analysed, mineralization style short description; and $\delta^{34}S$ values and age dates when available. n.d. (no data).

Drillhole	Depth (m)	# analyses by sulfide type	Mineralization style	$\delta^{34}S$ (‰)	Re-Os Dating (Ma)
MDQ0132	355.40	Mo (20)	Breccia infill	Mo -2.3	1529/1534
MDQ0150	170.80	Mo (21) Py (15)	Breccia infill & disseminated	Mo -1.8 Py -2.7	1539/1541/ 1533
MDQ0235	175.00	Mo (13)	Breccia infill & disseminated	Mo -2	n.d.
MDQ0252	393.40	Mo (10) Py (9) Cpy (13)	Vein	Mo -2.2	n.d.
MDQ0252	459.65	Mo (12) Py (15)	Vein	Mo 1.4	1521
MDQ0252	487.90	Mo (16)	Stylolite	Mo -3.2	1520
MDQ0132	376.30	Mo (15)	Stylolite & Disseminated	Mo -2.6	n.d.
MDQ0222	403.20	Py (8) Cpy (8)	Carbonate breccia	Py 2 Cpy 1.9	n.d.
MDQ0221	351.20	Cpy (18)	Carbonate vein Breccia	Cpy 2.8	n.d.
LAD0001	158.50	Mo (10)	Carbonate vein	Mo -5.90	1559
LAD0002	118.00	Mo (8)	Carbonate vein	n.d.	n.d.
LAD0002	122.60	Mo (11)	Small veins	Mo -3.0	n.d.
LAD0002	119.30	Mo (20) Py (20)	Small veins	Mo -6.9	1560
LAD0002	144.85	Py (15)	Network of veins	Py 2.3 Cpy 3.1	-
LAD0001	178.50	Py (15)	Disseminated	-	-

For the Mount Dore and Merlin deposit the W and Te results of molybdenite were plotted against the S/Se ratio (Fig. 7:2). The W versus S/Se graph shows the two representative samples of the matrix-supported with rounded clasts mineralized breccias with a distinct slope relative to the remaining samples which are representative of the vein, stylolites, and disseminations mineralization stage. Both mineralized breccia samples are dated by Re-Os and consist of the older molybdenite (~1535 Ma), while two of the five remaining samples yielded ~1520 Ma ages.

In the Te versus S/Se plot the same geochemical distinction between mineralization styles is apparent although not as pronounced, with the older dated samples showing higher values of S/Se with the exception of one sample. This sample was used in the Sm-Nd study (Chapter 6). The Te values show a similar difference between the younger Mo mineralization, with slightly higher values, relative to the older Mo mineralization.

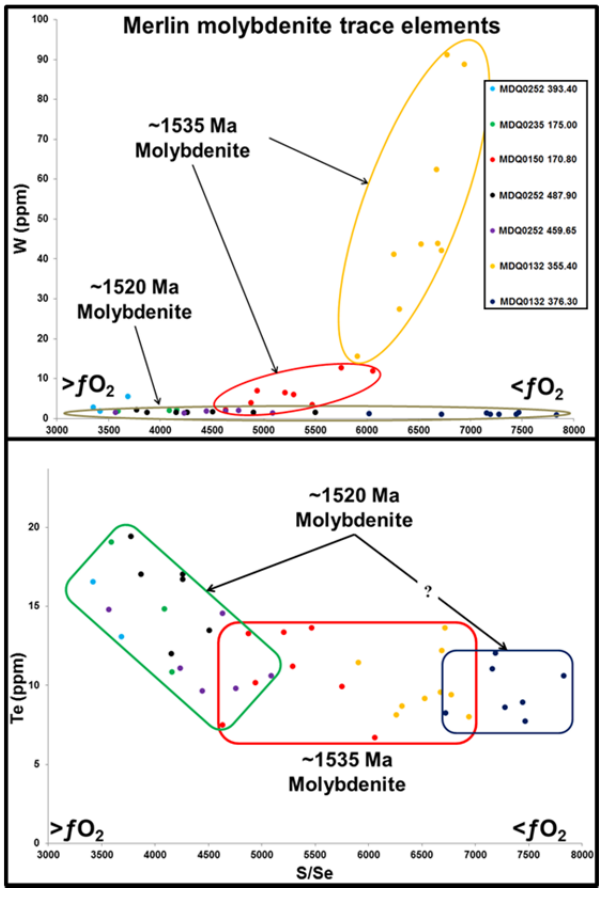

Figure 7:2 – Tungsten and Te versus S/Se ratios of molybdenite mineralization of 7 samples from the Mount Dore and Merlin deposit. Colour ellipses highlight mineralization types and Re-Os age dating. The annotations > < fO_2 indicate the higher and lower oxygen fugacity relative to the S/Se ratios, respectively (see discussion for details). Sample and ellipses color are the same for samples where more than one sulfide was analysed (see Fig. 7:3 and 7:4).

The trace element geochemistry of pyrite at the Mount Dore and Merlin deposit was plotted using Mo and S/Se ratios (Fig. 7:3). Three geochemically distinct groups were defined, with one sample consisting of pyrite co-precipitating with breccia infill molybdenite (Fig. 6:7c –

Chapter 6), another sample is of pyrite that has reacted strongly with molybdenite in a vein (Fig. 6:7a – Chapter 6), and the remaining two samples are of pyrite associated with chalcopyrite of the Cu-polymetallic stage and pyrite associated with chalcopyrite being cut by a molybdenite vein. Pyrite that co-precipitated with the older molybdenite mineralization has high values of S/Se and Mo. The pyrite that reacted with a molybdenite vein displays low values of S/Se and Mo. The other two samples show similar values of S/Se to the former and similar Mo values to the latter.

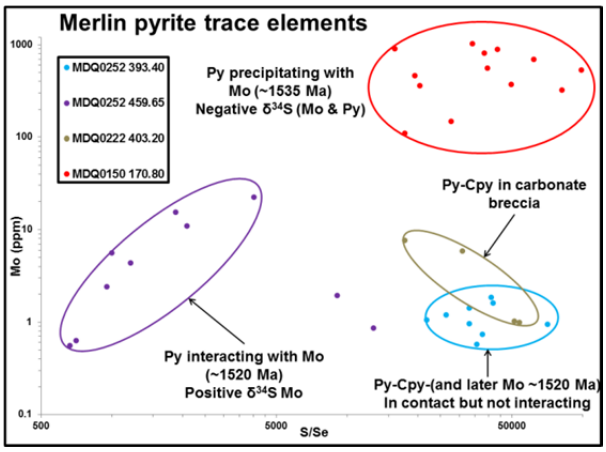

Figure 7:3 - Molybdenum versus S/Se ratios of pyrite mineralization of 4 samples from the Mount Dore and Merlin deposit. Coloured ellipses highlight mineralization types, Re-Os age dating, $\delta^{34}S$ data, and interaction with other sulfides. Sample and ellipses color are the same for samples were more than one sulfide was analysed (see Fig. 7:2 and 7:4).

The chalcopyrite trace element geochemistry was only conducted in three representative samples of the Mount Dore and Merlin deposit (Fig. 7:4); chalcopyrite associated with Na-(Ca) alteration in banded calc-silicate rocks located a few metres below the Mo-Re mineralization zone; chalcopyrite associated with the Cu-polymetallic stage as infill of angular clasts carbonate breccia; and chalcopyrite being cut by a molybdenite vein. The three samples are geochemically distinct as illustrated by Zn, Pb, and Ag variations in Figure 7:4. The chalcopyrite that appears associated with molybdenite mineralization displays the lowest values of Ag and relatively low values of Zn and Pb, in a well constrained cluster. The chalcopyrite analysed from banded calc-silicates have well constrained values of Zn, which are the lowest of the three samples, and Ag. The Pb values on this sample show a bigger spread of values. The Cu-polymetallic chalcopyrite displays a scatter of values in all three elements.

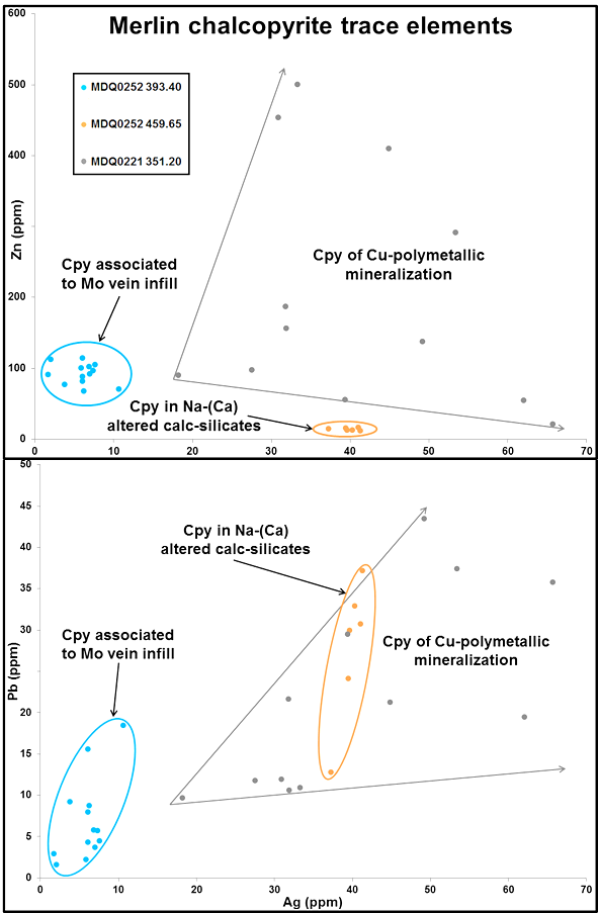

Figure 7:4– Zinc, Pb and Ag geochemistry of chalcopyrite mineralization of 3 samples from Mount Dore and Merlin deposit. Colour shapes and arrows highlight each chalcopyrite sample and colors are the same for samples where more than one sulfide was analysed (see Figs. 7:2 and 7:3).

From the six polished sections selected from the Lanham's Shaft prospect, only three were analysed for just molybdenite, two were used for pyrite analyses, and the remaining sample for both molybdenite and pyrite (Fig. 7:5). Two different molybdenite mineralization styles were defined, that consist of thicker and thinner mineralized veins. Both types of veins have similar mineral assemblage. It is important to note that the wider veins contain more abundant molybdenite mineralization relative to the thinner veins. The pyrite samples consist of one sample being composed of a vein network with pyrite and minor quartz infill; another sample displaying disseminations of pyrite of both sides of a sharp contact between carbonaceous slates and calc-silicate rocks; and the last sample consists of pyrite associated with a thin molybdenite vein. Both mineral results were plotted using Te versus S/Se ratios and in the case of the disseminated pyrite sample the analyses done on the carbonaceous slates side are displayed separately from the ones conducted on the calc-silicate side (Fig. 7:5).

The molybdenite trace element results show a geochemical distinction between the molybdenite present in the wider veins and the molybdenite in the thinner veins, with the smaller veins of molybdenite displaying higher values of Te and lower of S/Se (Fig. 7:5).

The pyrite results show a similar trend with the samples higher in Te being the lowest in S/Se. The sample where both molybdenite and pyrite were analysed display for both minerals the lowest S/Se values and higher Te. The pyrite in the vein network and the disseminated crystals in the calc-silicate rock side of the sample, which has two rock types in sharp contact, display well constrain medium values. The pyrite crystals that have the highest S/Se values and mostly lower Te values are the disseminations hosted in the carbonaceous slate side of the sharp contact sample.

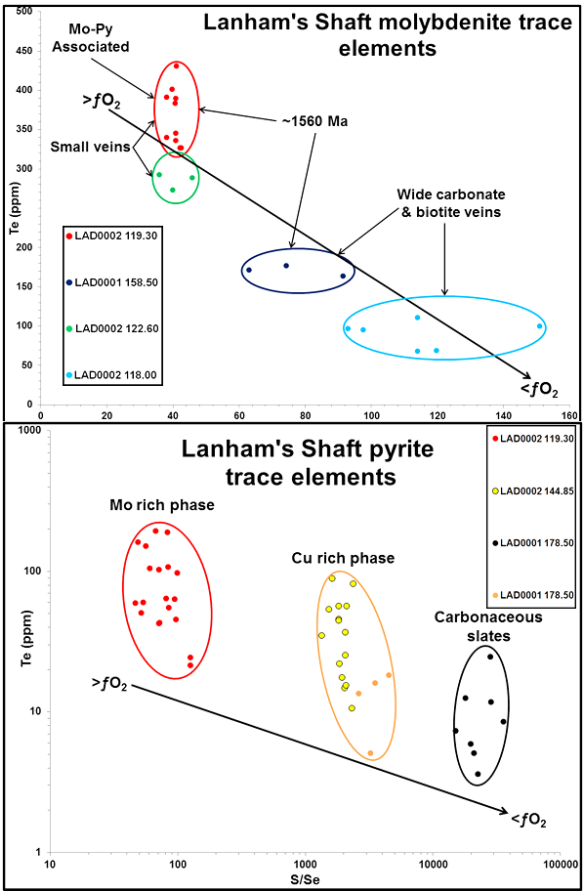

Figure 7:5 – Tellurium versus S/Se ratios of 4 molybdenite samples and 3 pyrite samples from the Lanham's Shaft prospect. The annotations > < fO_2 indicate the higher and lower oxygen fugacity relative to the S/Se ratios and Te content, respectively (see discussion for details). Coloured ellipses highlight mineralization types, Re-Os age dating, and interaction with other sulfides. Sample and ellipses color are the same for samples where more than one sulfide was analysed.

The values of Re are of great interest due to the high grades present at the Mount Dore and Merlin deposit, and because of the affinity between the Mo and Re. The very high values of Re are significant although the Re content of the various molybdenite analysed in both localities shows no significant variation between samples (Fig. 7:6).

Several elements, such as Se, Te, and W can be used to differentiate the molybdenite mineralization of the Mount Dore and Merlin deposit from the Lanham's Shaft prospect mineralization (Fig. 7:6). The Re content of the Mount Dore and Merlin deposit is typically much higher than the mineralization at the Lanham's Shaft prospect, although several spot analyses overlap. The W content trends the opposite way with the Lanham's Shaft prospect

molybdenite having higher values than the mineralization at the Mount Dore and Merlin deposit. The same previous distinction between the older molybdenite mineralization and younger molybdenite at the Mount Dore and Merlin deposit is apparent with the W values (Figs. 7:2 and 7:6). The Re and W values of the dated molybdenite at the Lanham's Shaft prospect are well constrained and consistent between the two samples analysed (Fig. 7:6).

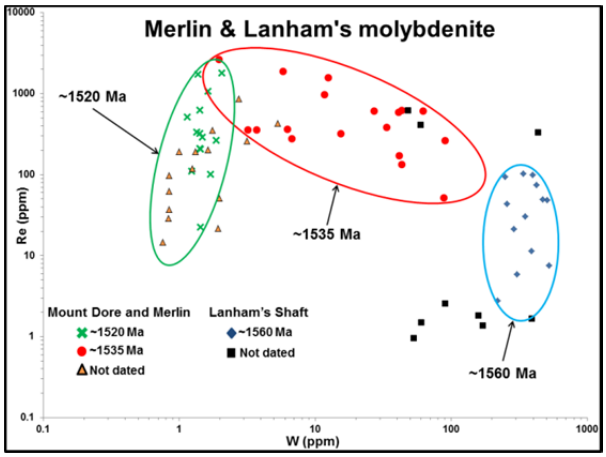

Figure 7:6 – Rhenium versus W of all samples analysed from the Mount Dore and Merlin deposit and the Lanham's Shaft prospect. Both localities samples highlighted, showing samples with and without corresponding age dates.

7.3. Discussion

7.3.1. Trace element geochemistry characterization of mineralization stages

Molybdenite

The petrographic characterization of the different Mo-Re mineralization styles has defined the bulk of this mineralization as the infill of matrix-supported breccias with rounded clasts. This mineralization style is dated at ~1535 Ma, which predates the ~1520 Ma mineralization stage that consists of vein infill, commonly stylolitic, and disseminations. Although these distinct mineralization styles display similar sulfur isotope signatures they are chemically distinct as shown by their content of W and S/Se ratios (Fig. 7:2). The same differentiation between mineralization styles is apparent with the S/Se ratios, with the exception of one sample (Fig. 7:2).

At the Lanham's Shaft prospect two molybdenite mineralization types were distinguished (Fig. 7:5). The molybdenite mineralization types were formed during the same mineralization stage with one sample dated from each type yielding the same Re-Os date (~1560 Ma). The chemical distinction between these two types is connected to the size of the molybdenite mineralized veins and the amount of molybdenite it contains, as the mineral assemblage present in both vein types is similar.

Pyrite

The trace element geochemistry of pyrite in the Mount Dore and Merlin deposit allows distinguishing different pyrite stages, based on their Mo content and S/Se ratios (Fig. 7:3). Three different pyrite groups were henceforth defined and correlated to sulfur isotopic signatures of associated pyrite and/or molybdenite. The three pyrite groups defined with trace element geochemistry and textural observations at the Mount Dore and Merlin deposit consist of:

1) Pyrite associated with Cu-rich mineralization in both the carbonaceous slates and the much less abundant and sparse Cu-rich mineralization in the calc-silicate rocks well below the main mineralization zones.
2) Pyrite co-precipitating with the older molybdenite mineralization, which comprises the bulk of the Mo-Re in the system. This pyrite stage is minor.
3) Pyrite that shows textural and chemical evidence of being dissolved by the younger Mo-Re mineralization stage. This Py-Mo reaction was rare in the deposit.

Most of the pyrite in the deposit occurs in the Cu-rich mineralization in carbonate breccias. This pyrite has the typical sulfur isotopic signatures of the Cu-rich mineralization (see chapter 6 for details) and although can appear associated with molybdenite mineralization, (e.g., sample MDQ0252 393.40), textural evidence indicates that the molybdenite was formed during a later mineralization event.

The sample that yields the highest Mo values consists of pyrite that co-precipitated with the molybdenite mineralization (Fig. 6:7 c – Chapter 6). The molybdenite mineralization in question belongs to the older stage and the sulfur isotope values conducted in both molybdenite and pyrite in this sample are negative, which is typical of the molybdenite mineralization signatures.

The third chemically distinct pyrite generation is associated with molybdenite that is representative of the drillhole core section where three samples yielded the only positive sulfur isotope values of molybdenite in the Mount Dore and Merlin deposit (Fig. 6:2 e – Chapter 6). This molybdenite was also dated by Re-Os, and analysed for trace elements and displays no significant chemical differences to the younger Mo stage. Interestingly, the minor pyrite that appears associated with this particular molybdenite shows textures of having strongly reacted with the later molybdenite mineralization (Fig. 6:7 a – Chapter 6). The textural observations together with the trace element data indicate that the molybdenite in this

particular core section has inherited sulfur from this pyrite, which resulted in the positive sulfur isotope values of the molybdenite and the lower S/Se ratios measured in the pyrite of the same sample (Figs. 7:2 and 7:3). Two of the spot analyses show S/Se ratios that are closer to the Cu-rich mineralization pyrite, which probably reflects the pyrite crystals cores, indicating that the original chemistry was similar to the main pyrite stage. The reason for this anomalous reaction between pyrite and molybdenite is probably connected with the host rocks (see Chapter 6 for details) and it represents the exception in this deposit, being the rule the low chemical reaction between the main Cu-rich mineralization and the subsequent Mo-Re mineralization stages.

The pyrite samples analysed at the Lanham's Shaft prospect defined three different pyrite groups (Fig. 7:5). The disseminated pyrite hosted in carbonaceous slates and the Cu-rich associated pyrite are interpreted as concomitant, with the Se and Te content difference interpreted to be host rock controlled. The molybdenite associated with pyrite has higher Te content and lower S/Se ratios, and is considered as a different generation to that which was formed during the Mo-rich mineralization stage.

Chalcopyrite

The Mount Dore and Merlin chalcopyrite trace element geochemistry was conducted in 3 samples that are distinct in their trace element geochemistry (Fig. 7:4). The sample with the lowest values of Ag and Pb in chalcopyrite is associated with pyrite and molybdenite, where the molybdenite is considered to have been formed at a later stage relative to the chalcopyrite based on textural observations and sulfur isotope data (see Chapters 3 and 6 for details). It is therefore reasonable to infer that the chalcopyrite that is associated with the molybdenite has precipitated from a fluid that was relatively low in Pb, Ag and Zn.

The reason for the scattering of values of Zn, Pb, and Ag in the representative sample of the Cu-polymetallic stage chalcopyrite is mostly due to micrometric inclusions that resulted from the co-precipitation of sphalerite, galena, and pyrite.

The third sample of chalcopyrite is associated with pyrite below the main mineralization zones in Na-(Ca) altered calc-silicate rocks. This chalcopyrite has very low values of Zn and medium to high values of Pb and Ag relative to the other two samples.

All three chalcopyrite types are interpreted to have formed during the same mineralization stage, as supported by the textural observations (see Chapter 3 for details), and sulfur isotopes (see Chapter 6 for details), so the differences in their geochemistry are

interpreted to be related to their location in the deposit. The Zn is strongly connected to the carbonaceous slates, likely being mostly sourced from those rocks where it precipitates forming the polymetallic mineralization together with chalcopyrite, pyrite and galena. The chalcopyrite that is formed below the polymetallic mineralization in altered calc-silicate rocks, which has low but still significant amounts of Pb and Zn, is mostly clean of micrometric inclusions because it was formed with neither sphalerite nor galena.

The chalcopyrite that was formed in the least altered calc-silicate rocks which has very low amounts of Zn and medium to high values of Pb and Ag is interpreted to have been formed in host rocks that were Pb and Ag rich but Zn poor, being in concordance with the Zn being sourced from the carbonaceous slates.

It is put forward that the copper bearing fluids sourced the Zn from the carbonaceous slates. The Pb and Ag were partly sourced from the carbonaceous slates and also from the less altered calc-silicate rocks located below the mineralization.

7.3.2. Physicochemical conditions of the mineralizing fluid

There are several factors when considering the S/Se system in sulfides such as, fluid source S/Se ratios, inheritance of host rock sulfur, pH, fO_2, and temperature.

The temperature and the pH are considered to have a minor effect on the S/Se and W/Mo ratios variation during ore genesis at the Mount Dore and Merlin deposit and at the Lanham's Shaft prospect. Previous studies are difficult to extrapolate for the conditions of these two localities, both due to strong inconsistencies in the thermodynamic calculations of different authors and because such calculations were done mostly under conditions of lower temperature and pH (McPhail, 1995; Huston et al., 1995). The temperatures of the Mount Dore and Merlin and the Lanham's Shaft hydrothermal systems are 450-580^{0}C and 400-500^{0}C, respectively (see Chapters 3 and 4) so it is therefore reasonable to consider that the fractionation of S/Se due to temperature changes is minor, since the temperature is high and the range is small (McPhail, 1995; Huston et al., 1995). Similarly, although there is little to no information on the effect of pH at higher temperatures, considering that the typical IOCG environments are neutral to mildly acidic, and rarely acidic (Richards and Mumin, 2013), it is reasonable extrapolate from the work of McPhail (1995) and Huston et al. (1995) that the pH effect on the fractionation of these elements is also minor. Although the pH difference between the calc-silicate rocks and carbonaceous slates might be substantial and possibly

have an effect on the ore genesis processes the trace element data strongly indicates that variation in the fO_2 conditions is the main ore genesis process in these mineralizing systems.

As discussed in the previous chapter, the fluid source for the Cu-rich mineralization is interpreted to be bittern brine, while the Mo-Re mineralization is of felsic igneous origin, for both the Mount Dore and Merlin deposit and the Lanham's Shaft prospect. A reasonable assumption that can be made about the S/Se ratios of the initial fluids is that the typical S/Se ratios for a felsic igneous rock are lower than the S/Se ratios of sedimentary rocks (e.g. Malisa, 2001). See below for further discussion.

The $\delta^{34}S$ values of molybdenite, pyrite and chalcopyrite from the Mount Dore and Merlin deposit and the Lanham's Shaft prospect, as discussed in the previous chapter, are indicative of sulfur exchange between the mineralizing fluids and the metasedimentary host rocks in both the Mo-rich and the Cu-rich mineralization stages. Therefore, absorption of S and Se by the fluid from the host rocks is an important factor to consider in the interpretation of the trace element data. Nevertheless, when considering the S/Se ratios in the Cu-rich and Mo-rich mineralization of both localities coupled with the Mo/W systematics in order to extrapolate mechanism/s of mineral precipitation, it is reasonable to assume that the S-Se and Mo-W systematics are indicative of the fO_2 conditions during ore genesis processes.

The chemical interaction between the host rocks and the mineralizing fluid, with metasedimentary sulfur absorption, is the mechanism by which the fO_2 of the fluid changes. Since the variation of S/Se ratios by absorption of S and Se from the host rocks impacts the S/Se ratios in the same manner as a drop in the fO_2, both chemical changes are considered as being driven by the same mechanism of fluid-rock reaction. Therefore, it is possible to use both the S-Se and the Mo-W systems relative to fO_2 variations to interpret the trace element results (Fig. 7:7). Similarly, changes in the pH conditions would be driven by the same mechanism, although it is considered as a less important factor than the fO_2 in the ore genesis of the Mount Dore and Merlin deposit and the Lanham's Shaft prospect.

The bulk of the Mo-Re mineralization at the Mount Dore and Merlin deposit (~1535 Ma, breccia-hosted) is considered to have been formed at lower fO_2 conditions relative to the younger (~1520 Ma) vein and disseminated Mo-Re mineralization. The sample that is the exception with the highest S/Se ratio values, and therefore indicative of the lowest fO_2 conditions of all the molybdenite samples analysed, is hosted in carbonaceous slates that, although they are intensely altered, still display dark bands with minor graphite (Fig. 6:6e – Chapter 6). Although it is not rare to find locations in the deposit where the Mo-Re hydrothermal system did not completely alter the metasedimentary mineral assemblage it is

not frequent and even less so in the carbonaceous slates. Since this sample has similar mineralization style and similar W contents to the younger dated molybdenite, it is interpreted as typical Mo-Re of the ~1520 Ma mineralization stage, and therefore only the fO_2 conditions at the time of ore precipitation are considered exceptional due to a relatively strong buffering of fO_2 by the host rock.

At the Lanham's Shaft prospect the trace element systematics of the thinner molybdenite veins indicate higher fO_2 conditions upon formation, relative to the wider veins that are more strongly mineralized at the prospect. The trace elements in the sample with pyrite associated with molybdenite also indicate that this pyrite generation was formed at higher fO_2 being in concordance with the molybdenite chemistry of the same sample. Pyrite from the Cu-rich mineralization shows higher S/Se ratios than the Mo-associated pyrite but lower than the pyrite formed in the carbonaceous slates (Fig. 7:13). The fact that the pyrite hosted by carbonaceous slates displays the lowest fO_2 agrees well with the reduction potential of those rocks that contain graphite. It is important to note that there are two chemically different pyrite groups in that same sample, which is a contact sample between carbonaceous slates and calc-silicate rocks. The pyrite on the side of the altered calc-silicates shows the same S/Se values as the Cu-rich associated pyrite (Fig. 7:13).

The following discussion is based on the diagrams presented in Figure 7:7 which were calculated and schematically drawn based on work done by Hsu (1977), Fitzpatrick (2008), Helmy et al. (2010), and Jenner et al. (2010). This way it is possible to combine the trace element data from the Mount Dore and Merlin deposit and Lanham's Shaft prospect and compare mineralization within one system and between both systems. It is important to note that the diagrams are used for qualitatively interpreting ore genesis, as no quantitative constraints on fO_2 values for these conditions currently exist (Hsu, 1977; Metrich and Clocchiatti, 1996; Johnson and Bullen, 2004; Jenner et al., 2010).

The bulk of the Cu-rich mineralization at the Mount Dore and Merlin deposit is characterized by higher S/Se ratios relative to the Cu-rich mineralization at the Lanham's Shaft prospect. These ratios at the Mount Dore and Merlin deposit are in fact similar to the S/Se ratios of the disseminated pyrite analysed in the carbonaceous slates at the Lanham's Shaft prospect, which agrees well with the petrographic observations that locate the bulk of the Cu-rich mineralization of the Mount Dore and Merlin deposit in the carbonaceous slates, while the Lanham's Shaft Cu-rich mineralization is hosted in calc-silicate rocks (see Chapters 3 and 4 for details). Therefore, it is considered that the S/Se ratios of these mineralization systems are connected to the fO_2 conditions at the time of precipitation (Figs. 7:3 and 7:5). It

is hence interpreted that the Cu-bearing mineralization fluid in both cases started at a relatively high fO_2 and precipitated the mineralization due to a reduction of the fO_2 the magnitude of which was greater in the Mount Dore and Merlin deposit than at the Lanham's Shaft prospect resulting in the higher S/Se ratios at the former (Fig. 7:7a).

The Mount Dore and Merlin deposit Mo-Re mineralization is characterized by two mineralization stages that based on the textural observations, Re-Os dating, and isotope studies are considered to be formed by the introduction of felsic igneous fluids in the ore system. The oldest Mo-Re, which is the bulk of the mineralization, was formed at ~1535 Ma and was interpreted to have been partly remobilized at ~1520 Ma due to the emplacement of the Mount Dore granite. Based on the W and S/Se geochemistry, it is interpreted that the difference between the two mineralization stages can be explained by a fO_2 change in the fluids involved (Fig. 7:7b). The bulk of the Mo-Re mineralization was formed by a high fO_2 fluid with capacity to transport Mo and W. A large drop in the fO_2 conditions caused extensive precipitation of molybdenite at the site of mineralization. The W/Mo and the S/Se ratios would therefore be similar to the initial fluid ratios (Fig. 7:7b).

The second Mo-Re mineralization stage, which is interpreted as a partial remobilization of the former, is considered to have started with similar fO_2 fluid conditions but it is interpreted to have precipitated the Mo-Re mineralization at a higher fO_2 than the initial Mo mineralization stage resulting in lower S/Se ratios (see below). The lower W content of this mineralization is consistent with the higher fO_2 conditions upon mineral precipitation, sufficient to retain most of the W in the fluid and carry it away from the mineralizing system. The main location of these two mineralization stages supports this model. The oldest stage is mainly located in the contact zone between the carbonaceous slates and calc-silicate rocks, which is therefore in a zone of higher fluid reducing potential due to the reduced nature of the graphite-bearing carbonaceous slates. The second stage is located mostly below the first, in calc-silicate rocks that have limited potential to cause fluid reduction.

The felsic igneous fluid responsible for the Mo-rich mineralization at the Lanham's Shaft prospect is interpreted to have been added to the system at a relatively low fO_2 compared to the Mo-Re bearing fluids at the Mount Dore and Merlin deposit (Fig. 7:7c). The lower fO_2 would be responsible for a lower level of Mo relative to W in the fluid, when comparing with the Mount Dore and Merlin deposit (Fig. 7:6). The Mo-rich mineralization at Lanham's Shaft is hosted in calc-silicate rocks with lesser reduction potential than the carbonaceous slates unit/s, which agrees well with a higher fO_2 conditions upon mineral

precipitation relative to the Mount Dore and Merlin Mo-Re mineralization. The higher fO_2 conditions during ore genesis are then responsible for the lower S/Se ratios and higher Te content of the Mo-rich mineralization at the Lanham's Shaft prospect relative to the Mount Dore and Merlin deposit (Figs. 7:2, 7:5, 7:7c). It is important to note that the intensity of the fO_2 drop during the Mo-rich formation at the Lanham's Shaft prospect is similar to the fO_2 drop intensity of the second Mo-Re mineralization stage at the Mount Dore and Merlin deposit, which is reasonable considering that both stages are hosted in calc-silicate rocks.

The difference between the two Mo-rich mineralization types at the Lanham's Shaft prospect can also be explained by differences in the fO_2 conditions upon precipitation, with the thinner veins being formed at higher fO_2 conditions than the thicker and richer in molybdenite veins.

The higher Re content of the molybdenite at the Mount Dore and Merlin deposit relative to the Lanham's Shaft prospect is difficult to explain with the limited amount of information in the literature. The classical view is that the Re grade in molybdenite mineralization is a function of the amount of molybdenite in the system, i.e. the lower the amount of molybdenite mineralization the higher the Re grade, due to mass balance (Giles and Shilling, 1972; Newberry, 1979; Stein et al., 2001). This view is in complete disagreement with the grades and Mo/Re ratios at Mount Dore and Merlin, and Lanham's Shaft. Other factors, such as metal source, temperature, pressure, fO_2, pH, Cl activity (e.g. Berzina et al., 2005 and references therein) must be the control of the Re grades in these two Mo-rich mineralized systems at Mount Dore and Merlin and Lanham's Shaft.

7.4. Conclusions

The two Mo-Re mineralization stages characterized at the Mount Dore and Merlin deposit display distinct chemistry in W, Te, and S/Se ratios. Two pyrite generations were also identified, the pyrite associated with the Cu-rich mineralization being the most important, followed by minor pyrite formation co-precipitating with the first Mo-Re stage. Three chalcopyrite styles were also identified but interpreted as being formed during the same mineralization stage that corresponds to the Cu-polymetallic association. The chemical distinction between the three types is considered to be a result of the location in the deposit. Zn, Pb, and Ag in pyrite are higher in the carbonaceous slates, and Zn in particular is interpreted to have been sourced from those host rocks. Pb and Ag are also present in the less

hydrothermally altered calc-silicate rocks below the main mineralization and may have contributed to this pyrite, but are very low in Zn.

In the Lanham's Shaft prospect two concomitant Mo-rich mineralization styles were identified corresponding to thinner veins with higher Te and Se and wider veins with lower Te and Se. The Lanham's Shaft prospect also has two pyrite generations, which similarly to the Mount Dore and Merlin deposit consists of pyrite formed with the Cu-rich mineralization and pyrite that is associated with the Mo-rich mineralization, the latter being a minor stage. The pyrite of the Cu-rich mineralization can also be distinguished geochemically relative to their host rocks, with the carbonaceous slates pyrite having lower contents of Se and Te relative to the pyrite formed in the calc-silicate rocks.

The interpretation of all the sulfides analysed in both localities relative to the system S/Se and W/Mo allows for the delineation of a best fit model of physicochemical fluid evolution and ore precipitation mechanism.

The Cu-rich mineralization in both localities was precipitated from the fluid due to a drop in the fO_2 that was bigger at the Mount Dore and Merlin deposit relative to the Lanham's Shaft prospect (Fig. 7:7a). The largest drop in the fO_2 at the Mount Dore and Merlin deposit is due to the bulk of the Cu-rich mineralization being hosted by the carbonaceous slates while at Lanham's Shaft prospect it is hosted in calc-silicate rocks.

These mineralization stages were followed by the formation of the main Mo-rich mineralization in both localities, which was also precipitated due to a drop in the fO_2 conditions (Fig. 7:7b, c). The Lanham's Shaft prospect Mo-rich mineralization was formed at higher fO_2 conditions relative to the Mount Dore and Merlin main Mo-Re stage (Fig. 7:7d). This is considered to be due to the proximity (partly hosting) of the Mo-Re to the carbonaceous slates at the Mount Dore and Merlin deposit, while at the Lanham's Shaft prospect this mineralization is hosted in calc-silicate rocks.

The second Mo-Re mineralization stage at the Mount Dore and Merlin deposit is interpreted as a remobilization of the first stage and was precipitated at higher fO_2 conditions relative to the main Mo-Re stage, although it displays similar fO_2 drop intensity to the Mo-rich mineralization of the Lanham's Shaft prospect. This is interpreted to be due to being hosted in the calc-silicate rocks below the first stage at Mount Dore and Merlin deposit, and therefore in similar rocks to the Mo-rich mineralization at the Lanham's prospect (Fig. 7:7b). In both localities, all the mineralization associations required a drop of the fO_2 conditions in order to precipitate. The carbonaceous slates had a stronger reducing potential, resulting in more abundant Mo-rich and Cu-rich mineralization in or very near the carbonaceous slates.

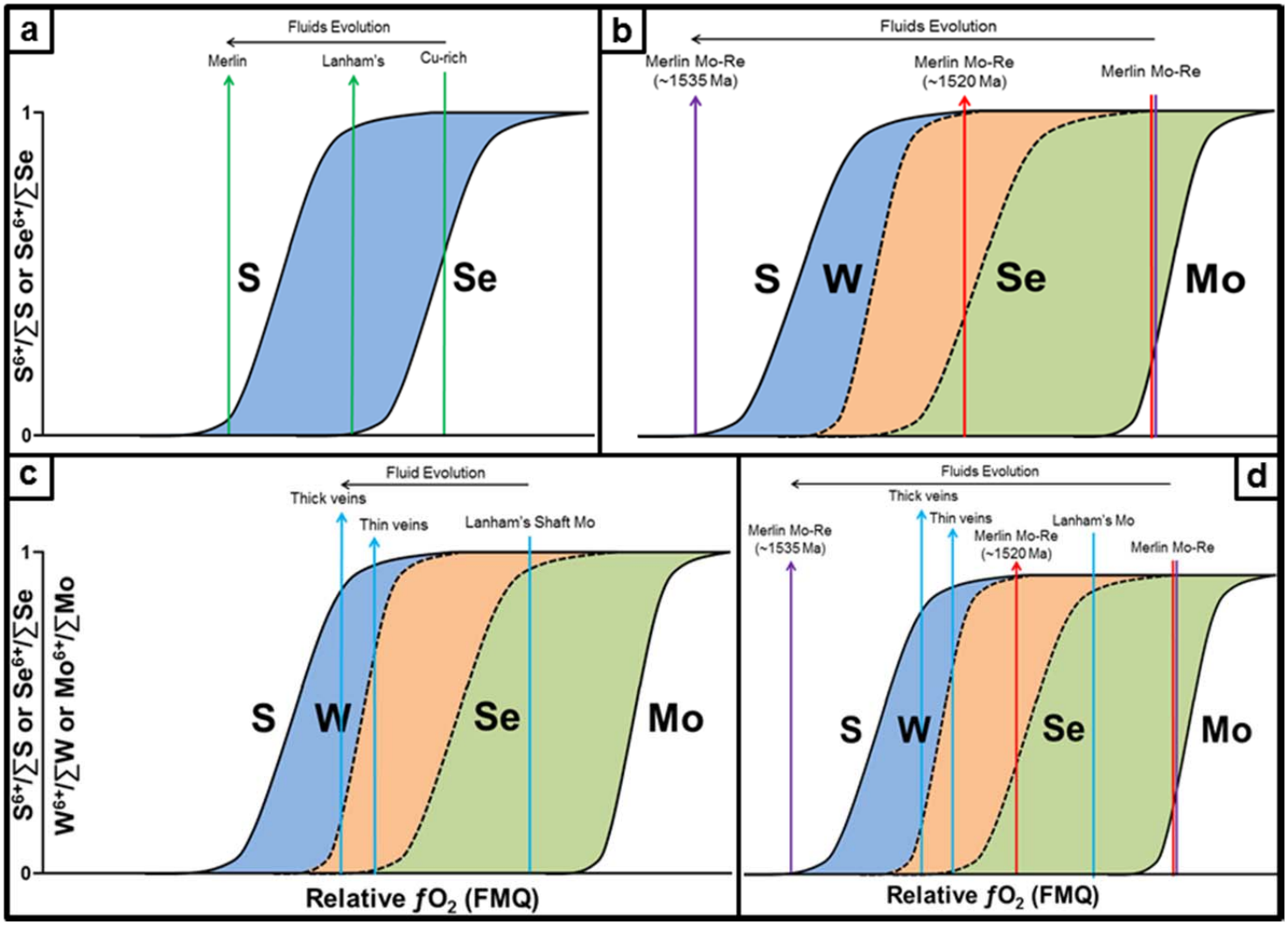

Figure 7:7 – Schematic diagrams as seen in Fig. 7:1 **a)** S/Se diagram with qualitative interpretation of Cu-rich fluid evolution from when is added to the mineralizing system until ore formation for both the Mount Dore and Merlin deposit and the Lanham's Shaft prospect. **b)** S/Se and W/Mo diagrams combined with qualitative interpretation of the Mo-rich mineralization at the Mount Dore and Merlin deposit. **c)** Same as previous for the Lanham's Shaft prospect. **d)** Same as previous for both the Mount Dore and Merlin deposit and the Lanham's Shaft prospect.

8. Chapter 8: Conclusions

The Mount Dore and Merlin deposit is hosted in metamorphosed sediments that were subject to three main hydrothermal alteration stages that are geometrically controlled by faulting, brecciation and host rock rheology.

The metasedimentary host rocks belong to the Kuridala Formation, which was deposited between 1690 and 1653 Ma. They consist of a package of interbedded phyllites and carbonaceous slates that overlie banded calc-silicate rocks, between intensely silicified siltstone at the footwall and the Mount Dore granite with a thrust contact at the hanging wall.

The mineralization consists of a Cu-polymetallic (chalcopyrite ± sphalerite ±± galena) mineralization zone located in the carbonaceous slates that overlies and is partly cut by Mo-Re mineralization that is located in breccias on the contact zone between the carbonaceous slates and calc-silicate rocks and, albeit in lesser amounts, in between the phyllites and carbonaceous slates.

In the time period that encompasses D_2 and D_3 deformation events (between 1580 and 1550 Ma) there was the development of the Mount Dore Ductile Shear Zone, which consists of tight isoclinal folding of the metasedimentary package and formation of reverse faults that dip towards the northeast. During these events initial fault brecciation of the contact zones between phyllites/carbonaceous slates/calc-silicate rocks was developed. Silicification within the Mount Dore Ductile Shear Zone, which corresponds to the silicified siltstones, created a low permeability barrier at the footwall of the subsequent mineralized system. The phyllites near the top had a ductile response to the deformation, with much less brecciation and fault formation, resulting in another low permeability barrier at the hanging wall. The low permeability barriers at the footwall and hanging wall constrained the fluid/s pathways, and the breccias and faults are the structural control of the hydrothermal alteration and mineralization.

Three hydrothermal stages characterize the Mount Dore and Merlin deposit (Table 8:1). The first hydrothermal stage is similar to the Na-(Ca) alteration that is widespread in the region and is the precursor alteration of most of the IOCG deposits in the Cloncurry District, and similar worldwide. The Na-(Ca) alteration was more intense in the calc-silicate rocks, and in the brecciated and faulted zones, forming an assemblage of albite + amphibole ± quartz ± titanite ± apatite ± carbonates.

The Cu-polymetallic mineralization was formed during the second hydrothermal alteration stage. This mineralization was accompanied by potassic alteration with formation of K-

feldspar, tourmaline, carbonates, and lesser quartz. This alteration sequence is also common in the IOCG deposits in the region and is probably a continuous system where the Na-(Ca) alteration results in the loss of potassium, iron, barium, and possibly copper and carbonate which are the main elements involved in the subsequent potassic alteration overprint.

The Cu-polymetallic mineralization is hosted in veins and angular clasts supported breccias located in the carbonaceous slates and partly in the calc-silicate rocks below. There are four main sulfide associations: Chalcopyrite + pyrite; chalcopyrite + galena; chalcopyrite + sphalerite + pyrite ± galena; and sphalerite. The chalcopyrite + pyrite association occurs mainly in the Mo-Re mineralization zone where the textures show that the Mo-Re is later relative to the Cu-polymetallic. This association also appears in minor amounts in the calc-silicates below the Mo-Re mineralization zone. The chalcopyrite + galena association appears mostly in the carbonaceous slates as minor disseminations aligned with the foliation. This association preceded the formation of the bulk of the Cu-polymetallic mineralization. The main mineralization stage is in the carbonate veins and angular clast breccias with chalcopyrite + sphalerite + pyrite ± galena. The last mineralizing pulse of this stage consists of small veins in carbonaceous slates with sphalerite and rare chalcopyrite that evolves from iron-rich to iron-poor in milimetric cross-cutting veins.

Mo-Re mineralization was formed during the third hydrothermal alteration stage, and was accompanied by the formation of K-feldspar and chlorite minor apatite, minor rutile, and trace monazite. Based on textural observations, the Mo-R,e mineralization styles are sub-divided into breccia infill, veins, stylolitic veins and disseminations. The bulk of the mineralization is focused in matrix-supported breccias with rounded clasts, where the matrix is locally composed of massive molybdenite. These structures, located mostly in the contact zones of the carbonaceous slates and calc-silicate rocks, gradually change downward at the top part of the calc-silicate rocks into mineralized veins, commonly stylolitic, and disseminations.

Geologic mapping carried out in the Lanham’s and Barnes Shafts prospects characterized the main rock units as: Calc-silicate rocks; carbonaceous slates; dolerite and granitic intrusives; and polymictic matrix-supported with rounded clasts fluidized breccias. The metasedimentary package is part of the Corella/Doherty Formation (1750-1725 Ma) and display parallel to bedding penetrative foliation developed during the regional D_1 event. NW-SE flexures were formed by ductile folding during the regional D_2 event which is late to post metamorphic peak. The flexures are best represented by the general trend of the carbonaceous slates unit which is interpreted as the main tectonic control for the Lanham’s and Barnes

Shafts prospects. The next main deformation stage is characterized by a SSW-NNE compressional regime which is responsible for the NW-SE trending, NE shallow dipping, dip-slip faults and later SW-NE trending sinistral faults. This deformation stage is more evident along rheological contacts and it can be related to the regional D_3, or an older event(s). During the regional D_4 event there was the emplacement of mafic (most abundant in the area) and felsic intrusives, although some of the intrusives might be of an older age. With the emplacement of the intrusive bodies there is the formation of the polymictic matrix-supported with rounded clasts fluidized breccias that cut the metasedimentary rocks and the mineralization, and locally overprint faults. During this event there is also the formation of minor NW-SE and NE-SW trending faults.

The Lanham's Shaft prospect mineralization is divided into three generations that, from oldest to youngest, are: Cu-Au; Mo; and U. The Cu-Au and Mo mineralization are hosted in calc-silicate rocks adjacent to the carbonaceous slates and a lesser part in intensely altered slates. The mineralization is controlled by angular clasts supported brecciation and veining. The Cu-Au mineralization was formed before the Mo mineralization and as in the Mount Dore and Merlin deposit. The U mineralization uses the same structures although it is also present in the fluidized discordant breccias that cut other mineralization.

The Barnes Shaft prospect displays similar structural controls although the mineralization consists of Cu-Co and no molybdenite has been found. The host rocks at the Barnes Shaft prospect are calc-silicate rocks and the discordant breccias also cut the mineralization. The most striking difference to the Lanham's Shaft prospect is the presence of a several metres thick dolerite intrusion, locally mineralized, which may be genetically linked to the mineralization.

The metasedimentary rocks in those two prospects are broadly similar to the host rocks of the Mount Dore and Merlin deposit despite the depositional age difference (Table 8:1). The hydrothermal system defined at the Lanham's Shaft prospect also shows important similarities with the Mount Dore and Merlin deposit (Table 8:1). It displays a pre-mineralizing hydrothermal stage consisting of Na-(Ca) alteration that is followed by potassic alteration and the formation of the Cu-rich mineralization. The potassic alteration continues during the subsequent precipitation of the Mo-rich mineralization. An important difference is the presence of Zn and Pb bearing minerals locally associated with the Cu-rich mineralization at the Mount Dore and Merlin deposit.

Geochronology studies were conducted at both the Mount Dore and Merlin deposit and Lanham's Shaft prospect (Table 8:1). U-Pb titanite dating at the Mount Dore and Merlin

deposit prospect constrains the timing of the Na-(Ca) hydrothermal alteration stage to 1557 ± 18 Ma. The molybdenite mineralization at the Mount Dore and Merlin deposit shows complexity with three age groups defined. The oldest molybdenite samples correspond to the breccia matrix infill mineralization, which comprises the bulk of the Mo-Re mineralization in the deposit, and is dated at ~1535 Ma, overlapping with the Na-(Ca) stage age dating. The second age group is ~1521 Ma and originates from molybdenite veins, stylolitic veins and disseminations. The youngest age group (~1502 Ma) is defined based on data obtained by other authors (Duncan et al., 2011; Duncan et al., 2013). The three ages obtained for the Mount Dore granite (~1517 Ma) in close proximity to the mineralization confirm the previously reported age, and indicates that the granite formed as a single intrusion event. Therefore, the bulk of the Mo-Re mineralization is Maramungee to Williams-Naraku age (~1557 to ~ 1535 Ma), the second Mo-Re mineralization is synchronous with the Mount Dore granite emplacement (~1521 to ~1517 Ma), and the very minor later Mo-Re mineralization (~1502 Ma) was possibly formed during thrust of the Mount Dore granite over the metasedimentary host rocks.

At Lanham's Shaft prospect there is overlap in the age of molybdenite (Re-Os age of 1560 ± 7 Ma), and hydrothermal titanite (U-Pb age of 1575 ± 24 Ma; Table 8:1). The Lanham's Shaft prospect shows similar temporal relationships between the hydrothermal stages and mineralization as the Mount Dore and Merlin deposit, although they are older than the Williams-Naraku Batholith event.

The mineralization ages of the Mount Dore and Merlin and Lanham's Shaft, and other reported deposit ages such as Starra (Duncan et al., 2011), are strong indications of ore deposit formation between the metamorphic peak and the start of the Williams-Naraku activity.

Sulfur isotope analysis of chalcopyrite, pyrite and molybdenite were conducted in all three locations (Table 8:1). The results obtained are similar and consistent with the Cu-rich mineralization sulfur yielding positive values (0 to 8‰) and the Mo-rich mineralization returning negative values (-7 to 0‰).

Trace element geochemistry was conducted in apatite of each of the three hydrothermal stages defined at the Mount Dore and Merlin deposit. This study confirmed the textural observations and distinguished the apatite cores from the rims, where the cores were formed during the respective hydrothermal stage, while the rims display similar geochemistry in all three samples being interpreted as either a reflection of the host rocks or formed at a later stage. The Na-(Ca) and Cu-polymetallic associations show Sm-Nd signatures in apatite

(Table 8:1) that lie in between the regional Williams-Naraku Batholith and the regional metasedimentary rock values. These results indicate that these hydrothermal associations do not completely reflect either the Williams-Naraku intrusives or the metasedimentary rocks. This means that the Na-(Ca) and Cu-polymetallic associations were formed either by a regionally unknown fluid, or a mix of Nd sources. The apatite grains formed during the second Mo-Re event show typical Williams-Naraku Sm-Nd signatures, which is consistent with the age dating conducted (Table 8:1).

Mo isotope analyses of the Mount Dore and Merlin deposit give some indication of being formed by a felsic igneous fluid although the limited information in the literature precludes any further considerations.

Trace element analysis of molybdenite, pyrite and chalcopyrite from Mount Dore and Merlin and molybdenite, and pyrite from Lanham's Shaft prospect allowed for the chemical characterization of the mineral stages and the interpretation of ore precipitation mechanisms. Sulfides from the first two Mo-Re mineralization stages at the Mount Dore and Merlin deposit display different Se, Te and W with the bulk of the mineralization showing higher W and lower Se and Te relative to the later stage (Table 8:1). Two distinct geochemical signatures were defined in sulfides from the single Mo-rich mineralization stage at the Lanham's Shaft prospect. Sulfides in the wider and more strongly mineralized veins have lower Se and Te contents relative to sulfides in the thinner veins, reflecting a stronger component of the fluid signal in the wider veins.

The pyrite trace element geochemistry at Mount Dore and Merlin and Lanham's Shaft distinguishes the Cu-polymetallic stage and a very minor later pyrite stage that was formed with the bulk of the Mo-rich mineralization. The molybdenite and pyrite trace elements also allowed for the understanding of the few atypical values of $\delta^{34}S$, showing that they are chemically distinct and resulted from uncommon and highly localized reactions between the Cu-rich and Mo-rich hydrothermal stages.

Three chemically distinct chalcopyrite samples are interpreted as belonging to the Cu-polymetallic stage, with Zn, Pb, and Ag contents varying as a function of their location in the deposit.

The Mount Dore and Merlin mineralizing stages are distinguished from the Lanham's Shaft prospect based on the content of Re, Te, Se, and W (Table 8:1). The variations in content of Te, Se, and W of the different stages and between the two localities are considered a function of the fO_2 conditions during ore genesis processes. In broad terms, higher amounts

of Se, Te and W are considered indicative of higher fO_2 conditions during ore genesis processes (see Chapter 7 for details).

The Na-(Ca) hydrothermal alteration and the Cu-rich mineralization in the two localities shows ore genesis processes that can be related to IOCG type deposits (*sensu lato*) in the region. The overprinting of Na-(Ca) alteration by potassic alteration that envelops the mineralization and the hydrothermal fluid/s and metal source/s of the Cu-rich mineralization at Mount Dore and Merlin deposit and Lanham's Shaft prospect are broadly similar to the IOCG type deposits in the region. Due to these similarities and the broad spectrum of ore deposits that have been grouped in the general designation of IOCG type deposits, it is proposed to consider this new deposit type as: Mo-rich IOCG type deposit. The Mo-rich mineralization key difference with the IOCGs proper appear to relate to derivation from felsic intrusions (more evolved, Mo-rich fluids) and a strong host rock control by carbonaceous metasedimentary rocks (stronger fO_2 changes at time of mineralization).

8.1. Ore genesis model

The ore genesis model put forward for the Mount Dore and Merlin deposit consists of five stages (Fig. 8:1):

Stage 1 - Na-(Ca) hydrothermal alteration (Table 8:1 and Fig. 8:1): Formed at 1557 ± 18 Ma, possibly synchronous with D_3 regional deformation event. It manifests as locally pervasive alteration of the metasedimentary host rocks with formation of albite + amphibole ± quartz (locally intense) ± titanite ± apatite ± carbonates. This alteration is more pervasive in the calc-silicate rocks and locally intense in the carbonaceous slates. This alteration was possibly due to influx of bittern brine fluids which has been proposed elsewhere in the Concurry district (Fisher, 2007; Fisher and Kendrick, 2008). The Na-(Ca) alteration is a regional event that results in the loss of K, Fe, Ba, and some Cu (Oliver et al., 2004; Mark et al., 2006a, Marshall and Oliver, 2006).

Stage 2 – Cu-polymetallic hydrothermal alteration (Table 8:1 and Fig. 8:1): The regional loss of K, Fe, Ba, and some Cu, is argued to have been the precursor to this alteration, which is interpreted as resulting from a bittern brine fluid that was enriched in those elements as a consequence of the Na-(Ca) alteration, and formed K-felspar + carbonates + tourmaline + quartz + chalcopyrite + pyrite ± sphalerite (locally intense) ± galena ± apatite. The Zn was probably sourced from the carbonaceous slates where the polymetallic mineralization is focused, and the Pb and Ag was available in minor amounts in the calc-

silicates and carbonaceous slates. The mineralization was precipitated by a strong drop of the fO_2 due to reaction of the mineralizing fluid with the carbonaceous slates unit where the bulk of this mineralization is located. The mineralizing fluid ($\delta^{34}S$ +10 to +20‰) inherited a substantial amount of sulfur from the host rocks ($\delta^{34}S$ < -8‰) due to that reaction, resulting in mixed sulfur isotope signals of the mineralization ($\delta^{34}S$ +1 to +6‰). εNd values of the bittern brine fluid are unknown although this alteration stage (εNd ~ -4) is interpreted to also have mixed signals between the fluid and the metasedimentary host rocks (εNd -8.3 to -6.3; Chapter 6).

Stage 3 – Mo-Re mineralization stage 1 (Table 8:1 and Fig. 8:1): This mineralization is dated at ~1535 Ma and locally cuts the previous formed Cu-polymetallic mineralization. The hydrothermal alteration formed K-feldspar + molybdenite + chlorite in fluidized breccias located in the faulted rheologic contacts between calc-silicate rocks and carbonaceous slates. The mineralizing fluids are interpreted as felsic igneous in origin, possibly from an early Williams-Naraku type intrusive, although a pre-Williams-Naraku intrusive source cannot be discounted. Similar to the Cu-polymetallic mineralization, the hydrothermal fluids reacted with the host rocks and precipitated the Mo-Re mineralization due to a strong fO_2 drop. A considerable amount of sulfur was inherited from the host rocks ($\delta^{34}S$ < -8‰) by the fluid ($\delta^{34}S$ +0 to +3‰) resulting in a mix sulfur isotope signal ($\delta^{34}S$ -4 to 0‰).

Stage 4 – Mo-Re mineralization stage 2 (Table 8:1 and Fig. 8:1): This mineralization consists of a minor remobilization of the previous massive Mo-Re breccia infill into a network of veins, commonly stylolitic, and microfracture controlled disseminations. The remobilization occurred at ~1521 Ma, synchronous with the emplacement of the Mount Dore granite and the start of D_4 regional deformation stage, and displays εNd values that are consistent with the Williams-Naraku intrusives. The sulfur isotope signatures were maintained during the remobilization. The ore precipitation occurred at higher fO_2 conditions due to being hosted below the main Mo-Re mineralization in the calc-silicate rocks with lower reduction potential relative to the carbonaceous slates.

Stage 5 – Mo-Re mineralization stage 3 (Table 8:1 and Fig. 8:1): This mineralization stage consists of a very minor remobilization of Mo-Re mineralization in small millimetric veins. This stage is dated at ~1502 Ma (Duncan et al., 2011; Duncan et al., 2013) and was probably formed during the thrusting of the Mount Dore granite at late-D_4 regional deformation stage.

Table 8:1 – Data summary table of the Mount Dore and Merlin deposit and the Lanham's Shaft prospect hydrothermal alteration and mineralization styles.

Hydrothermal Stages	Data	Mount Dore and Merlin deposit	Lanham's Shaft prospect
Na-(Ca)	*Minerals*	Albite + amphibole ± quartz ± titanite ± apatite ± carbonates	Albite + amphibole ± clinopyroxene ± titanite ± apatite
	Age (Ma)	1557 ± 18 (Maramungee ? to Williams-Naraku)	1575 ± 24 (Metamorphic peak ? - Maramungee ?)
	δ^{34} S (‰)	n.d.	n.d.
	εNd	-3.51 & -4.14	n.d.
	Hydrothermal Fluid/s	Bittern brine (?)	Bittern brine (?)
	Sulfur and εNd source/s	Metasedimentary host rocks (εNd -8.3 to -6.3)	n.d.
	Sufides trace elements geochemistry	n.d.	n.d.
Cu-rich	*Minerals*	K-feldspar + carbonates + tourmaline + quartz + chalcopyrite + pyrite ± sphalerite ± galena ± apatite	K-feldspar + quartz + chalcopyrite + pyrite ± tourmaline ± apatite
	Age (Ma)	~1557 to ~1535 (Maramungee ? to Williams-Naraku)	~1575 to ~1560 (Metamorphic peak ? - Maramungee ?)
	δ^{34} S (‰)	+1 to +6	-1 to +5
	εNd	-4.08	n.d.
	Hydrothermal Fluid/s	Bittern brine	Bittern brine (?)
	Sulfur and εNd source/s	Bittern brine (δ^{34}S 10 to 20‰) + Metasedimentary host rocks (δ^{34}S < -8‰) (εNd -8.3 to -6.3)	Bittern brine (δ^{34}S 10 to 20‰) + Metasedimentary host rocks (δ^{34}S < -8‰ ?)
	Sufides trace elements geochemistry	Very Low Se + Te	Moderate Se + Te
Mo-rich (Stage 1)	*Minerals*	K-feldspar + molybdenite + chlorite	K-feldspar + molybdenite + calcite + biotite ± amphibole ± clinopyroxene
	Age (Ma)	~1535 (Williams-Naraku)	~1560 (Maramungee ?)
	δ^{34} S (‰)	-4 to 0	-7 to -1
	εNd	n.d.	n.d.
	Hydrothermal Fluid/s	Felsic Igneous	Felsic Igneous
	Sulfur and εNd source/s	Felsic Igneous (δ^{34}S 0 to 3‰) (εNd -3.7 to -2.1 ?) + metasedimentary host rocks (δ^{34}S < -8‰) (εNd -8.3 to -6.3)	Felsic Igneous (δ^{34}S 0 to 3‰) (εNd -3.7 to -2.1 ?) + metasedimentary host rocks (δ^{34}S < -8‰ ?) (εNd -8.3 to -6.3)
	Sufides trace elements geochemistry	Very high Re Moderate W Low Se + Te	High W + Se + Te Moderate to low Re
Mo-rich mineralization (Stage 2)	*Minerals*	K-feldspar + molybdenite + chlorite ± rutile ± apatite ± pyrite ±± monazite	
	Age (Ma)	~1521 (Mount Dore granite)	
	δ^{34} S (‰)	-4 to 0	
	εNd	-3.22	
	Hydrothermal Fluid/s	Felsic Igneous (Williams-Naraku)	
	Sulfur and εNd source/s	Remobilization of Phase 1 Mo-Re mineralization (δ^{34}S -4 to 0‰) (εNd -3.7 to -2.1 ?)	
	Sufides trace elements geochemistry	Very high Re Moderate Se + Te Low W	
Mo-rich mineralization (Stage 3)	Very minor remobilization of the previous at ~1502 Ma (Thrusting of the Mount Dore Granite ?)		

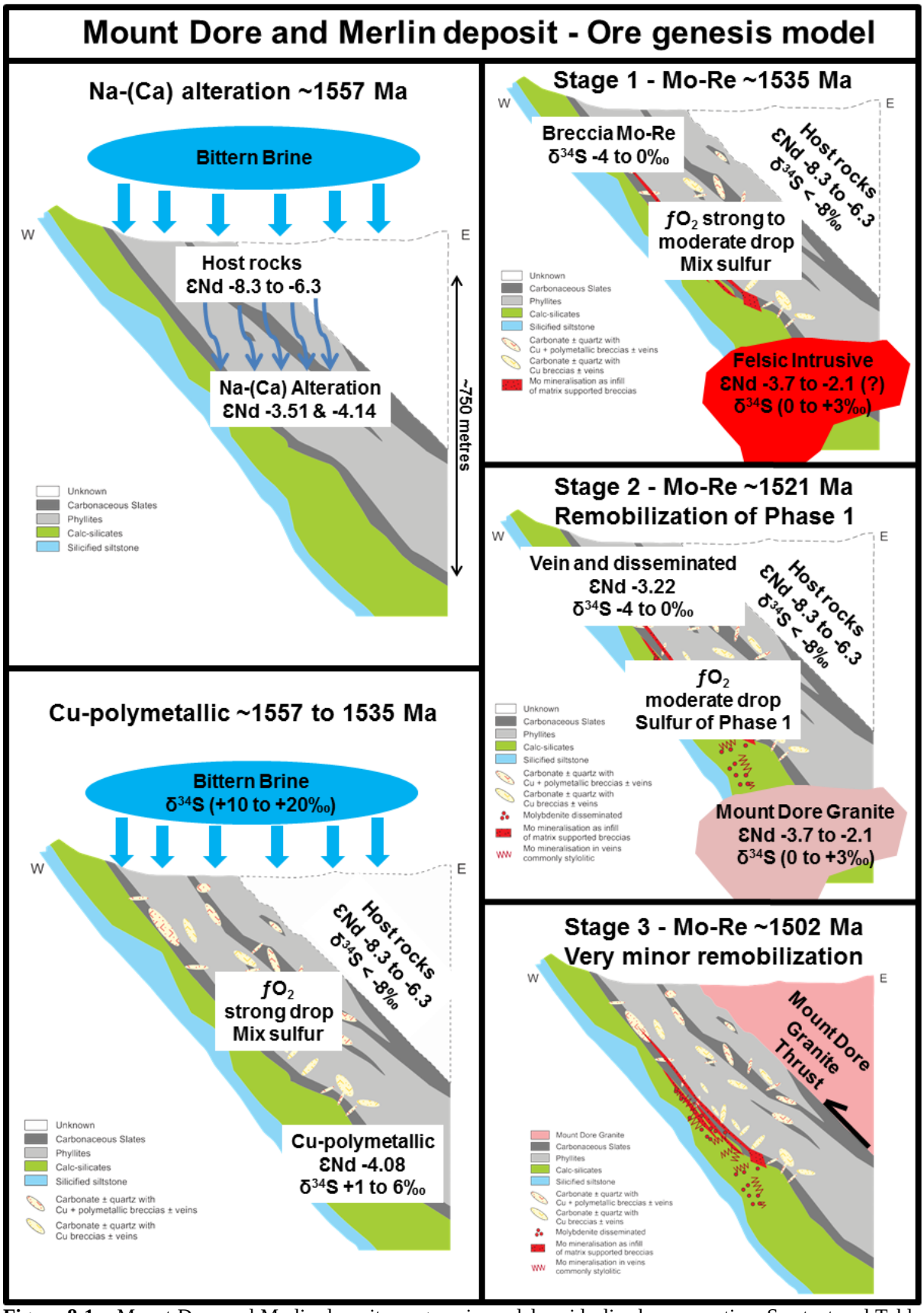

Figure 8:1 – Mount Dore and Merlin deposit ore genesis model on idealized cross-section. See text and Table 8:1 for details. *Scale in the first cross-section.*

8.2. Exploration recommendations

The ore genesis model presented above is considered to be broadly applicable to the Lanham's Shaft prospect, with the main exceptions being the absolute timing of events, only a single Mo-rich stage at Lanham's, and less pronounced fO_2 drop in the precipitation of both Cu-rich and Mo-rich stages due to being primarily hosted in calc-silicate rocks a few metres from the carbonaceous slates units. The existence of Mo-rich mineralization with similar features and genesis at both the Lanham's Shaft prospect, and at the Mount Dore and Merlin deposit indicates that this mineralization type may be more widespread in the Cloncurry District than is currently recognised.

The comparison and contrasting of these two Mo-rich mineralization occurrences allows for delineating the ore formation key ingredients and therefore assists in the exploration targeting of other potential Mo-rich finds in the region:

- These Mo-rich mineralization type occurrences are structurally controlled, therefore a suitable tectonic trap must exist in order for these deposits to be formed. Nevertheless, the location of the trap (with respect to reactive host rocks) appears to be of greater importance than the trap itself.
- Carbonaceous slates have the greatest fluid reducing potential, and hence are interpreted to be crucial for ore precipitation. The closer such rocks are to the structural trap, the greater the potential to find this mineralization type in significant quantities.
- The carbonaceous slates units in the Lanham's and Barnes Shafts extend both north and south of those prospects. The area extending to the south is relatively unexplored, and is recommended as the most fertile terrain for prospectivity of more Mo-rich mineralization.
- Zones where the carbonaceous slates units are faulted and/or folded are of particular importance since they combine the potential for the existence of a suitable tectonic trap with the reduction potential of these units.
- Proximity to Williams-Naraku intrusives should not be considered as a crucial factor, although these areas are potentially favourable for mineralization, since the age dating presented here indicates the existence of mineralizing potential between the metamorphic peak at ~1600 to 1580 Ma and the Williams-Naraku Batholith (at ~1540 to 1480 Ma).

References

Abu Sharib, A. S. A. A., and Sanislav, I. V., 2013. Polymetamorphism accompanied switching in horizontal shortening during Isan Orogeny: Example from the Eastern Fold Belt, Mount Isa Inlier, Australia. *Tectonophysics* **587**, 146-167.

Adshead, N. D., 1995. Geology, alteration and geochemistry of the Osborne Cu-Au deposit, Cloncurry district, NW Queensland, Australia. *PhD Thesis, James Cook University*.

Adshead-Bell, N. S., 1998. Evolution of the Starra and Selwyn High-Strain Zones, Eastern Fold Belt, Mount Isa Inlier Implications for Au-Cu Mineralization. *Economic Geology* **93**, 1450-1462.

Alt, J. C., Muehlenbachs, K., Honnorez, J., 1986. An oxygen isotopic profile through the upper kilometer of the oceanic crust, DSDP Hole 504B. *Earth and Planetary Science Letters* **80**, 217-229.

Andrew, A. S., Heinrich, C. A., Wilkins, R. W. T., Patterson, D. J., 1989. Sulfur isotope systematics of copper ore formation at Mount Isa, Australia. *Economic Geology* **84**, 1614-1626.

Archer, C., Vance, D., 2008. The isotopic signature of the global riverine molybdenum flux and anoxia in the ancient oceans. *Nature Geoscience* **1**, 597-600.

Arnold, G. L., Anbar, A. D., Barling, J., Lyons, T. W., 2004. Molybdenum isotope evidence for widespread anoxia in mid-Proterozoic oceans. *Science* **304**, 87-90.

Austin, J. R, 2005. The Cloncurry Lineament: Interpretation of a major crustal worm. *In:* **Blenkinsop, T. G. (Ed.),** Final Report, Total Systems Analysis of the Mt Isa Eastern Succession. *Predictive Mineral Discovery CRC*, 271-287.

Austin, J. R., Blenkinsop, T. G., 2008. The Cloncurry Lineament: Geophysical and geological evidence for a deep crustal structure in the Eastern Succession of the Mount Isa Inlier. *Precambrian Research* **163**, 50-68.

Austin, J. R., Blenkinsop, T. G., 2009. Local to regional scale structural controls on mineralisation and the importance of a major lineament in the eastern Mount Isa Inlier, Australia: Review and analysis with autocorrelation and weights of evidence. *Ore Geology Reviews* **35**, 298-316.

Babo, J., 2009. The molybdenum-(U-Cu-Au) mineralization of the Lanhams prospect, Cloncurry District, Australia: *BSc. Hons. Thesis, James Cook University*.

Baker, T., Laing, W. P., 1998. Eloise Cu-Au deposit, East Mt Isa Block: Structural environment and structural controls on ore. *Australian Journal of Earth Sciences* **45**, 429-444.

Baker, T., Perkins, C., Blake, K. L., Williams, P. J., 2001. Radiogenic and stable isotope constraints on the genesis of the Eloise Cu-Au deposit, Cloncurry district, northwest Queensland. *Economic Geology* **96**, 723-742.

Barling, J., Arnold, G. L., Anbar, A. D., 2001. Natural mass-dependent variations in the isotopic composition of molybdenum. *Earth and Planetary Science Letters* **193**, 447-457.

Barling, J., Anbar, A. D., 2004. Molybdenum isotope fractionation during adsorption by manganese oxides. *Earth and Planetary Science Letters* **217**, 315-329.

Barnes, S., Savard, D. L., Bédard, P., Maier, W. D., 2009. Selenium and sulfur concentrations in the Bushveld Complex of South Africa and implications for formation of the platinum-group element deposits. *Mineralium Deposita* **44**, 647-663.

Beardsmore, T. J., Newbery, S. P., Laing, W. P., 1988. The Maronan Supergroup: an inferred early volcanosedimentary rift sequence in the Mount Isa Inlier, and its implications for ensialic rifting in the Middle Proterozoic of northwest Queensland. *Precambrian Research* **40**, 487-507.

Beardsmore, T. J., 1992. Petrogenesis of Mount Dore-style breccia hosted copper ± gold mineralization in the Kuridala–Selwyn region of North Western Queensland. *PhD thesis, James Cook University*.

Bell, T. H., Hickey, K. A., 1998. Multiple deformations with successive subvertical and subhorizontal axial planes in the Mount Isa region: Their impact on geometry development and significance for mineralization and exploration. *Economic Geology* **93**, 1369-1389.

Bell, T. H., 1983. Thrusting and duplex formation at Mount Isa, Queensland, Australia. *Nature* **304**, 493-497.

Bertelli, M., Baker T., 2010. A fluid inclusion study of the Suicide Ridge Breccia Pipe, Cloncurry district, Australia: Implication for Breccia Genesis and IOCG mineralization. *Precambrian Research* **179**, 69-87.

Berzina, A., N., Sotnikov, V. I., Economou-Eliopoulos, M., Eliopoulos, D. G., 2005. Distribution of rhenium in molybdenite from porphyry Cu–Mo and Mo–Cu deposits of Russia (Siberia) and Mongolia. *Ore Geology Reviews* **26**, 91-113.

Betts, P. G., Giles, D., Mark, G., Lister, G. S., Goleby B. R., Aillères, L., 2006. Synthesis of the proterozoic evolution of the Mt Isa Inlier. *Australian Journal of Earth Sciences* **53**, 187-211.

Bingen, B., Stein, H., 2003. Molybdenite Re–Os dating of biotite dehydration melting in the Rogaland high-temperature granulites, S Norway. *Earth and Planetary Science Letters* **208**, 181-195.

Blake D. H., 1987. Geology of the Mount Isa Inlier and environs, Queensland and Northern Territory. *Bureau of Mineral Resources Bulletin* **219**.

Blake, D. H., Stewart, A. J., 1992. Stratigraphic and Tectonic framework, Mount Isa Inlier. *In:* **Stewart A. J., and Blake D. H., (eds),** Detailed Studies of the Mount Isa Inlier. *Australian Geological Survey Organization Bulletin* **243**, 1-11.

Blenkinsop, T., C. Huddlestone-Holmes, D. R. W. Foster, G. Mark, J. Austin, M. Edmiston, P. Lepong, A. Ford, F. C. Murphy, M. Stark, 2005a. 3-D model and crustal architecture of the Mt Isa Eastern Succession. *In:* **Blenkinsop, T. G. (Ed.),** Final Report, Total Systems Analysis of the Mt Isa Eastern Succession. *Predictive Mineral Discovery CRC*, 211-242.

Blenkinsop, T., Mustard, R., Bierlein, F., 2005b. Fault roughness, length and mineral endowment. *In:* **Blenkinsop, T. G. (Ed.),** Final Report, Total Systems Analysis of the Mt Isa Eastern Succession. *Predictive Mineral Discovery CRC*, 403-414.

Blenkinsop, T. G., Huddlestone-Holmes, C. R., Foster, D. R. W., Edmiston, M. A., Lepong, P., Mark, G., Austin, J. R., Murphy, F. C., Ford, A., Rubenach, M. J., 2008. The crustal scale architecture of the Eastern Succession, Mount Isa: The influence of inversion. *Precambrian Research* **163**, 31-49.

Bodon, S. B, 1998. Paragenetic relationships and their implications for ore genesis at the Cannington Ag-Pb-Zn deposit, Mount Isa Inlier, Queensland, Australia. *Economic Geology* **93**, 1463-1488.

Brown, M., Lazo, F., Kirwin, D., Corlett, G., 2009. The Swan and Mount Elliot IOCG deposits. *In:* **Williams, P. J., Baker, T., Adshead, N. (Eds.)**, Biennial SGA Meeting, 10th, Townsville, Australia: *Extended conference abstract*. Vol. **1**, 47-49.

Brown, M., Lazo F., Carter P., Goss B., Kirwin D, 2010. The geology and discovery of the Merlin Mo-Re zone of the mount Dore deposit, mount Isa Inlier, NW Queensland, Australia. *SGA News* **27**, 9-15.

Butera, K., Oliver, N. H. S., Rubenach, M., Collins, W., Cleverley, J., 2005. Multiple generations of metal and sulphur contribution from mafic rocks to the IOCG budget of the Mt Isa Eastern Succession. *In:* **Blenkinsop, T. G. (Ed.),** Final Report, Total Systems Analysis of the Mt Isa Eastern Succession. *Predictive Mineral Discovery CRC*, 325-342.

Carter, E. K., Brooks, J. H., Walker, K. R., 1961. The Precambrian mineral belt of north-western Queensland. *Bureau of Mineral Resources, Australia*. Bulletin **51**.

Chapman, L. H., Williams, P. J., 1998. Evolution of pyroxene-pyroxenoid-garnet alteration at the Cannington Ag-Pb-Zn deposit, Cloncurry District, Queensland, Australia. *Economic Geology* **93**, 1390-1405.

Champion, D.C., 2013. Neodymium depleted mantle model age map of Australia: explanatory notes and user guide. *Geoscience Australia*, Record 2013/**44**

Coleman, M. L., 1977. Sulphur isotopes in petrology. *Journal of the Geological Society* **133**, 593-608.

Collins, W. J., Beams, S. D., White, A. J. R., Chappell, B. W., 1982. Nature and origin of A-type granites with particular reference to southeastern Australia. *Contributions to mineralogy and petrology* **80**, 189-200.

Criss, R. E. and Taylor, H. P., 1986. Meteoric-Hydrothermal systems. *In:* **Valley, J.W., Taylor, H.P., O´Neil, J.R. (Eds).** Stable isotopes in high temperature geological processes. *Reviews in Mineralogy* **16**, 373-424.

Cygan, G. L., Chou, I. M., 1987. Calibration of the WO_2-WO_3 buffer. *Eos* **68**, 451

Davidson, G. J., Large, R. R., Kary, G., Osborne, R., 1989. The deformed iron formation-hosted Starra and Trough Tank Au-Cu mineralisation: a new association from the Proterozoic Eastern Succession of Mount Isa, Australia. *Economic Geology Monograph* **6,** 135-150.

Davidson, G. J., Dixon, G. H., 1992. Two sulphur isotope provinces deduced from ores in the Mount Isa Eastern Succession, Australia. *Mineralium Deposita* **27**, 30-41.

Davidson, G. J., Garner, A., 1997. Advances in the understanding of the Cloncurry Cu–Au field. *In:* **Pollard PJ (Ed),** AMIRA P438: Cloncurry base metals and gold final report. *Australian Mineral Industry Research Association* **14**, 1-11.

Davidson, G. J., 1998. Variation in copper-gold styles through time in the Proterozoic Cloncurry goldfield, Mt Isa Inlier: A reconnaissance view. *Australian Journal of Earth Sciences* **45**, 445-462.

Davis, B. K., Pollard, P. J., Lally, J. H., Blake, K., Williams, P. J., 2001. Deformation history of the Naraku Batholith, Mt Isa Inlier, Australia: implications for pluton ages and geometries from structural study of the Dipvale Granodiorite and Levian Granite. *Australian Journal of Earth Sciences* **48**, 113-129.

Deines, P., 2002. The carbon isotope geochemistry of mantle xenoliths. *Earth-Science Reviews* **58**, 247-278.

De Jong, G., Williams, P. J., 1995. Giant metasomatic system formed during exhumation of mid-crustal Proterozoic rocks in the vicinity of the Cloncurry Fault, northwest Queensland. *Australian Journal of Earth Sciences* **42**, 281-290.

Duncan, R. J., Stein, H. J., Evans, K. A., Hitzman, M. W., Nelson, E. P., Kirwin D. J., 2011. A new geochronological framework for mineralization and alteration in the Selwyn-Mount Dore Corridor, Eastern Fold Belt, Mount Isa Inlier, Australia: Genetic implications for iron oxide copper-gold deposits. *Economic Geology* **106**, 169-192.

Duncan, R. J., Stein, H. J., Hitzman, M. W., Nelson, E. P., 2013. Age constraints on the Merlin Molybdenum-Rhenium Deposit, Cloncurry District, Queensland, Australia: Are We Dealing with a Unique Addition to the IOCG family? *In:* **Jonsson, E. (Ed),** Biennial SGA Meeting, 12th, Uppsala, Sweden: *Extended conference abstract*. Vol. **3**, 1359-1362.

Duncan, R. J., Hitzman, M. W., Nelson, E. P., Togtokhbayar, O., 2014. Structural and Lithological Controls on Iron Oxide Copper-Gold Deposits of the Southern Selwyn-Mount Dore Corridor, Eastern Fold Belt, Queensland, Australia. *Economic Geology* **109**, 419-456.

Fitzpatrick, J., 2008. The measurement of the Se/S ratios in sulphide minerals and their application to ore deposit studies. *PhD thesis, Queen's University, Canada*.

Fisher, L. A., 2007. Hydrothermal processes at the Osborne Fe-Oxide-Cu-Au deposit, NW Queensland: Integration of multiple micro-analytical data sets to trace ore fluid sources. *PhD thesis, James Cook University*.

Fisher, L. A., Kendrick, M. A., 2008, Metamorphic fluid origins in the Osborne Fe oxide- Cu- Au deposit, Australia: Evidence from noble gases and halogens. *Mineralium Deposita* **43**, 483- 497.

Foster, J. G.,. Lambert, D. D., Frick, L. R., Maas, R., 1996. Re–Os isotopic evidence for genesis of Archaean nickel ores from uncontaminated komatiites. *Nature* **382**, 703-706.

Foster, D. R. W., Austin, J. R., 2005. Revised chronostratigraphy for the Mt Isa Inlier with emphasis on the Eastern Sucession. *In:* **Blenkinsop, T. G. (Ed.),** Final Report, Total Systems Analysis of the Mt Isa Eastern Succession. *Predictive Mineral Discovery CRC*, 169-207

Foster, D. R. W., Rubenach, M., 2006. Isograd pattern and regional low-pressure, high-temperature metamorphism of politic, mafic and calc-silicate rocks along an east-west section through the Mt Isa Inlier. *Australian Journal of Earth Sciences* **53**, 167-186.

Foster, D. R. W., Austin, J. R., 2008. The 1800–1610 Ma stratigraphic and magmatic history of the Eastern Succession, Mount Isa Inlier, and correlations with adjacent Paleoproterozoic terranes. *Precambrian Research* **163**, 7-30.

Friedman, I., O'Neil, J. R., 1977. Compilation of stable isotope fractionation factors of geochemical interest. *USGPO* **440**.

Fu, B., Williams, P. J., Oliver, N. H., Dong, G., Pollard, P. J., Mark, G. M., 2003. Fluid mixing versus unmixing as an ore-forming process in the Cloncurry Fe-oxide-Cu-Au District, NW Queensland, Australia: evidence from fluid inclusions. *Journal of Geochemical Exploration* **78**, 617-622.

Gauthier, L., Hall, G., Stein, H., Schaltegger, U., 2001, The Osborne deposit, Cloncurry District: a 1595Ma Cu–Au skarn deposit. *In:* **Williams, P.J. (Ed.),** A Hydrothermal Odyssey. *Extended Conference Abstracts*, 58–59.

Georgiev, S., Stein, H. J., Hannah, J. L., Weiss, H. M., Bingen, B., Xu, G., Rein, E., 2012. Chemical signals for oxidative weathering predict Re–Os isochroneity in black shales, East Greenland. *Chemical Geology* **324,** 108-121.

Gibson, G. M., Henson, P. A., Neumann, N. L., Southgate, P. N., Hutton, L. J., 2012. Paleoproterozoic-earliest Mesoproterozoic basin evolution in the Mount Isa region, northern Australia and implications for reconstructions of the Nuna and Rodinia supercontinents. *Episodes-Newsmagazine of the International Union of Geological Sciences* **35**, 131-141.

Giles, D. L., Schilling, J. H., 1972. Variation in rhenium content of molybdenite. Proceedings of the 24th *International Geological Congress Section* **10**, 145-152

Giles, D., Nutman, A. P., 2003. SHRIMP U–Pb zircon dating of the host rocks of the Cannington Ag–Pb–Zn deposit, southeastern Mt Isa Block, Australia. *Australian Journal of Earth Sciences* **50**, 295-309.

Goldberg, T., Archer, C., Vance, D., Thamdrup, B., McAnena, A., Poulton, S. W., 2012. Controls on Mo isotope fractionations in a Mn-rich anoxic marine sediment, Gullmar Fjord, Sweden. *Chemical Geology* **296,** 73-82.

Greber, N. D., Hofmann, B. A., Voegelin, A. R., Villa, I. M., Nägler, T. F., 2011. Mo isotope composition in Mo-rich high-and low-T hydrothermal systems from the Swiss Alps. *Geochimica et cosmochimica acta* **75**, 6600-6609.

Greber, N. D., Siebert, C., Nägler, T. F., Pettke, T., 2012. δ98/95Mo values and molybdenum concentration data for NIST SRM 610, 612 and 3134: Towards a common protocol for reporting Mo data. *Geostandards and Geoanalytical Research* **36**, 291-300.

Groves, D. I., Bierlein, F. P., Meinert, L. D., Hitzman, M. W., 2010. Iron oxide copper-gold (IOCG) deposits through Earth history: Implications for origin, lithospheric setting, and distinction from other epigenetic iron oxide deposits. *Economic Geology* **105**, 641-654.

Hammerli, J., Kemp, A. I. S., Spandler, C., 2012. Neodymium isotope equilibration during crustal metamorphism revealed by in situ microanalysis of REE-rich accessory minerals. *Earth and Planetary Science Letters* **392,** 133-142.

Hannah, J. L., Stein, H. J., Wieser, M. E., De Laeter, J. R., Varner, M. D., 2007. Molybdenum isotope variations in molybdenite: Vapor transport and Rayleigh fractionation of Mo. *Geology* **35**, 703-706.

Hattori, K. H., Arai, S., Clarke, D. B., 2002. Selenium, tellurium, arsenic and antimony contents of primary mantle sulfides. *The Canadian Mineralogist* **40**, 637-650.

Helmy, H. M., Ballhaus, C., Berndt, J., Bockrath, C., Wohlgemuth-Ueberwasser, C., 2007. Formation of Pt, Pd and Ni tellurides: experiments in sulfide–telluride systems. *Contributions to Mineralogy and Petrology* **153**, 577-591.

Helmy, H. M., Ballhaus, C., Wohlgemuth-Ueberwasser, C., Fonseca, R O. C., Laurenz, V., 2010. Partitioning of Se, As, Sb, Te and Bi between monosulfide solid solution and sulfide melt–Application to magmatic sulfide deposits. *Geochimica et Cosmochimica Acta* **74**, 6174-6179.

Hitzman, M. W., Oreskes, N., Einaudi, M. T., 1992. Geological characteristics and tectonic setting of proterozoic iron oxide (Cu-U-Au-REE) deposits. *Precambrian Research* **58**, 241-287.

Holcombe, R. J., Pearson, P. J., Oliver, N. H. S., 1991. Geometry of a middle Proterozoic extensional décollement in northeastern Australia. *Tectonophysics* **191**, 255-274.

Howard, H., 1977. Geochemistry of selenium: formation of ferroselite and selenium behavior in the vicinity of oxidizing sulfide and uranium deposits. *Geochimica et Cosmochimica Acta* **41**, 1665-1678.

Hsu, L. C., 1977. Effects of oxygen and sulfur fugacities on the scheelite-tungstenite and powellite-molybdenite stability relations. *Economic Geology* **72**, 664-670.

Hutton, L. J., Denaro, T. J., Dhnaram, C., Derrick, G. M., 2012. Mineral Systems in the Mount Isa Inlier. *Episodes-Newsmagazine of the InternationalUnion of Geological Sciences* **35**, 120.

Huston, D. L., Sie, S. H., Suter, G. F., Cooke, D. R., Both, R. A., 1995. Trace elements in sulfide minerals from eastern Australian volcanic-hosted massive sulfide deposits; **Part I**, Proton microprobe analyses of pyrite, chalcopyrite, and sphalerite, and **Part II**, Selenium levels in pyrite; comparison with delta 34 S values and implications for the source of sulfur in volcanogenic hydrothermal systems. *Economic Geology* **90**, 1167-1196.

Ivanhoe Australia Annual Report, 2012. *Mineral Resources and Reserves*, 18-25.

Jacob, J. A., 2009. Evolution of the Saxby and Mt. Angelay Igneous Complexes and their role in Cloncurry Fe Oxide-Cu-Au ore genesis. *PhD thesis, James Cook University*, 247 pp.

Jackson, M. J., Rawlings, D. J., 2000. Stratigraphic framework for the Leichhardt and Calvert Superbasins: Review and correlations of the pre-1700 Ma successions between Mt Isa and McArthur River. *Australian Journal of Earth Sciences* **47**, 381-403.

Jackson, S.E., Pearson, N.J., Griffin, W.L. and Belousova, E.A., 2004. The application of laser ablation-inductively coupled plasma-mass spectrometry to in situ U-Pb zircon geochronology. *Chemical Geology* **211**, 47-69.

Jaffe, L. A., Peucker-Ehrenbrink B., Petsch, S. T., 2002. Mobility of rhenium, platinum group elements and organic carbon during black shale weathering. *Earth and Planetary Science Letters* **198**, 339-353.

Jenner, F. E., O'Neill, H. S. T. C., Arculus, R. J., Mavrogenes, J. A., 2010. The magnetite crisis in the evolution of arc-related magmas and the initial concentration of Au, Ag and Cu. *Journal of Petrology* **51**, 2445-2464.

Jenner, F. E., O'Neill, H. S. T. C., 2012. Analysis of 60 elements in 616 ocean floor basaltic glasses. *Geochemistry, Geophysics, Geosystems* **13**.

Johnson, T. M., Bullen, T. D., 2004. Mass-dependent fractionation of selenium and chromium isotopes in low-temperature environments. *Reviews in mineralogy and geochemistry* **55**, 289-317.

Kendrick, M. A., Duncan, R., Phillips. D., 2006. Noble gas and halogen constraints on mineralizing fluids of metamorphic versus surficial origin: Mt Isa, Australia. *Chemical geology* **235**, 325-351.

Kendrick, M. A., Mark, G., Phillips, D., 2007. Mid-crustal fluid mixing in a Proterozoic Fe oxide–Cu–Au deposit, Ernest Henry, Australia: evidence from Ar, Kr, Xe, Cl, Br, and I. *Earth and Planetary Science Letters* **256**, 328-343.

Kendrick, M. A., Baker, T., Fu, B., Phillips, D., Williams, P. J., 2008. Noble gas and halogen constraints on regionally extensive mid-crustal Na–Ca metasomatism, the Proterozoic Eastern Mount Isa Block, Australia. *Precambrian Research* **163**, 131-150.

Kirkby, P. G., 2009. Characteristics and origin of IOCG-associated Mo-Re mineralization in the Merlin deposit, Mt Isa Inlier. *BSc.Hons. Thesis, University of Tasmania*.

Laing, W. P., 1998. Structural-metasomatic environment of the East Mt Isa Block base-metal-gold province. *Australian Journal of Earth Sciences* **45**, 413-428.

Large, R. R., Danyushevsky, L., Hollit, C., Maslennikov, V., Meffre, S., Gilbert, S., Bull, S., 2009. Gold and trace element zonation in pyrite using a laser imaging technique: implications for the timing of gold in orogenic and Carlin-style sediment-hosted deposits. *Economic Geology* **104**, 635-668.

Layton-Matthews, D., Peter, J. M., Scott, S. D., Leybourne, M. I., 2008. Distribution, mineralogy, and geochemistry of selenium in felsic volcanic-hosted massive sulfide deposits of the Finlayson Lake district, Yukon Territory, Canada. *Economic Geology* **103**, 61-88.

Lazo, F., Pal, T., 2009. The Merlin Mo-Re Zone, a new discovery in the Cloncurry District, Australia. *In:* **Williams, P. J., Baker, T., Adshead, N. (Eds.)**, Biennial SGA Meeting, 10th, Townsville, Australia: *Extended conference abstract*. Vol. **1**, 56-58.

Lepong, P., Blenkinsop, T., 2005. Reprocessing and reinterpretation of the My Isa seismic section. *In:* **Blenkinsop, T. G. (Ed.)**, Final Report, Total Systems Analysis of the Mt Isa Eastern Succession. *Predictive Mineral Discovery CRC*, 261-287.

Ludwig, K.R., 2003. User's Manual for Isoplot 3.00. A Geochronological Toolkit for Microsoft Excel. *Berkley Geochronology Centre Special Publication* **4**.

Maas, R., McCulloch, M. T., Campbell. I. H., Page, R. W., 1987. Sm-Nd isotope systematics in uranium rare-earth element mineralization at the Mary Kathleen uranium mine, Queensland. *Economic Geology* **82**, 1805-1826.

Maas, R., McCulloch, M. T., 1991. The provenance of Archean clastic metasediments in the Narryer Gneiss Complex, Western Australia: Trace element geochemistry, Nd isotopes, and U-Pb ages for detrital zircons. *Geochimica et Cosmochimica* **55**, 1915-1932.

MacCready, T., 2006. Structural cross-section based on the Mt Isa Deep Seismic Transect. *Australian Journal of Earth Sciences* **53**, 5-26.

Malinovsky, D., Rodushkin, I., Baxter, D. C., Ingri, J., Öhlander, B., 2005. Molybdenum isotope ratio measurements on geological samples by MC-ICPMS. *International Journal of Mass Spectrometry* **245**, 94-107.

Malisa, E. P., 2001. The behaviour of selenium in geological processes." *Environmental geochemistry and health* **23**, 137-158.

Mathur, R., Brantley, S., Anbar, A., Munizaga, F., Maksaev, V., Newberry, R., Vervoort, J., Hart, G., 2012. Variation of Mo isotopes from molybdenite in high-temperature hydrothermal ore deposits. *Mineralium Deposita* **45**, 43-50.

Marjoribanks, R., 2008. Structural observations on mines and prospects in the Selwyn region, Eastern Mt Isa Inlier. *Ivanhoe Australia Limited internal report.*

Mark, G., Oliver, N. H. S., Williams, P. J., Valenta, R. K., Crookes, R. A., 2000. The evolution of the Ernest Henry hydrothermal system. *In:* **Porter, T. M., (Ed)**, Hydrothermal iron oxide copper-gold and related deposits: A global perspective. *Adelaide, Australian Mineral Foundation*, 132-136.

Mark, G., 2001. Nd isotope and petrogenetic constraints for the origin of the Mount Angelay igneous complex: implications for the origin of intrusions in the Cloncurry district, NE Australia. *Precambrian Research* **105**, 17-35.

Mark, G., Williams, P. J., Boyce, A. J., 2004a. Low-latitude meteoric fluid flow along the Cloncurry Fault, Cloncurry district, NW Queensland, Australia: geodynamic and metallogenic implications. *Chemical geology* **207**, 117-132.

Mark, G., Stein, H., Salt, C., 2004b. Re-Os isotopic evidence for two periods of sulfide mineralization in the vicinity of the Ernest Henry Cu-Au deposit, Northwest Queensland, Australia. *In:* **McPhie, J., and McGoldrick, P. (Eds.)**, 17th Australian Geological Convention, Hobart, Tasmania, Australia **73**, 96.

Mark, G., Foster, D. R. W., Pollard, P. J., Williams, P. J., Tolman, J., Darvall, M., Blake, K. L., 2004c. Stable isotope evidence for magmatic fluid input during large-scale Na–Ca alteration in the Cloncurry Fe oxide Cu–Au district, NW Queensland, Australia. *Terra Nova* **16**, 54-61.

Mark, G., Pollard, P., Foster, D., McNaughton, N., Mustard, R., 2005a. Episodic syn-tectonic magmatism in the Eastern Sucession, Mt Isa Block, Autralia: Implications for the origin, derivation and tectonic setting of "A-Type" magmas. *In:* **Blenkinsop, T. G. (Ed.)**, Final Report, Total Systems Analysis of the Mt Isa Eastern Succession. *Predictive Mineral Discovery CRC*, 51–74.

Mark, G., Foster, D. R. W., Mustard, R., 2005b. Sr-Nd isotopic constrains on the crustal architecture and evolution of the Eastern Succession, Mt Isa Block, Australia. *In:* **Blenkinsop, T. G. (Ed.)**, Final Report, Total Systems Analysis of the Mt Isa Eastern Succession. *Predictive Mineral Discovery CRC*, 75-98.

Mark, G., Oliver, N. H. S., Carew, M. J., 2006a. Insights into the genesis and diversity of epigenetic Cu–Au mineralisation in the Cloncurry district, Mt Isa Inlier, northwest Queensland. *Australian Journal of Earth Sciences* **53**, 109-124.

Mark, G., Oliver, N. H. S., Williams, P. J., 2006b. Mineralogical and chemical evolution of the Ernest Henrcy Fe oxide–Cu–Au ore system, Cloncurry district, northwest Queensland, Australia. *Mineralium Deposita* **40**, 769-801.

Markey, R. J., Stein, H. J., Morgan, J. W., 1998. Highly precise Re-Os dating for molybdenite using alkaline fusion and NTIMS. *Talanta* **45**, 935–946.

Markey, R. J., Stein, H. J., Hannah, J. L., Selby, D., Creaser, R. A., 2007. Standardizing Re-Os geochronology: A new molybdenite Reference Material (Henderson, USA) and the stoichiometry of Os salts. *Chemical Geology* **244**, 74-87.

Marshall, L. J., Oliver, N. H. S., Davidson, G. J., 2006. Carbon and oxygen isotope constraints on fluid sources and fluid–wallrock interaction in regional alteration and iron-oxide–copper–gold mineralisation, eastern Mt Isa Block, Australia. *Mineralium Deposita* **41**, 429-452.

Marshall, L. J., Oliver, N. H. S., 2006. Monitoring fluid chemistry in iron oxide–copper–gold-related metasomatic processes, eastern Mt Isa Block, Australia. *Geofluids* **6**, 45-66.

Marshall, L. J., Oliver, N. H. S., 2008. Constraints on hydrothermal fluid pathways within Mary Kathleen Group stratigraphy of the Cloncurry iron-oxide–copper–gold District, Australia. *Precambrian Research* **163**, 151-158.

McCulloch, M. T., 1987. Sm-Nd isotopic constraints on the evolution of Precambrian crust in the Australian continent. *Proterozoic Lithospheric Evolution*, 115-130.

McFarlane, C. R. M., McCulloch, M. T., 2007. Coupling of in-situ Sm–Nd systematics and U–Pb dating of monazite and allanite with applications to crustal evolution studies. *Chemical geology* **245**, 45-60.

McLaren, S., Sandiford, M., Hand, M., 1999. High radiogenic heat–producing granites and metamorphism: An example from the western Mount Isa inlier, Australia. *Geology* **27**, 679-682.

McLellan, J. G., Oliver, N. H. S., 2005. Discrete element modelling of stress portioning and fluid flow in the Eastern Succession of the Mt Isa Block. *In:* **Blenkinsop, T. G. (Ed.),** Final Report, Total Systems Analysis of the Mt Isa Eastern Succession. *Predictive Mineral Discovery CRC*, 435-503

McLellan, J. G., and Oliver, N. H. S., 2008. Discrete element modelling applied to mineral prospectivity analysis in the eastern Mount Isa Inlier. *Precambrian Research* **163**, 174-188.

McManus, J., Nägler, T. F., Siebert, C., Wheat, C. G., Hammond, D. E., 2002. Oceanic molybdenum isotope fractionation: Diagenesis and hydrothermal ridge-flank alteration. *Geochemistry, Geophysics, Geosystems* **3**, 1-9.

McPhail, D. C., 1995. Thermodynamic properties of aqueous tellurium species between 25 and 350°. *Geochimica et Cosmochimica Acta* **59**, 851-866.

Metrich, N., Clocchiatti, R., 1996. Sulfur abundance and its speciation in oxidized alkaline melts. *Geochimica et Cosmochimica Acta* **60**, 4151-4160.

Murphy, F. C., 2005. Composition of multi-scale wavelets (worms) in the potential field of the Mt Isa region. *In:* **Blenkinsop, T. G. (Ed.)**, Final Report, Total Systems Analysis of the Mt Isa Eastern Succession. *Predictive Mineral Discovery CRC*, 243-260.

Mustard, R., Mark, G., Ulrich, T., Gillen, D., Foster, D. R. W., 2005. Critical ingredients in Cu-Au ± iron oxide deposits: NW Queensland: An evaluation of our current understanding using GIS spatial data modelling. *In:* **Blenkinsop, T. G. (Ed.)**, Final Report, Total Systems Analysis of the Mt Isa Eastern Succession. *Predictive Mineral Discovery CRC*, 359-382.

Mutschler, F. E., Wright, E. G., Ludington, S., Abbot, J. T., 1981. Granite molybdenite systems. *Economic Geology* **76**, 874-897.

Nägler, T. F., Neubert, N., Böttcher, M. E., Dellwig, O., Schnetger, B., 2011. Molybdenum isotope fractionation in pelagic euxinia: Evidence from the modern Black and Baltic Seas. *Chemical Geology* **289**, 1-11.

Neubert, N., Heri, A. R., Voegelin, A. R., Nägler, T. F., Schlunegger, F., Villa, I. M., 2011. The molybdenum isotopic composition in river water: constraints from small catchments. *Earth and planetary science letters* **304**, 180-190.

Newberry, R. J., 1979. Polytypism in molybdenite (II): Relationships between polytypism, ore deposition/alteration stages and rhenium contents. *American mineralogist* **64**, 768-775.

Ohmoto, H., 1972. Systematics of sulfur and carbon isotopes in hydrothermal ore deposits. *Economic Geology* **67**, 551-578.

O'Neill, H. C., Berry, A. J., Eggins, S. M., 2008. The solubility and oxidation state of tungsten in silicate melts: implications for the comparative chemistry of W and Mo in planetary differentiation processes. *Chemical Geology* **255**, 346-359.

Oliver, N. H. S., Wall, V., 1987. Metamorphic plumbing system in Proterozoic calc-silicates, Queensland, Australia. *Geology* **15**, 793-796.

Oliver, N. H. S., 1988. A metamorphic plumbing system: The Mary Kathleen fold belt, northwest Queensland, Australia. *PhD thesis, Monash University*.

Oliver, N. H. S., Holcombe, R. J., Hill, E. J., Pearson, P. J., 1991. Tectono-metamorphic evolution of the Mary Kathleen Fold Belt, northwest Queensland: a reflection of mantle plume processes? Australian. *Journal of Earth Sciences* **38**, 425-55.

Oliver, N. H. S., Wall, V.J., Cartwright, I., 1992. Internal control of fluid compositions in amphibolite-facies scapolitic calc-silicates, Mary Kathleen, Australia. *Contributions to Mineralogy and Petrology* **111**, 94-112.

Oliver, N. H. S., 1995. Hydrothermal history of the Mary Kathleen Fold Belt, Mt Isa Block, Queensland. *Australian Journal of Earth Sciences* **42**, 267-279.

Oliver, N. H. S., Cleverley, J. S., Mark, G., Pollard, P. J., Bin Fu, Marshall, L. J., Rubenach, M. J., Williams, P. J., Baker, T., 2004. Modeling the role of sodic alteration in the genesis of Iron Oxide-Copper-Gold deposits, Eastern Mount Isa Block, Australia. *Economic Geology* **99**, 1145-1176.

Oliver, N. H. S., Pearson, P. J., Holcombe, R. J., Ord, A., 1999. Mary Kathleen metamorphic–hydrothermal uranium – rare-earth element deposit: ore genesis and numerical model of coupled deformation and fluid flow. *Australian Journal of Earth Sciences* **46**, 467-484.

Oliver, N. H. S., Rubenach, M. J., Fu, B., Baker, T., Blenkinsop, T. G., Cleverley, J. S., Marshall, L. J., Ridd, P. J., 2006. Granite-related overpressure and volatile release in the mid crust: Fluidized breccias from the Cloncurry District, Australia. *Geofluids* **6**, 346-358.

Oliver, N. H. S, Butera, K. M., Rubenach, M. J., Marshall, L. J., Cleverley, J. S., Mark, G., Tullemans, F., Esser, D., 2008. The protracted hydrothermal evolution of the Mount Isa Eastern Succession: A review and tectonic implications. *Precambrian Research* **163**, 108-130.

Oliver, N. H. S., Rubenach, M. J., 2009. Distinguishing Basinal- and Magmatic-hydrothermal IOCG Deposits, Cloncurry District, Northern Australia. *In:* **Williams, P. J. et al. (eds)**, SGA conference 2009, *extended abstracts*, 647-649.

Paces, J. B. and Miller, J. D., 1993. Precise U–Pb ages of the Duluth Complex and related mafic intrusions, northeastern Minnesota: geochronological insights to physical, petrogenetic, paleomagnetic, and tectonomagmatic processes associated with the 1.1 Ga midcontinent rift system. Journal of *Geophysical Research* **98**, 13997–14013.

Page, R. W., Sun, S. S., 1998. Aspects of geochronology and crustal evolution in the Eastern Fold Belt, Mt Isa Inlier. *Australian Journal of Earth Sciences* **45**, 343-361.

Peucker-Ehrenbrink, B., Hannigan, R. E., 2000. Effects of black shale weathering on the mobility of rhenium and platinum group elements. *Geology* **28**, 475-478.

Perkins, C., Wyborn, L. A. I., 1998. Age of Cu-Au mineralisation, Cloncurry district, eastern Mt Isa Inlier, Queensland, as determined by 40Ar/39Ar dating. *Australian Journal of Earth Sciences* **45**, 233-246.

Pollard, P. J., McNaughton, N., 1997. U–Pb geochronology and Sm/Nd isotope characteristics of Proterozoic intrusive rocks in the Cloncurry district, Mount Isa Inlier, Australia. *In:* **Pollard, PJ (Ed.)** AMIRA P438 Final Report: Cloncurry Base Metals and Gold Australian, *Mineral Industry Research Association* **4**.

Pollard, P. J., Mark, G., Mitchell, L. C., 1998. Geochemistry of post-1540 Ma granites in the Cloncurry district, northwest Queensland. *Economic Geology* **93**, 1330-1344.

Pollard, P. J., 2001, Sodic(-calcic) alteration in Fe oxide-Cu-Au districts: an origin via unmixing of magmatic H2O-CO2-NaCl + CaCl2-KCl fluids. *Mineralium Deposita* **36**, 93-100.

Pollard, P. J., 2006. An intrusion-related origin for Cu–Au mineralization in iron oxide–copper–gold (IOCG) provinces. *Mineralium Deposita* **41**, 179-187.

Poulson, R. L. B., McManus, J., Severmann, S., Berelson, W. M., 2009. Molybdenum behavior during early diagenesis: Insights from Mo isotopes. *Geochemistry, Geophysics, Geosystems* **10**.

Queffurus, M., Barnes, S. J., 2014. Selenium and sulfur concentrations in country rocks from the Duluth complex, Minnesota, USA: Implications for formation of the Cu-Ni-PGE sulfides. *Economic Geology* **109**, 785-794.

Rempel, K. U., Williams-Jones, A. E., Migdisov, A. A., 2009. The partitioning of molybdenum (VI) between aqueous liquid and vapour at temperatures up to 370 C. *Geochimica et Cosmochimica Acta* **73**, 3381-3392.

Richards, J. P., Mumin, A. H., 2013. Magmatic-hydrothermal processes within an evolving Earth: Iron oxide-copper-gold and porphyry Cu±Mo±Au deposits. *Geology* **41**, 767-770.

Rose-Weston, L., Brenan, J. M., Fei, Y., Secco, R. A., Frost, D. J., 2009. Effect of pressure, temperature, and oxygen fugacity on the metal-silicate partitioning of Te, Se, and S: Implications for earth differentiation. *Geochimica et Cosmochimica Acta* **73**, 4598-4615.

Rotherham, J. F., 1997a. A metasomatic origin for the iron-oxide Au-Cu Starra orebodies, Eastern Fold Belt, Mount Isa Inlier. *Mineralium Deposita* **32**, 205-218.

Rotherham, J.F., 1997b. Origin and Fluid Chemistry of the Starra Ironstones and High Grad Au-Cu Mineralisation, Cloncurry District, Mount Isa Inlier, Australia. *PhD thesis, James Cook University*.

Rotherham, J. F., Blake, K. L., Cartwright, I., Williams, P. J., 1998. Stable isotope evidence for the origin of the Mesoproterozoic Starra Au-Cu deposit, Cloncurry district, northwest Queensland. *Economic Geology* **93**, 1435-1449.

Rubenach, M. J., 1992. Proterozoic low-pressure/high-temperature metamorphism and an anticlockwise P–T–t path for the Hazeldene area, Mount Isa Inlier, Queensland, Australia. Journal of Metamorphic Geology **10**, 333-346.

Rubenach, M., Adshead, N., Oliver, N., Tullemans, F., Esser, D., Stein, H., 2001. The Osborne Cu–Au deposit – Geochronology and genesis of mineralization in relation to host albitites and Ironstones. *In:* **Williams, P.J. (Ed.),** A Hydrothermal Odyssey. *Extended Conference Abstracts*, 172-173.

Rubenach, M. J., 2005a. Relative timing of albitization and chlorine enrichment in biotite in proterozoic schists, Snake Creek Anticline, Mount Isa Inlier, Northeastern Australia. *The Canadian Mineralogist* **43**, 349-366.

Rubenach, M. J., 2005b. Tectonothermal evolution of the Eastern Fold Belt, Mt Isa Inlier. *In:* **Blenkinsop, T. G. (Ed.)**, Final Report, Total Systems Analysis of the Mt Isa Eastern Succession. *Predictive Mineral Discovery CRC*, 99-168.

Rubenach, M. J., Oliver, N. H. S., 2005c. Geochemistry of albititees and related metasomatic rocks, Eastern Succession of the Mount Isa Block. *In:* **Blenkinsop, T. G. (Ed.)**, Final Report, Total Systems Analysis of the Mt Isa Eastern Succession. *Predictive Mineral Discovery CRC*, 343-358.

Rubenach, M. J., Foster, D. R. W., Evins, P. M., Blake, K. L., Fanning, C. M., 2008. Age constraints on the tectonothermal evolution of the Selwyn Zone, Eastern Fold Belt, Mount Isa Inlier. *Precambrian Research* **163**, 81-107.

Rye, R. O., Ohmoto, H., 1974. Sulfur and carbon isotopes and ore genesis: a review. *Economic Geology* **69**, 826-842.

Scott, K. M., Smith, J. W., Sun, S. S., Taylor, G. F., 1985. Proterozoic copper deposits in NW Queensland, Australia: Sulfur isotopic data. *Mineralium deposita* **20**, 116-126.

Selby, D., Creaser, R. A., 2004. Macroscale NTIMS and microscale LA-MC-ICP-MS Re-Os isotopic analysis of molybdenite: Testing spatial restrictions for reliable Re-Os age determinations, and implications for the decoupling of Re and Os within molybdenite. *Geochimica et Cosmochimica Acta* **68**, 3897-3908.

Shannon, R. D., 1976. Revised effective ionic radii and systematic studies of interatomic distances in halides and chalcogenides. *Acta Crystalography* **A32**, 751-767.

Siebert, C., Nägler, T. F., Kramers, J. D., 2001. Determination of molybdenum isotope fractionation by double-spike multicollector inductively coupled plasma mass spectrometry. *Geochemistry, Geophysics, Geosystems* **2**.

Siebert, C., Nägler, T. F., Blanckenburg, F., Kramers, J. D., 2003. Molybdenum isotope records as a potential new proxy for paleoceanography. *Earth and Planetary Science Letters* **211**, 159-171.

Siebert, C., McManus, J., Bice, A., Poulson, R., Berelson, W. M., 2006. Molybdenum isotope signatures in continental margin marine sediments. *Earth and Planetary Science Letters* **241**, 723-733.

Sillitoe, R. H., 1985. Ore-related breccias in volcanoplutonic arcs. *Economic Geology* **80**, 1467-1514.

Sillitoe, R. H., 2003. Iron oxide-copper-gold deposits: an Andean view. *Mineralium Deposita* **38**, 787-812.

Skirrow, R. G., Bastrakov, E. N., Barovich, K., Fraser, G. L., Creaser, R. A., Fanning, M. C., Raymond, O. L., Davidson, G. J., 2007. Timing of iron oxide Cu-Au-(U) hydrothermal activity and Nd isotope constraints on metal sources in the Gawler Craton, South Australia. *Economic Geology* **102**, 1441-1470.

Southgate, P. N., Scott, D. L., Sami, T. T., Domagala, J., Jackson, M. J., James, N. P., Kyser, T. K., 2000. Basin shape and sediment architecture in the Gun Supersequence: A strike-slip model for Pb–Zn–Ag ore genesis at Mt Isa. *Australian Journal of Earth Sciences* **47**, 509-531.

Southgate, P. N., Neumann, N. L., Gibson, G. M., 2013. Depositional systems in the Mt Isa Inlier from 1800 Ma to 1640 Ma: Implications for Zn–Pb–Ag mineralisation. *Australian Journal of Earth Sciences* **60**, 157-173.

Spandler, C., Pettke, T., Rubatto, D., 2011. Internal and external fluid sources for eclogite-facies veins in the Monviso meta-ophiolite, Western Alps: implications for fluid flow in subduction zones. *Journal of Petrology* **52**, 1207-1236.

Stein, H. J., Sundblad, K., Markey, R. J., Morgan, J. W., Motuza, G., 1998. Re-Os ages for Archean molybdenite and pyrite, Kuittila-Kivisuo, Finland and Proterozoic molybdenite, Kabeliai, Lithuania: testing the chronometer in a metamorphic and metasomatic setting. *Mineralium Deposita* **33**, 329-345.

Stein, H. J., Markey, R. J., Morgan, J. W., Hannah, J. L., Scherstén, A., 2001. The remarkable Re–Os chronometer in molybdenite: how and why it works. *Terra Nova* **13**, 479-486.

McDonough, W. F., Sun, S. S., 1995. The composition of the Earth. *Chemical geology* **120**, 223-253.

Tchalenko, J. S., Ambraseys, N. N., 1970. Structural Analysis of the Dasht-e Bayaz (Iran) Earthquake Fractures. *Geological Society of America Bulletin* **81**, 41-60.

Thode, H. G., Monster, J., Dunford, H. B., 1961. Sulphur isotope geochemistry. *Geochimica et Cosmochimica Acta* **25**, 159-174.

Tossell, J. A., 2005. Calculating the partitioning of the isotopes of Mo between oxidic and sulfidic species in aqueous solution. *Geochimica et Cosmochimica Acta* **69**, 2981-2993.

Twyerould, S. C., 1997. The geology and genesis of the Ernest Henry Fe-Cu-Au deposit, NW Queensland, Australia. *PhD Thesis, University of Oregon*.

Van Achterbergh, E., Ryan, C. G., Griffin, W. L., 2001. Glitter user's manual, On-line Interactive Data Reduction for the LA-ICPMS Microprobe.

Voegelin, A. R., Nägler, T. F., Samankassou, E., Villa, I. M., 2009. Molybdenum isotopic composition of modern and Carboniferous carbonates. *Chemical geology* **265**, 488-498.

Wang, S., Williams, P. J., 2001. Geochemistry and origin of Proterozoic skarns at the Mount Elliott Cu–Au (–Co–Ni) deposit, Cloncurry district, NW Queensland, Australia. *Mineralium Deposita* **36**, 109-124.

Williams, P. J., Phillips, G. N., 1992. Cloncurry mapping project 1990. *EGRU contribution* **40**.

Williams, P. J., Heinemann, M., 1993. Maramungee: a Proterozoic Zn skarn in the Cloncurry District, Mount Isa Inlier, Queensland, Australia. *Economic Geology* **88**, 1114-1134.

Williams, P. J., 1998. Metalliferous economic geology of the Mt Isa Eastern Succession, Queensland. *Australian Journal of Earth Sciences* **45**, 329-341.

Williams, P. J., Dong, G., Ryan, C. G., Pollard, P. J., Rotherham, J. F., Mernagh, T. P., Chapman, L. H., 2001. Geochemistry of hypersaline fluid inclusions from the Starra (Fe oxide)-Au-Cu deposit, Cloncurry District, Queensland. *Economic Geology* **96**, 875-883.

Williams, P. J., Barton, M. D., Fontbote, L., deHaller, A., Johnson, D. A., Mark, G., Oliver, N. H. S., Marschik, R., 2005, Iron oxide–copper–gold deposits: geology, space-time distribution and possible modes of origin. *In:* 100th Anniversary Volume. *Society of Economic Geologists*, 371–405.

Wyborn, L. A. I., Page, R. W., McCulloch, M. T., 1988. Petrology, geochronology and isotope geochemistry of the post-1820 Ma granites of the Mount Isa Inlier: mechanisms for the generation of Proterozoic anorogenic granites. *Precambrian Research* **40**, 509-541.

Wyborn, L., 1998. Younger ca 1500 Ma granites of the Williams and Naraku Batholiths, Cloncurry district, eastern Mt Isa Inlier: Geochemistry, origin, metallogenic significance and exploration indicators. *Australian Journal of Earth Sciences* **45**, 397-411.

Wyborn, L. A. I., Wyborn, D., Warren, R. G., Drummond, B. J., 1992. Proterozoic granite types in Australia: implications for lower crust composition, structure and evolution. *Transactions of the Royal Society of Edinburgh: Earth Sciences* **83**, 201-209.

Xiong, Y., 2003. Predicted equilibrium constants for solid and aqueous selenium species to 300 C: applications to selenium-rich mineral deposits. *Ore Geology Reviews* **23**, 259-276.

Yamamoto, M., 1976. Relationship between Se/S and sulfur isotope ratios of hydrothermal sulfide minerals. *Mineralium Deposita* **11**, 197-209.

Appendix 1

Lanham’s and Barnes Shafts geological mapping.

459400 459600 459800 460000 460200 460400 460600 460800

7654000 7653800 7653600 7653400 7653200 7653000 7652800 7652600 7652400 7652200 7652000 7651800 7651600 7651400

Lanham's Shaft

LAD0001

LAD0002

Barnes Shaft

Legend

Williams - Naraku (~1540 - 1490 Ma)

- Pegmatite
- Granite (altered)
- Gabbro/Dolerite (altered)
- Discordant calc-silicate Breccia

Corella/ Doherty Formation (~1750 - 1725 Ma)

- Banded to weakly brecciated calc-silicate
- Carbonaceous Slate (unit 1)/ Altered Slate (unit 1)
- Carbonaceous Slate (unit 2)
- Calc-silicate Slates (unit 1)
- Calc-silicate Slates (unit 2)

- Ironstone
- Cu showings

- Bedding inferred
- Fault
- Inferred fault / fracture
- Bedding measurement with dip
- Sub-vertical bedding
- Sinistral strike-slip
- Dextral strike-slip
- Dip-slip
- Strike slip Oblique dip-slip
- Drill hole
- Prospects

UTM Grid Zone 54, GDA94

Metres

0 75 150 225 300

Appendix 2

Tables of the samples selected for analyses.

Mount Dore and Merlin deposit								
Sample Hole	**Sample Depth**	**Re-Os Dating**	**Pb-U Zircon Dating**	**Pb-U Titanite Dating**	**Sulfur Isotopes**	**Molybdenum Isotopes**	**Sm-Nd Isotopes**	**Sulfide trace elements**
MDQ0112	301.20				Pyrite			
MDQ0112	311.95				Chalcopyrite			
MDQ0112	355.45				Chalcopyrite / Pyrite			
MDQ0112	381.95			X			Apatite & Titanite	
MDQ0119	411.10				Molybdenite			
MDQ0120	282.05				Chalcopyrite			
MDQ0120	349.90				Molybdenite			
MDQ0132	300.50				Pyrite			
MDQ0132	311.30				Pyrite			
MDQ0132	350.65				Pyrite			
MDQ0132	355.40	X			Molybdenite	X		Molybdenite
MDQ0132	360.35				Molybdenite			
MDQ0132	364.80				Molybdenite			
MDQ0132	366.10				Molybdenite			
MDQ0132	370.20				Molybdenite			
MDQ0132	376.30				Molybdenite		Apatite	Molybdenite
MDQ0132	384.65				Molybdenite			
MDQ0132	385.20				Molybdenite			
MDQ0132	388.85				Molybdenite			
MDQ0133	193.00				Pyrite			
MDQ0133	358.25				Chalcopyrite			
MDQ0133	373.85				Chalcopyrite			
MDQ0149	103.45				Pyrite			
MDQ0150	170.80	X			Molybdenite / Pyrite			Molybdenite / Pyrite
MDQ0150	171.30				Molybdenite			
MDQ0209	174.70				Molybdenite	X		
MDQ0220	571.20				Molybdenite			
MDQ0221	351.20				Chalcopyrite / Pyrite			Chalcopyrite
MDQ0221	369.95				Chalcopyrite / Pyrite			
MDQ0221	453.30				Pyrite			
MDQ0221	467.75				Molybdenite			
MDQ0221	471.65				Molybdenite			
MDQ0221	472.55	X			Molybdenite	X		
MDQ0221	473.80				Molybdenite			
MDQ0221	487.40				Molybdenite			
MDQ0222	262.15		X					
MDQ0222	301.15				Chalcopyrite		Apatite	
MDQ0222	381.60				Pyrite			
MDQ0222	391.25				Chalcopyrite / Pyrite			
MDQ0222	403.20				Chalcopyrite / Pyrite			Pyrite / Chalcopyrite
MDQ0230	177.25				Molybdenite			
MDQ0234	314.60				Molybdenite			
MDQ0234	320.50				Molybdenite			
MDQ0235	172.50				Molybdenite			
MDQ0235	175.00				Molybdenite			Molybdenite
MDQ0237	176.30				Pyrite			
MDQ0237	180.80				Molybdenite			
MDQ0237	181.30				Molybdenite			
MDQ0245	214.00		X					
MDQ0245	251.80				Pyrite			
MDQ0245	270.20				Pyrite			
MDQ0245	326.55				Pyrite			
MDQ0252	191.95		X					
MDQ0252	217.15				Pyrite			
MDQ0252	226.95				Chalcopyrite			
MDQ0252	343.85				Molybdenite	X		
MDQ0252	367.45				Molybdenite / Chalcopyrite			
MDQ0252	392.75				Chalcopyrite			
MDQ0252	393.40				Molybdenite			Molybdenite / Chalcopyrite / Pyrite
MDQ0252	396.25				Molybdenite			
MDQ0252	459.65	X			Molybdenite			Molybdenite / Pyrite
MDQ0252	466.25				Molybdenite			
MDQ0252	469.75				Molybdenite			
MDQ0252	487.90	X			Molybdenite	X		Molybdenite
MDQ0252	532.10				Molybdenite / Chalcopyrite			
MDQ0252	537.95				Pyrite			
MDQ0264	91.30	X			Molybdenite			
MDQ0287	77.40				Molybdenite	X		

Lanham's Shaft prospect					
Sample Hole	**Sample Depth**	**Re-Os Dating**	**Pb-U Titanite Dating**	**Sulfur Isotopes**	**Sulfide trace elements**
LAD0001	143.37			Chalcopyrite / Pyrite	
LAD0001	158.50	X		Molybdenite	Molybdenite
LAD0001	158.95			Molybdenite	
LAD0001	164.95			Chalcopyrite	
LAD0001	169.50			Molybdenite	
LAD0001	173.30		X		
LAD0001	178.50				Pyrite
LAD0002	118.00				Molybdenite
LAD0002	119.30	X		Molybdenite	Molybdenite / Pyrite
LAD0002	122.60			Molybdenite	Molybdenite
LAD0002	143.75			Molybdenite / Pyrite	
LAD0002	144.85			Chalcopyrite / Pyrite	Pyrite
LAD0002	158.50			Pyrite	
LAD0002	171.30			Pyrite	
LAD0003	134.15			Molybdenite	
LAD0003	141.60			Molybdenite	
LAD0003	142.35			Molybdenite	
LAD0003	175.75			Pyrite	
LAD0004	167.85			Pyrite	
LAD0004	171.40			Molybdenite / Chalcopyrite	
LAD0004	172.90			Pyrite	
LAD0004	180.95			Pyrite	
LAD0004	214.00			Pyrite	
LAD0004	215.55			Chalcopyrite / Pyrite	
LAD0009	249.85			Molybdenite / Chalcopyrite	
LAD0009	250.80			Chalcopyrite	

Lanham's Shaft prospect		
Sample Hole	**Sample Depth**	**Sulfur Isotopes**
BAD0001	148.80	Pyrite
BAD0001	199.30	Pyrite
BAD0001	214.25	Pyrite
BAD0001	75.20	Pyrite
BAD0006	101.65	Chalcopyrite
BAD0006	179.40	Pyrite
BAD0006	259.80	Pyrite
BAD0006	262.95	Chalcopyrite
BAD0006	286.35	Pyrite
BAD0006	37.55	Chalcopyrite
BAD0006	38.25	Py
BAD0006	41.40	Py
BAD0007	103.75	Py
BAD0007	137.45	Py
BAD0007	156.50	Py
BAD0007	56.70	Py
BAD0007	62.45	Chalcopyrite
BAD0007	65.20	Py

Appendix 3

Regional geochronology tables of references.

Igneous Intrusives	U-Pb	U-Pb Titanite	Reference
Gin Creek Granite	1741 ± 7		Page and Sun (1998)
Levian Granite	1746 ± 8		Davis et al. (2001)
Ernest Henry diorite		1660 ± 13	Pollard and McNaughton (1997)
Ernest Henry diorite	1657 ± 7		Pollard and McNaughton (1997)
Ernest Henry diorite	1658 ± 10		Pollard and McNaughton (1997)
Maramungee Granite	1545 ± 11		Page and Sun (1998)
Boorama Tank Gneiss	1547 ± 5		Page and Sun (1998)
Mount Dore Granite	1516 ± 10		Pollard and McNaughton (1997)
Mount Dore Granite	1513 ± 13		This Study
Mount Dore Granite	1516 ± 12		This Study
Mount Dore Granite	1521 ± 10		This Study
Mt Angelay Granite	1523 ± 4		Pollard and McNaughton (1997)
Mt Angelay Granite	1524 ± 4		Pollard and McNaughton (1997)
Mt Angelay Granite	1529 ± 4		Pollard and McNaughton (1997)
Mt Angelay tonalite	1552 ± 42		Pollard and McNaughton (1997)
Mt Margaret Granite	1528 ± 6		Page and Sun (1998)
Mt Margaret Granite	1530 ± 8		Page and Sun (1998)
Saxby Granite	1520 ± 8		Pollard and McNaughton (1997)
Saxby Granite	1527 ± 4		Rubenach et al. (2008)
Saxby Granite	1536 ± 12		Pollard and McNaughton (1997)
Saxby Granite (felsic)	1536 ± 20		Pollard and McNaughton (1997)
Saxby Granite (xenocrysts)	1666 ± 24		Pollard and McNaughton (1997)
Squirrel Hills Granite	1511 ± 9		Pollard and McNaughton (1997)
Squirrel Hills Granite	1514 ± 5		Pollard and McNaughton (1997)
Wimberu Granite	1512 ± 4		Pollard and McNaughton (1997)
Yellow Waterhole Granite	1493 ± 8		Page and Sun (1998)
Yellow Waterhole Granite	1510 ± 8		Pollard and McNaughton (1997)
Malakoff Granite	1505 ± 5		Page and Sun (1998)

Ore Deposits	U-Pb	Ar/Ar	Re-Os	U-Pb Titanite	Reference
Mount Elliot and Swan		1510 ± 3			Wang and Williams (2001)
Mount Elliot and Swan		1496			Perkins and Wyborn (1998)
Mount Elliot and Swan			1513 ± 5		Duncan et al. (2011)
Mount Elliot and Swan				1530 ± 11	Duncan et al. (2011)
Mount Elliot and Swan	1540				Duncan et al. (2011)
Mount Elliot and Swan			1515 ± 6		Duncan et al. (2011)
Lady Ella			1487 ± 5		Duncan et al. (2011)
Starra		1503			Perkins and Wyborn (1998)
Starra			1568 ± 7		Duncan et al. (2011)
Starra				1594 ± 8	Duncan et al. (2011)
Mount Dore and Merlin			1497 ± 6		Duncan et al. (2011)
Mount Dore and Merlin			1501 ± 5		Duncan et al. (2011)
Mount Dore and Merlin			1508 ± 5		Duncan et al. (2011)
Mount Dore and Merlin			1503 ± 5		Duncan et al. (2011)
Mount Dore and Merlin			1503 ± 5		Duncan et al. (2011)
Mount Dore and Merlin			1502 ± 7		Duncan et al. (2011)
Mount Dore and Merlin			1552 ± 6		Duncan et al. (2011)
Mount Dore and Merlin			1523 ± 6		This Study
Mount Dore and Merlin			1521 ± 6		This Study
Mount Dore and Merlin			1520 ± 6		This Study
Mount Dore and Merlin			1539 ± 6		This Study
Mount Dore and Merlin			1541 ± 6		This Study
Mount Dore and Merlin			1533 ± 6		This Study
Mount Dore and Merlin			1529 ± 6		This Study
Mount Dore and Merlin			1534 ± 6		This Study
Mount Dore and Merlin			1591 ± 7		This Study
Mount Dore and Merlin			1802 ± 7		This Study
Lanham's Shaft Prospect			1559 ± 6		This Study
Lanham's Shaft Prospect			1560 ± 7		This Study

Ore Deposits	U-Pb	Ar-Ar	Re-Os	U-Pb Titanite	Reference
Osborne			1600 ± 6		Gauthier et al. (2001)
Osborne			1595 ± 5		Gauthier et al. (2001)
Osborne				1595 ± 6 Ma	Gauthier et al. (2001)
Osborne		1595			Perkins and Wyborn (1998)
Osborne		1568			Perkins and Wyborn (1998)
Osborne		1540			Perkins and Wyborn (1998)
Osborne		1540			Perkins and Wyborn (1998)
Osborne		1465			Perkins and Wyborn (1998)
Osborne		1465			Perkins and Wyborn (1998)
Osborne	1573 ± 20#				Rubenach et al. (2008)
Osborne	1599 ± 10#				Rubenach et al. (2008)
Osborne	1636 ± 17#				Rubenach et al. (2008)
Osborne	1667 ± 8#				Rubenach et al. (2008)
Eloise		1555 ± 4			Baker et al. (2001)
Eloise		1530 ± 3			Baker et al. (2001)
Eloise		1530 ± 3			Baker et al. (2001)
Eloise		1521 ± 3			Baker et al. (2001)
Eloise		1514 ± 3			Baker et al. (2001)
Ernest Henry		1610 ± 2			Twyerould (1997)
Ernest Henry		1611 ± 4			Twyerould (1997)
Ernest Henry		1514 ± 6			Twyerould (1997)
Ernest Henry		1504 ± 3			Twyerould (1997)
Ernest Henry		1476 ± 3			Twyerould (1997)
Ernest Henry				1514 ± 24	Mark et al. (2006b)
Ernest Henry				1529 ± 11/8	Mark et al. (2006b)
Ernest Henry		1526			Perkins and Wyborn (1998)
Ernest Henry		1478			Perkins and Wyborn (1998)
Ernest Henry		1515 ± 15*			Perkins and Wyborn (1998)
Ernest Henry			1651 ± 6		Mark et al. (2004b)
Ernest Henry			1650 ± 6		Mark et al. (2004b)
Ernest Henry			1647 ± 6		Mark et al. (2004b)
Ernest Henry			1525		Mark et al. (2004b)